



NOVEL FABRICATION ROUTES TO NICKEL-BASED
CERMET ELECTRODES FOR
SOLID OXIDE CELLS

by

MA'AYAN MARINA LOMBERG

Department of Earth Science and Engineering

Imperial College London

United Kingdom

Submitted in partial fulfillment of the requirements for the
degree of Doctor of Philosophy and the Diploma of Imperial
College London

December, 2014

ABSTRACT

Solid oxide cells (SOCs) are promising energy conversion devices in which the chemical energy of fuels is converted into electrical energy in an efficient manner. It is generally accepted that electrode microstructure plays an important role in determining the performance and durability of SOCs. The electrode is required to contain large amount of active reaction sites, termed triple phase boundaries (TPBs), to promote the electrochemical reaction. At the same time, effective transport pathways need to be established to and from each TPB. Therefore, the microstructure-performance relationships need to be understood in order to develop highly efficient electrodes.

In this study a novel electrode, prepared by infiltration of nickel nano-particles into Gadolinium doped Ceria porous scaffold, is proposed. The research aims to understand the fundamental phenomena underpinning SOC operation for steam electrolysis/H₂ oxidation in these electrodes and to establish the relationship between the microstructure of the infiltrated electrode and electrode performance. The electronic conductivity of infiltrated electrodes was tested by the van der Pauw method over the temperature range 20-700 °C. Electrochemical behaviour was assessed for fuel cell and electrolysis modes using three electrode AC and DC measurements. The microstructure was studied by SEM and FIB techniques, including 3-D imaging and quantification. Ultimately, this is to allow electrodes to be designed with desired characteristics.

In addition, a novel approach for electrode preparation by Selective Laser Sintering (SLS) was evaluated by conducting a proof of concept study. This fabrication technique enables the porosity and pattern of the electrode to be controlled by regulating the parameters of the laser (laser power and laser speed). The feasibility of using this novel technique for solid oxide cells was demonstrated.

A method for the fabrication of high performance 'electrodes by design' through the combination of the two techniques in which the scaffold preparation by SLS is followed by infiltration is in prospect.

DECLARATION OF ORIGINALITY

I hereby confirm that the thesis is my own original work. I have compiled the thesis in my own words and have only included my own results except where indicated by referencing.

COPYRIGHT DECLARATION

The copyright of this thesis rests with the author and is made available under a Creative Commons Attribution Non-Commercial No Derivatives licence. Researchers are free to copy, distribute or transmit the thesis on the condition that they attribute it, that they do not use it for commercial purposes and that they do not alter, transform or build upon it. For any reuse or redistribution, researchers must make clear to others the licence terms of this work.

Copyright © 2014 by Marina Lomberg

ACKNOWLEDGEMENTS

I would like to express my deepest appreciation to all those who made it possible for me to complete this research.

First, I would like to express my gratitude to my supervisors – Professor Nigel Brandon, Dr Gregory Offer and Professor John Kilner. Particularly, I would like to thank Professor Nigel Brandon for his expert advice, constructive feedback and very positive attitude; and Dr Gregory Offer for his guidance and support throughout my project.

I would like to express my special appreciation to the Research Associates – Enrique Ruiz-Trejo, Vladimir Yufit and Masashi Kishimoto for valuable discussions and for sharing their knowledge and experience. Specifically, I would like to thank Enrique for his extraordinary support in setting experiments, Vladimir for the assistance with data analysis and Masashi for the collaboration on 3-D imaging.

I am grateful to Dr Chris Bocking from 3-D Systems for his guidance and help throughout the laser sintering project, for being open-minded and letting me to explore new directions.

A special thanks to all members of the Electrochemical Science and Engineering group for creating a friendly and cheerful atmosphere in the laboratory and the office, insightful conversations during lunch breaks and conference trips and fun activities outside the College.

This project would have been impossible without the financial support of the Alan Howard Foundation that provided me with the scholarship and additional funds for the project.

In addition, I would like to express my appreciation to Mrs Rivka and Professor David Jacobson for being to me like parents in London, for supporting my aspirations, and for their warm hospitality and precious advices.

Finally, I would like express my gratitude to my beloved partner Vladislav Duboviks, whom I could always rely on, for his support and love. Words cannot do justice to my feelings of gratitude towards my parents, Dina and Gregory, for their unconditional love and care, for nurturing my curiosity and for being there for me when I need them the most.

For my parents,

Dina and Gregory

ACRONYMS AND ABBREVIATIONS

| | |
|--------------------|---|
| E | Elastic modulus |
| E^0 | Reversible cell voltage in standard conditions |
| E_T | Reversible electrochemical cell potential |
| E_{Tn} | Thermo-neutral voltage |
| ρ | Material resistivity |
| T_0 | Temperature in standard conditions ($T_0 = 300K$) |
| ν | The Poisson's ratio |
| $\sigma_{thermal}$ | Thermal stress |
| E_{th} | Thermoneutral cell voltage |
| E_{td} | Thermodynamically predicted cell voltage |
| R_{avg} | Average ohmic resistance |
| R_s | Series resistance |
| j_0 | Exchange current density |
| η_{act} | Activation overpotential |
| η_{conc} | Overpotential due to transport limitations |
| η_{ohm} | Ohmic overpotential |
| ΔG^0 | Change in Gibbs free energy at standard conditions |
| ΔG | Change in Gibbs free energy |
| ΔH | Change in enthalpy |
| ΔS | Change in entropy |
| 2-D | Two dimensions |
| 3-D | Three dimensions |
| A | Electrode area |
| A | Exponential coefficient |
| AC | Alternating current |
| a_i | Activity of species i |
| ALM | Additive laser manufacturing |
| ASR | Area specific resistance |
| C | Capacity |
| c | Crack length |
| CAD | Computer-aided design |
| CE | Counter electrode |
| CHP | Combined heat and power |

| | |
|-----------|--|
| CPE | Constant phase element |
| CVD | Chemical vapour deposition |
| d | Electrode thickness |
| DFT | Density functional theory |
| DMLS | Direct metal laser sintering |
| DPB | Double-phase boundary |
| E_a | Activation energy |
| EC | Electrolysis cell |
| EDS | Energy-dispersive X-ray spectroscopy |
| EIS | Electrochemical impedance spectroscopy |
| EVD | Electrochemical vapour deposition |
| F | Faraday constant |
| FC | Fuel cell |
| FIB | Focused ion beam |
| GDC | Gadolinia-doped ceria |
| GHG | Greenhouse gas |
| HAZ | Heat-affected zone |
| h | Heat transfer coefficient |
| i | Current |
| K | Equilibrium constant |
| K_{Ic} | Fracture toughness |
| k | Thermal conductivity |
| L | Electrolyte thickness |
| L | Inductance |
| P | Laser Power |
| S | Laser Speed |
| LSCF | Strontium cobalt doped lanthanum ferrite |
| LSM | Strontium doped lanthanum manganite |
| LSR | Linear specific resistance |
| l_{TPB} | Triple phase boundary density |
| MEMS | Micro-electro-mechanical system |
| MIEC | Mixed ionic and electronic conductor |
| OCP | Open circuit potential |
| P | Gas partial pressure |
| P_{tot} | Total gas pressure |

| | |
|------------|--|
| PEMFC | Polymer Electrolyte Membrane Fuel Cell |
| R | Gas constant |
| R | Ohmic cell resistance |
| R_h | High frequency resistance |
| R_{hfi} | High frequency intercept resistance |
| R_l | Low frequency resistance |
| R_m | Medium frequency resistance |
| RE | Reference electrode |
| SDC | Samaria-doped ceria |
| SE | Sense electrode |
| SEM | Scanning electron microscopy |
| SLS | Selective laser sintering |
| SOC | Solid oxide cell |
| SOEC | Solid oxide electrolysis cell |
| SOFC | Solid oxide fuel cell |
| T | Temperature |
| TEC | Thermal expansion coefficient |
| TEM | Transmission electron microscopy |
| TPB | Triple phase boundary |
| U | Actual cell potential difference |
| V | Voltage |
| WE | Working electrode |
| YSZ | Yttria stabilised zirconia |
| Z | Impedance |
| Z_0 | Impedance magnitude |
| α | Charge transfer coefficient |
| α | Thermal expansion coefficient |
| σ_e | Electronic conductivity |
| σ_i | Ionic conductivity |
| σ | Surface free energy |
| ϕ | Phase shift |
| j | Current density |
| λ | Wavelength |
| μ_i | Chemical potential of species i |

Table of Contents

| | |
|---|-----------|
| 1. INTRODUCTION AND OBJECTIVES..... | 21 |
| 1.1 Background and motivation | 21 |
| 1.2 Objectives and scope of the thesis | 24 |
| 1.3 Brief outline of the thesis..... | 25 |
| References for Chapter I | 26 |
| 2. LITERATURE REVIEW..... | 27 |
| 2.1 Introduction..... | 27 |
| 2.2 Principles of Solid Oxide Cells..... | 28 |
| 2.3 Thermodynamics of fuel cells and electrolyzers..... | 31 |
| 2.4 Kinetics of Solid Oxide Cells..... | 33 |
| 2.5 General requirements for Solid Oxide Cell components | 36 |
| 2.5.1 Electrolytes | 36 |
| 2.5.2 General requirements for SOC electrodes | 40 |
| 2.6 Oxygen electrode for high temperature SOCs | 41 |
| 2.7 Fuel electrode for high temperature SOCs..... | 43 |
| 2.7.1 Factors affecting performance of SOC fuel electrodes..... | 43 |
| 2.7.2 Materials and performance of fuel electrodes..... | 47 |
| 2.8 Manufacturing methods for SOC electrodes..... | 53 |
| 2.8.1 Microstructural engineering..... | 53 |
| 2.8.2 Wet infiltration techniques for electrodes fabrication | 57 |
| 2.9 Direct Metal Laser Sintering for SOC electrode fabrication..... | 59 |
| 2.9.1 Introduction..... | 59 |
| 2.9.2 Principles of DMLS..... | 59 |
| 2.9.3 Process parameters..... | 62 |
| 2.9.4 Relevance to fuel cells | 65 |
| 2.10 Summary of the literature review..... | 66 |
| 2.11 Scope of this thesis..... | 67 |

| | |
|--|-----------|
| References for Chapter II..... | 68 |
| 3. GENERAL METHODOLOGY..... | 73 |
| 3.1 Introduction..... | 73 |
| 3.2 Cell preparation..... | 74 |
| 3.2.1 GDC ink preparation for fuel electrode scaffold | 75 |
| 3.2.2 Screen printing and sintering of electrodes..... | 76 |
| 3.2.3 Infiltration of Ni nano-particles in ceramic scaffolds for fuel electrodes | 78 |
| 3.2.4 Reduction of the electrode | 79 |
| 3.3 Experimental set-up for electrochemical performance measurements..... | 80 |
| 3.4 Cell performance measurements | 81 |
| 3.4.1 Electronic conductivity measurements of infiltrated electrodes | 82 |
| 3.4.2 Calculation of the theoretical open circuit potential (OCP) of the cell..... | 84 |
| 3.4.3 Electrochemical Impedance Spectroscopy | 85 |
| 3.4.4 Conditions for electrochemical performance measurements | 88 |
| 3.5 Microstructure characterisation methods | 91 |
| 3.5.1 General aspects | 91 |
| 3.5.2 3-D imaging and reconstruction methodology | 92 |
| 3.6 Summary | 94 |
| References for Chapter III..... | 95 |
| 4. NICKEL-INFILTRATED GDC ELECTRODES | 97 |
| 4.1 Introduction..... | 97 |
| 4.2 Characterisation of Ni-infiltrated GDC fuel electrodes | 98 |
| 4.2.1 2-D Microstructural analysis (SEM)..... | 98 |
| 4.2.2 3-D image reconstruction of infiltrated electrodes | 105 |
| 4.2.4 Estimation of the Ni phase content in infiltrated electrodes | 108 |
| 4.2.3 Electronic conductivity measurements | 109 |
| 4.3 Results and discussion of the electrochemical performance of Ni-infiltrated GDC electrodes in fuel cell and electrolysis mode in humidified H ₂ -H ₂ O atmospheres..... | 112 |
| 4.3.1 Validation of the 3-electrode setup measurements using symmetrical cells..... | 112 |

| | |
|--|------------|
| 4.3.2 The effect of Ni loading..... | 114 |
| 4.3.3 The effect of scaffold porosity..... | 121 |
| 4.3.4 The effect of temperature..... | 124 |
| 4.3.5 Effect of gas composition..... | 127 |
| 4.3.6 Activation energies calculation..... | 129 |
| 4.3.7 Short-term degradation study..... | 131 |
| 4.4 Conclusions for Chapter IV | 137 |
| References for Chapter IV | 142 |
| 5. LASER SINTERING FOR SOC ELECTRODE FABRICATION..... | 144 |
| 5.1 Introduction..... | 144 |
| 5.2 Objectives..... | 145 |
| 5.3 Methodology of electrode fabrication using direct laser metal sintering..... | 145 |
| 5.3.1 Equipment and design of the experiment..... | 145 |
| 5.3.2 Materials selection..... | 146 |
| 5.3.3 Flowability test of powders in Step I..... | 147 |
| 5.3.4 Estimation of the thermal shock resistance of the YSZ substrate..... | 148 |
| 5.4 Results and discussion..... | 150 |
| 5.4.1 General design of experiments | 150 |
| 5.4.2 Step I – initial investigation | 150 |
| 5.4.3 Step II – further investigation | 157 |
| 5.4.4. Step III – full cell preparation and electrochemical testing | 163 |
| 5.5 Overall conclusions..... | 172 |
| References for Chapter V..... | 174 |
| 6. GENERAL CONCLUSIONS AND OUTLOOK..... | 176 |
| 6.1 General conclusions and significance of this study | 176 |
| 6.2 Outlook..... | 179 |
| 6.3 Disseminations | 182 |
| References for Chapter VI | 184 |

Table of Figures

| | |
|---|----|
| Figure 1.1. Diagram of high temperature electrolysis for CO ₂ or H ₂ O dissociation integrated into the closed loop of CO ₂ capture and liquid synthetic fuel production using renewable energy (12)..... | 23 |
| Figure 1.2. Schematic representation of the holistic approach adopted in this study to contribute towards the ‘electrode by design’ vision..... | 24 |
| Figure 2.1. Schematics that shows key components and the working principle of a Solid Oxide Cell. The cell can operate in (a) galvanic mode (SOFC) or (b) electrolysis mode (SOEC)..... | 30 |
| Figure 2.2. Thermodynamics of H ₂ O and CO ₂ electrolysis at 1atm (18)..... | 32 |
| Figure 2.3. Schematic representation of a typical polarisation curve. The cell potential for a fuel cell decreases with increasing in cell current due to activation, ohmic and concentration polarisation (20). | 33 |
| Figure 2.4. Formation of ionically conductive YSZ cubic fluorite structure (25). | 38 |
| Figure 2.5. Effect of temperature on electrolyte ionic conductivities (7). | 40 |
| Figure 2.6. Impedance spectra taken in air at 750 °C for LSCF (left) and LSCF-50 wt% GDC (right) cathodes, adapted from (42)..... | 42 |
| Figure 2.7. Schematic view of reaction pathway at SOFC anode cermet (left); close-up of anode cermet TPB and corresponding processes (right) (44)..... | 44 |
| Figure 2.8. Variation of electrical conductivity measured at 1000 °C as a function of nickel concentration of Ni/ZrO ₂ (Y ₂ O ₃) cermet fired at different temperatures (57)..... | 46 |
| Figure 2.9. Potential of electrolyte supported cells (H ₂ electrode/YSZ electrolyte/Pt reference electrode), having Ni-YSZ, Ni-GDC and Ni/Ru-GDC H ₂ electrode as a function of current density when the electrode operated under steam electrolysis (H ₂ O/H ₂ = 50/50: 38% H ₂ O + 38% H ₂ + 24% N ₂), CO ₂ electrolysis mode (CO ₂ /CO = 50/50: 25% CO ₂ + 25% CO + 50% N ₂), and co-electrolysis of H ₂ O/CO ₂ (22% CO ₂ , 22% CO, 22% H ₂ O, 22% H ₂ , 12% N ₂) at 800 °C (41). | 51 |
| Figure 2.10. Current/overpotential of GDC-impregnated Ni-YSZ, Rh-GDC-impregnated Ni-YSZ, composite Ni-YSZ, and composite Ni-GDC electrode during electrolysis and galvanic mode (800 °C, H ₂ O/H ₂ = 70/30) (105)..... | 52 |
| Figure 2.11. Impedance spectra of fuel cell Ni-GDC anode measured under open circuit conditions at 500-650 °C using a two electrode configuration. Both NiO and GDC in the anode are synthesised by the glycine – nitrate process (92). | 52 |
| Figure 2.12. SEM micrographs of: (A) YSZ made with addition of 36wt% PMMA, (B) PMMA, (C) YSZ made with addition of 36wt% graphite and (D) graphite (117)..... | 57 |
| Figure 2.13. Infiltrated nano-structured electrodes on pre-sintered porous electrode or electrolyte scaffold/skeleton (114)..... | 58 |
| Figure 2.14. Schematic diagram of the DMLS system. | 60 |
| Figure 2.15. Diagram of laser coupling with powder. | 61 |
| Figure 2.16. Different scanning patterns of the laser beam. | 64 |

| | |
|---|----|
| Figure 2.17. Schematic diagram illustrating differences in mechanical properties through different axes of the SLS part. | 64 |
| Figure 2.18. Scan parameters in SLS (136). | 65 |
| Figure 3.1. Flow chart representing the manufacturing processes of cell preparation (1). | 75 |
| Figure 3.2. Schematic representation of the screen-printing process (2). | 76 |
| Figure 3.3. Typical process for the infiltration of metal salt nitrate solution or nanoparticle suspension into a pre-sintered electrode or electrolyte porous structure (5). | 78 |
| Figure 3.4. Thermogravimetric profile of $\text{Ni}(\text{NO}_3)_2 \cdot 6\text{H}_2\text{O}$ (6). | 79 |
| Figure 3.5. Overview of the experimental system. Underlined bold font indicates items controlled/monitored by the software on PC. | 80 |
| Figure 3.6. Schematic illustration of the rig used for electrochemical performance measurements of SOCs (7). | 81 |
| Figure 3.7. DC 4-probe electrical conductivity measurement apparatus (9). | 82 |
| Figure 3.8. Measurement of a square conductivity sample in the Van der Pauw geometry. The two resistance measurements are combined with the thickness of the sample to give the conductivity (10). | 83 |
| Figure 3.9. Theoretical calculations of the cell OCP. | 84 |
| Figure 3.10. Nyquist plots for (a) a capacitor, (b) a capacitor in series with a resistor, (c) a capacitor in parallel with a resistor, and (d) a resistor in series with a parallel RC-circuit (16). | 85 |
| Figure 3.11. Equivalent electrical circuit and schematic Nyquist plot for an electrochemical system governed by charge and mass transfer. | 86 |
| Figure 3.12. Example of an impedance spectrum. (A) Nyquist and (B) Bode plots. Numbers in Figure A indicate the measuring frequency. Points are experimental data, continuous lines represent equivalent circuit fitting and dotted lines represent the individual contributions. (C) Equivalent circuit used for fitting (20). | 87 |
| Figure 3.13. Three electrode measurements, WE – working electrode, SE – sense electrode, CE – counter electrode and RE – reference electrode. | 89 |
| Figure 3.14. Reference potential drifts with frequency. (a) Thick electrolyte — small reference drift (b) Thin electrolyte — large reference drift (24). | 90 |
| Figure 3.15. Symmetrical rig (a) four-probe set-up; (b) direction of gas flow. | 91 |
| Figure 3.16. Schematic diagram of FIB-SEM setting (31). | 93 |
| Figure 3.17 (a) Example of Ni-YSZ cermet electrode cross-sectional image obtained by FIB-SEM, in this work secondary electrons detector was used (37); (b) Reconstructed Ni-YSZ anode microstructure ($25.722 \mu\text{m} \times 11.624 \mu\text{m} \times 6.572 \mu\text{m}$; green: Ni, yellow: YSZ) (31). | 93 |
| Figure 4.1. (a) A cross section of fabricated SOC with screen printed GDC scaffold of the fuel electrode fabricated from ink#2 (at the top) and air electrode; (b) A cross section of a screen printed GDC scaffold fabricated from ink#1 and infiltrated 10 times with Ni and (c) A cross-section of a | |

screen printed GDC scaffold fabricated from ink#2 and infiltrated 10 times with Ni (at the bottom).
..... 100

Figure 4.2. The 2-D microstructure of GDC scaffolds fabricated from (a) ink#1; (b) ink#1, higher magnification and (c) ink#2 (macro-pore and micro-pore); (d) ink#2, higher magnification close up (inside the macro-pore). 101

Figure 4.3. (a) GDC scaffold covered with Ni nano particles after 5 infiltrations, reduced at 750 °C; (b) GDC scaffold covered with Ni nano particles after 5 infiltrations, reduced at 1000 °C; (c) GDC scaffold (ink#2) covered with Ni nano-particles after 10 Ni infiltrations, reduced at 750 °C; (d) SEM-EDX map of Ni distribution after 10 infiltrations of GDC ink#1 based scaffold, reduced at 750 °C (Ni in green). 102

Figure 4.4. The development of the 10 times Ni-infiltrated GDC fuel electrode microstructure after experiments performed in humidified H₂-N₂ and in the temperature range of 550-750 °C. (a)-(b) ink#2-based electrode after ~5 hrs experiment; (c)-(e) ink#2-based electrode after ~100 hrs experiment at 600 °C; (d) close-up on Ni agglomerates; (e) cross-section near the electrode-electrolyte interface; (f) ink#1-based electrode after ~320 hrs experiment at 600 °C. 104

Figure 4.5. Cross-sectional 2-D images of the electrode samples. (a) GDC scaffold; (b) 1xNi-GDC and (c) 10xNi-GDC (3). 106

Figure 4.6. Reconstructed 3-D microstructure of 1xNi-GDC and 10xNi-GDC samples. (a) Ni (green) and GDC (yellow) phases; (b) Ni with GDC (transparent grey) and (c) TPB lines with GDC (transparent grey) (3). 107

Figure 4.7. Mean vol% and wt% of Ni in Ni-infiltrated GDC electrodes as a function of number of infiltrations. 109

Figure 4.8. Temperature dependence of the DC electronic conductivity, measured by the Van der Pauw method, of infiltrated electrodes with different Ni loadings. Also shown are the electronic conductivity of nickel (9), the mixed conductivity of GDC (10) and cermet Ni-GDC electrode fabricated by screen printing. 110

Figure 4.9. Ni film formed on top of the electrode following ten Ni infiltrations; The Ni ‘islands’ are ~1 µm in thickness. 111

Figure 4.10. EIS spectra (100 mHz-100 kHz) measured in a symmetrical cell at different temperatures in 50% H₂ – 50% N₂, normalised for the individual electrode. 112

Figure 4.11. EIS spectra (100 mHz-100 kHz) measured at 690 °C in 50% H₂ – 50% N₂ in (a) symmetrical cell and (b) a fuel cell between reference and working electrodes. Note that the Ωcm² value refers to the total polarisation resistance contributed by both electrodes. 113

Figure 4.12. Current density vs overpotential of the cell with ink#2-based fuel electrodes infiltrated 0, 6 and 10 times, as measured between the reference and the working electrodes (the voltage drop includes the contributions from the infiltrated electrode and the uncompensated iR drop between the RE and WE). The cells were tested in humidified 50% H₂ – 50% N₂ at 600 °C. 114

Figure 4.13. (a) Galvanostatic impedance spectra (100 mHz-100 kHz) of the ink#2-based fuel electrodes with 0, 6 and 10 Ni infiltration repetitions at open circuit and humidified 50% H₂ – 50% N₂ at 600 °C as measured between reference and working electrodes; (b) – corresponding equivalent circuit for 0 and 6 Ni infiltrations; (c) – alternative equivalent circuit for 0 and 6 Ni infiltrations and (d) – corresponding equivalent circuit for 10x Ni infiltrations of the ink#2-based GDC scaffold. 116

| | |
|---|-----|
| Figure 4.14. (a) Temperature dependance of the oxygen partial pressure according to different hydrogen partial pressures on the fuel electrode; (b) Temperature dependance of the GDC electronic conductivity according to different hydrogen partial pressures on the fuel electrode..... | 117 |
| Figure 4.15. Schematic diagram showing the hydrogen electro-oxidation pathways (left) on Ni-YSZ-pore TPB and (right) on GDC-pore DPB. Adapted from (18)..... | 118 |
| Figure 4.16. High, medium and low frequency resistances and total electrode polarisation at open circuit for ink#2-based fuel electrodes infiltrated 0, 6 and 10 times, as measured between the reference and the working electrodes at 600 °C in humidified 50% H ₂ – 50% N ₂ . The values were taken from the best fit to the equivalent circuits shown in Figure 4.13b for 0 and 6 infiltrations, and Figure 4.13d for 10 infiltrations. | 118 |
| Figure 4.17. Current density vs overpotential of the cell with 10 times Ni infiltrated GDC fuel electrodes based on ink#1 and ink#2, as measured between the reference and the working electrodes (the voltage drop includes the contributions from the infiltrated electrode and the uncompensated iR drop between the RE and WE). The cells were tested in humidified 50% H ₂ – 50% N ₂ at 700 °C.... | 121 |
| Figure 4.18. Galvanostatic impedance spectra (100 mHz-100 kHz) of the 10xNi infiltrated GDC ink#1 and ink#2-based fuel electrodes at 700 °C in humidified 50% H ₂ – 50% N ₂ under OCP, as measured between reference and working electrodes. The inset represents the corresponding equivalent electrical circuit. | 122 |
| Figure 4.19. High and low frequency resistances and total electrode polarisation of 10xNi-GDC electrodes prepared from ink#1 and ink#2 tested at 700 °C in 50% H ₂ – 50% N ₂ under OCP, as measured between reference and working electrodes. | 122 |
| Figure 4.20. A schematic representation of the ASR as a function of porosity / infiltrated material fraction ratio for different average pore size..... | 123 |
| Figure 4.21. The <i>j-V</i> performance of the 10 times infiltrated ink#2-based GDC electrode in the range of 550-750 °C in a humidified 50% H ₂ – 50% N ₂ atmosphere in a two-electrode set-up..... | 124 |
| Figure 4.22. EIS measurements of the 10 times Ni infiltrated GDC electrode based on ink#2 at 550-750 °C in humidified 50% H ₂ – 50% N ₂ under OCP in two electrode set-up, i.e. as measured between working and counter electrodes. | 125 |
| Figure 4.23. Galvanostatic impedance spectra (100 mHz-100 kHz) at open circuit and different temperatures for 50% H ₂ – 50% N ₂ as measured between reference and working electrodes. An inset demonstrates the corresponding equivalent circuit. The value of the series resistance (R _{hfi}) was set to zero for the data presented in this study to compensate for the variable uncompensated iR drop between the WE and RE under different conditions (16). | 126 |
| Figure 4.24. High and low frequency resistances and total electrode polarisation at different temperatures and open circuit for 50% H ₂ – 50% N ₂ as measured between reference and working electrodes. | 126 |
| Figure 4.25. Galvanostatic impedance spectra (100 mHz-100 kHz) at open circuit for different H ₂ -N ₂ concentrations at 690 °C as measured between the reference and working electrodes. The inset shows the corresponding equivalent electrical circuit. | 127 |
| Figure 4.26. High and low frequency resistances and total electrode polarisation at open circuit for different H ₂ -N ₂ concentrations at 690 °C as measured between the reference and working electrode. | 128 |

| | |
|--|-----|
| Figure 4.27. Arrhenius plot of the electrode ASR associated with higher frequency polarisation over the range of temperature and H ₂ /N ₂ gas mixture ratios tested at ~OCP. Corresponding values for activation energies in both the symmetrical cell and the fuel cell are denoted..... | 129 |
| Figure 4.28. Arrhenius plot of the electrode ASR associated with low frequency polarisation over the range of temperature and H ₂ /N ₂ gas mixture ratios tested at ~OCP. | 130 |
| Figure 4.29. Current density vs overpotential on the first and fourth day of operation in 50% H ₂ – 50% N ₂ at 690 °C as measured between the working and reference electrodes (the voltage drop includes the contributions from the infiltrated electrode and the uncompensated iR drop between the RE and WE)..... | 131 |
| Figure 4.30. Galvanostatic impedance spectra (100 mHz-100 kHz) at OCP over time for 50% H ₂ – 50% N ₂ at 690 °C as measured between the reference and the working electrodes. The inset shows the corresponding equivalent circuit..... | 132 |
| Figure 4.31. Potential variations with time of the cell with GDC Ink#1-based fuel electrode with 10 Ni infiltrations in fuel cell and electrolysis modes over a period of 40-60 hrs at 600 °C in a humidified 50% H ₂ – 50% N ₂ atmosphere under 10mA and -10mA current loadings, as measured between the working and the reference electrodes. The measurements were run sequentially on the same cell.... | 134 |
| Figure 4.32. Galvanostatic impedance spectra (100 mHz-100 kHz) of the GDC Ink#1-based fuel electrode with 10 Ni infiltrations at 600 °C under OCP in a humidified 50% H ₂ – 50% N ₂ atmosphere as measured between the reference and the working electrodes on the 1 st and 13 th days of the experiment. The inset displays the corresponding equivalent circuit. | 135 |
| Figure 4.33. Current density vs overpotential of the GDC Ink#1-based fuel electrode with 10 Ni infiltrations at 600 °C under OCP in a humidified 50% H ₂ – 50% N ₂ atmosphere as measured between the working and reference electrodes on the 1 st and 13 th days of the experiment. | 135 |
| Figure 5.1. (a-b) different magnifications of the Ni – YSZ powder N3 after sintering at 1000 °C for 3 hrs; (c) original Ni powder N4. Powders specifications are listed in Table 5.1..... | 148 |
| Figure 5.2. Diagram of the YSZ pellet (substrate) carrying 5 sub-samples (S1-S5) to be laser sintered. | 150 |
| Figure 5.3. (a) top view of laser sintered sample; (b) cross section of the sample 1, sub-sample S5, fabricated with 0.25 J/mm laser energy; (c) cross section of the sample 3, sub-sample S4 fabricated with 0.05 J/mm..... | 154 |
| Figure 5.4. Tensile and compressive stresses caused to the substrate upon Ni powder melting and cooling during the laser sintering process (16). | 155 |
| Figure 5.5. (a) Cross section showing laser sintered Ni stripe on the YSZ substrate and (b) top view of a feature sintered from YSZ powder of Sample 3 (S3). | 155 |
| Figure 5.6. Sub-samples S2 and S4 (Sample 3) produced with 0.05 J/mm laser energy density using laser parameters of (a) 100 W and 2000 mm/s (b) 190 W and 3800 mm/s, respectively. | 156 |
| Figure 5.7. Laser sintering chamber during the experiment. (a) Four rows of five YSZ substrates (pellets) each used in Step II, in the last row (R4) of samples are Ni pre-metallised; (b) adjustment of a blade spreading the layers of powder (the image was taken before experiment); (c) YSZ substrates covered with Ni powder; (d) pellets with five laser sintered sub-samples each, after the experiment. | 159 |

| | |
|--|-----|
| Figure 5.8. The surface of the laser sintered patterned fuel electrodes with (a) non-metallised YSZ surface (Sample 2.2) and (b) pre-metallised YSZ surface (Sample 4.2)..... | 161 |
| Figure 5.9. (a) Wetting of a liquid on a solid substrate and the Young equation with σ_{sv} , σ_{SL} and σ_{LV} the surface free energies of the solid-vapour, solid-liquid and liquid-vapour interfaces, respectively; (b) transition from half cylinder to sphere depending on the dimensions of the molten laser pool (16). | 161 |
| Figure 5.10. Process window for iron-based powder (16). | 162 |
| Figure 5.11. Diagram of the YSZ pellet with screen-printed LSCF-GDC air electrode on one side and patterned laser sintered Ni electrode on the other side; dimensions are included..... | 164 |
| Figure 5.12. Current linear density (per unit length of TPB) vs overpotential of the cell with laser sintered patterned electrode (Sample 2.2), as measured between the reference and the working electrodes (the voltage drop includes the contributions from the infiltrated electrode and the uncompensated iR drop between the RE and WE). The cell was tested in humidified 50% H ₂ – 50% N ₂ under OCP in a 600-700 °C temperature range. Parameters for electrode fabrication are Energy Density = 0.03 J/mm (Laser Speed = 4000 mm/sec, Laser Power = 120 W). | 166 |
| Figure 5.13. Ni-YSZ anode overpotentials in various temperatures at 3% humidified condition (23). | 167 |
| Figure 5.14. Galvanostatic impedance spectra (100 mHz-100 kHz) of the laser sintered patterned electrodes normalised for length of TPB on (a) YSZ substrate (Sample 2.2) and on (b) YSZ substrate pre-metallised with Ni (Sample 4.2), tested in humidified 50% H ₂ – 50% N ₂ under OCP over a 600-700 °C temperature range, as measured between reference and working electrodes. Conditions for both electrodes fabrication are Energy Density = 0.03 J/mm (Laser Speed = 4000 mm/sec, Laser Power = 120 W). | 169 |
| Figure 5.15. (a) – (d) Laser sintered Ni pattern on pre-metallised YSZ surface, (a) and (c) SEM image; (b) and (d) SEM-EDX map of Ni distribution (green); (e) – (f) Laser sintered Ni pattern on non-metallised YSZ surface, (e) SEM image, (f) SEM-EDX map of Ni distribution (green). | 170 |

Table of Tables

| | |
|--|-----|
| Table 2.1. Comparison of fuel cell technologies (4)..... | 28 |
| Table 2.2. Comparison of the methods for producing thin and dense films for SOFC applications, adapted from (111)..... | 55 |
| Table 2.3. Examples of materials and applications of DMLS-fabricated parts (http://gpiprototype.com/)..... | 61 |
| Table 2.4. Material and process parameters in DMLS..... | 62 |
| Table 3.1. Summary of fuel cell configurations, cell dimensions and fabrication methods used in this study..... | 74 |
| Table 3.2. Materials and equipment used for ink fabrication..... | 75 |
| Table 3.3. Screen printing parameters and conditions..... | 77 |
| Table 4.1. Microstructural parameters from quantitative analysis (3)..... | 108 |
| Table 4.2. ASR values extracted from the equivalent circuit in the inset of Figure 4.30 for the cell operation over approximately 100 hrs at 690 °C under OCP and in 50% H ₂ – 50% N ₂ atmosphere.. | 132 |
| Table 4.3. ASR values extracted from the equivalent circuit in inset of Figure 4.32 for the cell operation over approximately 320 hrs at 600 °C in a humidified 50% H ₂ – 50% N ₂ atmosphere..... | 136 |
| Table 5.1. List of cermet Ni-YSZ powders used in DMLS experiment..... | 146 |
| Table 5.2. Material properties of YSZ..... | 149 |
| Table 5.3. Matrix of experiments in Step I..... | 151 |
| Table 5.4. Laser parameters used in Step I for sample 1 and the image of sample 1 after laser sintering..... | 151 |
| Table 5.5. Laser parameters used in Step I for sample 2 and the image of sample 2 after laser sintering..... | 152 |
| Table 5.6. Laser parameters used in Step I for sample 3 and the image of sample 3 after laser sintering..... | 152 |
| Table 5.7. Laser parameters used in Step I for sample 4 and the image of sample 4 after laser sintering..... | 153 |
| Table 5.8. Matrix of substrates (YSZ pellets) in Step II..... | 158 |
| Table 5.9. Laser parameters used in Step II for each sub-sample..... | 158 |
| Table 5.10. Matrix of samples and details of experiments in Step III (full cell preparation)..... | 164 |
| Table 5.11. Parameters for Ni-YSZ cermet electrode taken for calculation of LSR (23)..... | 167 |
| Table 5.12. Conclusions from the study linked to the objectives..... | 172 |

CHAPTER I

INTRODUCTION AND OBJECTIVES

1.1 Background and motivation

A rapid depletion of fossil fuels along with the pollution associated with these fuels creates major energy security and environmental concerns. According to recent estimates, the atmospheric CO₂ concentration will double by the year 2050 compared to current levels. These will result in the increase of the global average temperature by more than 2-3 °C, and may pose a serious threat to environment and socio-economic stability (1). It is likely that many delicate eco-systems will not be able to adapt, and therefore an anthropogenic increase of global average temperature can potentially lead to the extinction of many current species and significantly reduce bio-diversity (2).

In order to minimise anthropogenic CO₂ emissions and reduce the risks of climate change, the United Nations Framework Convention on Climate Change promotes innovative, cost-effective and carbon-emission-free technologies that have the potential to meet the increasing demand for primary energy without causing a negative impact on the environment (3). Hence, the investigation of renewable energy sources aiming to minimise the release of greenhouse gases (GHG) to the atmosphere has been the subject of extensive research during the past few decades (4).

Renewable energy such as solar energy, wind, tidal or ocean wave energy as well as geothermal heat are low carbon alternatives to fossil fuels. These energy sources are CO₂-neutral and therefore do

not contribute to anthropogenic CO₂ emissions. However, the implementation of these technologies on a large scale is still limited because of the cost constraints (4, 5). Equally, hydropower is an excellent alternative to fossil fuels, but the availability of hydropower is site-specific and in some areas it is already being utilized at maximum capacity (6). Geothermal power is also not ubiquitous and therefore can only provide limited and local solutions. Wind and solar energy has a very significant global potential, but requires the development of efficient, cost-effective and scalable storage capabilities because of these energy sources' inherent intermittency.

Before the full transition to renewable and carbon neutral energy can be achieved, increasing the efficiency of current technologies, both in terms of energy conversion, supply and demand, is important in order to reduce the associated anthropogenic GHG emissions. High temperature fuel cells represent a key enabling technology for the efficient power generation and storage. High temperature fuel cells are able to generate electricity as a result of electrochemical reactions between the fuel (e.g. H₂) and the oxidant (e.g. O₂) and release H₂O and heat as by-products (7). On the other hand, operation of a high temperature fuel cell in the reverse mode offers an efficient way to produce H₂ via steam electrolysis, which can be stored until required. The principles of fuel cells will be discussed in detail in the literature review. However, if hydrogen will become a significant part of global energy economy, there are number of concerns associated with H₂ production, distribution and storage, that need to be solved (8). While representing an important technology of the future hydrogen economy, high temperature fuel cells are also an essential part of the transitional energy economy, because of the unique ability to efficiently generate electricity from fossil fuels (e.g. methane) and convert GHG (e.g. CO₂) into fuel when a surplus of electricity is available. Thus, this technology can be employed to balance the grid even before the transition to a H₂ economy (9, 10).

The advantages of solid oxide fuel cells (SOFC), operating at high temperatures (700-1000 °C), are the flexibility in terms of fuel (e.g. hydrocarbons can be used as fuel) as well as higher efficiency compared to low temperature fuel cells. In addition, SOFC can be operated in a reverse mode – it is then referred to as solid oxide electrolysis cell (SOEC) – to produce fuel when excess electricity is available. One of the promising applications is biogas upgrade, the process in which CO₂ component

of the biogas mix is converted to CO via electrolysis. Equally, SOECs can be used to produce a syngas (a mixture of CO and H₂) from the electrolysis of CO₂ and steam (11-14). These fuels can either be stored or transported using the existing infrastructure.

Electricity generated by a renewable or nuclear source can be used to produce fuel in SOEC (12, 13, 15, 16). Schematics of zero-carbon emission route, where SOEC is coupled with a renewable or nuclear energy source, is illustrated in Figure 2.1 (12):

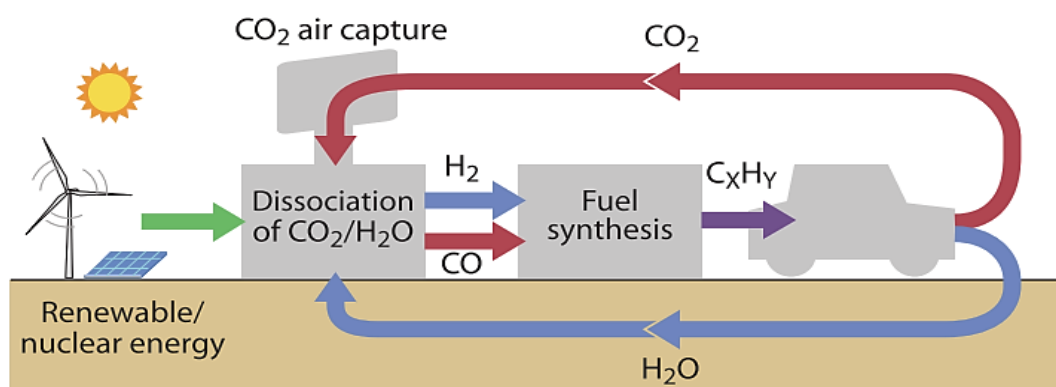


Figure 2.1. Diagram of high temperature electrolysis for CO₂ or H₂O dissociation integrated into the closed loop of CO₂ capture and liquid synthetic fuel production using renewable energy (12).

In order to operate the cell at high temperature and maximise its performance, more sophisticated materials, design and manufacturing techniques are required. In recent years, extensive research has been done in the field, as will be discussed in detail in the literature review. The main challenges associated with the SOC technology, are operation without significant degradation, high performance and low cost. Manufacturing methods along with the materials selection have an impact on the microstructure of the cell electrodes, which in turn affects the performance. Therefore, finding both an appropriate combination of materials and a way to control the microstructure during cell fabrication is a key for the optimisation of solid oxide cell (SOC) performance.

The strategy ‘electrode by design’ is adopted in this study. The concept means that the microstructure and the performance of the electrode will have to be determined by carefully tailoring the processing parameters and/or using different materials combinations. To achieve the ‘electrode by design’ vision, a holistic approach is used. This includes establishing an empirical relationship

between the experimental data and the results of 3-D image reconstruction and modeling. This approach is schematically shown in Figure 2.2.

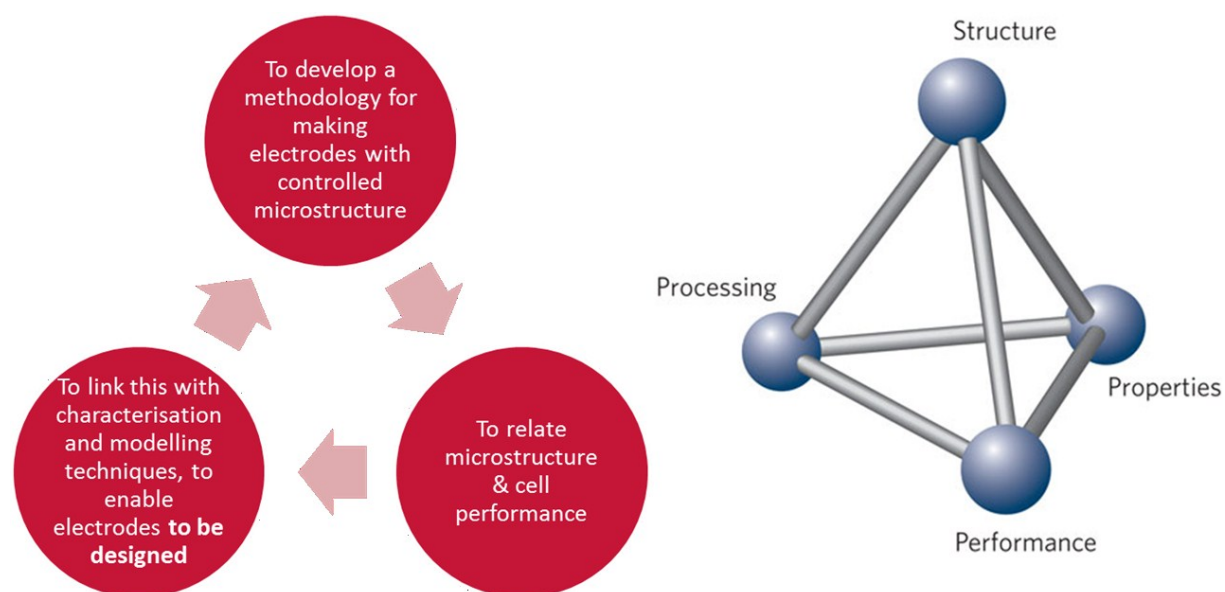


Figure 2.2. Schematic representation of the holistic approach adopted in this study to contribute towards the ‘electrode by design’ vision.

1.2 Objectives and scope of the thesis

The objectives of this thesis are twofold. The first objective was to explore the capabilities of the infiltration technique for fuel electrode fabrication. Specifically, the fuel electrode was fabricated by infiltration of a porous Gadolinia-doped Ceria (GDC) scaffold with Ni nano-particles. The combination of Ni and GDC was chosen due to the high catalytic activities of these materials towards H_2 and/or CO_2 oxidation, the high electronic conductivity of Ni, and the mixed-conductivity of GDC. The main attractiveness of infiltration technique is that the key parameters of the porous scaffold can be controlled independently of the fraction of infiltrated material. While Ni and GDC have been used in SOC electrodes in the past, the infiltration of GDC scaffolds with Ni has not been previously reported. This study explores the microstructural development during multiple Ni infiltrations, the electrochemical performance of these electrodes, as well as short-term degradation performance in H_2 atmospheres at 550-750 °C. For the first time the 3-D image reconstruction method was applied to characterize the microstructure of infiltrated electrodes.

The second objective of this work is to evaluate a Selective Laser Sintering (SLS) technique for SOC electrode fabrication as a proof of concept. No studies have been reported regarding the fabrication of SOC electrodes using SLS, thus making the present research the first of its kind. By regulating the parameters of the laser (laser power and laser speed) this method enables the porosity and pattern of the electrode to be controlled. Furthermore, this technique is scalable and thus can potentially offer an effective way of manufacturing the cells. The feasibility of this novel technique for the use in the field of solid oxide cells is demonstrated.

As the next step, SLS and infiltration techniques may be combined together to form unique microstructures of SOC electrodes with in a highly controllable and defined way. Ceramic or metal scaffolds may be infiltrated with catalyst, enabling the ‘electrodes by design’ in order to create SOC electrodes with high performance.

1.3 Brief outline of the thesis

The structure of the thesis is as follows. In Chapter II the principles of fuel cells and the materials requirements for SOC components are outlined. The key publications on fuel electrode materials and performance are also discussed in this chapter. A large part of this chapter is dedicated to the relationship between electrode material, fabrication methods, microstructure and performance, as well as identifying current gaps in knowledge in this field. The concepts of the SLS technology and the process parameters, critical for the microstructure, are introduced.

In Chapter III, the experimental methodology is described. This includes techniques for electrode fabrication, cell performance testing and characterisation of the electrode microstructure. Chapter IV presents the results of the electrochemical performance of the cells and characterisation of the Ni-infiltrated GDC electrodes, followed by discussion and conclusions.

Chapter V outlines the design of the experiments and the procedure of the electrodes’ fabrication by laser sintering technique. The results are discussed in terms of microstructure and electrochemical

performance. This is followed by discussion regarding the feasibility of this technique for SOC electrode fabrication and recommendations for future work.

Finally, general conclusions of this study and the outlook are summarized in Chapter VI.

References for Chapter I

1. M. Mastrandrea and S. Schneider, *Science*, **304**, 571 (2004).
2. S. Solomon, Q. Dahe and M. Manning, Intergovernmental Panel on Climate Change (IPCC), in *Climate Change 2007*, p. 996, Cambridge Univ Press, New York (2007).
3. United Nations Framework Convention on Climate Change, in *UNEP/WMO, Climate Change Secretariat*, Geneva (1992).
4. M. Ni, M. Leung and D. Leung, *International Journal of Hydrogen Energy*, **33**, 2337 (2008).
5. S. H. Jensen, P. H. Larsen and M. Mogensen, *International Journal of Hydrogen Energy*, **32**, 3253 (2007).
6. A. Kumar, T. Schei, A. Ahenkorah, R. Caceres Rodriguez, J.-M. Devernay, M. Freitas, D. Hall, Å. Killingtveit, Z. Liu, Hydropower: In IPCC Special Report on Renewable Energy Sources and Climate Change Mitigation, Cambridge, United Kingdom and New York, NY, USA (2011).
7. L. Schlapbach and A. Züttel, *Nature*, **414**, 353 (2001).
8. S. Satyapal, J. Petrovic, C. Read, G. Thomas and G. Ordaz, *Catalysis Today*, **120**, 246 (2007).
9. R. P. O'Hayre, *Fuel cell fundamentals*, John Wiley & Sons (2006).
10. W. K. Zhongliang Zhan, James R. Wilson, Manoj Pillai, Ilwon Kim, Scott A. Barnett, *Energy & Fuels* **23**, 3089 (2009).
11. S. D. Ebbesen, C. Graves and M. Mogensen, *International Journal of Green Energy*, **6**, 646 (2009).
12. C. Graves, S. D. Ebbesen and M. Mogensen, *Solid State Ionics*, **192**, 398 (2011).
13. C. Graves, S. D. Ebbesen, M. Mogensen and K. S. Lackner, *Renewable and Sustainable Energy Reviews*, **15**, 1 (2011).
14. M. Mogensen, S. H. Jensen, A. Hauch, I. Chorkendorff and T. Jacobsen, *Fuel Cell*, 1 (2006).
15. S. C. Singhal, *Solid State Ionics*, **135**, 305 (2000).
16. A. Hauch, S. D. Ebbesen, S. H. Jensen and M. Mogensen, *Journal of Materials Chemistry*, **18**, 2331 (2008).

CHAPTER II

LITERATURE REVIEW

2.1 Introduction

The aim of this literature review is to outline the challenges in materials and microstructure of state of the art SOCs, and to highlight the importance of the present study to the field of solid oxide fuel cells. The literature survey starts with an overview of the fundamental principles of Solid Oxide Cells. In this part the thermodynamics and kinetics of SOCs will be explained. Then, the materials used for the cell electrodes and the electrolyte, as well as the requirements dictating the selection of these materials, will be outlined. The emphasis is put on ceria and nickel based electrodes for SOCs. The role of electrode microstructure will be discussed in detail, as it is directly related to the fabrication method. The review includes an introduction to conventional techniques for electrode fabrication, and highlights the relevance of novel approaches deployed in this research, such as infiltrated ceria scaffolds and laser sintering.

2.2 Principles of Solid Oxide Cells

Brief history of fuel cells

The principle of a fuel cell, i.e. conversion of chemical energy into electrical energy, was first described in the Philosophical Magazine and Journal of Science by Welsh scientist and barrister Sir William Robert Grove (1811-1896) in 1839 (1). At the end of the 19th century, German chemists Walther Hermann Nernst (1864-1941) and Fritz Haber (1868 –1934) devoted much effort to investigate direct carbon-oxidizing fuel cells (2). Since then, in spite of potentially high efficiencies and environmental benefits associated with fuel-cell technology, it has proved difficult to develop the early scientific experiments into commercial products. This was due to the lack of appropriate materials or manufacturing routes that would enable the cost-efficient production (3).

However, in the past decades several types of fuel cells have been proposed. Fuel cells can be divided into groups according to electrolyte type or operating temperatures. Their main features, technological applications and working conditions are summarized in Table 2.1 (4).

Table 2.1. Comparison of fuel cell technologies (4).

| Fuel Cell Type | Common Electrolyte | Operating Temperature | Typical Stack Size | Efficiency | Applications | Advantages | Disadvantages |
|---|--|--|------------------------------|--------------------------------------|--|--|--|
| Polymer Electrolyte Membrane (PEM) | Perfluoro sulfonic acid | 50-100°C 122-212° typically 80°C | < 1kW-100kW | 60% transportation 35% stationary | <ul style="list-style-type: none"> • Backup power • Portable power • Distributed generation • Transportation • Specialty vehicles | <ul style="list-style-type: none"> • Solid electrolyte reduces corrosion & electrolyte management problems • Low temperature • Quick start-up | <ul style="list-style-type: none"> • Expensive catalysts • Sensitive to fuel impurities • Low temperature waste heat |
| Alkaline (AFC) | Aqueous solution of potassium hydroxide soaked in a matrix | 90-100°C 194-212°F | 10-100 kW | 60% | <ul style="list-style-type: none"> • Military • Space | <ul style="list-style-type: none"> • Cathode reaction faster in alkaline electrolyte, leads to high performance • Low cost components | <ul style="list-style-type: none"> • Sensitive to CO₂ in fuel and air • Electrolyte management |
| Phosphoric Acid (PAFC) | Phosphoric acid soaked in a matrix | 150-200°C 302-392°F | 400 kW 100 kW module | 40% | <ul style="list-style-type: none"> • Distributed generation | <ul style="list-style-type: none"> • Higher temperature enables CHP • Increased tolerance to fuel impurities | <ul style="list-style-type: none"> • Pt catalyst • Long start up time • Low current and power |
| Molten Carbonate (MCFC) | Solution of lithium, sodium, and/or potassium carbonates, soaked in a matrix | 600-700°C 1112-1292°F | 300 kW-3 MW 300 kW module | 45-50% | <ul style="list-style-type: none"> • Electric utility • Distributed generation | <ul style="list-style-type: none"> • High efficiency • Fuel flexibility • Can use a variety of catalysts • Suitable for CHP | <ul style="list-style-type: none"> • High temperature corrosion and breakdown of cell components • Long start up time • Low power density |
| Solid Oxide (SOFC) | Yttria stabilized zirconia | 700-1000°C 1202-1832°F | 1 kW-2 MW | 60% | <ul style="list-style-type: none"> • Auxiliary power • Electric utility • Distributed generation | <ul style="list-style-type: none"> • High efficiency • Fuel flexibility • Can use a variety of catalysts • Solid electrolyte • Suitable for CHP & CHHP • Hybrid/GT cycle | <ul style="list-style-type: none"> • High temperature corrosion and breakdown of cell components • High temperature operation requires long start up time and limits |

The development of the fuel cell technology led to the improvement of the fuel cell performance and, consequently, to an emergence of cost effective commercially available fuel cell products, such that micro-combined heat and power (CHP) PEMFC units (produced by Ene-Farm, Japan) or SOFC units (produced by Ceramic Fuel Cells Limited, Germany) (5).

Solid Oxide Cells operation

The focus of the present study is a Solid Oxide Cell (SOC). A SOC can be operated in two modes. First mode is a power generator, known as Solid Oxide Fuel Cell (SOFC), in which hydrogen or hydrocarbons are utilized as a fuel and are converted directly into electrical energy by means of electrochemical reactions. In contrast to an internal combustion engine, in which chemical energy is transformed into heat and then into electrical energy, in an SOFC this intermediate step is avoided. Therefore, the SOFC efficiency is not limited by the Carnot cycle and, theoretically, higher efficiencies can be achieved (6, 7).

In the second mode an SOC can be operated in reverse. In this case SOC is normally referred to as a Solid Oxide Electrolysis Cell (SOEC), where fuel production (hydrogen or syngas) is possible through high temperature electrolysis of steam and/or CO₂ (8-10). Therefore, an advantage of an SOC is the ability to have a unit where either electricity or fuel can be produced according to demand. This feature is of particular interest when fuel cells and electrolyzers are coupled with intermittent renewable power sources to convert a surplus energy into gas or liquid fuels (11). Also the capability of utilising hydrocarbon fuels enables natural gas and its derivatives to be used more efficiently and in a sustainable manner, for example in micro-CHP systems for residential purposes (12, 13). When operating on hydrogen, SOFC offers an environmentally friendly energy source with zero local emissions (14).

SOCs possess other advantages with respect to other cell fuel types. Since SOC operate at high temperatures, no precious metal catalysts (such as platinum used in low temperature fuel cells) are

required (15). Elevated temperatures (500 – 1000 °C) are favourable for the chemical reaction kinetics which leads to decreased internal cell resistances, resulting in increased cell efficiencies.

An SOC consists of a solid dense electrolyte and two porous electrodes: anode and cathode. The cathode is the electrode at which the reduction of the reactant takes place, and the anode is the electrode at which the oxidation occurs (16).

Figure 2.1 shows the key components and working principles of a SOFC and a SOEC. When a system with H_2 fuel is considered in galvanic (spontaneous process, thermodynamically favoured) normally referred to as SOFC mode (Figure 2.1a), fuel (H_2) is fed to the anode (negative electrode) and the oxidant (O_2 or air) is fed to the cathode (positive electrode). Fuel reacts (oxidizes) with oxygen ions, conducted through the electrolyte, to form products (H_2O), heat and electrons, which are transferred through the external circuit forming electric current. The reaction continues as long as fuel is provided to the cell and the load is applied to the external circuit.

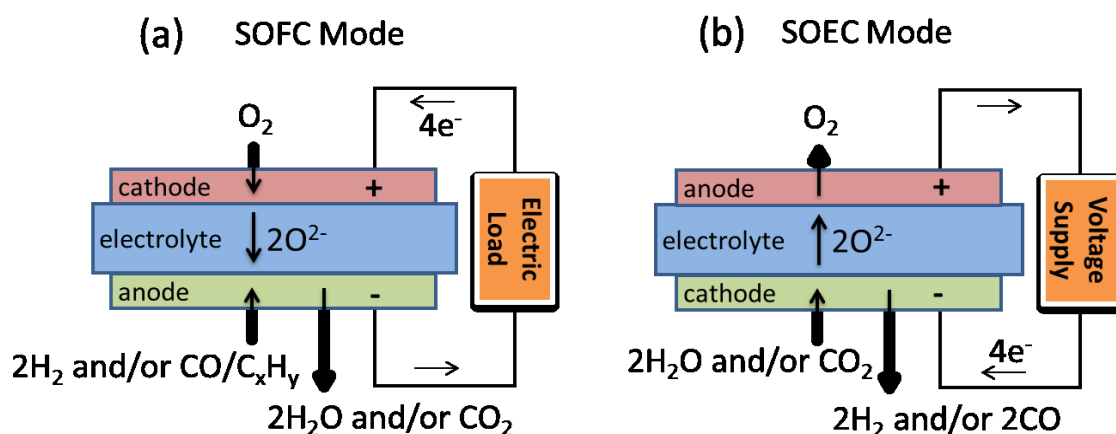


Figure 2.1. Schematics that shows key components and the working principle of a Solid Oxide Cell. The cell can operate in (a) galvanic mode (SOFC) or (b) electrolysis mode (SOEC).

In electrolysis mode (Figure 2.1b), electrons are supplied to the cathode from the external power source. Under electric current and heat, steam, which is supplied to the anode, is reduced to products (H_2 and O^{2-}). Oxygen ions then migrate through the electrolyte from the cathode to the anode and are oxidized to form oxygen molecules (17).

Electrochemical reactions on the electrodes in fuel cell mode can be summarized as follows:

| | |
|---|---|
| <p>Oxidation of fuel (hydrogen and/or reformed hydrocarbons) is catalysed on the anode. Half-cell reactions on the anode:</p> $H_{2(g)} + O^{2-} \xrightarrow{\text{heat, catalyst}} H_2O + 2\bar{e}$ $CO_{(g)} + O^{2-} \xrightarrow{\text{heat, catalyst}} CO_2 + 2\bar{e}$ | <p>Reduction of oxygen is catalysed on the cathode. Half-cell reaction on the cathode:</p> $\frac{1}{2}O_2 + 2\bar{e} \rightarrow O^{2-}$ |
| <p>The overall reaction:</p> $H_2 + \frac{1}{2}O_2 \xrightarrow{\text{heat}} H_2O \quad \text{and/or} \quad CO + \frac{1}{2}O_2 \xrightarrow{\text{heat}} CO_2$ | |

The thermodynamic and kinetic aspects of an SOC are described in the next section.

2.3 Thermodynamics of fuel cells and electrolyzers

In terms of thermodynamics, the total energy demand (ΔH , the enthalpy change in J/mol) for a reaction is expressed as:

$$\Delta H = \Delta G + T\Delta S \quad 2.1$$

where ΔG is electrical energy (Gibbs free energy change, in J/mol) and $T\Delta S$ is the thermal energy (T - temperature of the reaction in K, ΔS - the formation entropy change, in J/K·mol) needed for the process.

The electrochemical processes in a fuel cell become increasingly exothermic with temperature, while the electrolysis reactions become increasingly endothermic with temperature. As the total energy demand (ΔH) is almost independent of temperature, as shown in Figure 2.2 (18), the electrical energy demand for electrolysis will, in theory, become lower at higher temperatures. For this reason (but not solely, as will be described further), it is desirable to operate SOCs at higher temperatures.

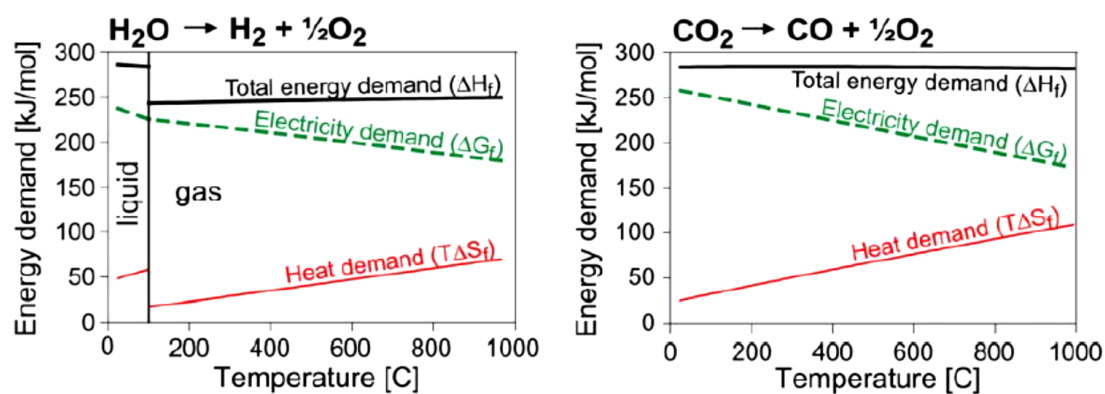


Figure 2.2. Thermodynamics of H_2O and CO_2 electrolysis at 1atm (18).

If the heat from irreversible losses (overpotentials) balances the endothermic requirement of electrolysis reaction, the cell operates at thermo-neutral conditions. The thermo-neutral voltage (E_{Tn}), required for thermo-neutral conditions, is defined as:

$$E_{Tn} \equiv \frac{\Delta H}{nF} = \frac{\Delta G}{nF} + \frac{T\Delta S}{nF} \quad 2.2$$

where n is the electron stoichiometry of the electrolysis reaction and F is the Faraday constant, $F = 96485 [\text{C} \cdot \text{mol}^{-1}]$.

If the cell voltage is above E_{Tn} , then excess heat is produced. Alternatively, if the cell voltage is below E_{Tn} , the heat needed for the electrolysis must be provided by external sources.

The reversible electrochemical cell voltage E known as open circuit potential (OCP) is determined by the Gibbs' free energy of the reaction and therefore depends on its chemical activity and temperature according to Nernst equation (2.3):

$$E = \frac{dG}{nF} = \frac{dH}{nF} - \frac{TdS}{nF} = E^0 - \frac{RT}{nF} \ln \frac{\prod a_{products}^{\nu}}{\prod a_{reactants}^{\nu}} \quad 2.3$$

where E^0 is the reversible cell potential at a standard pressure and temperature (1atm, 300K), R is the gas constant ($R = 8.314 \text{ J/K} \cdot \text{mol}$), a - activity of products or reactants and ν is a corresponding stoichiometric coefficient in a chemical reaction. For reactants/products in gas state (assuming ideal gas) $a = \frac{P}{P_{tot}}$, where P is the partial pressure of individual gasses and P_{tot} is the total

pressure of all present gases. At the temperature $T \neq T_0$, where T_0 is a temperature at standard conditions ($T_0 = 300K$), the reversible electrochemical cell potential E_T is given as:

$$E_T = E^0 + \frac{\Delta S}{nF}(T - T_0) \quad 2.4$$

2.4 Kinetics of Solid Oxide Cells

Thermodynamics provides the theoretical (or ideal) limits for fuel cells performance. Even though the thermodynamically attainable efficiency of SOFCs is high in comparison with that of combustion engines, overpotentials (or polarisation losses) prevent the cell from achieving its maximum theoretical performance (19). Therefore, thermodynamics alone cannot account for cell behaviour, since thermodynamic calculations are only valid when all the cell species exist in the equilibrium conditions and the internal losses are not taken into account. For that reason, kinetic calculations are necessary in order to fully describe electrochemical behaviour.

Major factors that contribute to the SOC resistance are activation overpotential, ohmic losses and concentration overpotential, as shown in Figure 2.3 (20).

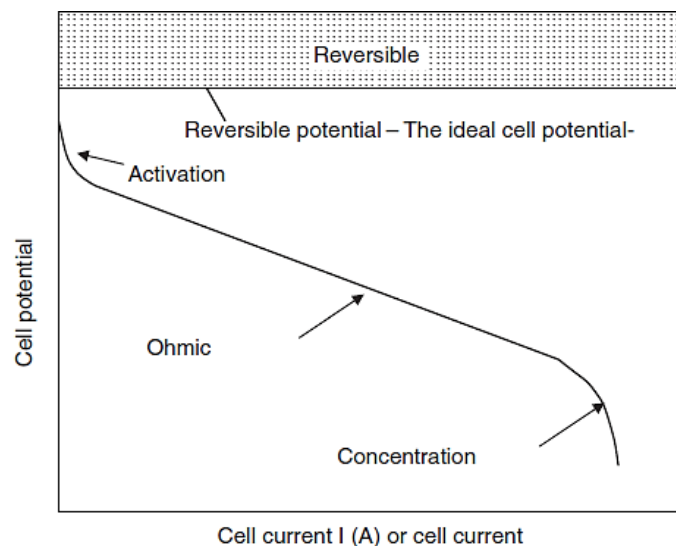


Figure 2.3. Schematic representation of a typical polarisation curve. The cell potential for a fuel cell decreases with increasing in cell current due to activation, ohmic and concentration polarisation (20).

Activation loss - η_{act}

Some part of the cell voltage is lost due to the activation barrier for the electrochemical reaction to occur. This voltage is known as activation overpotential, η_{act} . Activation polarisation is usually dominant at low current densities (7). Activation loss is related to the charge transfer process and depends on the concentration of electrode/electrolyte/gas triple-phase boundaries (TPBs) and the electrocatalytic properties of the electrode (21). TPBs will be discussed in detail in further sections.

In the absence of activation overpotential, the exchange current density, j_0 (in Acm^{-2}), measures the equilibrium flow of electrons, both in forward and backward directions. The relationship between actual current density output, j , and the activation overpotential, η_{act} , is described by the Butler-Volmer Equation:

$$j = j_0 \left(\exp \left[\frac{\alpha n F \eta_{act}}{RT} \right] - \exp \left[\frac{-(1-\alpha) n F \eta_{act}}{RT} \right] \right) \quad 2.5$$

where α is called the charge transfer coefficient and indicates the symmetry of an electrochemical reaction on the electrodes, namely the effect of the forward versus reverse activation barrier on the change in electrical potential. Its values are between 0 and 1 and are assumed to be 0.5 for typical fuel cell electrode materials.

At high activation overpotentials the graph of η_{act} versus the logarithm of current density approximates to a straight line. In this region the Butler-Volmer equation can be simplified and reduced to the Tafel Equation for an oxidation reaction:

$$j = j_0 \exp \left[\frac{\alpha n F \eta_{act}}{RT} \right] \quad 2.6$$

This equation may be used to find exchange current density and activation overpotential. Activation polarisation can be minimised by maximising the effective exchange current density which, in turn, depends on catalyst activity, temperature, concentration of reactants and especially on the number of reaction sites, where electrochemical reaction takes place.

Ohmic loss or charge transport loss - η_{ohm}

The voltage that is expended to drive conductive charge transport (electrons and ions) represents an ohmic loss to a cell potential. This voltage loss obeys Ohm's law in the absence of concentration gradients:

$$\eta_{ohm} = i \cdot R \quad 2.7$$

where R is Ohmic cell resistance (in Ω) and depends on the material resistivity, ρ , the thickness of electrolyte, L , and electrode surface area, A as:

$$R = \rho \frac{L}{A} \quad 2.8$$

The ohmic overpotential is usually dominated by the electrolyte resistance, since ion conductivity in typical SOC electrolyte materials is four to eight orders of magnitude lower than the electron conductivity of the relevant SOC components and therefore might become a limiting parameter in SOC performance. The electrolyte conductivity increases with temperature. For this reason operating SOCs at elevated temperatures results in better cell performance (7).

The other factor that can contribute to the ohmic loss is the electrical resistance of the SOC electrode which is comprised of internal resistance and contact resistance. The internal resistance refers to the poor transport of electrons within the electrode, and therefore, is determined by the magnitude of electronic resistivity and thickness of electrode. Additional contact resistance may be caused by poor adherence between electrodes and electrolyte (21).

Usually, area-specific cell resistance (ASR, in Ωcm^2) is used to be able to compare the performance of the cells with different sizes. ASR is defined as:

$$ASR = A \cdot R, \quad 2.9$$

where A is geometrical area of electrode.

Concentration loss or mass transport loss - η_{conc}

The supply and removal of reactants and products in a fuel cell or electrolyser are governed by mass transport, which is typically dominated by diffusion of the fuel to the reactant sites and diffusion of products out of the cell. Concentration polarisation becomes rate determining at higher current densities and/or low reactant partial pressures. Poor mass transport leads to reduced reactant concentration (reactant depletion) at the TPBs, and results in the decrease of the cell potential because of the sluggish kinetics. As concentration polarisation is related to the transport of gaseous species through the porous electrodes, its magnitude is dictated by the microstructure of the electrode, i.e. porosity, pore size, and the tortuosity factor (22). These will be discussed in detail in section 2.7.1.

Taking into account overpotentials associated with different mechanisms, the actual cell potential, U , can be expressed as:

$$U = E - \eta_{act,anode} - \eta_{act,cathode} - \eta_{ohmic} - \eta_{conc,anode} - \eta_{conc,cathode} \quad 2.10$$

Thus, microstructure optimisation and careful material selection are essential to minimise potential losses and therefore improve cell performance.

2.5 General requirements for Solid Oxide Cell components

There is a strong link between material properties and the performance of the SOC in terms of electrical and fuel efficiency, durability, and chemical and mechanical stability. It is desirable to gain a good SOC performance in both FC and EC modes, therefore understanding the challenges related to both processes is essential. This section outlines requirements and state-of-the-art materials used for SOC (with an emphasis on fuel electrode materials).

2.5.1 Electrolytes

The electrolyte in high temperature fuel cells functions as an ionic conductor between two electrodes. It carries the oxygen ions from cathode to anode (or vice versa depending on the mode of

operation) to balance the charge from the electron flow and complete the electrical circuit in the cell as shown in Figure 2.1.

The electrolyte materials for SOCs are therefore required to be (21, 23):

- Stable at high operating temperatures,
- Stable in both highly reducing and highly oxidizing environments,
- Of high ionic conductivity (normally higher than $1 \times 10^{-3} \text{ Scm}^{-1}$) and low electronic conductivity,
- Compatible with electrode materials in terms of chemical stability and thermal expansion,
- Dense to avoid gas leakage,
- Thin to reduce ionic resistance,
- Resistant to thermal cycling and mechanically stable,
- Of low cost.

The most common material for this application is Y_2O_3 -stabilized ZrO_2 (YSZ) (24). This material exhibits good thermal and chemical stability, high ionic conductivity, does not conduct electrons and is mechanically robust at elevated temperature.

Pure zirconia possesses polymorphism – different crystalline structures at different temperatures. At high temperatures (above $\sim 2400^\circ\text{C}$) it has a dense cubic structure, but at lower temperatures its structure transforms into tetragonal (above $\sim 1000^\circ\text{C}$) and monoclinic phases, which are less dense. Due to low thermal conductivity and polymorphism with associated lattice expansion, pure zirconia has low thermal shock resistance. However, the cubic fluorite structure can be stabilized at lower temperatures by doping zirconia with divalent or trivalent larger cations such as Ca^{2+} or Y^{3+} (Figure 2.4).

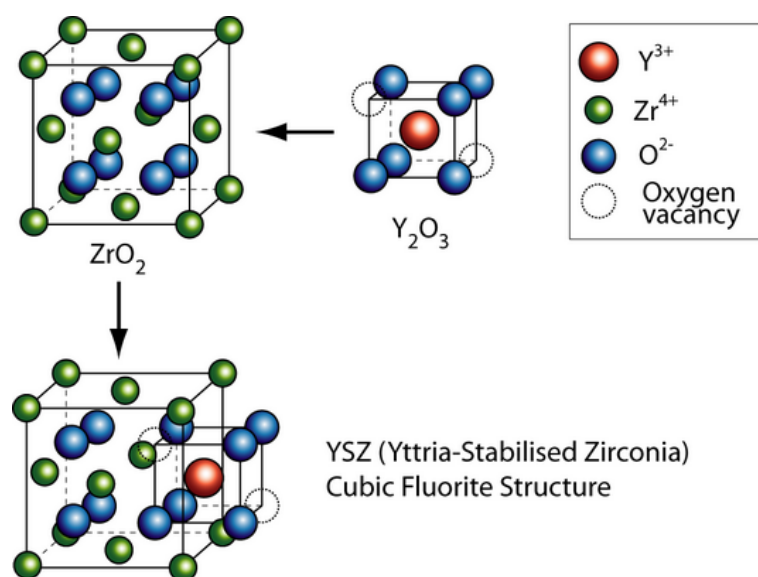
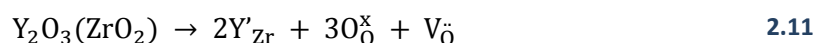


Figure 2.4. Formation of ionically conductive YSZ cubic fluorite structure (25).

When some fraction of Zr^{4+} ions are substituted by lower valence cations, the concentration of oxygen ions decrease to maintain electro-neutrality, thereby introducing oxygen vacancies. The concentration of vacancies is defined by the concentration of dopant, i.g. $2[Y'_{Zr}] = [V_{O\cdot}]$ in the case of yttria stabilized zirconia. Oxygen vacancies enable the ionic (O^{2-}) conductivity of YSZ. The vacancies formation can be shown by Kroger-Vink notation in eq. 2.11.



About 8-9 mol% Y_2O_3 is needed for stabilization of the cubic structure of zirconia (7). Another commonly used stabilising dopants are CaO, MgO, Sc_2O_3 and certain rare earth oxides such as Nd_2O_3 , Sm_2O_3 , and Yb_2O_3 . A correlation has been found between dopant ionic radius and the ionic conductivity. The highest ionic conductivity was observed for the Sc^{3+} cations, having the ionic radius closest to that of Zr^{4+} (26).

Ceria (or cerium oxide) based ceramics can also be used as electrolytes in SOCs (14). Ceria possesses a cubic fluorite structure that is stable throughout the whole temperature range relevant to SOC operation. Dopants, used to introduce ionic conductivity, mostly include samarium, $(Ce_{0.85}Sm_{0.15})O_{1.925}$ (SDC) and gadolinium $(Ce_{0.90}Gd_{0.10})O_{1.95}$ (GDC). Ceria based electrolytes are mostly favourable for intermediate (500-800 °C) temperature application, due to their high ionic conductivity in this temperature range. Since cerium has two oxidation states (Ce^{4+} and Ce^{3+}), mixed

ionic and electronic conductivity appears at high temperatures ($> 600\text{ }^{\circ}\text{C}$) in reducing environments (27-29). Mineshige et al found that SDC becomes electronically conductive when the partial pressure of oxygen is less than 10^{-8} atm , and total conductivity increases with decreasing $P(\text{O}_2)$ (30). The boundary between electronically conductive and non-conductive behaviour moves to higher oxygen partial pressures as the temperature increases, as expected from the temperature dependence of electronic conductivity (31).

However, electronic conductivity is an unwanted property for SOC electrolytes, therefore co-doping or use of a blocking layer are needed to avoid unwanted reduction (32). Nevertheless, mixed ionic-electronic conductivity could be a favourable property when ceria-based ceramics are used in scaffolds for SOC electrodes, as discussed further in section 2.7.2.

Variation of the electrolyte ionic conductivity with temperature usually obeys Arrhenius law and is a function of dopant concentration (7) according to eq. 2.12 (33).

$$\sigma = \frac{A}{T} [V_{\ddot{o}}](1 - [V_{\ddot{o}}]) \exp\left(-\frac{E_a}{RT}\right) \quad 2.12$$

where E_a is the activation energy for conduction, R – the gas constant, T – absolute temperature, and A – the exponential coefficient.

The ionic conductivity at constant temperature increases with the concentration of vacancies in the lattice. However, there is a maximum concentration after which ionic conductivity will further decrease due to interaction between the substitutional cations and the oxygen vacancies they introduce.

As can be seen the ionic conductivity of the electrolyte increases with temperature (Figure 2.5), therefore operating SOCs at higher temperatures will lead to lower ohmic resistances.

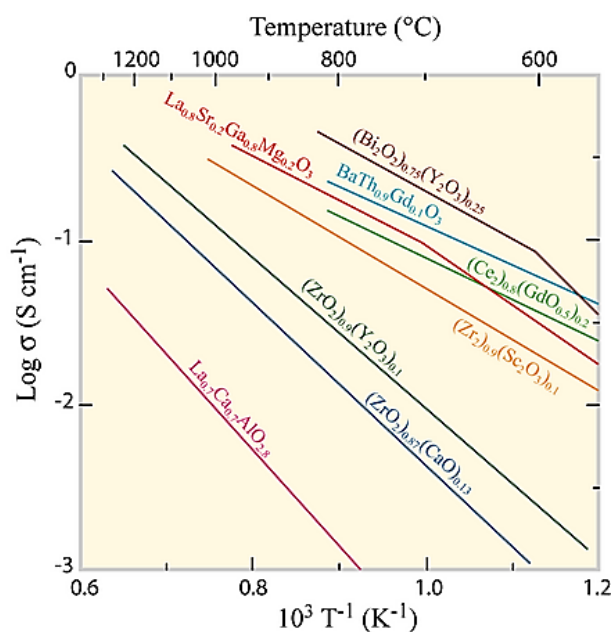


Figure 2.5. Effect of temperature on electrolyte ionic conductivities (7).

Another important parameter of the electrolyte is its thickness. The resistance of the cell can be reduced using thinner electrolytes. In this case the temperature of operation can be considerably reduced (34). However, the mechanical stability of the cell might be affected (23).

2.5.2 General requirements for SOC electrodes

In order to facilitate the electrode reactions, the following requirements for SOC electrodes' materials should be fulfilled (17, 24, 35, 36):

- Both electrodes should be chemically stable in the highly reducing/oxidizing environments and high temperatures.
- Electrodes should have good electronic conductivity, ionic conductivity and catalytic activity.
- Electrodes should be mechanically stable.
- Both electrodes should have porosity in order to:
 - Support gas transport between the electrode surface and the electrode–electrolyte interface
 - Allow the reactants and products to enter or exit the active sites in the electrode.
 - Provide high TPB densities.

- Thermal expansion coefficients of both electrodes should be close to that of the electrolyte to prevent material failure of the electrolyte due to high mechanical stress induced by thermal expansion mismatch.
- Electrodes should be durable at high current density operation.

In general, factors which affect electrode performance are intrinsic properties of the materials used (electrical and ionic conductivities, catalytic properties), interaction between different materials in the electrode (wettability, chemical interactions), manufacturing process (sintering temperature and duration), powder quality (particle size and powder purity) and microstructure (porosity, pore size, distribution across the electrode). Aspects relevant to this study will be discussed further.

2.6 Oxygen electrode for high temperature SOCs

The main functions of the cathodes in SOFCs (anode in SOEC) are: transport of oxygen to the electrode-electrolyte interface, reduction of oxygen, transport of oxygen ions to the electrolyte and distribution of the electrical current associated with the oxygen reduction reaction. It is generally recognized that a significant portion of the total polarisation losses originate in the cathode (37).

The state-of-the-art oxygen electrode is a porous electronically conductive ceramic composite, typically the mixture of Sr doped LaMnO_3 (LSM) and YSZ (LSM-YSZ). The thermal expansion coefficient of LSM is close to that of the YSZ electrolyte ($10.6\text{-}11 \times 10^{-6} \text{ K}^{-1}$), which ensures good adhesion between these materials. However, in electrolysis mode delamination at the electrode/electrolyte (LSM-YSZ/YSZ) interface caused by pressure differences occurring upon O_2 evolution in closed pores has been reported (38). When tested in fuel cell mode, degradation of the O_2 electrode performance is known to be caused by formation of secondary poorly conductive phases such as $\text{La}_2\text{Zr}_2\text{O}_7$ or SrZrO_3 (39).

The electrochemical properties of $\text{La}_{0.8}\text{Sr}_{0.2}\text{MnO}_3$ (LSM) – YSZ, $\text{La}_{0.8}\text{Sr}_{0.2}\text{FeO}_3$ (LSF) – YSZ, and $\text{La}_{0.8}\text{Sr}_{0.2}\text{CoO}_3$ (LSCo) – YSZ electrodes for use in fuel cell and electrolysis modes have been previously assessed (40). According to this study, LSF-YSZ and LSCo-YSZ composites exhibit

similar performance under anodic and cathodic polarisation. In contrast, LSM-YSZ composites showed good performance only after cathodic activation, and this activated state was lost during operation in electrolysis mode. Therefore, it was concluded that LSM-based electrodes do not appear to be optimal for use as oxygen electrode in a reversible SOCs.

The activity under anodic and cathodic polarisation of $(\text{La,Sr})(\text{Co,Fe})\text{O}_3$ (LSCF), LSF and LSM-YSZ electrodes have been investigated in (41). It was found that the activity of all electrodes in fuel cell mode was generally higher compared to the operation in electrolysis mode. The order of performance was found to be as follows: $\text{LSCF} > \text{LSF} > \text{LSM-YSZ}$ (in both electrolysis and fuel cell modes).

The addition of 30-50 vol% $(\text{Ce,Gd})\text{O}_3$ (GDC) to LSCF cathodes screen printed on YSZ electrolytes has been reported to result in a factor of 10 reduction in the electrode polarisation resistance as shown in Figure 2.6 (42, 43).

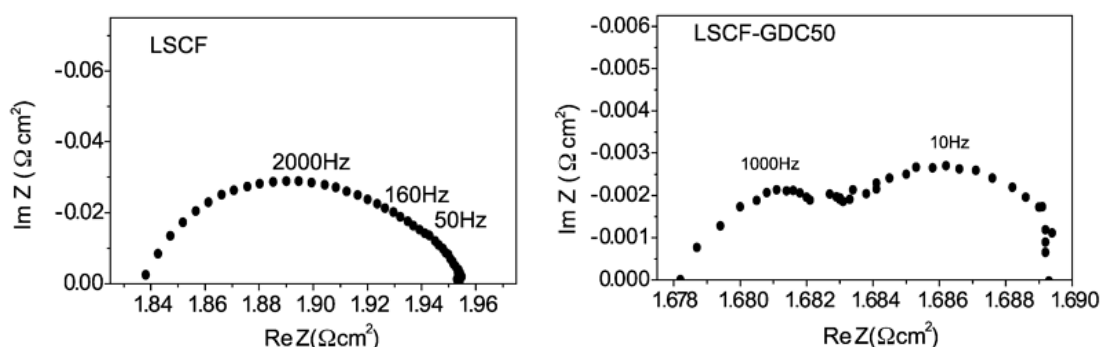


Figure 2.6. Impedance spectra taken in air at 750 °C for LSCF (left) and LSCF-50 wt% GDC (right) cathodes, adapted from (42).

The enhanced electrochemical performance may be explained by the high ionic conductivity of GDC that leads to the expansion of the electrochemical reaction zone further from the electrode/electrolyte interface.

Taking into account the enhanced performance of these electrodes, LSCF-GDC was used for the oxygen electrode in this study.

2.7 Fuel electrode for high temperature SOCs

2.7.1 Factors affecting performance of SOC fuel electrodes

Triple Phase Boundaries

As described earlier, the fuel electrode for SOCs should be catalytically active for either hydrogen oxidation (fuel cell mode) or steam reduction (electrolysis mode), and exhibit acceptable ionic and electronic conductivities (typically 100 Scm^{-1}). Catalytic reaction occurs at the active sites, called triple phase boundaries (TPBs). A TPB is the conjunction of pore phase, ionic conductor (typically YSZ), and electronic conductor (typically Ni), as shown in Figure 2.7 for a Ni-based cermet electrode and H_2 as fuel (44). The presence of all three phases is essential for the reaction to occur. The role of the pore phase is to allow gas reactants to effectively access the TPB and to enable product removal from the cell. The main functions of the electronic conductor are to facilitate electro-oxidation of the fuel by catalysing the reaction, assisting in charge transfer and conducting electrons away from the TPB to the external circuit. The ionic conductor carries oxygen ions to the TPB to accomplish the oxidation reaction. For a TPB to contribute to current generation, the gaseous, ionic, and electronic phases must have a contiguous connection to the rest of the microstructure. That is, the pore must be connected through the pore network to the fuel stream, the electronic conductor phase should be connected to the external circuit, and the ionic conductor phase needs to be in a good contact with the electrolyte (45). The total length of all TPBs is called the TPB length.

The corresponding reaction steps on the TPB according to numbers on Figure 2.7 could be summarized as follows (44):

1. H_2 adsorption and dissociation
2. $\text{H}_{(\text{ads})}$ surface migration and O^{2-} bulk migration through ionic conductor to TPB
3. Charge transfer reaction on TPB
4. Electron migration through the electronic conductor to the external circuit; H_2O desorption and diffusion (removal) through the pore phase.

It is therefore clear that the concentration of interconnected active sites in the electrode, i.e. TPB length, is a critical parameter that will affect the electrode, and consequently, the cell performance. To extend one dimensional TPB length to the two-dimensional active area, the use of mixed ionic and electronic conducting ceramic materials, such as doped ceria, is also being investigated (46). This will be discussed in details in ‘Ce-based electrodes’ section.

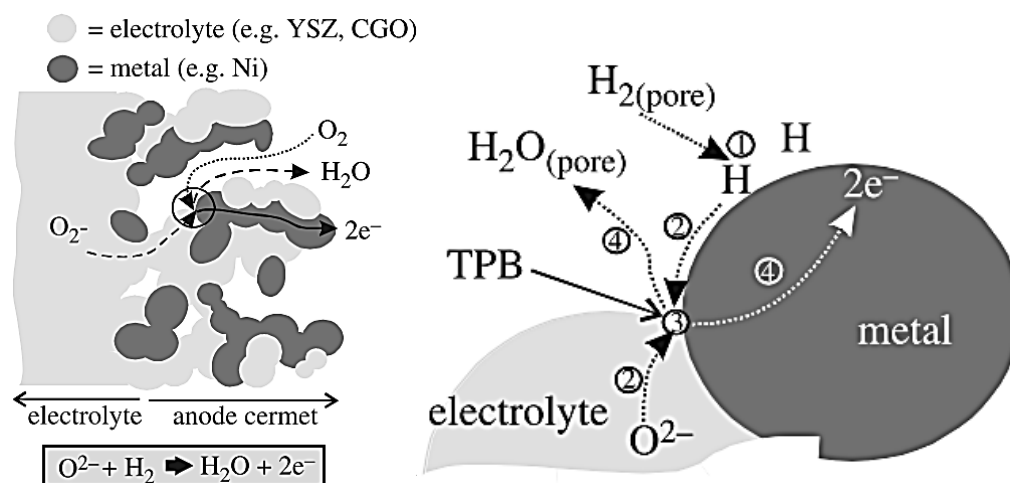


Figure 2.7. Schematic view of reaction pathway at SOFC anode cermet (left); close-up of anode cermet TPB and corresponding processes (right) (44).

Improvement of the understanding of the electrochemical processes occurring at TPBs, the optimisation of the microstructure through maximisation of the effective TPB length and the search for the optimal combination of materials are the subjects of major research effort for the optimisation of SOC electrode performance.

Active region

Even though TPBs are distributed throughout the porous electrodes they are not equally active (47). It has been recognized that an electrochemically active zone (or active layer) exists in SOFC electrodes where electronic conductivity is typically orders of magnitude higher than ionic conductivity, i.e. in the case of composite Ni–YSZ anodes. Electronic conductivity is higher than ionic conductivity and therefore the TPBs closer to the electrode – electrolyte interface are expected to be preferred reaction sites to those at the gas – electrode interface (48). Other reasons for the

existence of active regions are a difficulty to maintain the continuity of the TPBs from the electrolyte/fuel electrode interface to the current collector, and the tortuosity of the anode that can prevent effective gas flow.

It was found, that the effective active region within the electrode, where electrochemical reactions take place, extends in the range of 5-20 μm from the electrolyte/anode interface in Ni-YSZ composite anodes (48-52). Maximising TPBs and concentration of fuel gas species through finer microstructure in the active region and graded porosity may be a solution (53). Kishimoto et al claim that the primary focus for optimisation of the fuel electrode microstructure should be the Ni percolation from the anode surface to the anode–electrolyte interface because it largely determines the active reaction region. Poor Ni percolation shifts the active region far away from the electrolyte resulting in high ohmic losses (52).

Porosity

Apart from the high concentration of TPBs desirable in SOC electrodes, it is also important that the active sites are fully accessible by fuel reactants. For this reason the electrode requires a continuous porous phase, as was mentioned above. In state-of-the-art electrodes more than 30 vol% of open porosity is required to facilitate the transport of fuel reactants and products (21).

Moreover, highly tortuous paths for the transport of gaseous species inhibit the exchange of H_2O and H_2 and may obstruct fuel access to the active sites (22, 54, 55). This can be observed as a limiting current behaviour at high current densities and/or low reactant partial pressures. Therefore, a low tortuosity factor of the porous medium is desirable in a fuel electrode (45).

Electronic conductivity of the fuel electrode

Electronic conductivity of the electrode is dependent on the content of the electronic conductor phase and its continuity, or percolation threshold (56). In a typical Ni-YSZ cermet above 30 vol% Ni

result in about three-orders of magnitude higher conductivity (56, 57), corresponding to a shift in conduction mechanism through the metallic phase, as shown in Figure 2.8.

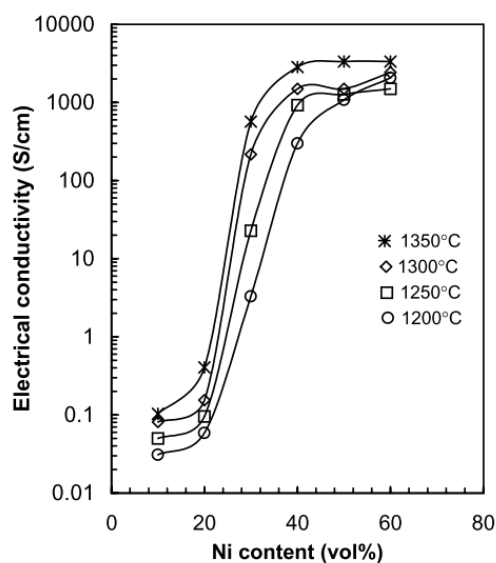


Figure 2.8. Variation of electrical conductivity measured at 1000 °C as a function of nickel concentration of Ni/ZrO₂(Y₂O₃) cermet fired at different temperatures (57).

Apart from composition, the electronic conductivity of the porous cermet is strongly influenced by processing parameters, such as sintering and reduction conditions. As can be seen from Figure 2.8, the conductivity of Ni-YSZ anodes was higher with higher sintering temperature. This difference was linked to lower porosity obtained at longer or higher firing temperatures (57).

It is widely assumed that insufficient electronic pathways in the cermet electrode result in reduced TPB length and lead to increasing overpotentials and losses in power output (56, 58-60). Ni agglomeration at elevated temperatures due to the poor adhesion between metal and ceramic materials may lead to the loss of the electronic pathways and subsequent decrease in performance (56, 58). Thus it is crucial to create a robust percolated Ni network in the electrode in order to ensure high performance and minimise degradation.

Reduction conditions

Reduction conditions, especially temperature and the timing of hydrogen introduction to the chamber, have a significant effect on the electronic conductivity and the microstructure of the porous Ni-YSZ cermet electrode (33). It was found that Ni-YSZ electrodes reduced at 1000 °C are about 2 to 4 times more conductive than those reduced at 800 °C (61). This difference was attributed to differences in morphology of the electrode. Cermets reduced at 1000 °C show close contact between Ni and YSZ particles than those reduced at 800 °C.

Furthermore, if hydrogen was introduced to the electrode at a high temperature (800 °C) after the cell had been heated up in air or N₂, the resulting electronic conductivity was high and the cell bulk resistance was about 100 times lower than that achieved in a cermet that was exposed to hydrogen starting from room temperature (33, 62). The reason for that is the formation of isolated spherical Ni particles during reduction of NiO at lower temperatures, rather than a formation of a continuous metal network, if NiO was reduced at high temperatures. When reduced at low temperatures, porous Ni particles tend to agglomerate and restrict the access of hydrogen to the Ni/NiO interface thereby preventing further reduction (63). In the light of these findings an appropriate procedure was used for reduction of samples as discussed in section 3.2.5.

2.7.2 Materials and performance of fuel electrodes

Ni-based electrodes

A Ni/YSZ porous cermet is a state-of-the-art fuel electrode for SOFC operated with H₂, due to its compliance with the requirements listed above (64-67). In comparison to electrochemical activities of Mn, Fe, Co, Ni, Ru, and Pt for H₂ reduction, Ni showed the highest activity (68). It also has good electronic properties and is relatively abundant. Therefore nickel is the most commonly used metal catalyst for SOC purposes (7, 66).

As was mentioned above, the main advantages of SOC over other fuel cells is the ability to operate in either power or fuel generating modes and fuel flexibility. To explore these capabilities, the

main research interests are the electrochemical performance in fuel cell and electrolysis modes, degradation issues and performance with different fuels (such as hydrogen and hydrocarbons) (69).

Eguchi et al investigated the electrochemical performance of Ni/YSZ electrodes in FC and EC modes for H₂ production. The *i*-*V* curves and polarisation characteristics using Ni-YSZ and Pt as the cathode was studied (60). It was found that the Ni-YSZ cermet performed well in SOFC mode but suffered from higher overpotentials in SOEC mode. It was postulated that the Ni particles were oxidized to form a less active layer, resulting in low activity under electrolysis conditions. Formation of the oxide may be prevented by the use of ceramic materials that are known to have oxygen storage capabilities as suggested by Kim et al (41). The authors conclude that higher electrochemical performance of Ni/GDC electrode compared to Ni/YSZ electrode is likely to be as a result the mechanism in which oxygen storage capacity of GDC helps to suppress the oxidation of the Ni surface (41).

Conventional fuel electrodes are fabricated by sintering a mixture of NiO and YSZ in air at high temperature (~1400 °C), followed by reduction. Reduction of NiO to Ni is accompanied by negligible change in the electrode dimensions (1%), hence introducing more porosity to the electrode (70). However, upon re-oxidation there is a significant total electrode volume change (~3-9%) that could be damaging for the electrode and cause electrolyte cracking due to internal stresses (71). This redox cycling damage is a major issue for SOFCs employing Ni-based anodes due to dimensional instability of the electrodes associated with irreversible expansion of Ni upon re-oxidation (62).

Performance degradation was also observed due to micro-structural changes, as Ni particles tend to agglomerate at high temperatures and H₂ environments, leading to a loss of the continuous conductive network (58). Other durability studies have shown that Ni-YSZ electrodes undergo degradation in oxidizing atmospheres, formation of undesirable glassy phases and suffer from the damaging impact of impurities and carbon poisoning, when cells are operated with CO₂ or hydrocarbons, either directly or with steam (38, 72-79).

The carbon formation in electrolyte-supported Ni/YSZ SOFC anodes exposed to CO/H₂ mixtures at 800 °C has been investigated (76). It was found that significantly more carbon was deposited on the

anodes exposed at OCP to feeds containing CO/H₂ mixtures than to pure CO. The mechanism of carbon formation from CO/H₂ mixtures is not fully understood but may imply that hydrogen possibly assists CO dissociation. At high temperatures, carbon dissolves in nickel, resulting in swelling and leads to eventual internal stress and electrode delamination (77).

The effect of carbon deposition on both Ni/YSZ and Ni/ScSZ cermet SOFC anodes was studied in a methane-rich environment (80). It was shown that carbon deposition was significantly less for Ni/ScSZ than for Ni/YSZ. The reduction in carbon deposition on the Ni/ScSZ anode was probably due to the presence of 1 mol% CeO₂ dopant within the ScSZ in the anode, which improved the catalytic activity and resistance to coke formation.

Degradation of the SOEC with a Ni/YSZ electrode for the electrolysis of CO₂ was studied for several thousand hours at 850 °C (72). It was found that the passivation is independent of the applied current density in the range up to -0.50 Acm^{-2} and is not caused by coke formation, but by impurities in the gas stream, most likely sulphur adsorbed on specific nickel sites in the cathode.

Sensitivity of Ni/YSZ electrodes for sulphur was studied in the SOFC mode across a wide range of H₂S concentrations (0.05 ppm to several thousand ppm) in H₂ fuel and temperatures (600-1000 °C) (81-83). The most important trends to draw from these studies are that the extent of sulphur poisoning increases with sulphur concentration, and decreases at a given concentration with increasing temperature. It was also shown that Ni/ScYSZ anodes demonstrated improved tolerance towards sulphur (83).

To summarize, the main issues of the Ni-YSZ electrodes are lower performance in the electrolysis mode compared to the fuel cell mode, low redox stability, microstructural degradation at elevated temperatures, decreased performance with CO₂/CO/CH₄ as Ni catalyzes the formation of carbon deposits, and sensitivity to sulphur poisoning.

Ceria-based electrodes

Fuel cells that operate by direct oxidation of hydrocarbons could have significant advantages over those that require hydrogen as the fuel. Unlike hydrogen, hydrocarbon fuels are readily available and are currently used in other applications. Thus, there is already an existing infrastructure to support the use of hydrocarbons on a wide scale. Moreover, significant problems associated with hydrogen storage have yet to be solved. For all of these reasons, it would be highly desirable to operate fuel cells on hydrocarbon fuels (49, 84).

Due to the issues with the performance of Ni-YSZ electrodes discussed above, especially carbon poisoning, much research is devoted to finding candidates to replace Ni-YSZ electrodes (67). Excellent reviews on alternative materials for SOC electrodes can be found in (64, 67, 85, 86). Doped ceria is a promising material for SOC electrodes because it displays mixed ionic and electronic conductivity in reducing atmospheres, provides high catalytic activity for H₂ and CH₄ oxidation and CO₂ reduction, and exhibits increased resistance toward coking and sulphide formation (11, 46, 87-92). Most common ceria-based ceramics are gadolinia (or samaria)-doped ceria (GDC or SDC). Ceria doped with a rare earth metal has the same oxygen-deficient fluorite structure as YSZ. In recent years there has been increasing interest to include ceria as a component in SOFC anodes, whether as a functional inter-layer, as an infiltrated catalyst or as the main oxide phase (46, 88, 93-96).

The combination of Ni and doped ceria based anodes for H₂ oxidation has been acknowledged previously as it exhibits better performance than conventional Ni-YSZ anodes with hydrogen or hydrocarbons (41, 89, 92, 97-103). The electrochemical performance of Ni/GDC and Ni/Ru-GDC electrodes was studied for high temperature co-electrolysis (41). It was found that the Ni-GDC and Ni/Ru-GDC electrodes had higher electrochemical performance in electrolysis mode than the Ni-YSZ electrode over a range of temperatures (550–800 °C) as shown in Figure 2.9. Authors suggested that even small additions of Ru accelerated the electrocatalytic properties of the electrode.

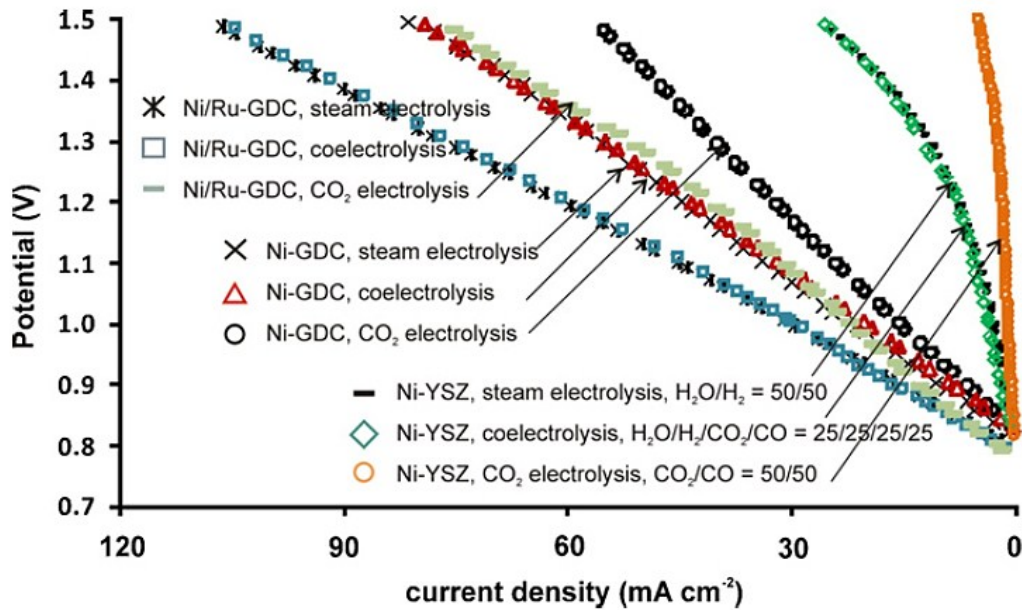


Figure 2.9. Potential of electrolyte supported cells (H_2 electrode/YSZ electrolyte/Pt reference electrode), having Ni-YSZ, Ni-GDC and Ni/Ru-GDC H_2 electrode as a function of current density when the electrode operated under steam electrolysis ($H_2O/H_2 = 50/50$: 38% H_2O + 38% H_2 + 24% N_2), CO_2 electrolysis mode ($CO_2/CO = 50/50$: 25% CO_2 + 25% CO + 50% N_2), and co-electrolysis of H_2O/CO_2 (22% CO_2 , 22% CO , 22% H_2O , 22% H_2 , 12% N_2) at 800 °C (41).

The use of samaria-doped ceria (SDC) cathode with dispersed Ni catalyst was evaluated for H_2O electrolysis at 900 °C (104). Low ohmic resistance and cathode overpotential was obtained for a 17vol%Ni-SDC cathode, probably due to the formation of sufficient reaction area and a good electronic network.

Even small additions of ceria have proven beneficial to the catalytic activity of the anode (84, 105). When the Ni-YSZ electrode was impregnated with the GDC solution (GDC loading of 0.26 $mgcm^{-2}$), the electrochemical performance in fuel cell or electrolysis mode in H_2/H_2O increased significantly (105) as shown in Figure 2.10. It was found that 10 wt% ceria additions to Cu-YSZ have a profound effect on the performance of SOFCs operated with H_2 and butane. This seems to be related to the ease with which ceria can be reduced by H_2 and hydrocarbon fuels (84).

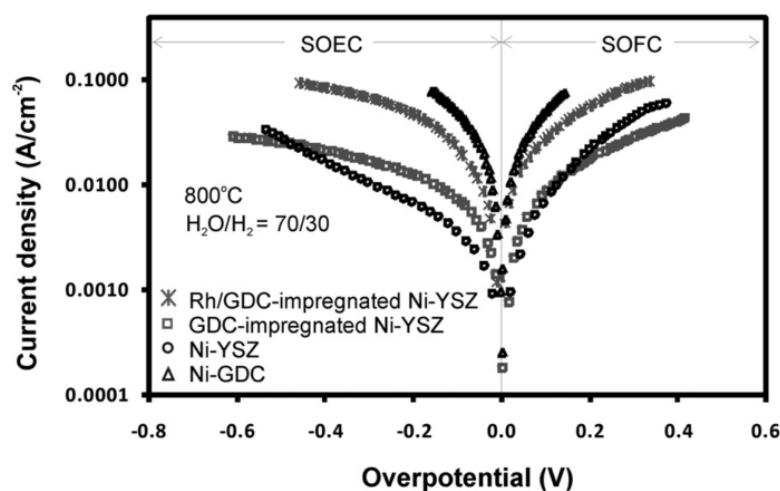


Figure 2.10. Current/overpotential of GDC-impregnated Ni-YSZ, Rh-GDC-impregnated Ni-YSZ, composite Ni-YSZ, and composite Ni-GDC electrode during electrolysis and galvanic mode (800 °C, $H_2O/H_2 = 70/30$) (105).

The effect of microstructure on the performance of Ni-GDC cermet anodes and GDC electrolyte has been explored by Zha et al (92). The interfacial polarisation resistance between electrolyte and the anode at 600 °C was decreased from $1.61 \Omega cm^2$ for the anodes prepared using commercially available powders to $0.06 \Omega cm^2$ for those prepared using fine precursor powders of NiO and GDC derived from a glycine – nitrate process (Figure 2.11). The excellent performance in humidified H_2 was attributed to a fine microstructure, obtained in the later anodes.

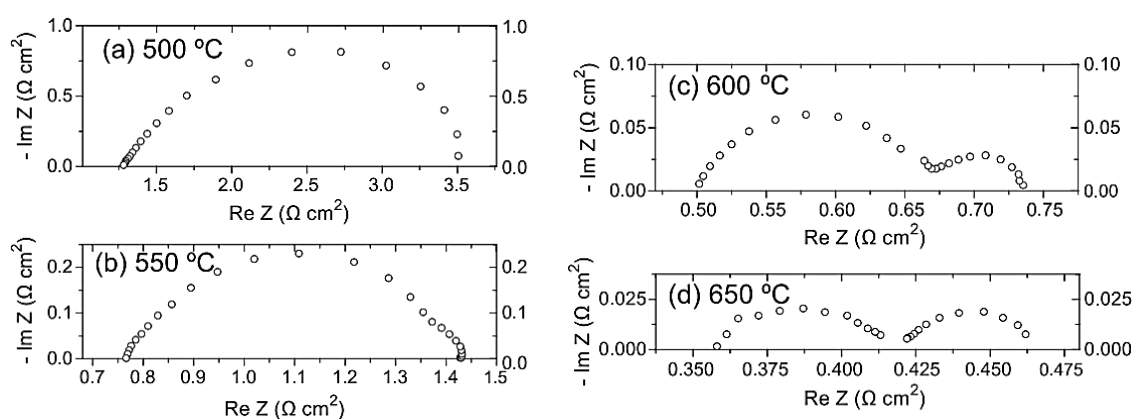


Figure 2.11. Impedance spectra of fuel cell Ni-GDC anode measured under open circuit conditions at 500-650 °C using a two electrode configuration. Both NiO and GDC in the anode are synthesised by the glycine – nitrate process (92).

As was mentioned previously, the mixed ionic and electronic conductivity nature of the doped ceria under reducing conditions is an advantage for SOFC electrodes. In the case when the fuel electrode exhibits solely electronic conduction the effective electrochemical reaction zone at electrode of SOFC is limited to the physical TPB length. In contrast, the use of mixed-conducting anode is expected to enlarge the effective electrochemical reaction zone (21, 46, 106). The results of the electrochemical measurements performed by Nakamura et al suggest that the reaction zone extends beyond the TPB in porous GDC anodes (107). This can lead to a significant drop in the activation polarisation and yield remarkable improvement in electrical efficiency (21). Chueh et al (46) further claim that metal-catalysed pathways do not contribute significantly to electrocatalysis, and that the metallic phase need not be contiguous because the mixed conducting oxide facilitates electron transport. However, Jiang et al (108) state that percolated structure of metal nano-particles would be more beneficial for electronic conductivity of the Ni-Ceria based electrode.

2.8 Manufacturing methods for SOC electrodes

2.8.1 Microstructural engineering

Fabrication methods play a crucial role in determining the properties of the electrode through microstructural optimization. Generally, there are two types of fabrication techniques (96, 109):

- (a) Deposition at room temperature followed by high temperature firing, for example, tape casting, tape calendaring, screen printing, sol-gel, and colloidal deposition such as slip casting, electrophoretic deposition and spray/dip coating.
- (b) Depositions at elevated temperature such as chemical vapour deposition (CVD), electrochemical vapour deposition (EVD), atmospheric or vacuum plasma spraying, laser reactive deposition and spray pyrolysis.

These techniques can also be classified according to the physical state through which the electrodes are fabricated (vapour, liquid, gas). Characteristics of different techniques are summarized in Table 2.2.

Among different fabrication techniques screen printing is currently the most widely used as it is suitable for both scientific and commercial use due to reproducibility, low cost and robustness (110).

Conventional fabrication methods for Ni-YSZ electrodes, such as tape casting or screen printing, involve ink preparation from a mixture of NiO and YSZ powders, followed by sintering at 1300-1400°C, and subsequent reduction in hydrogen rich atmospheres at 800-1000°C. However, operating cell at high temperatures can lead to Ni particles agglomeration and coarsening, with associated loss of connectivity and reduction in TPB length (64).

This limits the ability to control and optimize electrode microstructure (106, 108). Additionally, it has been shown that conventionally produced electrodes can exhibit high tortuosity obstructing gas access to/from some of the active sites (45, 54). Furthermore, under reduction-oxidation (redox) cycles Ni-YSZ cermets experience dimensional changes due to the formation of nickel oxide resulting in decreased mechanical stability of the cell (62, 78).

Table 2.2. Comparison of the methods for producing thin and dense films for SOFC applications, adapted

| Technique | Film characteristics | | Process features | |
|-----------------------------------|------------------------------------|--------------------------------------|--|--|
| | Microstructure | Deposition rate or thickness | Cost | Characteristics and limitations |
| Vapor phase | | | | |
| Thermal spray technologies | | 100-500 $\mu\text{m h}^{-1}$ | | High deposition rates, various compositions possible, thick and porous coatings, high temperatures necessary |
| EVD | Columnar structures | 3-50 $\mu\text{m h}^{-1}$ | Expensive equipment and processing costs | High reaction temperatures necessary, corrosive gases |
| CVD | Columnar structures | 1-10 $\mu\text{m h}^{-1}$ | Expensive equipment | Various precursor materials possible, high reaction temperatures necessary, corrosive gases |
| PVD (RF and magnetron sputtering) | Columnar structures | 0.25-2.5 $\mu\text{m h}^{-1}$ | Expensive equipment | Tailor-made films, dense and crack-free films, low deposition temperatures, multipurpose technique, relatively small deposition rate |
| Laser ablation | | | Expensive equipment (laser) | Intermediate deposition temperatures, difficult upscaling, time-sharing of laser, relatively small deposition rate |
| Spray pyrolysis | Amorphous to polycrystalline | 5-60 $\mu\text{m h}^{-1}$ | Economical | Robust technology, upsealing possible, easy control of parameters, corrosive salts, post-thermal treatment usually necessary |
| Liquid phase | | | | |
| Sol-gel, Liquid precursor route | Polycrystalline | 0.5-1 μm for each coating | Economical | Various precursors possible, very thin films, low temperature sintering, coating and drying/heating processes have to be repeated 5-10 times, crack formation during drying, many process parameters |
| Solid phase | | | | |
| Tape casting | Polycrystalline, slightly textured | 25-200 μm | | Robust technology, upscaling possible, crack formation, porous |
| Slip casting and slurry coating | Polycrystalline | 25-200 μm | Economical | Robust technology, crack formation, slow |
| Tape calendaring | Polycrystalline | 5-200 μm | | Upscaling possible, co-calendering possible |
| EPD | Polycrystalline | 1-200 μm | | Short formation time, little restriction to shape of substrate, suitable for mass production, high deposition rates, inhomogeneous thickness |
| Transfer printing | Polycrystalline | 5-100 μm | Economical | Robust technology, rough substrate surfaces possible, adhesion on smooth substrates difficult |
| Screen printing | Polycrystalline | 10-100 μm | Economical | Robust technology, upscaling possible, crack formation, porous |

from (111)

As discussed earlier, apart from material composition issues, the microstructure of the anodes, particularly if they are cermets, plays a key role in their performance (44). 3-D representations of the importance of the anode microstructure for SOFC performance was studied by Barnett et al (112, 113). Specifically, a well-defined ceramic scaffold is necessary to avoid agglomeration of the metallic particles in the cermet electrodes. It is important to ensure a good connectivity along the metallic pathways of the cermet, since the metal is more prone to the generation of isolated, and therefore electrochemically inactive, areas than the ceramics (113).

In addition to good connectivity, low tortuosity and sufficient porosity, the activation polarization resistance of the electrode can be decreased by shifting the effective particle diameter of the catalytic phase from the micro- to the nano-scale. This dramatically increases the three-dimensional triple phase boundary (TPB) density (114). However, this particle size reduction must be done without negatively impacting percolation of the ionic/electronic and gas phase conduction paths that contribute to the electrode ohmic and concentration polarization, respectively (114). Therefore, different nanostructured scaffold approaches have been proposed to allow better control of the microstructure and materials selection (49, 99, 115, 116).

The porosity of the electrodes can be controlled by addition of pore formers – polymethyl methacrylate (PMMA) beads or graphite. The shape of the pore formers defines the shape of pores in the porous YSZ matrix as shown in Figure 2.12 (117). The YSZ made with the addition of PMMA shows large spherical pores between 50 and 100 μ m in diameter Figure 2.12a. The pores were similar in shape and slightly smaller than the PMMA beads (Figure 2.12b). Irregular graphite particles (Figure 2.12d) led to the formation of a porous structure with irregular pores (Figure 2.12c).

Alternatively, a highly porous YSZ scaffold can also be prepared by acid leaching Ni from a Ni/YSZ cermet (118). Ni leaching of the 80 wt% NiO – 20 wt% YSZ led to 47 % porosity. Recently, Almar et al reported homogenous, continuous and interconnected networks of Ni, GDC and open porosity fabricated by synthesizing a mesoporous NiO–CGO composite (99).

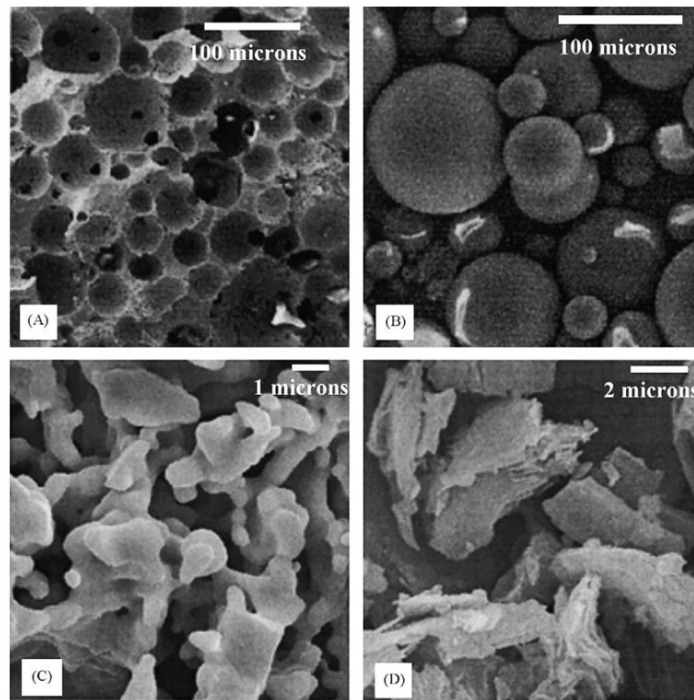


Figure 2.12. SEM micrographs of: (A) YSZ made with addition of 36wt% PMMA, (B) PMMA, (C) YSZ made with addition of 36wt% graphite and (D) graphite (117).

The key consideration in the development of nano-structured SOFC electrodes is to bypass the high processing temperature via the deposition of catalytically and/or electrochemically active nanoparticles into a rigid and pre-fired electronic and/or ionic conducting electrode scaffold (119). Among other fabrication methods, wet infiltration enables this, as will be further discussed in section 2.8.2.

2.8.2 Wet infiltration techniques for electrodes fabrication

An infiltration process involves the deposition of a metal salt or nanoparticle suspension solutions into a pre-fired porous scaffold of the electrode to form nano-sized particles on the scaffold after decomposition at relatively low temperatures (~ 500 °C). The infiltrated catalytically and/or electrochemically active nanoparticles can form discrete distributions or a thin and continuous network on the surface of the porous scaffold, as schematically shown in Figure 2.13 (114). The sequence of deposition – decomposition can be repeated several times to achieve higher loadings of infiltrated material (115).

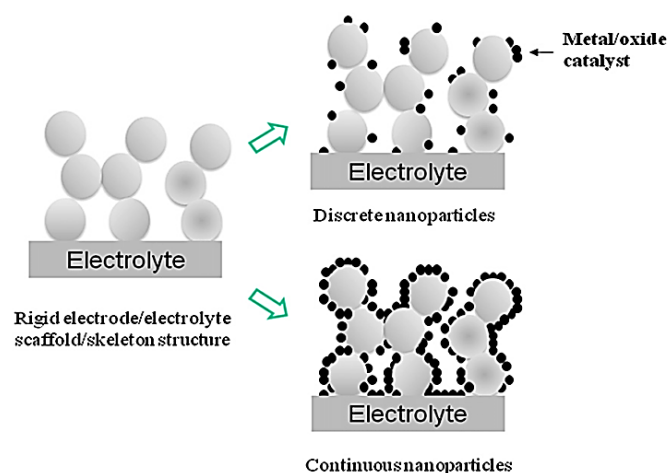


Figure 2.13. Infiltrated nano-structured electrodes on pre-sintered porous electrode or electrolyte scaffold/skeleton (114).

This method has been widely investigated (87, 108, 116-119). Infiltration of materials into a ceramic support can be used as an integral technique for introducing catalysts, such as Pd, Ru, Rh or ceria (41, 105, 120). Since the amount of infiltrated material is low, this prevents the loss in porosity and allows better control of the microstructure (96, 119). Analysis show that the TPB length of infiltrated electrodes may be about two orders of magnitude higher than of that of more conventional composite cermet electrodes (121). By avoiding the use of elevated processing temperatures it should be possible to prevent Ni coarsening without compromising the electrocatalytic properties of the electrode. It was found that YSZ porous electrodes infiltrated with Ni nano-particles show better redox performance due to their dimensional stability (108, 122).

Small (catalytic) amounts of Ni (90, 104, 123-127) or GDC (105, 116, 127, 128) added into metal, ceramic or cermet scaffolds by wet infiltration have proven to improve electrochemical performance. However in these studies the infiltrated phases are not interconnected and therefore their efficiency is site-dependent. A repeating infiltration step, leading to a connected network of nanoparticles, provides substantially improved electrode performance (108). The total amount of infiltrated material needed to achieve a percolated structure by wet infiltration techniques is significantly lower than by conventional techniques. It was shown that only 9 wt% of infiltrated Ni was required to attain a percolated structure (129) in comparison with 30-40 wt% for conventional electrodes (21, 122, 129). Percolated structures are potentially expected to allow better current

distribution along the electrode and to enhance both conductivity and electrochemical performance (108). Synergistically interconnected metal and ceramic phases create a complex structure with increased number of active sites for electro-chemical reaction and multiple pathways for charge carriers. At the same time the scaffold ensures the structural stability of the electrode (122).

In this thesis the wet infiltration technique for SOC electrode fabrication is used to create porous GDC scaffolds with an interconnected network of infiltrated nanosize Ni particles.

2.9 Direct Metal Laser Sintering for SOC electrode fabrication

2.9.1 Introduction

Selective Laser Sintering/Melting (SLS/M), is an additive laser manufacturing (ALM) process that initially was developed in the early 1990s for 3-D rapid prototyping (130). In SLS 3-D freeform objects with a CAD (Computer-Aided Design) - defined geometric model are produced by sintering together successive layers of powder material. The SLS process is capable of sintering complex geometries from wide range of materials (wax, polymers, cermets, metals, alloys and some ceramics) offering a cost-effective and rapid production of physical parts.

Although SLS has been developed for 3-D prototyping, it is now used for variety of applications, such as tooling, molds, bio-medical, aerospace and automotive parts, etc. Direct Metal Laser Sintering (DMLS) is an SLS process, in which only metallic powders are used. Being a relatively new technique, DMLS is still in a development stage and parameters for many applications and materials have not been developed yet and therefore the process relies on empirical knowledge (131).

2.9.2 Principles of DMLS

A diagram illustrating the principle of the DMLS system is shown in Figure 2.14. In the process the heat from the laser beam is selectively transferred to the powder by scanning cross-sections generated from a 3-D CAD drawing of the part. A scanner system ensures that the laser is precisely

switched on and off, exposing only designated areas. The metal powder absorbs the laser energy. When the laser couples with the powder, plasma above the powder is formed thus providing the heat to melt the powder. Sintering occurs between the powder particles within single layer and already solidified areas from the previous layers.

After completing each cross-section the powder bed is lowered by one layer thickness and powder delivery system is raised by one layer thickness. This is followed by application of a new layer of powder material on the top of the part surface by a roller. This process is repeated until the 3-D part is completed.

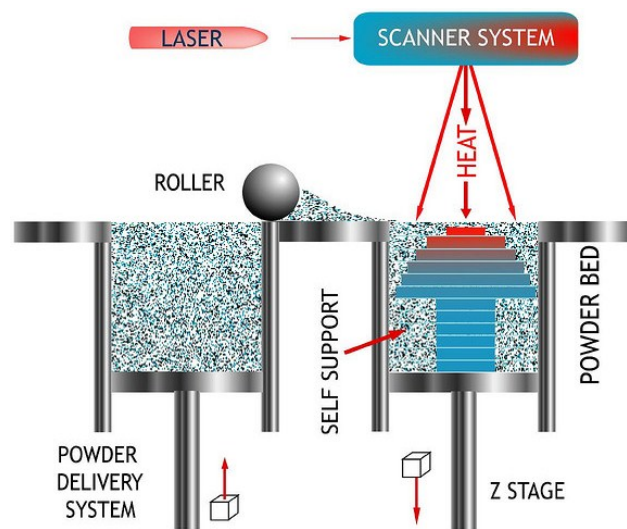


Figure 2.14. Schematic diagram of the DMLS system.

Depending on process parameters that will be described later in this section it is possible to produce three-dimensional parts with high complexity and accuracy and in a relatively short time.

Heat transfer in SLS occurs due to a coupling effect, in which the radiation of the laser is adsorbed by the powder as illustrated in Figure 2.15. The heat is then transferred to the inner layers of the powder binding together the upper and the inner layers.

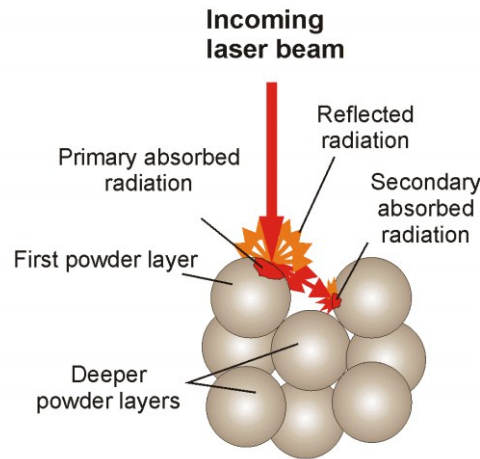


Figure 2.15. Diagram of laser coupling with powder.

A wide range of metals/alloys for variety of applications could be sintered using DMLS. Table 2.3 outlines examples of materials, advantages and applications for parts fabricated by DMLS (<http://gpiprototype.com/>).

Table 2.3. Examples of materials and applications of DMLS-fabricated parts (<http://gpiprototype.com/>).

| Material | Advantages / Applications |
|--------------------------------------|---|
| Stainless Steel (PH1) | <ul style="list-style-type: none"> • Prototype / Production Parts • High Toughness, Ductility, Strength |
| Stainless Steel (GP1) | <ul style="list-style-type: none"> • Prototype / Production Parts • Good Mechanical Properties |
| Cobalt Chrome (MP1) | <ul style="list-style-type: none"> • Turbines & Engine Parts • High Temperature Resistance |
| Maraging Steel (MS1) - Tooling Steel | <ul style="list-style-type: none"> • Injection Molding Tooling • Conformal Cooling Channels • Easily Machinable & Excellent Polishability |
| Titanium Alloy Ti-64 | <ul style="list-style-type: none"> • Aerospace Parts • High Strength & Light Weight |
| Aluminum AlSi10Mg | <ul style="list-style-type: none"> • Low Weight Applications • Automotive & Racing Applications • Thermal Parts |
| Nickel Alloy IN718 | <ul style="list-style-type: none"> • Turbine Engines • Rocket & Aerospace Applications • Chemical Industry Parts • Heat & Corrosion Resistant |

2.9.3 Process parameters

There are many parameters in DMLS that determine the quality and the properties (mechanical properties, density, etc) of the sintered object. To achieve optimum characteristics process parameters are set in accordance with sintered material and the requirements of application for the object. The parameters can be classified to material, laser, scanning and environment parameters, as summarised in Table 2.4.

The effect of materials and some of the process parameters on the properties of the sintered part is explained in the following sub-sections.

Table 2.4. Material and process parameters in DMLS.

| Materials parameters | Laser parameters | Scan parameters | Environment parameters |
|-----------------------------|-----------------------------|-----------------|------------------------|
| Powder chemical composition | Mode (continuous or pulsed) | Scan speed | Preheating temperature |
| Powder dimensions | Wave length | Scan distance | Pressure |
| Shape of grains | Power | Hatch spacing | Gas environment |
| Powder flow properties | Frequency | Layer thickness | |
| Wettability | Spot size (diameter) | Scan pattern | |
| Thermal properties | Beam offset | | |

Materials Parameters

The choice of powder material will dictate the mechanism by which sintering of the powder occurs. Physical mechanisms responsible for sintering in SLS are solid-state sintering, liquid-phase sintering, viscous flow binding, curvature effect and whole melting. For example, in nano-crystalline materials, the particle curvature is a driving force for sintering. Often a combination of two materials with different melting points is used, where the low melting temperature material serves as glue between the particles. If the temperature in the powder bed reaches melting point this would be advantageous for densification of the part, though shrinkage in dimensions can occur (131). Wetting between particles, when two or more materials used, is a very important parameter to ensure

homogeneous structure and to prevent ‘balling phenomena’ or separation between different materials (132).

Powder flow property defines how easily the powder will be spread over the surface. This property will depend mostly on powder particle size and its shape. It is preferable to use round-shaped particles and there is a minimum particle size that can be used for each material. Smaller particles provide larger surface area and increased surface energy and therefore are capable to absorb more laser energy leading to a higher sintering rate (133). Smaller powder particle sizes enable better surface finish, higher accuracy, and thinner layers. However, smaller powder particle sizes have a tendency to become airborne and float as a cloud of particles in the chamber and some materials can become explosive (134). The minimum particle size is normally defined by the SLS equipment manufacturer.

Laser and Scan Parameters

Laser, scan and environment parameters control the laser sintering process. The combination of these process parameters defines the amount of energy delivered to the powder surface. Given the same material properties, the amount of the energy available for laser irradiation-material interaction in a single layer is mostly dependent on laser type, laser power (P), scan rate (V), hatch spacing (H), layer thickness (T) and scan pattern.

Laser Power is the power available from the laser beam at part surface. This parameter should be set to ensure that the temperature at the powder bed surface will reach a material melting point during scanning (135). On the other hand, the evaporation of the powder may occur if the temperature on the powder surface is too intensive (133).

The scanning system can be programmed to follow different patterns as shown in Figure 2.16. Depending on a scan pattern, variations in mechanical properties in different directions, e.g. tensile strength, can occur, as shown schematically in Figure 2.17. Therefore the pattern is to be chosen varies according to application of the part.

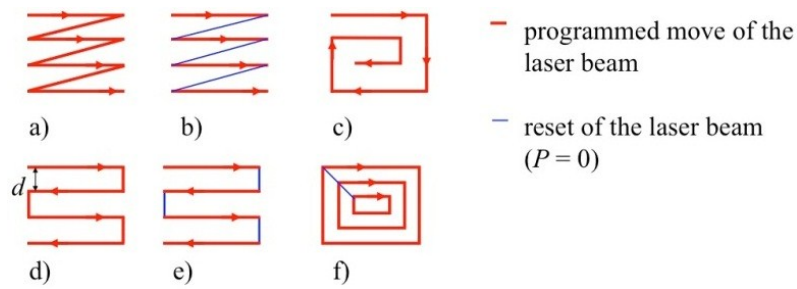


Figure 2.16. Different scanning patterns of the laser beam.

Laser beam diameter is a characteristic of a laser (Figure 2.18). But the diameter of the sintered zone is larger than laser diameter (effective laser beam) due to the heat-affected zone (HAZ). To compensate for the dimensional error the laser beam is shifted by half of the HAZ width from the contour of the part to the inside. This shift is a process parameter named beam offset (Figure 2.18) and it is directly related to the dimensional accuracy of the object (136).



Figure 2.17. Schematic diagram illustrating differences in mechanical properties through different axes of the SLS part.

Hatch spacing is a distance between the two closest sintered lines (Figure 2.18). Hatch spacing should be set to a value that will assure sintering of all particles, and therefore it affects the integrity of the part and its density. Normally it is set about quarter of the laser beam.

Scan rate is the speed of the laser when it scans the powder. It defines the duration of the heat exposure on a single powder segment. Together with laser power it will define the amount of the energy per segment, according to eq. 2.13:

$$\text{Energy density [J/m]} = \frac{\text{Laser Power [W]}}{\text{Laser Speed [m/sec]}} \quad 2.13$$

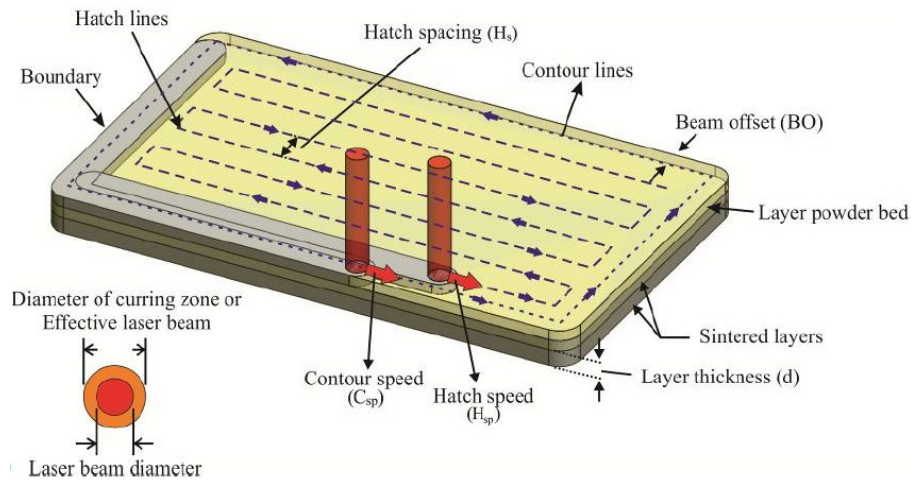


Figure 2.18. Scan parameters in SLS (136).

Energy density increases with higher laser power input and lower scan speed. If the temperature exceeds the melting point at high scan rates, it can be beyond the boiling point at low scan rates.

Layer thickness parameter is another important parameter. If its value is too high the temperature gradient from the laser may be insufficient to sinter together subsequent layers and in this case the integrity of the part will be compromised. Generally, with increasing the layer thickness lower density is achieved. Also the layer thickness will affect the total processing time.

2.9.4 Relevance to fuel cells

Direct Laser Metal Sintering could potentially offer a highly controllable technology for microstructure optimisation of SOC electrodes. Due to flexibility in process parameters and variety of materials that can be used, it is possible to create a microstructure with different porosity and pattern by regulating the parameters of the laser.

Only limited studies employing SLS for the fabrication of ceramic parts have been reported. Some studies identify a challenge to achieve high density of ceramic parts produced by SLS (137). Whilst low density remains a drawback for certain applications, porosity might be turned into a benefit in ceramic or cermet porous scaffolds for SOC electrodes.

There are only few studies on using SLS in the fuel cells field. Recent publications discuss the use of SLS for manufacturing PEMFC graphite current collectors (138-141). However, to date there are no studies reported on using SLS for fabricating electrodes for SOCs.

Due to the potential advantages it seems to be attractive to evaluate the feasibility of using laser-based additive manufacturing technology for SOC electrodes fabrication.

2.10 Summary of the literature review

The present literature review outlines general aspects of SOC as well as highlights the requirements for SOC components – electrolyte and electrodes. In summary, the possible pathways for SOC fuel electrodes performance optimisation are two-fold: materials development to achieve good catalytic properties; and improvement of the microstructure to enlarge the number of active sites and to ensure effective access of the fuel species to the active sites.

Mixed ionic and electronic conductors (MIEC), especially ceria-based materials for fuel electrodes, have been acknowledged in many studies due to their good catalytic properties for H₂ and CH₄ oxidation and CO₂ reduction, increased resistance toward coking and sulphide formation (46, 87). Compared to state-of-the-art Ni-YSZ, ceria based fuel electrodes show better performance when operated with hydrocarbon fuels at lower temperatures (103, 105).

The microstructure can be optimized through fabrication techniques. The most common fabrication methods for electrode preparation are screen printing or tape casting. As was stressed in the review, the main drawbacks of these methods are exposure to high temperatures during cell preparation and relatively low ability to control the microstructure. Infiltration technique, in which catalytic amounts of the metal phase are incorporated into porous ceramic matrix, is potential solution. The main advantages of this method are that the porous phase and the amount of infiltrated material(s) can be independently controlled, and that no exposure to high temperatures is required. Jiang et al also point out the importance of the percolated metal phase in nanostructured electrodes (108, 114).

Therefore, the combination of percolated Ni-ceria based electrodes and nanostructured approach seems to be promising for high performance fuel electrodes. However in the studies mentioned above such combination was not investigated. Demonstrated was performance of electrodes with only catalytic amounts of ceria or Ni infiltrated into YSZ or other scaffolds. This gap is addressed in the present research that explores the benefits the two-fold approach brings about – a combination of ceria-based electrodes infiltrated with Ni nanoparticles forming percolated microstructures.

The principles and advantages of the additive manufacturing techniques, specifically Direct Metal Laser Sintering, were outlined. Using DMLS the microstructure can be controlled by regulating the parameters of laser. Furthermore, this technique is easily scalable and thus can potentially offer an effective way of mass production of the cells. No studies have been reported regarding the fabrication of SOC electrode using DMLS, thus making the present research the first of its kind.

2.11 Scope of this thesis

As was mentioned, the appropriate combination of materials and microstructure is a key requirement to meet both performance and lifetime targets. Aiming to meet both materials and microstructural requirements, in this study an electrode for SOC application was made by infiltration of a porous GDC scaffold with Ni nano-particles to form a percolated structure. The study explores the microstructure and electrochemical performance of these electrodes.

In addition, a novel approach for electrode preparation by Selective Laser Sintering (SLS) was evaluated as a proof of concept study. By regulating the parameters of the laser (laser power and laser speed) this method enables the porosity and pattern of the electrode to be controlled. The feasibility of using this novel technique for solid oxide cells was demonstrated. In prospect, the combination of the two techniques may allow the scaffold preparation by SLS followed by infiltration, as a method for preparing high performance ‘electrodes by design’.

References for Chapter II

1. W. R. Grove, *Philosophical Magazine and Journal of Science*, **XIV**, 127 (1839).
2. K. V. Kordesch, *Journal of The Electrochemical Society*, **125**, 77C (1978).
3. B. C. H. Steele and A. Heinzl, *Nature*, **414**, 345 (2001).
4. U.S. Dept of Energy, in *Energy Efficiency & Renewable Energy Center* <http://www.hydrogenandfuelcells.energy.gov>.
5. D. Carter and J. Wing, The Fuel Cell Industry Review 2013, in, *Fuel Cell Today* (2013).
6. N. Q. Minh, *Journal of the American Ceramic Society*, **76**, 563 (1993).
7. Subhash C Singhal and K. Kendall, *High Temperature Solid Oxide Fuel Cells: Fundamentals, Design and Applications*, Elsevier (2003).
8. M. Mogensen, S. H. Jensen, A. Hauch, I. Chorkendorff and T. Jacobsen, *Fuel Cell* 1(2006).
9. F. He, D. Song, R. Peng, G. Meng and S. Yang, *Journal of Power Sources*, **195**, 3359 (2010).
10. M. A. Laguna-Bercero, *Journal of Power Sources*, **203**, 4 (2012).
11. C. Graves, S. D. Ebbesen, M. Mogensen and K. S. Lackner, *Renewable and Sustainable Energy Reviews*, **15**, 1 (2011).
12. A. Hawkes, I. Staffell, D. Brett and N. Brandon, *Energy & Environmental Science*, **2**, 729 (2009).
13. D. J. L. Brett, A. R. Kucernak, P. Aguiar, S. C. Atkins, N. P. Brandon, R. Clague, L. F. Cohen, G. Hinds, C. Kalyvas, G. J. Offer, B. Ladewig, R. Maher, A. Marquis, P. Shearing, N. Vasileiadis and V. Vesovic, *ChemPhysChem*, **11**, 2714 (2010).
14. A. B. Stambouli and E. Traversa, *Renewable and Sustainable Energy Reviews*, **6**, 433 (2002).
15. N. Sammes, *Fuel Cell Technology: Reaching Towards Commercialization*, Springer (2007).
16. R. P. O'Hayre, *Fuel cell fundamentals*, John Wiley & Sons (2006).
17. S. H. Jensen, P. H. Larsen and M. Mogensen, *International Journal of Hydrogen Energy*, **32**, 3253 (2007).
18. J. G. E. Erdle, V. Meyringer, in *Third International Workshop High Temperature Technology and its Applications*, B. M Editor, p. 727 (1986).
19. I. Chorkendorff and J. W. Niemantsverdriet, *Concepts of Modern Catalysis and Kinetics*, WILEY-VCH Verlag GmbH & Co. KGaA, Weinheim (2003).
20. K.-D. K. T. S. Zhao, Trung Van Nguyen, *Advances in Fuel Cells*, Elsevier (2007).
21. W. Z. Zhu and S. C. Deevi, *Materials Science and Engineering: A*, **362**, 228 (2003).
22. A. V. Virkar, J. Chen, C. W. Tanner and J.-W. Kim, *Solid State Ionics*, **131**, 189 (2000).
23. D. J. L. Brett, A. Atkinson, N. P. Brandon and S. J. Skinner, *Chemical Society Reviews*, **37**, 1568 (2008).
24. M. Ni, M. K. H. Leung and D. Y. C. Leung, *International Journal of Hydrogen Energy*, **33**, 2337 (2008).
25. University of Cambridge, Dissemination of IT for the Promotion of Materials Science (DoITPoMS), in.
26. J. A. Kilner and R. J. Brook, *Solid State Ionics*, **6**, 237 (1982).
27. M. Mogensen, N. M. Sammes and G. A. Tompsett, *Solid State Ionics*, **129**, 63 (2000).
28. V. Kharton, F. Marques and A. Atkinson, *Solid State Ionics*, **174**, 135 (2004).
29. B. C. H. Steele, *Solid State Ionics*, **129**, 95 (2000).
30. A. Mineshige, T. Taji, Y. Muroi, M. Kobune, S. Fujii, N. Nishi, M. Inaba and Z. Ogumi, *Solid State Ionics*, **135**, 481 (2000).
31. W. Lai and S. M. Haile, *Journal of the American Ceramic Society*, **88**, 2979 (2005).
32. F. M. B. Marques and L. M. Navarro, *Solid State Ionics*, **100**, 29 (1997).
33. J. W. Fergus, R. Hui, X. Li, D. P. Wilkinson and J. Zhang, *Solid Oxide Fuel Cells: Materials Properties and Performance*, p. 95 (2009).
34. R. Basu, in *Recent Trends in Fuel Cell Science and Technology*, S. Basu Editor, p. 286, Springer New York (2007).
35. M. I. Hoffert, K. Caldeira, A. K. Jain, E. F. Haites, L. D. D. Harvey, S. D. Potter, M. E. Schlesinger, S. H. Schneider, R. G. Watts, T. M. L. Wigley and D. J. Wuebbles, *Nature*, **395**, 881 (1998).

36. United Nations Framework Convention on Climate Change, in *UNEP/WMO, Climate Change Secretariat*, Geneva (1992).
37. R. E. Williford and P. Singh, *Journal of Power Sources*, **128**, 45 (2004).
38. A. Hauch, S. D. Ebbesen, S. H. Jensen and M. Mogensen, *Journal of Materials Chemistry*, **18**, 2331 (2008).
39. M. J. L. Østergård, C. Clausen, C. Bagger and M. Mogensen, *Electrochimica Acta*, **40**, 1971 (1995).
40. W. Wang, Y. Huang, S. Jung, J. M. Vohs and R. J. Gorte, *Journal of The Electrochemical Society*, **153**, A2066 (2006).
41. P. Kim-Lohsoontorn and J. Bae, *Journal of Power Sources*, **196**, 7161 (2011).
42. E. Perry Murray, M. J. Sever and S. A. Barnett, *Solid State Ionics*, **148**, 27 (2002).
43. V. Haanappel, in *Fuel Cell Science and Engineering*, p. 247, Wiley-VCH Verlag GmbH & Co. KGaA (2012).
44. N. P. Brandon and D. J. Brett, *Philosophical Transactions of the Royal Society A: Mathematical, Physical and Engineering Sciences*, **364**, 147 (2006).
45. J. R. Wilson, W. Kobsiriphat, R. Mendoza, H. Y. Chen, J. M. Hiller, D. J. Miller, K. Thornton, P. W. Voorhees, S. B. Adler and S. A. Barnett, *Nat Mater*, **5**, 541 (2006).
46. W. C. Chueh, Y. Hao, W. Jung and S. M. Haile, *Nature Materials*, **11**, 155 (2012).
47. A. Konno, H. Iwai, M. Saito and H. Yoshida, *Heat Transfer—Asian Research*, **41**, 700 (2012).
48. Q. Cai, C. S. Adjiman and N. P. Brandon, *Electrochimica Acta*, **56**, 10809 (2011).
49. R. J. Gorte and J. M. Vohs, *Current Opinion in Colloid & Interface Science*, **14**, 236 (2009).
50. M. Brown, S. Primdahl and M. Mogensen, *Journal of The Electrochemical Society*, **147**, 475 (2000).
51. S. Primdahl and M. Mogensen, *Journal of The Electrochemical Society*, **144**, 3409 (1997).
52. M. Kishimoto, K. Miyawaki, H. Iwai, M. Saito and H. Yoshida, *Fuel Cells*, **13**, 476 (2013).
53. F. Zhao and A. V. Virkar, *Journal of Power Sources*, **141**, 79 (2005).
54. P. R. Shearing, Q. Cai, J. I. Golbert, V. Yufit, C. S. Adjiman and N. P. Brandon, *Journal of Power Sources*, **195**, 4804 (2010).
55. C.-T. Wang and J. M. Smith, *AIChE Journal*, **29**, 132 (1983).
56. D. W. Dees, T. D. Claar, T. E. Easler, D. C. Fee and F. C. Mrazek, *Journal of The Electrochemical Society*, **134**, 2141 (1987).
57. S. K. Pratihari, R. N. Basu, S. Mazumder and H. S. Maiti, in *Proceedings of the Sixth International Symposium on Solid Oxide Fuel Cells (SOFC-VI)*, S. C. Singhal and M. Dokiya Editors, p. 513, Honolulu, Hawaii (1999).
58. D. Simwonis, F. Tietz and D. Stöver, *Solid State Ionics*, **132**, 241 (2000).
59. C. Jin, C. Yang and F. Chen, *Journal of The Electrochemical Society*, **158**, B1217 (2011).
60. K. Eguchi, T. Hatagishi and H. Arai, *Solid State Ionics*, **86–88, Part 2**, 1245 (1996).
61. L. Grahl-Madsen, P. Larsen, N. Bonanos, J. Engell and S. Linderoth, *J Mater Sci*, **41**, 1097 (2006).
62. D. Sarantaridis and A. Atkinson, *Fuel Cells*, **7**, 246 (2007).
63. T. A. Utigard, M. Wu, G. Plascencia and T. Marin, *Chemical Engineering Science*, **60**, 2061 (2005).
64. J. B. Goodenough and Y.-H. Huang, *Journal of Power Sources*, **173**, 1 (2007).
65. J. Udagawa, P. Aguiar and N. P. Brandon, *Journal of Power Sources*, **180**, 354 (2008).
66. N. P. Brandon, S. Skinner and B. C. H. Steele, *Annual Review of Materials Research*, **33**, 183 (2003).
67. A. Atkinson, S. Barnett, R. J. Gorte, J. T. S. Irvine, A. J. MCEvoy, M. Mogensen, S. C. Singhal and J. Vohs, *Nature Materials*, **3**, 17 (2004).
68. T. Setoguchi, K. Okamoto, K. Eguchi and H. Arai, *Journal of The Electrochemical Society*, **139**, 2875 (1992).
69. A. J. Jacobson, *Chemistry of Materials*, **22**, 660 (2009).
70. M. Radovic and E. Lara-Curzio, *Acta Materialia*, **52**, 5747 (2004).
71. J. Malzbender, E. Wessel and R. W. Steinbrech, *Solid State Ionics*, **176**, 2201 (2005).
72. S. D. Ebbesen and M. Mogensen, *Journal of Power Sources*, **193**, 349 (2009).

73. A. Hauch, S. D. Ebbesen, S. H. Jensen and M. Mogensen, *Journal of The Electrochemical Society*, **155**, B1184 (2008).
74. A. Hauch, S. r. H. j. Jensen, J. r. B. Bilde-Sorensen and M. Mogensen, *Journal of The Electrochemical Society*, **154**, A619 (2007).
75. S. D. Ebbesen, C. Graves and M. Mogensen, *International Journal of Green Energy*, **6**, 646 (2009).
76. V. Alzate-Restrepo and J. M. Hill, *Journal of Power Sources*, **195**, 1344 (2010).
77. H. He and J. M. Hill, *Applied Catalysis A: General*, **317**, 284 (2007).
78. J.-H. Koh, Y.-S. Yoo, J.-W. Park and H. C. Lim, *Solid State Ionics*, **149**, 157 (2002).
79. O. A. Marina, L. R. Pederson, M. C. Williams, G. W. Coffey, K. D. Meinhardt, C. D. Nguyen and E. C. Thomsen, *Journal of The Electrochemical Society*, **154**, B452 (2007).
80. K. Eguchi, K. Tanaka, T. Matsui and R. Kikuchi, *Catalysis Today*, **146**, 154 (2009).
81. J. F. B. Rasmussen and A. Hagen, *Journal of Power Sources*, **191**, 534 (2009).
82. E. Brightman, D. G. Ivey, D. J. L. Brett and N. P. Brandon, *Journal of Power Sources*, **196**, 7182 (2011).
83. A. Hagen and J. F. B. Rasmussen, in *9th European solid oxide fuel cell Forum* Luzern, Switzerland (2010).
84. S. McIntosh, J. M. Vohs and R. J. Gorte, *Electrochimica Acta*, **47**, 3815 (2002).
85. S. McIntosh and R. J. Gorte, *Chemical Reviews*, **104**, 4845 (2004).
86. S. Tao and J. T. S. Irvine, *Chemical Record*, **4**, 83 (2004).
87. R. J. Gorte and J. M. Vohs, *Journal of Catalysis*, **216**, 477 (2003).
88. O. A. Marina, C. Bagger, S. Primdahl and M. Mogensen, *Solid State Ionics*, **123**, 199 (1999).
89. S. J. A. Livermore, J. W. Cotton and R. M. Ormerod, *Journal of Power Sources*, **86**, 411 (2000).
90. B. Mirfakhraei, S. Paulson, V. Thangadurai and V. Birss, *Journal of Power Sources*, **243**, 95 (2013).
91. R. D. Green, C.-C. Liu and S. B. Adler, *Solid State Ionics*, **179**, 647 (2008).
92. S. Zha, W. Rauch and M. Liu, *Solid State Ionics*, **166**, 241 (2004).
93. W. Bao, H. Guan and J. Cheng, *Journal of Power Sources*, **175**, 232 (2008).
94. S. P. Jiang, *J Mater Sci*, **39**, 4405 (2004).
95. T. Z. Sholklapper, *Nano letters*, **7**, 2136 (2007).
96. P. I. Cowin, C. T. G. Petit, R. Lan, J. T. S. Irvine and S. Tao, *Advanced Energy Materials*, **1**, 314 (2011).
97. U. P. Muecke, K. Akiba, A. Infortuna, T. Salkus, N. V. Stus and L. J. Gauckler, *Solid State Ionics*, **178**, 1762 (2008).
98. M. B. Joerger and L. J. Gauckler, *Catalytically active anodes for SOFC*, p. 662, Electrochemical Society Inc, Pennington (2001).
99. L. Almar, B. Coldeforns, L. Yedra, S. Estrade, F. Peiro, A. Morata, T. Andreu and A. Tarancon, *Journal of Materials Chemistry A*, **1**, 4531 (2013).
100. M. Chen, B. H. Kim, Q. Xu, B. G. Ahn and D. P. Huang, *Solid State Ionics*, **181**, 1119 (2010).
101. K. T. Lee, C. M. Gore and E. D. Wachsman, *Journal of Materials Chemistry*, **22**, 22405 (2012).
102. C. Xia and M. Liu, *Solid State Ionics*, **144**, 249 (2001).
103. C. Xia and M. Liu, *Solid State Ionics*, **152–153**, 423 (2002).
104. N. Osada, H. Uchida and M. Watanabe, *Journal of The Electrochemical Society*, **153**, A816 (2006).
105. P. Kim-Lohsoontorn, Y.-M. Kim, N. Laosiripojana and J. Bae, *International Journal of Hydrogen Energy*, **36**, 9420 (2011).
106. M. Kishimoto, M. Lomberg, E. Ruiz-Trejo and N. P. Brandon, *Journal of Power Sources*, **266**, 291 (2014).
107. T. Nakamura, K. Yashiro, A. Kaimai, T. Otake, K. Sato, T. Kawada and J. Mizusaki, *Journal of The Electrochemical Society*, **155**, B1244 (2008).
108. S. P. Jiang, *Materials Science and Engineering: A*, **418**, 199 (2006).
109. R. Bove, in *Recent Trends in Fuel Cell Science and Technology*, S. Basu Editor, p. 267, Springer New York (2007).
110. N. Hart, N. Brandon and J. Shemilt, *Materials and Manufacturing Processes*, **15**, 47 (2000).

111. J. Will, A. Mitterdorfer, C. Kleinlogel, D. Perednis and L. J. Gauckler, *Solid State Ionics*, **131**, 79 (2000).
112. J. R. Wilson, R. Kobsiriphat W Fau - Mendoza, H.-Y. Mendoza R Fau - Chen, J. M. Chen Hy Fau - Hiller, D. J. Hiller Jm Fau - Miller, K. Miller Dj Fau - Thornton, P. W. Thornton K Fau - Voorhees, S. B. Voorhees Pw Fau - Adler, S. A. Adler Sb Fau - Barnett and S. A. Barnett.
113. J. R. Wilson, J. S. Cronin and S. A. Barnett, *Scripta Materialia*, **65**, 67 (2011).
114. E. D. Wachsman and K. T. Lee, *Science*, **334**, 935 (2011).
115. T. Z. Sholklapper, H. Kurokawa, C. P. Jacobson, S. J. Visco and L. C. De Jonghe, *Nano letters*, **7**, 2136 (2007).
116. D. Neagu, G. Tsekouras, D. N. Miller, H. Ménard and J. T. S. Irvine, *Nat Chem*, **5**, 916 (2013).
117. M. Boaro, J. M. Vohs and R. J. Gorte, *Journal of the American Ceramic Society*, **86**, 395 (2003).
118. H. Kim, C. da Rosa, M. Boaro, J. M. Vohs and R. J. Gorte, *Journal of the American Ceramic Society*, **85**, 1473 (2002).
119. S. P. Jiang, *International Journal of Hydrogen Energy*, **37**, 449 (2012).
120. Y. Huang, J. M. Vohs and R. J. Gorte, *Journal of The Electrochemical Society*, **151**, A646 (2004).
121. S. P. Jiang, S. Zhang, Y. D. Zhen and A. P. Koh *Electrochemical and Solid-State Letters*, **7**, A282 (2004).
122. R. Craciun, S. Park, R. J. Gorte, J. M. Vohs, C. Wang and W. L. Worrell, *Journal of The Electrochemical Society*, **146**, 4019 (1999).
123. H. Uchida, H. Suzuki and M. Watanabe, *Journal of The Electrochemical Society*, **145**, 615 (1998).
124. E. Ruiz-Trejo and J. T. S. Irvine, *Solid State Ionics*, **252**, 157 (2013).
125. G. Kim, S. Lee, J. Y. Shin, G. Corre, J. T. S. Irvine, J. M. Vohs and R. J. Gorte, *Electrochemical and Solid-State Letters*, **12**, B48 (2009).
126. E. Hardjo, D. S. Monder and K. Karan, *ECS Transactions*, **35**, 1823 (2011).
127. A. N. Busawon, D. Sarantaridis and A. Atkinson, *Electrochemical and Solid-State Letters*, **11**, B186 (2008).
128. B. Hua, W. Zhang, M. Li, X. Wang, B. Chi, J. Pu and J. Li, *Journal of Power Sources*, **247**, 170 (2014).
129. S. Primdahl and Y. L. Liu, *Journal of The Electrochemical Society*, **149**, A1466 (2002).
130. S. Primdahl and M. Mogensen, *Solid State Ionics*, **152–153**, 597 (2002).
131. H. Uchida, S. Suzuki and M. Watanabe, *Electrochemical and Solid-State Letters*, **6**, A174 (2003).
132. J. Nielsen, T. Klemensø and P. Blennow, *Journal of Power Sources*, **219**, 305 (2012).
133. S. McIntosh, J. M. Vohs and R. J. Gorte, *Electrochimica Acta*, **47**, 3815 (2002).
134. T. Klemensø, K. Thydén, M. Chen and H.-J. Wang, *Journal of Power Sources*, **195**, 7295 (2010).
135. J. P. Kruth, M. C. Leu and T. Nakagawa, *CIRP Annals - Manufacturing Technology*, **47**, 525 (1998).
136. S. Kumar, *Jom-Journal of the Minerals Metals & Materials Society*, **55**, 43 (2003).
137. D. L. Bourell, J. J. Beaman and Tms, *POWDER MATERIAL PRINCIPLES APPLIED TO ADDITIVE MANUFACTURING*, p. 537, Minerals, Metals & Materials Soc, Warrendale (2012).
138. A. Simchi, *Materials Science and Engineering a-Structural Materials Properties Microstructure and Processing*, **428**, 148 (2006).
139. I. Gibson, D. Rosen and B. Stucker, *Additive Manufacturing Technologies. Rapid Prototyping to Direct Digital Manufacturing*, Springer US (2010).
140. I. Gibson and D. P. Shi, *Rapid Prototyping Journal*, **3**, 129 (1997).
141. A. R. R. Bineli, A. P. G. Peres, A. L. Jardini and R. M. Filho, in *6th BRAZILIAN CONFERENCE ON MANUFACTURING ENGINEERING*, Caxias do Sul – RS – Brazil (2011).
142. P. Bertrand, F. Bayle, C. Combe, P. Goeriot and I. Smurov, *Applied Surface Science*, **254**, 989 (2007).

143. S. Chen, J. Murphy, J. Herlehy, D. L. Bourell and K. L. Wood, *Rapid Prototyping Journal*, **12**, 275 (2006).
144. N. Guo and M. C. Leu, *Journal of Fuel Cell Science and Technology*, **11** (2014).
145. N. Guo and M. C. Leu, *International Journal of Hydrogen Energy*, **37**, 3558 (2012).
146. H. Husby, O. E. Kongstein, A. Oedegaard and F. Seland, *International Journal of Hydrogen Energy*, **39**, 951 (2014).

CHAPTER III

GENERAL METHODOLOGY

3.1 Introduction

The goal of this chapter is to outline a methodology for cell preparation, testing and characterisation used in this research to study the performance of Ni-infiltrated GDC fuel electrodes for SOCs. First the procedure of cell preparation is explained, including the fabrication of the Gadoped ceria (GDC) ink for screen printing, screen printing procedure for porous GDC scaffold fabrication, and the incorporation of Ni nano-particles into the GDC porous structure by the infiltration method. Then the experimental set-up for cell testing is demonstrated.

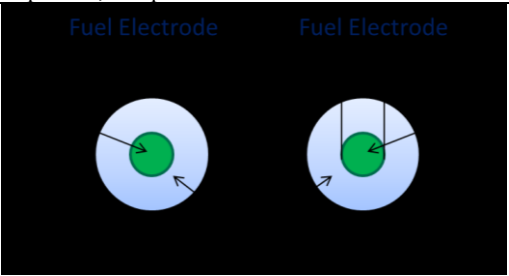
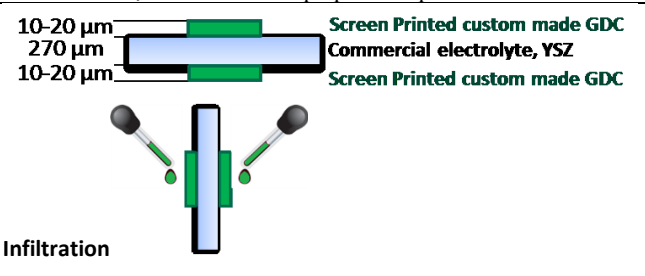
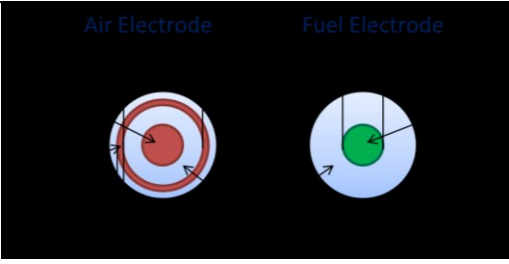
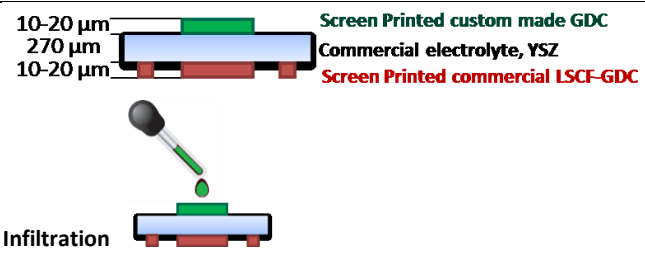
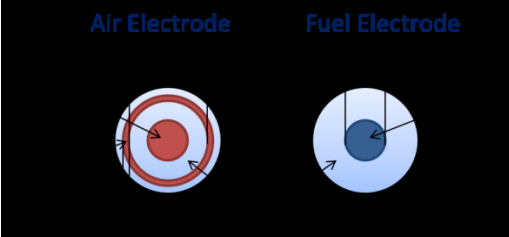
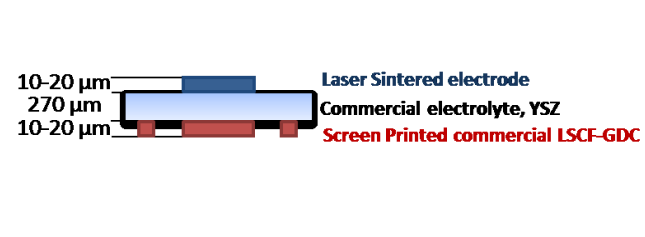
This is followed by the detailed explanation of the cell testing methodology including electronic conductivity measurements of infiltrated electrodes and electrochemical performance assessed by Electrochemical Impedance Spectroscopy (EIS) in a symmetrical cell and a three electrode cell configurations. Finally, methods for two-dimensional and three-dimensional imaging by SEM and FIB-SEM, respectively, to study the microstructural evolution of the infiltrated electrodes, are outlined.

The methodology of electrode fabrication by laser sintering is described in Chapter V (laser sintering for SOC electrode fabrication).

3.2 Cell preparation

In this section the process of cell fabrication is described. There are two types of cell configuration used in this study, symmetrical cells in two electrode configuration and full cells in three electrode configuration. Symmetrical cells consist of two identical fuel electrodes, one on each side of the electrolyte. The full fuel cells consist of anode (also referred to as the fuel or working electrode (WE)) fabricated on one side of the electrolyte, and the cathode (also referred to as the air or counter electrode (CE)) and reference electrodes (RE) fabricated on the other side. Taking into account the differing fabrication methods used, three types of cells were used in the research: symmetrical and full cells with infiltrated fuel electrode, and full cells with laser sintered fuel electrodes. Table 3.1 summarizes the fuel cell configurations with component dimensions and fabrication methods used in the research. Only the methodology for infiltrated electrodes preparation is included in this chapter.

Table 3.1. Summary of fuel cell configurations, cell dimensions and fabrication methods used in this study.

| Cell | Top View, components and dimensions | Cross Section, dimensions and preparation processes |
|---|---|--|
| Symmetrical (two electrode) cell with Ni infiltrated GDC electrodes |  |  <p>Infiltration</p> |
| Full Cell (three electrode) with Ni infiltrated GDC fuel electrode |  |  <p>Infiltration</p> |
| Full cell (three electrode) with laser sintered fuel electrode |  |  |

The manufacturing steps of cell preparation are shown in diagram in Figure 3.1.

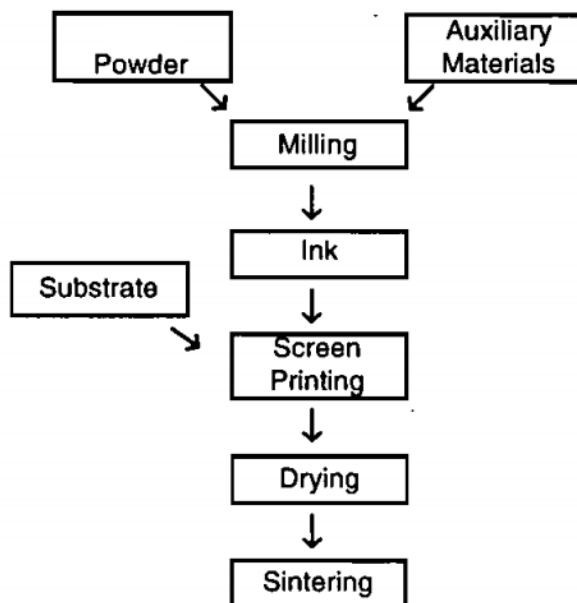


Figure 3.1. Flow chart representing the manufacturing processes of cell preparation (1).

3.2.1 GDC ink preparation for fuel electrode scaffold

In this study two GDC scaffolds were studied. The resultant scaffolds varied in pore size depending on the pore formers (or their absence) used for ink preparation. For the ink number 1 (ink#1) no pore formers were used and for the ink number 2 (ink#2) 20 μm microbeads were used as pore formers (40 vol%). Materials and equipment used for ink fabrication are detailed in Table 3.2.

Table 3.2. Materials and equipment used for ink fabrication.

| Equipment or material | Details | Supplier |
|--|---|---------------------|
| Ce _{0.9} Gd _{0.1} O _{1.95} (GDC) powder | Particle size: 0.1-0.4 μm Surface area: 5-8 m^2/g | Fuel Cell Materials |
| PMMA microbeads for ink#2 | 20 μm | |
| Dispersant | Hypermer KD15 | Croda |
| Binder | Ethylcellulose N7 grade | IMCD UK/Hercules |
| Solvent | Terpineol | Sigma Aldrich |
| Triple Roll Mill | Three horizontal zirconia rolls rotating in opposite directions and different speeds relative to each other | EXAKT 80E, Germany |

The steps for the GDC ink fabrication are detailed below:

1. Mixing GDC powder with dispersant and acetone for 24 hrs using a ball mill.
2. Drying the wet powder in an oven at 90 °C for 3 hrs.
3. Mixing dry powder with the binder and the solvent in an agate mortar.
4. Homogenizing the resultant mixture using a triple roll mill.

The total solid fraction in the ink was 75 wt%.

3.2.2 Screen printing and sintering of electrodes

In this research SMTech-90 series screen-printer was used for fabrication of the following components.

- GDC scaffold for both electrodes in symmetrical (two-electrode) cell
- GDC scaffold for the anode in a full fuel cell
- LSCF-GDC cathode for full fuel cells

The screen printing steps are schematically shown in Figure 3.2.

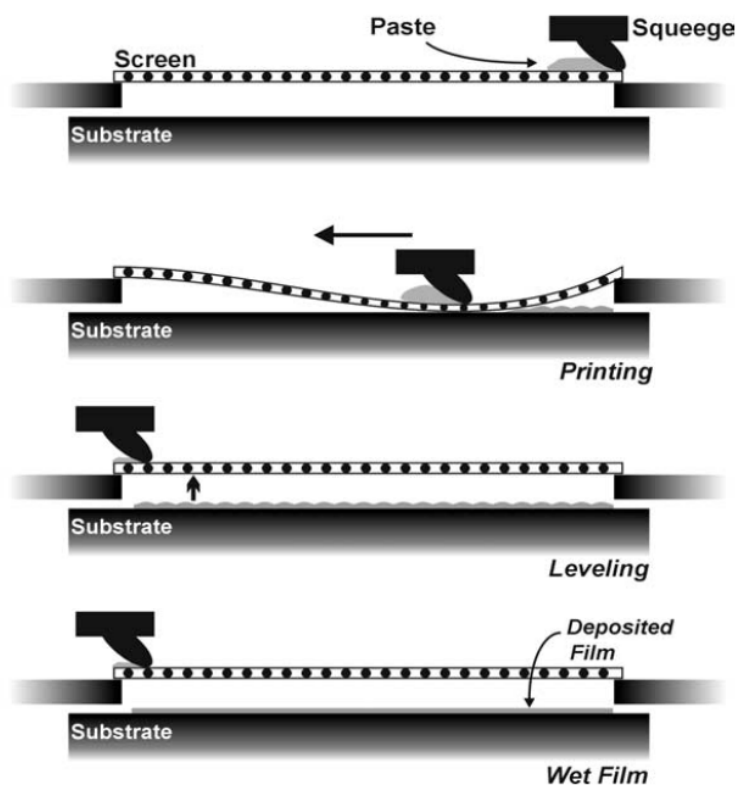


Figure 3.2. Schematic representation of the screen-printing process (2).

The main elements in screen printing are: the screen, which is the image carrier, the squeegee and the ink. The screen uses a porous mesh stretched tightly over a frame made of metal. The ink is placed on top of the screen. The ink is then drawn across the screen using a squeegee, applying pressure and thereby forcing the ink through the open areas of the screen, forming a film on the printing substrate (2). The conditions of screen printing parameters used in this research are summarised in Table 3.3.

Table 3.3. Screen printing parameters and conditions.

| Parameter | Conditions |
|----------------------|-------------------|
| Print speed | 0.02 m/s |
| Squeegee type | Polyurethane |
| Squeegee load | 6 kg |
| Squeegee length | 12.7 cm |
| Number of passes | 2 |
| Screen mesh type | 325 |
| Snap off (print gap) | 2 mm |

The GDC film (approx. 20 μm in thickness) was screen printed on 8YSZ disk-shaped electrolytes of 270 μm thickness (Fuel Cells Materials) and then sintered at 1350 °C for 2 hrs aiming to achieve 50% porosity in the resultant GDC scaffold. For the symmetrical (two-electrode) cell the GDC scaffold was fabricated on both sides of the electrolyte following the same procedure.

According to Sammes et al, ceria and fully stabilised zirconia show only limited solubility in one another (3). Tompsett et al reported that the reactivity of Gd-doped CeO_2 with YSZ is low, and only after treatment at 1300 °C for 72 hrs did the diffusion of ions occur between polished ceramic discs in intimate contact (4). The sintering procedure in this research included a dwell time of only 2 hrs in 1350 °C and therefore significant reaction between doped ceria and stabilized zirconia reaction is not likely.

For (three-electrode) fuel cells the air (counter and reference) electrodes were screen printed simultaneously on the other side of the electrolyte using an LSCF-GDC ink (Fuel Cells Materials) and

subsequently sintered at 1100 °C for 2 hrs. The ink comprised 50 wt% $(\text{La}_{0.60}\text{Sr}_{0.40})_{0.95}(\text{Co}_{0.20}\text{Fe}_{0.80})\text{O}_{3-x}$ and 50 wt% $(\text{Ce}_{0.90}\text{Gd}_{0.10})\text{O}_{1.95}$ with a total solid fraction in the ink of 65-75 wt%.

The identical disk-shaped anode and cathode electrodes were 11 mm in diameter with a surface area of 0.95 cm². A ring-shaped reference electrode had internal and external diameters of 16 mm and 18 mm, respectively (all dimensions are shown in Table 3.1).

3.2.3 Infiltration of Ni nano-particles in ceramic scaffolds for fuel electrodes

The typical infiltration process is demonstrated schematically in Figure 3.3.

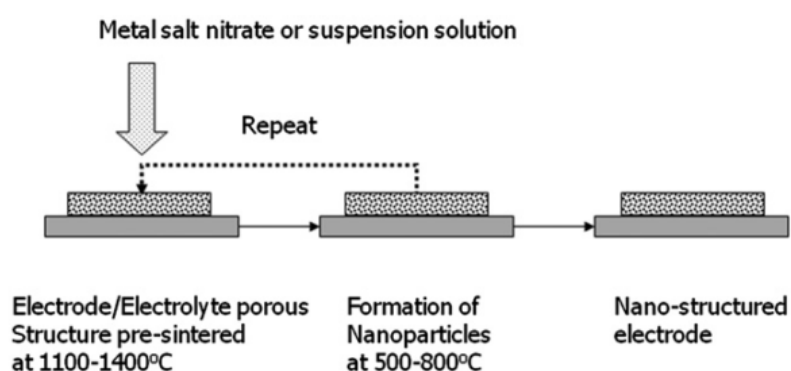


Figure 3.3. Typical process for the infiltration of metal salt nitrate solution or nanoparticle suspension into a pre-sintered electrode or electrolyte porous structure (5).

The solution for infiltration was prepared by mixing nickel nitrate $\text{Ni}(\text{NO}_3)_2 \cdot 6\text{H}_2\text{O}$ with ethanol to a concentration of 2M. Ethanol was used as a solvent for two reasons. Firstly, the solubility of $\text{Ni}(\text{NO}_3)_2 \cdot 6\text{H}_2\text{O}$ in ethanol is higher than in water and secondly the solution based on ethanol provides smaller surface energy which enables better wettability and fluidity on the ceramic surface and, as a consequence, deeper penetration of the porous structure.

A micro-pipette was used to deposit measured drops (2 μl) of the solution on top of a sintered ceramic scaffold. The solution was infiltrated into GDC scaffolds by capillary action. The excess solution on the electrode surface was wiped with a soft tissue and dried. The sample was then fired at 500 °C for 0.5 hr in air to decompose the nickel nitrate salt to form NiO nano-particles. The profile of $\text{Ni}(\text{NO}_3)_2 \cdot 6\text{H}_2\text{O}$ decomposition with temperature is shown in Figure 3.4 (6).

The loading of the infiltrated nickel phase was estimated by measuring the weight differences before infiltration and after the heat treatment and reduction. The whole process was repeated up to ten times to increase the loading of the metal phase. Ten infiltrations of nickel led to a nickel content of 25 ± 3 wt% (18.6-24 vol%).

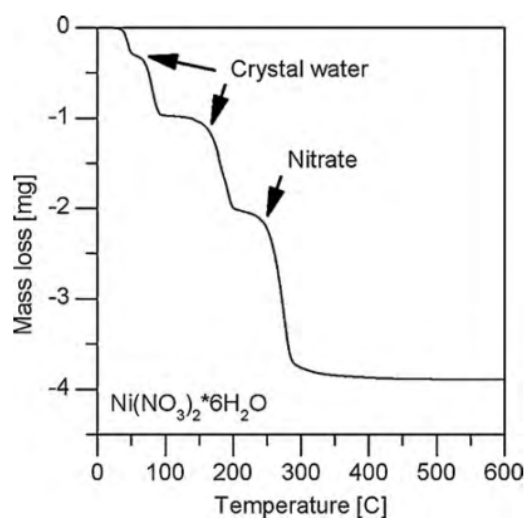


Figure 3.4. Thermogravimetric profile of $\text{Ni}(\text{NO}_3)_2 \cdot 6\text{H}_2\text{O}$ (6).

3.2.4 Reduction of the electrode

Taking into account the impact of reduction conditions on the properties of fuel electrodes discussed in the literature survey (section 2.7.1), the reduction procedure used in this research was as follows.

1. The cell was heated up from room temperature at a heating rate of $5^\circ\text{C}/\text{min}$ to the reduction temperature of 750°C . During heating the fuel electrodes were exposed to a protective atmosphere (100% N_2).
2. At 750°C the electrode was exposed to reducing conditions of 50% H_2 and 50% N_2 , for 0.5-1 hrs.
3. After reduction the electrodes were maintained under a reducing atmosphere during the whole period of the experiment. The proportions between N_2 and H_2 in a gas mixture were defined according to the experiment.
4. At the end of the experiment the cell was cooled down to the room temperature at a rate of $5^\circ\text{C}/\text{min}$ in 10% H_2 – 90% N_2 .

3.3 Experimental set-up for electrochemical performance measurements

Electrochemical tests of the button cells were performed using a custom-built test station, as illustrated in Figure 3.5.

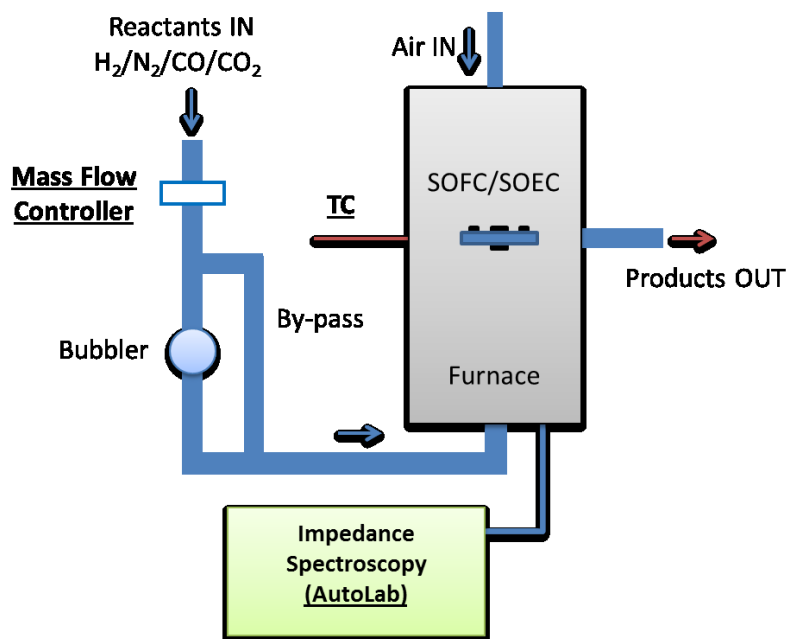


Figure 3.5. Overview of the experimental system. Underlined bold font indicates items controlled/monitored by the software on PC.

Composition of the reactant/carrying gases ($\text{H}_2/\text{N}_2/\text{CO}_2/\text{CO}$) was regulated by mass flow controllers (connected and controlled by a computer via Bronkhorst software interface) and carried through a water bubbler to achieve humidification of ca. 3% H_2O (in ambient temperature). Humidified gas was then supplied to the SOC, held in the furnace.

The SOC was attached to the end of an alumina tube with gas supplied through a narrower alumina tube directly to the fuel electrode. The air electrode was exposed to the laboratory atmosphere (21 % O_2), such that oxygen depletion was negligible for the duration of the experiment. The cell temperature was monitored via computer software (PicoLog Recorder) interface using a K-Type Thermocouple, positioned ca. 5 mm above the surface of the anode. A close-up schematic of the equipment can be seen in Figure 3.6 (7).

Electrical connections were made to the electrodes via silver wires and paste and the ohmic resistance of the leads is compensated for using a sense electrode. The cell was sealed using alumina-based cement (Aron Ceramic, Japan).

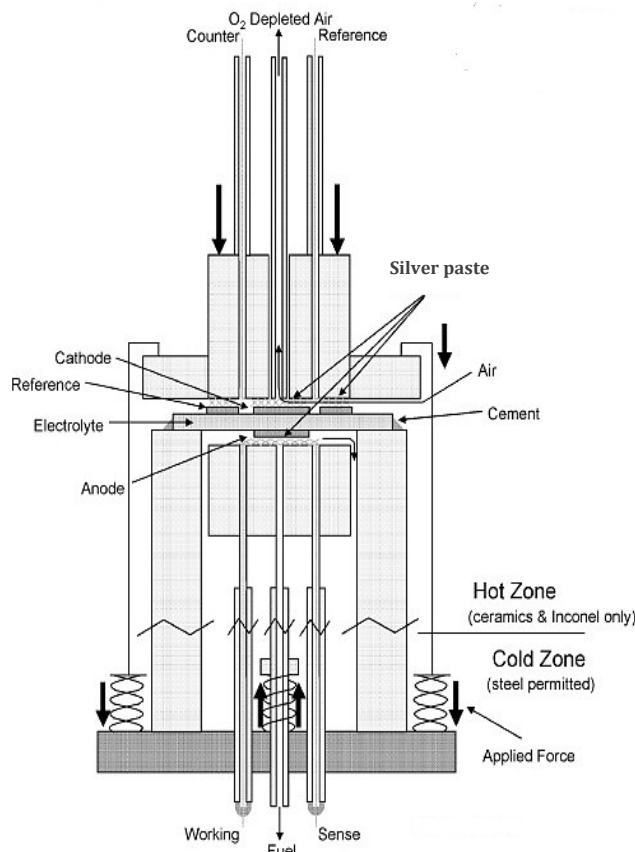


Figure 3.6. Schematic illustration of the rig used for electrochemical performance measurements of SOCs (7).

3.4 Cell performance measurements

Initially, the electronic conductivity of infiltrated electrodes was assessed using a DC 4-probe electrical conductivity method (also referred to as Van der Pauw method) as a function of the nickel loading introduced by infiltration of the GDC scaffold. Then the electrochemical performance of the fuel electrode was estimated in a symmetrical cell configuration using Electrochemical Impedance Spectroscopy (EIS). Finally, the electrochemical performance of the full cell was evaluated in three electrode and two electrode modes.

3.4.1 Electronic conductivity measurements of infiltrated electrodes

The DC 4-probe electrical conductivity of the reduced electrodes was measured using the van der Pauw technique (8) in custom made apparatus demonstrated in Figure 3.7 (9).

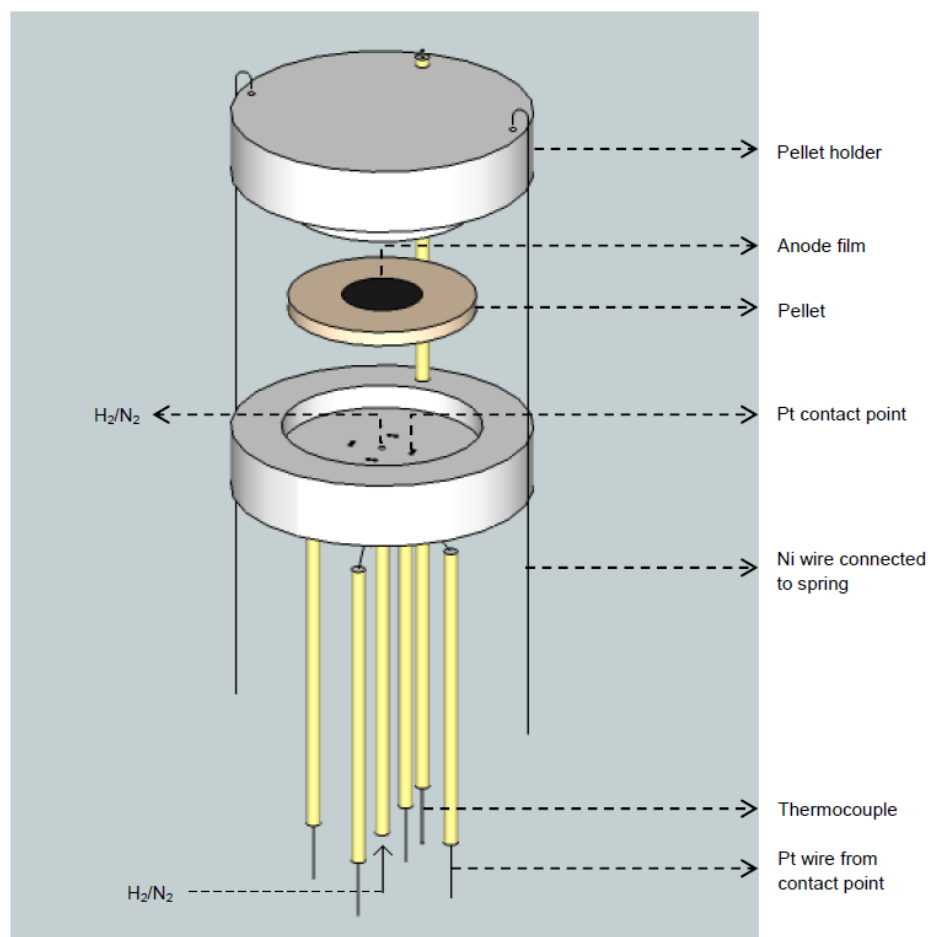


Figure 3.7. DC 4-probe electrical conductivity measurement apparatus (9).

The four contact points made from 0.25 mm Pt wires arranged in the corners of the 5.5 x 5.5 mm² square. Each point is noted as a number 1, 2, 3 and 4 as shown in Figure 3.8. The cell is placed inside the holder such that the electrode surface remains in a contact with the probes during the measurements. The tight contact between the probes and the electrode surface is maintained by the pressure on the holder by Ni wires connected to a rigid spring.

During the experiment four consecutive measurements were performed, with a constant current applied to two adjacent sides of the sample (e. g. points 1 and 2) and the voltage measured at the opposite side of the current contacts (e. g. points 3 and 4) as shown schematically in Figure 3.8.

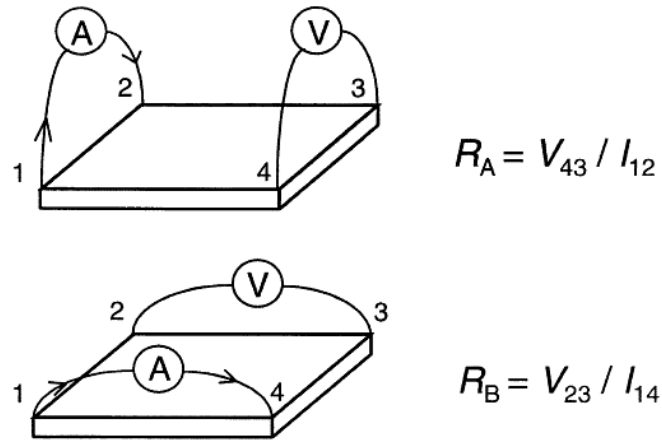


Figure 3.8. Measurement of a square conductivity sample in the Van der Pauw geometry. The two resistance measurements are combined with the thickness of the sample to give the conductivity (10).

Based on Ohm's law, an average resistance, R_{avg} , can be calculated using the four measured values according to Equation 3.1.

$$R_{avg} = \frac{1}{4} \times \left(\frac{V_{43}}{I_{12}} + \frac{V_{23}}{I_{14}} + \frac{V_{12}}{I_{34}} + \frac{V_{14}}{I_{23}} \right) \quad 3.1$$

The conductivity of the electrode, σ , depends on its thickness, d , and can be calculated according to Equation 3.2 (8). The thickness of the electrode, d , is determined from the image obtained by the scanning electron microscope.

$$\sigma = \frac{\ln(2)}{R_{avg} \pi d} \quad 3.2$$

The Van der Pauw method has been widely used to assess the electronic conductivity of solid oxide cell porous cermet electrodes (11-14).

The electronic conductivity of the 3, 6 and 10 times Ni infiltrated GDC electrodes was measured in a humidified 50% H_2 – 50% N_2 atmosphere in the 100-700 °C temperature range to study the impact of the metal phase loading in the electrode.

3.4.2 Calculation of the theoretical open circuit potential (OCP) of the cell

The theoretical OCP was calculated according to the formation of 1 mole of water using the Nernst equation (2.3) as follows.

| | |
|---|---|
| $H_2 + \frac{1}{2}O_2 \rightarrow H_2O$ $K = \frac{[red]}{[ox]} = \frac{P(H_2O)}{P(H_2)P(O_2)^{0.5}}$ | $\Delta G = -247500 + 55.85 \cdot T \quad (15)$ $\Delta G = -RT \ln K$ $E = \frac{RT}{nF} \ln K = \frac{RT}{nF} \ln \frac{[red]}{[ox]}$ |
|---|---|

Decrease (in the absolute value) of the calculated OCP with temperature is shown in Figure 3.9.

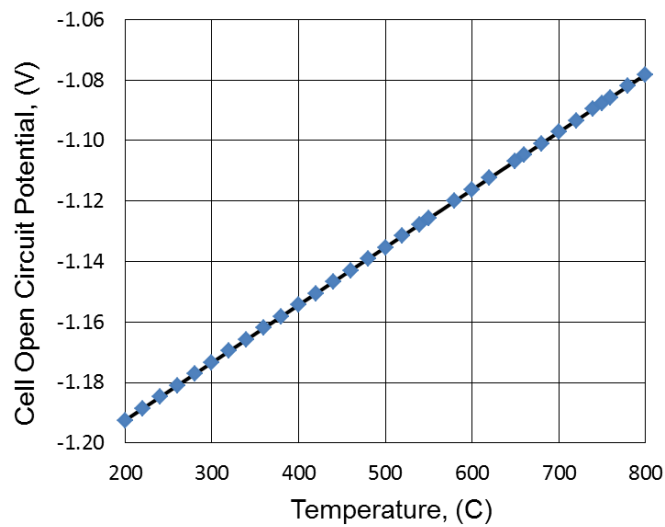


Figure 3.9. Theoretical calculations of the cell OCP.

The OCP measured in the experiment can differ from the theoretical value. This can happen due to cell leakage that leads to partial pressure change. Thus, the measured OCP can give an indication of the cell sealing quality.

3.4.3 Electrochemical Impedance Spectroscopy

As was discussed in the literature review, the potential losses associated with each of the compartments and interfaces in the cell, are caused by different mechanisms of electrical, chemical or mixed nature and hence vary in speed and activation energy required for each process. It is important, therefore, to identify these processes in order to optimize fuel cell performance.

Electrochemical Impedance Spectroscopy (EIS) is a non-destructive technique commonly used for characterisation of the electrochemical performance of fuel cells. In this method alternating current (or potential) is passed over a range of frequencies across the cell with a wave-form $x = x_0 \sin(\omega t)$, where x_0 is an amplitude < 10 mV (i.e. in a potentiostatic mode) resulting in an output signal of the same frequency ω . The output signal is defined by the function $y = y_0 \sin\{(\omega + \varphi)t\}$, where φ is the phase angle. The impedance at the corresponding frequency is a complex number determined by y/x ratio (16). The impedance spectrum, separated as a function of frequency, is represented in terms of complex numbers and could be plotted as an imaginary vs real part of the complex number (Nyquist plot) as represented in Figure 3.10 (16).

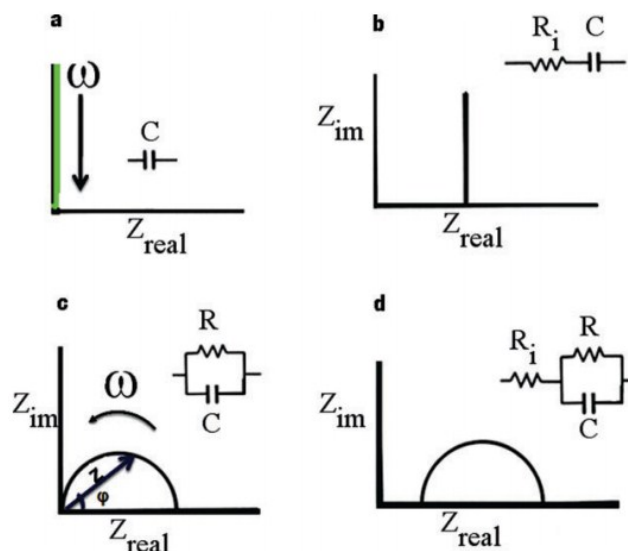


Figure 3.10. Nyquist plots for (a) a capacitor, (b) a capacitor in series with a resistor, (c) a capacitor in parallel with a resistor, and (d) a resistor in series with a parallel RC-circuit (16).

The results can be interpreted in terms of the components of an electrical circuit: resistors, capacitors and inductors connected in series or in parallel (17). For example, pure resistive behaviour

lacks an imaginary part, hence $\varphi=0^\circ$, and pure capacitive behaviour lacks the real component, hence $\varphi=-90^\circ$ (Figure 3.10a). However, typically the plots form several semi-circles indicating mixed behaviour (Figure 3.10b-d). The polarisation of the processes having different time constants can then be extracted by fitting the results into an equivalent electrical circuit model as shown in insets of Figure 3.10.

Then the components of the equivalent circuit can be assigned to the corresponding electrochemical processes. For example, the high frequency semi-circle often represents a charge transfer polarisation and a lower frequency semi-circle may account for the mass transfer resistance. Diffusion processes can be often modelled by a Warburg impedance element ($\varphi=45^\circ$). The high frequency intercept (or series resistance, R_s) is of an ohmic nature and normally describes the electrolyte resistance Figure 3.11.

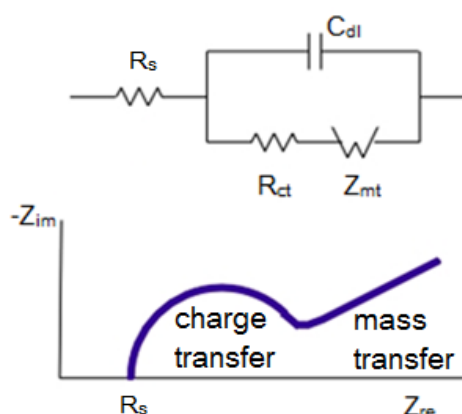


Figure 3.11. Equivalent electrical circuit and schematic Nyquist plot for an electrochemical system governed by charge and mass transfer.

Due to the capability to determine the polarisation resistance resulting from charge transfer, ohmic and mass transport losses, and correlate them to cell performance, EIS is a valuable diagnostic tool for SOC electrochemical performance characterisation (18, 19).

However, one of the problems associated with EIS analysis is overlapping between semi-circles which make it difficult to identify and to de-convolute the data into individual components. In this case the response will result in non-symmetrical semicircle(s) as demonstrated in Figure 3.12. This impedance data corresponds to the oxygen reduction reaction at a nanostructured LSCF cathode (20).

In addition to a pure resistor or capacitor, the response can also be fitted by a Warburg element as described previously, and a constant phase element (CPE) that models the behaviour of a double layer for an imperfect capacitor ($\varphi = -90^\circ \cdot n$, $0 < n < 1$). The double layer can also be associated with gaseous species adsorbed on the electrode surface or with capacitance due to the mixed-conductive nature of the GDC electrode (21).

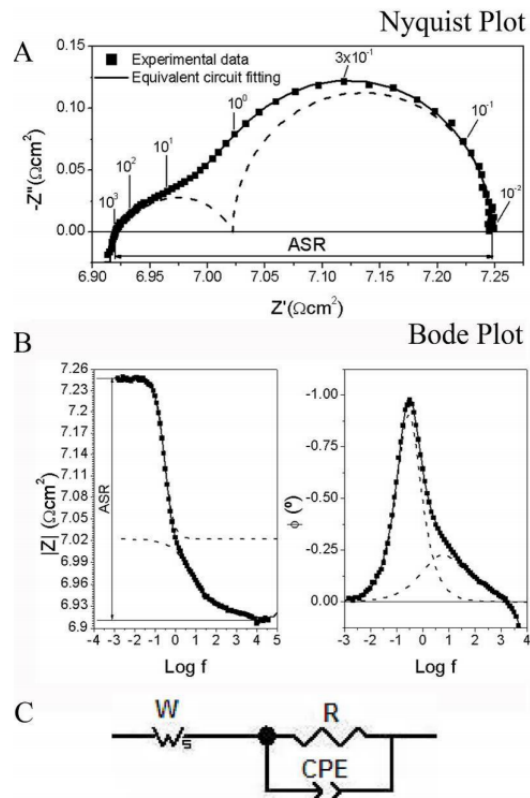


Figure 3.12. Example of an impedance spectrum. (A) Nyquist and (B) Bode plots. Numbers in Figure A indicate the measuring frequency. Points are experimental data, continuous lines represent equivalent circuit fitting and dotted lines represent the individual contributions. (C) Equivalent circuit used for fitting (20).

An overlapping between semi-circles can occur due to several processes having similar kinetics (or time constants), for example, processes of the same origin occurring simultaneously on the anode and cathode. One of the possible methods to deal with this problem is to change some of the experiment conditions whilst keeping others constant. Since impedance spectroscopy is sensitive towards various cell parameters, i.e. fuel concentration, temperature, current, etc, the change will be reflected in impedance spectra (22).

Another way to overcome the problem mentioned above is to use a three electrode cell configuration. The principles of three electrode measurements are discussed in section 3.4.4. This configuration allows the influence of the counter electrode on the impedance spectra to be excluded, reducing the number of components in the equivalent circuit and making data analysis more precise. However, the presence of the reference electrode may cause other problems related to data analysis. Therefore to clarify and assist interpreting data analysis the EIS measurements in this study were also performed in two electrode configuration in a full cell and in a symmetrical cell.

3.4.4 Conditions for electrochemical performance measurements

The electrochemical performance of the cell was estimated in both electrolytic (SOEC) and galvanic (SOFC) modes. The measurements were carried out in two or three-electrode cell configurations over a range of temperatures (580-750 °C) and gas compositions (20-80% H₂ – 20-80% N₂) in dry or humidified conditions. Humidified gas conditions were achieved by forcing a gas feed through a water bubbler to achieve approximately 2-3% H₂O content. The total flow rate of gas feed was 100 ml/min.

The performance of the electrode in a symmetrical cell was measured over the same range of temperatures (580-750 °C) in 50% H₂ – 50% N₂. These data were used to validate the results obtained in a three-electrode configuration as will be described further.

Durability studies of infiltrated electrodes were performed at a constant operating temperature of 600 °C under 10mA/cm² current density and humidified 50% H₂ – 50% N₂ gas composition for 100 – 320 hrs.

Electrochemical measurements including polarisation (i - V) curves and impedance spectra (EIS) were logged and analysed in real time by an Autolab PGSTAT302 (Eco Chemie BV, The Netherlands) with a Frequency Response Analysis (FRA) module, interfaced to a computer through Autolab FRA and Nova software. Galvanostatic impedance spectra were measured in the frequency

range of 100 mHz – 100 kHz at OCP (with an AC amplitude of 6 mA) and at different current densities (5-20 mA/cm²).

To obtain the area-specific resistance (ASR) the polarisation resistance measured in three electrode measurements was multiplied by the electrode surface area. The values for the polarisation resistance in the symmetrical cell were divided by two and multiplied by the geometric area to obtain the ASR of one electrode. The EIS data were processed and fitted into equivalent electrical circuits using ZView software (Scribner Associates).

Three-electrode measurements for SOC testing

The principle of three-electrode measurements is such that electrical current flows between the working and the counter electrodes, while the potential is measured between the reference and the working electrodes as shown schematically in Figure 3.13.

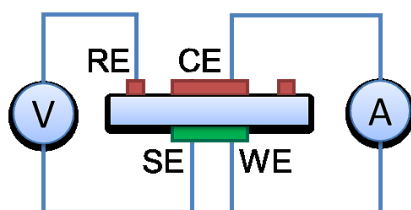


Figure 3.13. Three electrode measurements, WE – working electrode, SE – sense electrode, CE – counter electrode and RE – reference electrode.

This allows working electrode overpotentials to be extracted under current load, however the interpretation is more complex due to concerns over reference electrode placement (13, 23-25). Therefore two electrode measurements in a symmetrical cell were also performed to avoid these concerns.

Symmetrical cells measurements

As has been discussed elsewhere (24-27), reference electrode placement in SOCs can be problematic, and experimental data gathered using a three-electrode configuration must be considered carefully.

Alignment of the counter and the reference electrode is essential to ensure the correct determination of the working electrode polarisation (24). When the counter and reference electrodes are perfectly aligned the only condition to ensure the validity of three-electrode measurements is the placement of the reference electrode far from the counter electrode (7, 28).

It was found that the potential along the gas-exposed surface of the electrolyte near the edges of the electrode varies with position, until a distance of about three electrolyte thickness (24). Beyond this distance the potential is uniform everywhere. In this work relatively thick ($270\mu\text{m}$) cells were used, and the reference electrode was positioned 3mm away from the counter electrode, greater than the three electrolyte thicknesses required to prevent interference from the counter electrode. However, any misalignment of the counter and the working electrode may bias the reference potential towards the active electrode, as shown in Figure 3.14 (24). Since an overlap of one of the electrodes by a value greater than the electrode thickness may lead to large errors in measurements, additional validation measurements were included in this work.

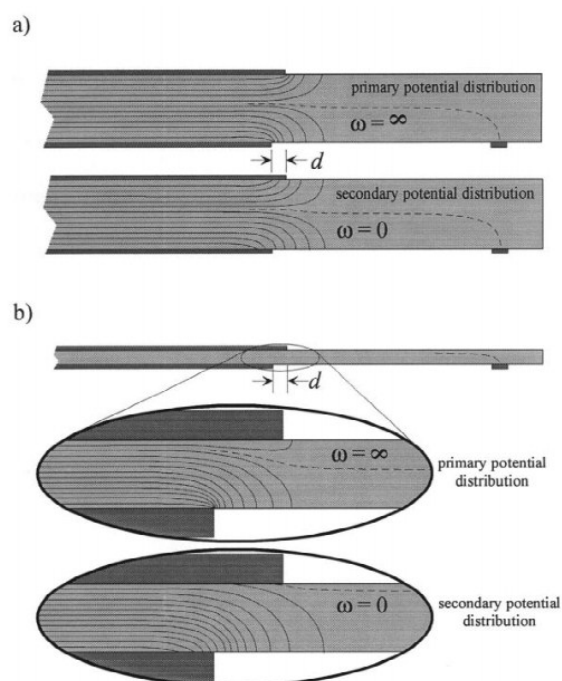


Figure 3.14. Reference potential drifts with frequency. (a) Thick electrolyte — small reference drift (b) Thin electrolyte — large reference drift (24).

The validation criterion for the three-electrode measurements is the potential difference between the working and the reference electrode. If the electrodes are perfectly aligned this difference should be approximately half of the cell potential (24). This condition is achieved if the potential at the reference electrode corresponds to the potential of the middle plane in the electrolyte, i.e. half of the electrolyte contribution to impedance is measured in three-electrode setup (26). An effective way to verify this is to compare results of the three-electrode fuel cell impedance spectrum with the impedance spectrum from the corresponding symmetrical cell. Therefore, electrochemical impedance was measured in a two-electrode symmetrical cell over a range of temperatures (580-750 °C) in 50% H₂ – 50% N₂ in a four-probe set-up. In a four-probe set-up the resistance of leads is compensated due to using sense and reference electrodes (Figure 3.15a). The gas in the rig for symmetrical cell testing flowed parallel to the electrodes as shown in Figure 3.15b, while the gas flow in the three-electrode fuel cell rig was perpendicular to the electrode (Figure 3.6).

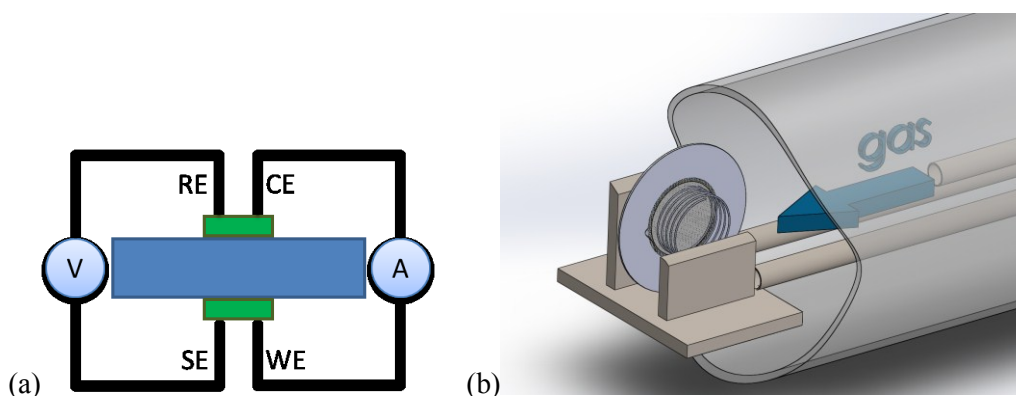


Figure 3.15. Symmetrical rig (a) four-probe set-up; (b) direction of gas flow.

3.5 Microstructure characterisation methods

3.5.1 General aspects

Analysis of the microstructure is crucial for understanding and optimizing of the SOC electrode properties. In SOCs the change from one phase into the other occurs at the nano-scale. Therefore, for a precise characterisation of the microstructure high spatial resolution techniques are required. The main tool used for morphology characterisation was a scanning electron microscope (SEM) with a

Field Emission Gun (FEG). Images with high magnification (>200k) can be acquired using FEG-SEM. Two-dimensional (2-D) microstructure evolution analysis was performed before and after testing. The cell was fractured, and the morphology of the electrode surface and a cross-section was examined using a Scanning Electron Microscope LEO Gemini 1525 FEG-SEM.

Distribution of Ni nano-particles inside the electrode was studied by mapping Ni on the cross-section of the infiltrated electrode. The micrograph was taken with JSM 6010 LA microscope fitted with Oxford instruments INCA energy dispersive X-ray spectrometer (EDX). The EDX data was accumulated from 20 sweeps with 0.1 ms point dwell time.

There is increased interest in three-dimensional (3-D) imaging techniques, such as focused ion beam scanning electron microscopy (FIB-SEM), used to study composite electrode microstructures (29-33). The insights generated from 3-D imaging were proven to offer the prospect of optimizing electrode microstructure to further improve performance and durability (31, 34-36).

However, microstructural information related to infiltrated electrodes still remains limited. In this study, the 3-D microstructure of Ni-infiltrated GDC electrodes was obtained using FIB-SEM, and microstructural parameters of the porous structures, such as surface area, TPB density, particle/pore sizes and porosity content, were quantitatively evaluated. The study of the 3-D microstructure of infiltrated electrodes is a collaboration in which the experimental data provided the basis for 3-D imaging and modelling work. The procedure of the 3-D imaging and reconstruction was done by Dr. Masashi Kishimoto and described below. The modelling of infiltrated electrodes performance is not in the scope of the present thesis.

3.5.2 3-D imaging and reconstruction methodology

The anode samples were reduced as described in section 3.2.4 and impregnated with epoxy resin (Specifix20, Struers) under vacuum conditions so that the open pores of the anodes could be easily distinguished in the SEM imaging. The cured samples were cut and mechanically polished to have a flat cross-section. The 3-D microstructure of the anodes was imaged by an Auriga (Zeiss) FIB-SEM system, the diagram of FIB-SEM setting is shown schematically in Figure 3.16.

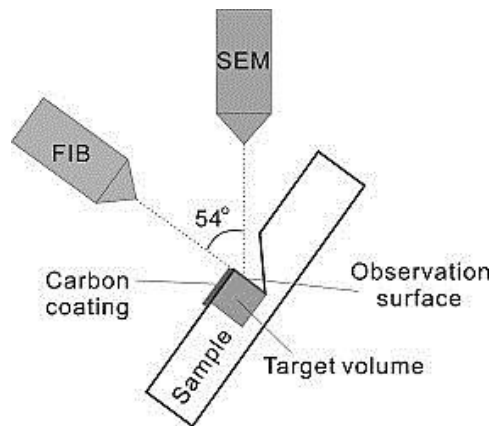


Figure 3.16. Schematic diagram of FIB-SEM setting (31).

The back-scattered electron (BSE) detector, which provides an intensity profile depending on the atomic number of the target atom, was used for imaging the Ni infiltrated GDC electrodes. Regions were selected for the microstructural analysis and segmented based on image brightness. After alignment and segmentation, the 3-D porous microstructure was reconstructed in a virtual field. For demonstration, an example of Ni-YSZ cermet electrode cross-sectional image obtained by FIB-SEM and a reconstructed 3-D structure are demonstrated in Figure 3.17 (31, 37).

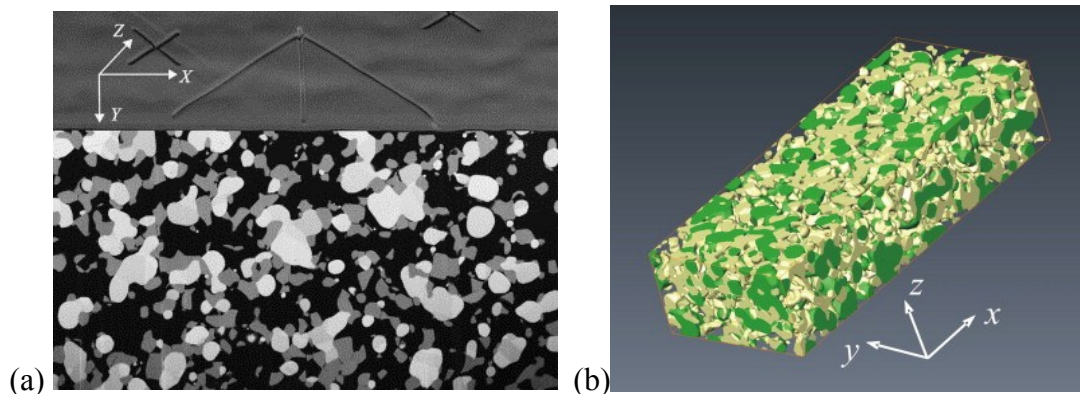


Figure 3.17 (a) Example of Ni-YSZ cermet electrode cross-sectional image obtained by FIB-SEM, in this work secondary electrons detector was used (37); (b) Reconstructed Ni-YSZ anode microstructure ($25.722 \mu\text{m} \times 11.624 \mu\text{m} \times 6.572 \mu\text{m}$; green: Ni, yellow: YSZ) (31).

From the reconstructed structures, phase volume fractions, surface information, particle/pore size and TPB density were quantified using commercial image processing software, Avizo (Mercury Computer Systems, Inc.). More details of the imaging and quantification methodologies can be found elsewhere (37, 38).

3.6 Summary

In this chapter the methodology for cell preparation, testing and characterisation used in this research to study the performance of Ni-infiltrated GDC fuel electrodes for SOCs is outlined.

Aiming to meet both materials and microstructural requirements, in this study an electrode for SOC application was made by infiltration of a porous GDC scaffold with Ni nano-particles to form a percolated structure. The resultant electrodes were assessed in terms of electrochemical performance in fuel cell and electrolysis modes at different temperatures and hydrogen concentrations using EIS. The effect of scaffold characteristics, H₂ partial pressures, and insights into degradation behaviour, using both symmetrical cell (two-electrode) and fuel cell (three-electrode) measurements, have been investigated.

The electrical conductivity of infiltrated electrodes with different Ni loadings was assessed by the Van der Pauw method in a hydrogen atmosphere in the 100-700 °C temperature range. The 2-D microstructure of Ni-infiltrated GDC electrodes was studied using FEG-SEM. The 3-D microstructure was obtained using FIB-SEM, and microstructural parameters of the porous structures, such as surface area, TPB density, particle/pore sizes and porosity volume, were quantified.

References for Chapter III

1. N. Hart, N. Brandon and J. Shemilt, *Materials and Manufacturing Processes*, **15**, 47 (2000).
2. D. S. Tsoukleris, I. M. Arabatzis, E. Chatzivasiloglou, A. I. Kontos, V. Belessi, M. C. Bernard and P. Falaras, *Solar Energy*, **79**, 422 (2005).
3. N. M. Sammes, G. A. Tompsett and Z. Cai, *Solid State Ionics*, **121**, 121 (1999).
4. G. A. Tompsett, N. M. Sammes and O. Yamamoto, *Journal of the American Ceramic Society*, **80**, 3181 (1997).
5. S. P. Jiang, *International Journal of Hydrogen Energy*, **37**, 449 (2012).
6. T. Klemensø, K. Thydén, M. Chen and H.-J. Wang, *Journal of Power Sources*, **195**, 7295 (2010).
7. G. J. Offer, P. Shearing, J. I. Golbert, D. J. L. Brett, A. Atkinson and N. P. Brandon, *Electrochimica Acta*, **53**, 7614 (2008).
8. L. J. A. Van Der Pauw, *Philips Res. Rep.*, **13**, 1 (1958).
9. M. Somalu, Fabrication and Characterization of Ni/ScSZ Cermet Anodes for Intermediate Temperature SOFCs, in *Earth Science and Engineering*, Imperial College London, London (2012).
10. G. Rietveld, C. V. Koiijmans, L. C. A. Henderson, M. J. Hall, S. Harmon, P. Warnecke and B. Schumacher, *Instrumentation and Measurement, IEEE Transactions on*, **52**, 449 (2003).
11. O. Demircan, C. Xu, J. Zondlo and H. O. Finklea, *Journal of Power Sources*, **194**, 214 (2009).
12. J. Nielsen, P. Hjalmarsson, M. H. Hansen and P. Blennow, *Journal of Power Sources*, **245**, 418 (2014).
13. M. Chen, B. H. Kim, Q. Xu, O. J. Nam and J. H. Ko, *Journal of the European Ceramic Society*, **28**, 2947 (2008).
14. A. Tarancón, A. Morata, G. Dezanneau, S. J. Skinner, J. A. Kilner, S. Estradé, F. Hernández-Ramírez, F. Peiró and J. R. Morante, *Journal of Power Sources*, **174**, 255 (2007).
15. D. R. Gaskell, *Introduction to the Thermodynamics of Materials*, Taylor&Francis New York (2003).
16. J. F. Rubinson and Y. P. Kayinamura, *Chemical Society Reviews*, **38**, 3339 (2009).
17. L. L. Scribner and S. R. Taylor, *The measurement and correction of electrolyte resistance in electrochemical tests*, ASTM (1990).
18. S. Basu, *Recent Trends in Fuel Cell Science and Technology*, Springer (2007).
19. M. Orazem and B. Tribollet, *Electrochemical Impedance Spectroscopy*, John Wiley & Sons, Inc (2008).
20. A. L. Soldati, L. C. Baqué, E. H. Troiani and A. C. Serquis, Hydrogen Energy - Challenges and Perspectives, in, D. Minic Editor (2012).
21. W. Lai and S. M. Haile, *Journal of the American Ceramic Society*, **88**, 2979 (2005).

22. A. Kromp, A. Leonide, A. Weber and E. Ivers-Tiffée, *Journal of The Electrochemical Society*, **158**, B980 (2011).
23. B. C. H. Steele, *Solid State Ionics*, **129**, 95 (2000).
24. S. B. Adler, B. T. Henderson, M. A. Wilson, D. M. Taylor and R. E. Richards, *Solid State Ionics*, **134**, 35 (2000).
25. J. Winkler, P. V. Hendriksen, N. Bonanos and M. Mogensen, *Journal of The Electrochemical Society*, **145**, 1184 (1998).
26. S. McIntosh, J. M. Vohs and R. J. Gorte, *Journal of The Electrochemical Society*, **150**, A1305 (2003).
27. H. Finklea, X. Chen, K. Gerdes, S. Pakalapati and I. Celik, *Journal of The Electrochemical Society*, **160**, F1055 (2013).
28. A. C. West and J. Newman, *Journal of The Electrochemical Society*, **136**, 139 (1989).
29. J. R. Wilson, W. Kobsiriphat, R. Mendoza, H. Y. Chen, J. M. Hiller, D. J. Miller, K. Thornton, P. W. Voorhees, S. B. Adler and S. A. Barnett, *Nat Mater*, **5**, 541 (2006).
30. J. Wilson and D. Tate, *J. Bone Joint Surg.-Br. Vol.*, **88B**, 541 (2006).
31. H. Iwai, N. Shikazono, T. Matsui, H. Teshima, M. Kishimoto, R. Kishida, D. Hayashi, K. Matsuzaki, D. Kanno, M. Saito, H. Muroyama, K. Eguchi, N. Kasagi and H. Yoshida, *Journal of Power Sources*, **195**, 955 (2010).
32. P. R. Shearing, Q. Cai, J. I. Golbert, V. Yufit, C. S. Adjiman and N. P. Brandon, *Journal of Power Sources*, **195**, 4804 (2010).
33. N. Vivet, S. Chupin, E. Estrade, T. Piquero, P. L. Pommier, D. Rochais and E. Bruneton, *Journal of Power Sources*, **196**, 7541 (2011).
34. J. R. Wilson, J. S. Cronin and S. A. Barnett, *Scripta Materialia*, **65**, 67 (2011).
35. M. Kishimoto, K. Miyawaki, H. Iwai, M. Saito and H. Yoshida, *Fuel Cells*, **13**, 476 (2013).
36. R. Clague, P. R. Shearing, P. D. Lee, Z. Zhang, D. J. L. Brett, A. J. Marquis and N. P. Brandon, *Journal of Power Sources*, **196**, 9018 (2011).
37. M. Kishimoto, H. Iwai, M. Saito and H. Yoshida, *Journal of Power Sources*, **196**, 4555 (2011).
38. M. Kishimoto, H. Iwai, K. Miyawaki, M. Saito and H. Yoshida, *Journal of Power Sources*, **223**, 268 (2013).

CHAPTER IV

NICKEL-INFILTRATED GDC ELECTRODES

4.1 Introduction

In this chapter a detailed characterisation of Ni infiltrated GDC electrodes is discussed. First, the qualitative and quantitative analysis of infiltrated electrode microstructure, using 2-D and 3-D imaging methods, is presented. Then the electronic conductivity results are shown, and the impact of Ni concentration on the electronic conductivity of the electrode is highlighted.

This is followed by results and discussion regarding AC and DC electrochemical performance measurements of the infiltrated electrodes in humidified hydrogen in both fuel cell and electrolysis modes. Initially, validation of the three electrode method is described. After that the effect of different experimental and fabrication parameters on the electrode electrochemical performance is assessed. These parameters include Ni concentration, scaffold porosity, temperature, and gas composition. Calculations of activation energies associated with high and low frequencies polarisation features are shown. Finally, the results of short-term degradation tests of infiltrated electrodes are discussed.

4.2 Characterisation of Ni-infiltrated GDC fuel electrodes

Infiltrated electrodes were characterised in terms of microstructure development and electrical conductivity. Microstructure was studied using SEM and FIB-SEM for 2-D and 3-D analysis, respectively, as described in section 3.5.

4.2.1 2-D Microstructural analysis (SEM)

A representative cross-section of the fabricated SOC is shown in

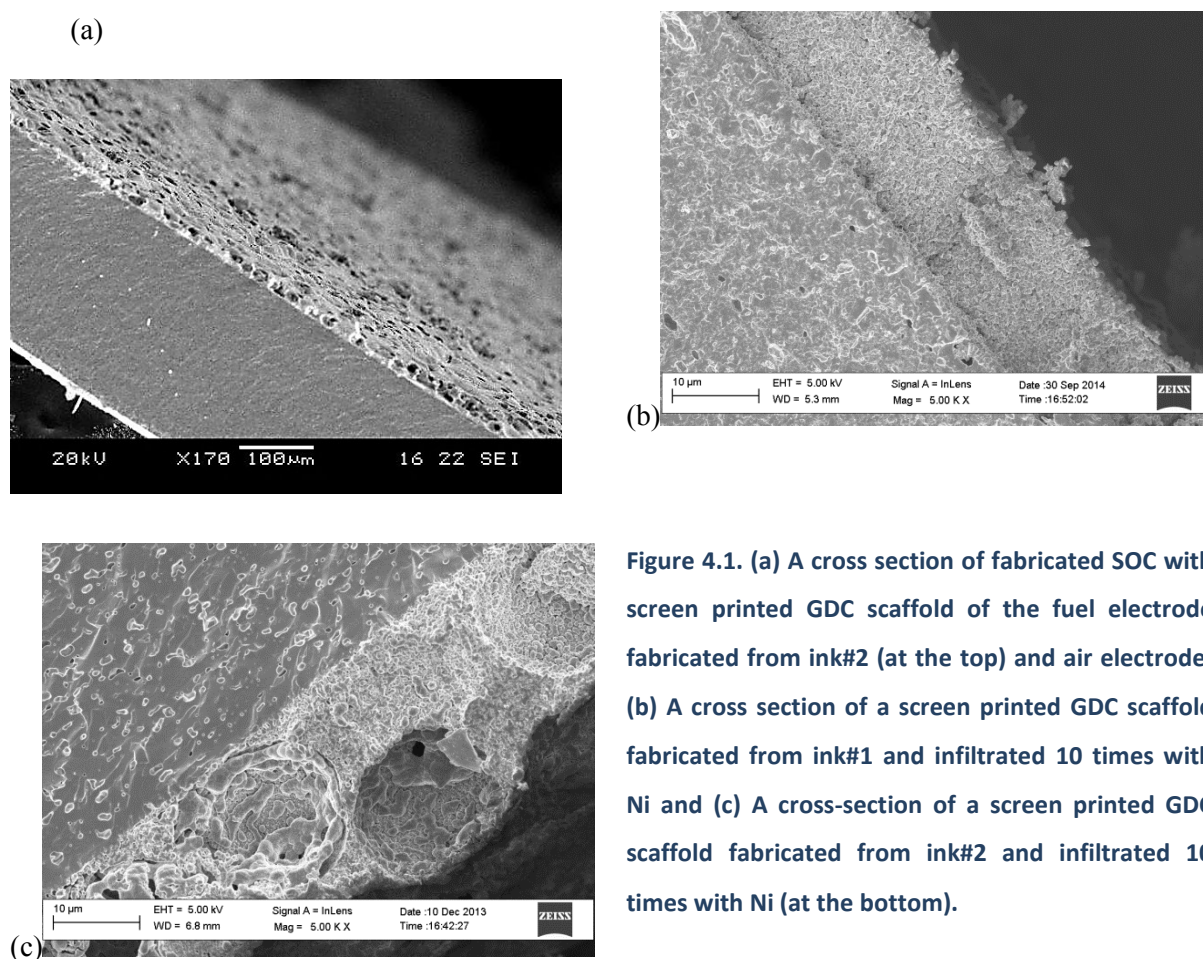


Figure 4.1. (a) A cross section of fabricated SOC with screen printed GDC scaffold of the fuel electrode fabricated from ink#2 (at the top) and air electrode; (b) A cross section of a screen printed GDC scaffold fabricated from ink#1 and infiltrated 10 times with Ni and (c) A cross-section of a screen printed GDC scaffold fabricated from ink#2 and infiltrated 10 times with Ni (at the bottom).

(a). For comparison, the fuel electrodes structures based on ink#1 and ink#2 are shown in

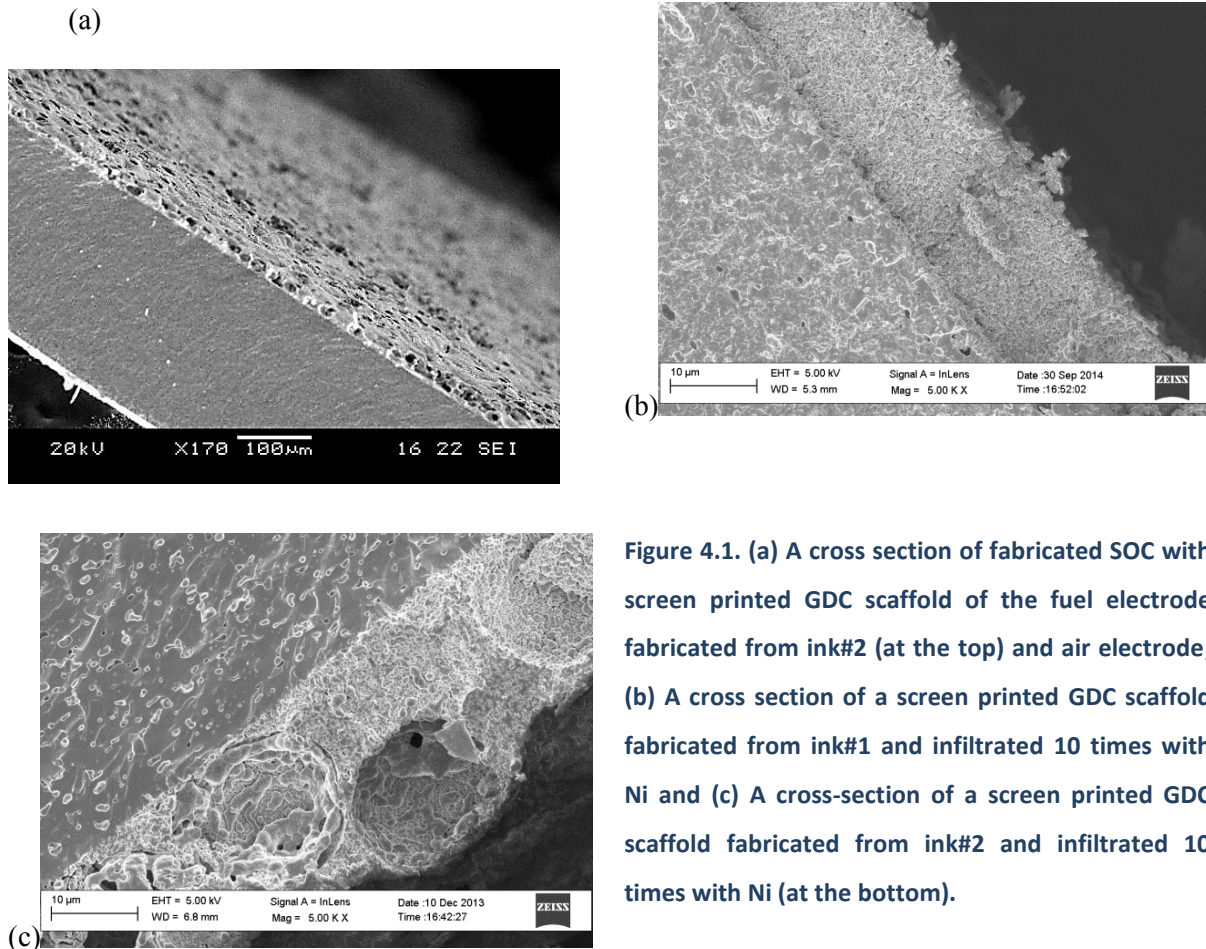
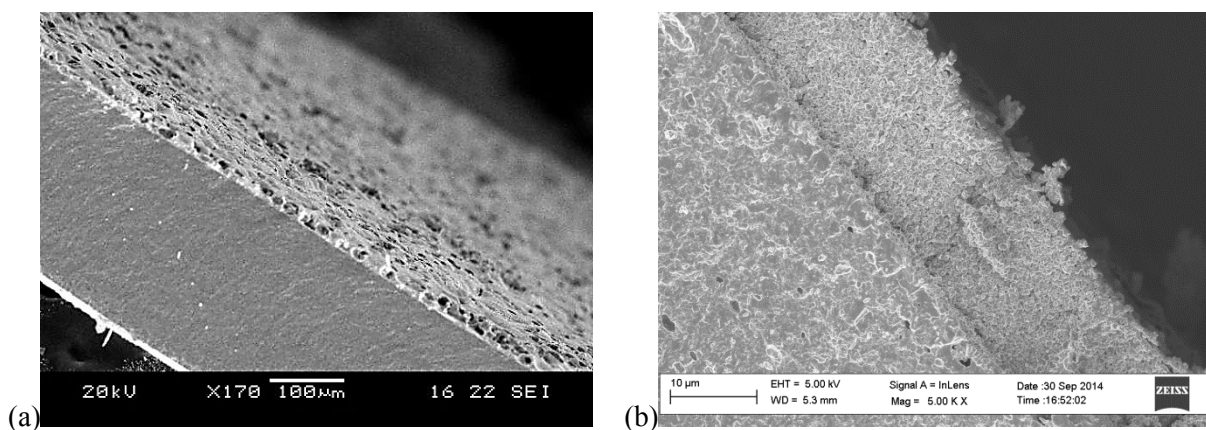


Figure 4.1. (a) A cross section of fabricated SOC with screen printed GDC scaffold of the fuel electrode fabricated from ink#2 (at the top) and air electrode; (b) A cross section of a screen printed GDC scaffold fabricated from ink#1 and infiltrated 10 times with Ni and (c) A cross-section of a screen printed GDC scaffold fabricated from ink#2 and infiltrated 10 times with Ni (at the bottom).

(b) and (c). The LSCF-GDC air electrode and the GDC scaffold (as a precursor for subsequent Ni infiltrations) for fuel electrodes were screen printed on both sides of the electrolyte to form a fuel cell, as described in methodology, section 3.2.2.



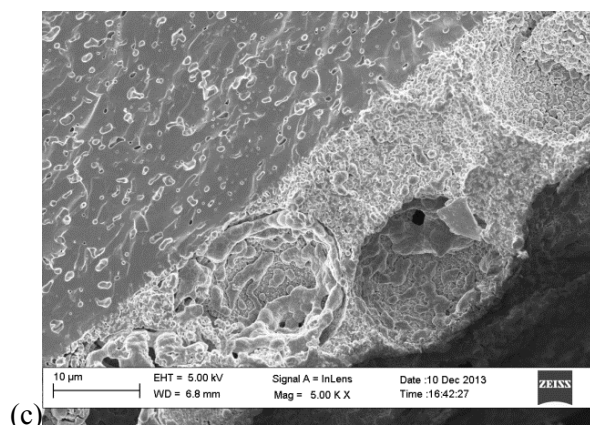


Figure 4.1. (a) A cross section of fabricated SOC with screen printed GDC scaffold of the fuel electrode fabricated from ink#2 (at the top) and air electrode; (b) A cross section of a screen printed GDC scaffold fabricated from ink#1 and infiltrated 10 times with Ni and (c) A cross-section of a screen printed GDC scaffold fabricated from ink#2 and infiltrated 10 times with Ni (at the bottom).

Two types of inks were used for fuel electrode fabrication in this research as described in section 3.2.1. Ink#1 did not contain any pore formers, whereas ink#2 included polymer micro-beads to increase porosity. Figure 4.2 shows the SEM images with different magnifications of the scaffolds obtained from ink#1 (Figure 4.2a-b) and ink#2 (Figure 4.2c-d). The fine porosity observed in ink#1-based scaffold is a result of combustion of the organic components in the ink during the sintering process. GDC branches in the porous network reached 100-750 nm in thickness after screen printing (Figure 4.2a). This microstructure is comparable or finer than that generally achieved by conventionally screen printed NiO-GDC electrodes (1). In the scaffold produced using ink#2 two types of porosity can be seen – micro-porosity, similar to ink#1, and macro-porosity (Figure 4.2c) as a result of combustion of the polymeric beads. Figure 4.2d depicts the microstructure inside the macro-pore.

The combination of micro- and macro-porosities in the electrode is interesting for two reasons. Firstly, macro-porosity assists gas transport to the active areas located closer to the electrolyte-electrode interface, as discussed in the literature review (section 2.7.1). In this case macro-porosity acts as a conduit for the reactants to the micro-pores, enabling better gas distribution and product removal inside the electrode. The second reason is that the porosity should assist the infiltration technique, enabling the solution to penetrate the scaffold to a greater depth.

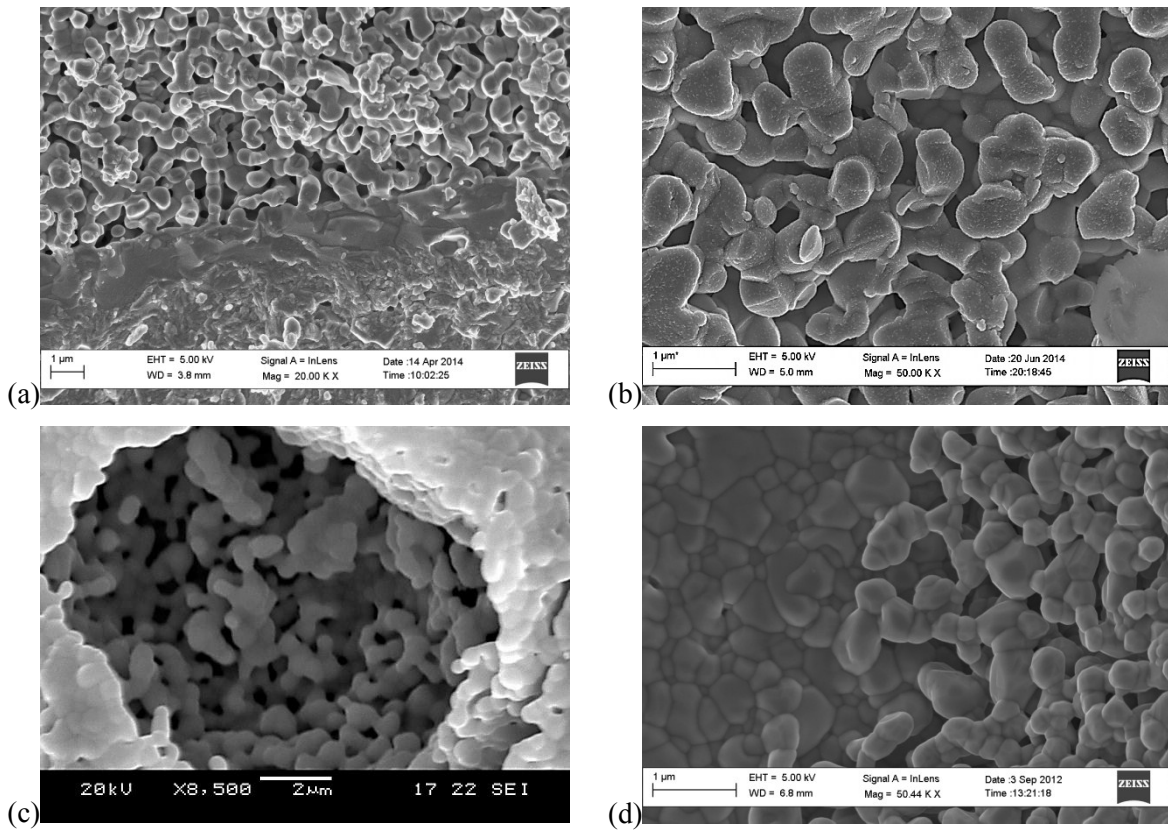
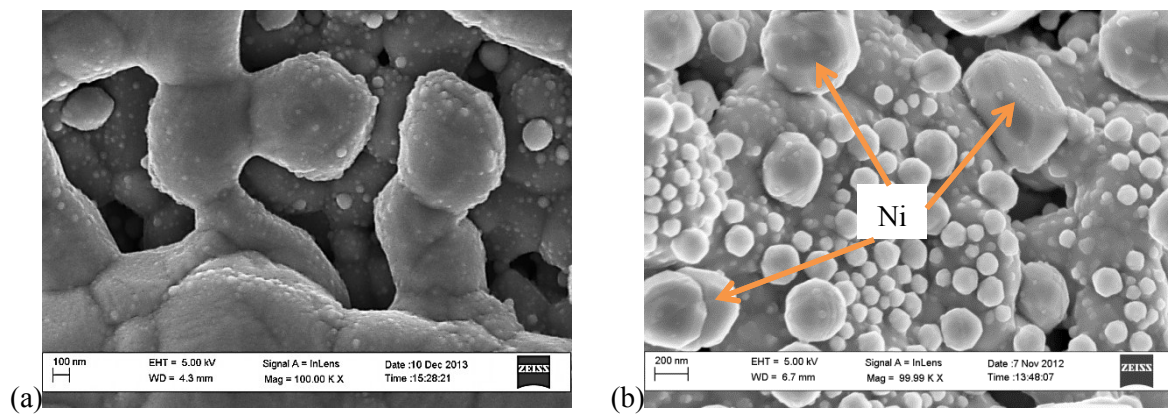


Figure 4.2. The 2-D microstructure of GDC scaffolds fabricated from (a) ink#1; (b) ink#1, higher magnification and (c) ink#2 (macro-pore and micro-pore); (d) ink#2, higher magnification close up (inside the macro-pore).

The evolution of the microstructure during the infiltration of the ceramic scaffold with Ni nanoparticles is shown in SEM micrographs Figure 4.3a-d.



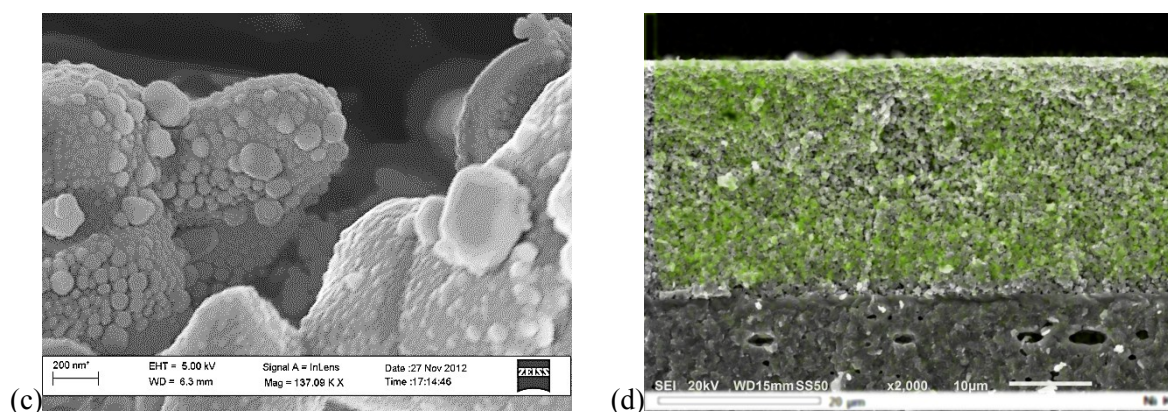


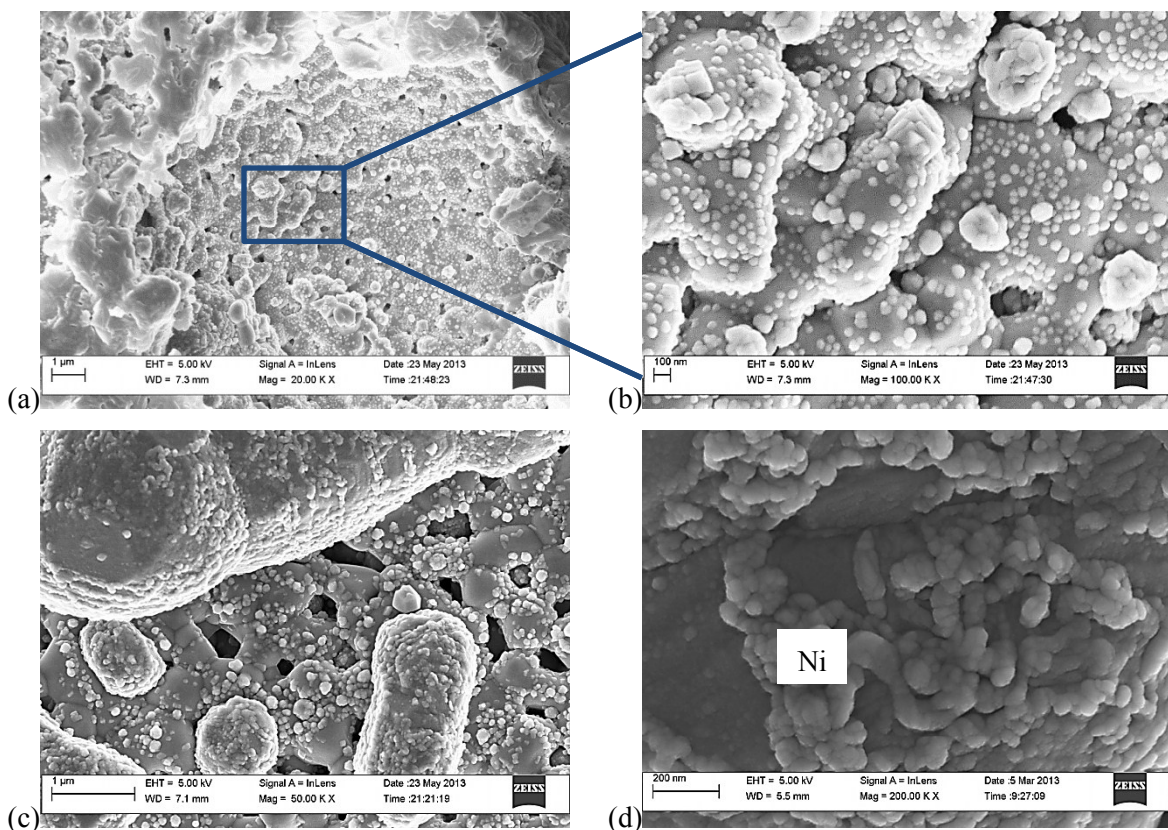
Figure 4.3. (a) GDC scaffold covered with Ni nano particles after 5 infiltrations, reduced at 750 °C; (b) GDC scaffold covered with Ni nano particles after 5 infiltrations, reduced at 1000 °C; (c) GDC scaffold (ink#2) covered with Ni nano-particles after 10 Ni infiltrations, reduced at 750 °C; (d) SEM-EDX map of Ni distribution after 10 infiltrations of GDC ink#1 based scaffold, reduced at 750 °C (Ni in green).

Here, the effect of the number of infiltrations, as well as a reduction temperature of the electrode after infiltration, is elucidated. Though a uniform coverage of Ni particles on GDC was observed following five infiltrations and reduction at 750 °C, the metal particles were distant from each other (Figure 4.3a). After ten infiltrations a higher coverage of almost equal size Ni nano-particles on a ceramic matrix was obtained in both ink#1-based and ink#2-based electrodes (Figure 4.3c). In spite of the higher coverage, the particles were individually dispersed. This may be as a result of poor wettability between the GDC scaffold and Ni (2). Ni particles do not agglomerate, due to a limited mobility at 500 °C, the temperature at which decomposition of $\text{Ni}(\text{NO}_3)_2$ occurs. The map of Ni distribution after 10 infiltrations (Figure 4.3d) indicates that Ni was distributed throughout the electrode following 10 infiltrations of the ink#1-based GDC scaffold.

Nickel particle growth from an average size of 30 nm to 100 nm was observed in the electrode reduced at 1000 °C (Figure 4.3b). Nickel particle growth occurred when the electrode was reduced at higher temperature (1000 °C); this could be seen as big non-uniform Ni agglomerates of 200-700 nm in Figure 4.3b. Therefore, to prevent Ni particles growth and to preserve a uniform structure, the reduction of the electrodes for testing was performed at 750 °C, (and not 1000 °C).

The 2-D microstructure of the 10 times Ni-infiltrated GDC electrodes after testing in different concentrations of humidified $\text{H}_2\text{-N}_2$ and in the range of temperatures 550-750 °C is shown in Figure 4.4. Ni particle coarsening can be identified in all cases, although to a different extent,

depending on the experiment duration. In comparison to individual Ni nano-particles obtained after infiltration (Figure 4.3c), after a short 5hr experiment only a minor coarsening occurred (Figure 4.4a-b). Following prolonged exposure to high temperatures (~ 100 hrs) the particles agglomerated into snake-like clusters as can be seen in a close-up view (Figure 4.4c-d). This modification of the microstructure can give rise to a local depletion of Ni on the GDC surface and, as a result, to a reduction of TPB length and connectivity between Ni particles (Figure 4.4d). The cross section of the ink#2-based electrode near the electrode-electrolyte interface is shown in Figure 4.4e. In this region a high amount of Ni particles can clearly be seen, confirming that full penetration of the infiltration solution occurred. Figure 4.4f demonstrates a microstructure obtained in ink#1-based electrode after ~ 320 hrs (in humidified 50% H_2 – 50% N_2 under OCP and biased (± 10 mA) conditions), where Ni agglomerates can be seen. These agglomerates can give rise to a blocking of the open porosity in the electrode thereby restricting gas access to active sites.



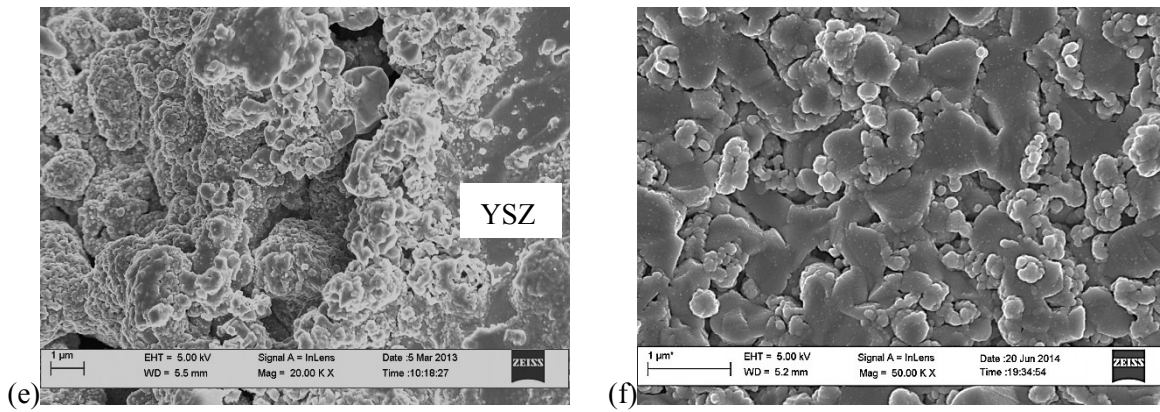


Figure 4.4. The development of the 10 times Ni-infiltrated GDC fuel electrode microstructure after experiments performed in humidified H_2-N_2 and in the temperature range of 550-750 °C. (a)-(b) ink#2-based electrode after ~5 hrs experiment; (c)-(e) ink#2-based electrode after ~100 hrs experiment at 600 °C; (d) close-up on Ni agglomerates; (e) cross-section near the electrode-electrolyte interface; (f) ink#1-based electrode after ~320 hrs experiment at 600 °C.

4.2.2 3-D image reconstruction of infiltrated electrodes

The 3-D microstructure of infiltrated electrodes was imaged by an Auriga (Zeiss) FIB-SEM system as explained in section 3.5.2. The backscattered electron (BSE) detector was used for imaging the electrodes in order to distinguish the two solid phases (Ni nanoparticles and GDC scaffold) in the SEM images. Regions were selected for the microstructural analysis and segmented based on image brightness. After alignment and segmentation, the 3-D porous microstructure was reconstructed. From the reconstructed structures, phase volume fractions, surface information, particle/pore size and TPB density were quantified to characterise Ni-infiltrated GDC electrodes. 3-D imaging and calculations of the valuable microstructural parameters were performed by Dr Masashi Kishimoto, who for the first time performed the quantitative analysis of the infiltrated electrodes from a tomography dataset. Therefore, in this thesis only results from 3-D imaging and reconstruction are provided, as this work was undertaken as part of this PhD study, rather than the development of 3-D imaging technique itself which was undertaken by Dr Kishimoto. The impact of the present work encompasses the experimental set of data that enabled Dr Kishimoto to evaluate and test the 3-D image reconstruction method for infiltrated electrodes and later on enabled him to develop a numerical model for infiltrated electrode optimisation. The results of this collaborative work have been published and presented elsewhere (3-7).

Three different microstructures, based on ink#1, were fabricated for 3-D imaging and characterised: the virgin GDC scaffold, GDC scaffold with one Ni infiltration (1xNi-GDC) and GDC scaffold with 10 infiltrations (10xNi-GDC). Representative 2-D cross-section images of the sample microstructures are shown in Figure 4.5.

Ni nano-particles with a size down to ~10 nm were successfully imaged using a lower electron acceleration voltage (1.5 kV). The distribution of the infiltrated nickel particles was found to be homogeneous in the thickness direction of the anode (corresponding to the horizontal direction in the images on Figure 4.5a-c). Reconstructed 3-D structures of the 1xNi-GDC and 10xNi-GDC samples, shown in Figure 4.6, similarly suggest that the nickel particles are homogeneously distributed inside the scaffold. This is in an agreement with the SEM-EDX map of Ni distribution (Figure 4.3d).

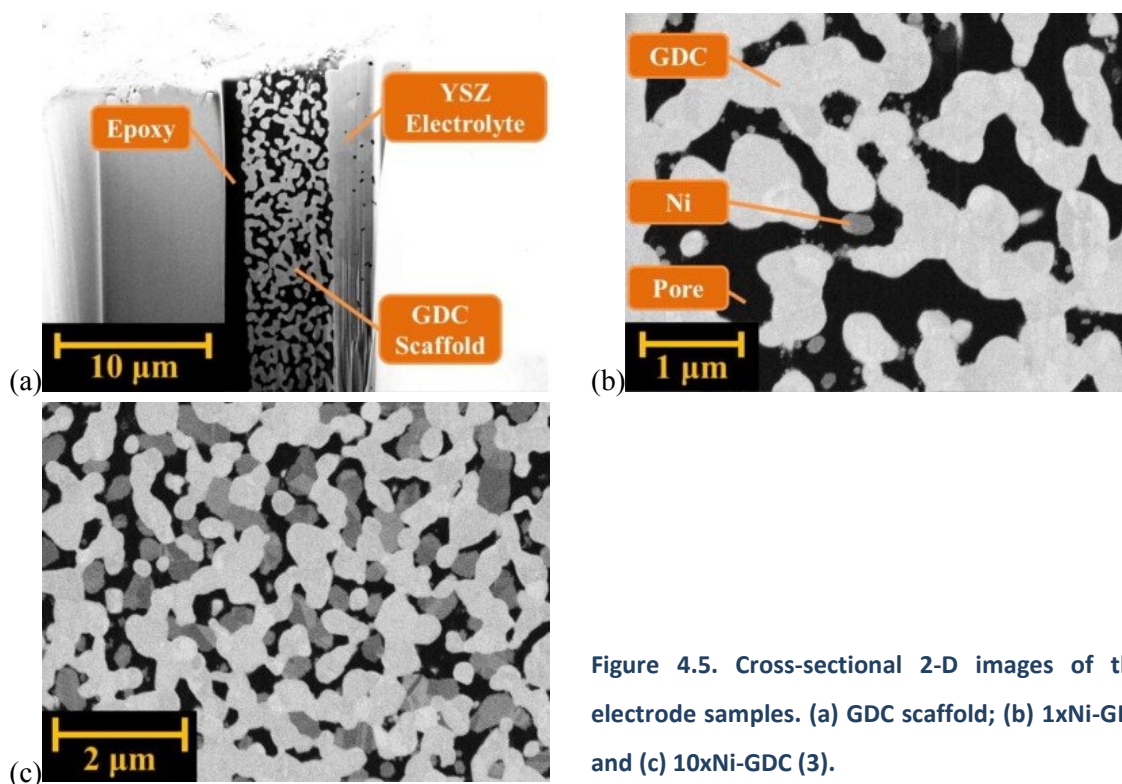


Figure 4.5. Cross-sectional 2-D images of the electrode samples. (a) GDC scaffold; (b) 1xNi-GDC and (c) 10xNi-GDC (3).

The GDC scaffolds in the three structures imaged in this study have similar features volume fraction, surface-to-volume ratio and average particle sizes. This ensures that the structures obtained from 1xNi-GDC and 10xNi-GDC are still large enough to be representative of the entire anode structure.

Microstructural parameters (sample size, voxel size, phase volume fractions, surface information, particle/pore size and TPB density) from quantitative analysis are summarised in Table 4.1. Typical values found in a conventional Ni-YSZ (50-50 vol%) electrode are also shown for comparison (8).

The pore volume fraction in ink#1-based 10xNi-GDC electrode was estimated to be 20.1% with an average pore size of 0.30 μm. The average characteristic dimension of the Ni particles was estimated as 0.35 μm, and the Ni volume fraction was found to be 19.8 vol%. The coverage of Ni particles on the GDC surface was 6% after the first infiltration and 39% after the 10th infiltration.

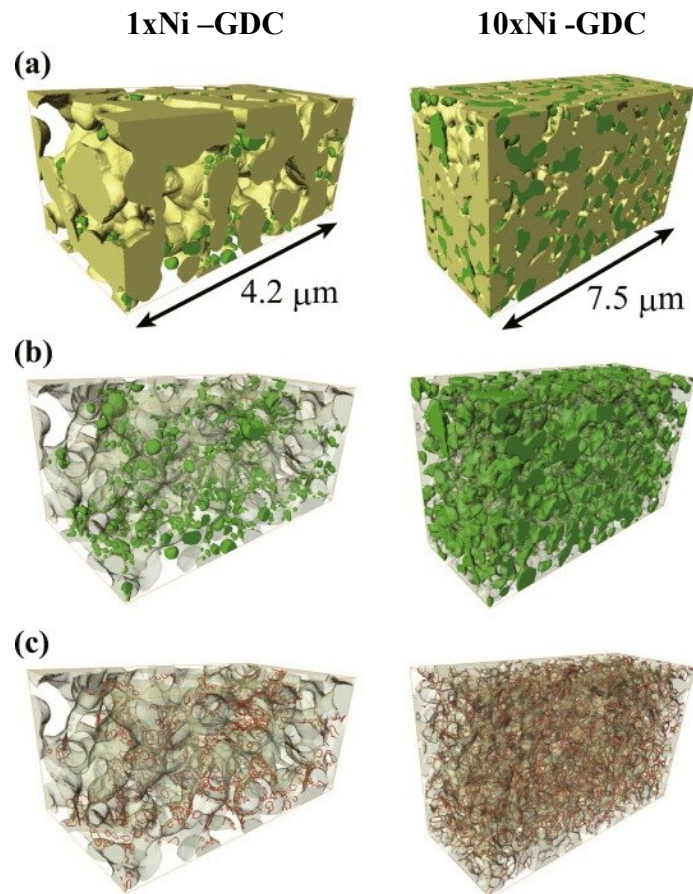


Figure 4.6. Reconstructed 3-D microstructure of 1xNi-GDC and 10xNi-GDC samples. (a) Ni (green) and GDC (yellow) phases; (b) Ni with GDC (transparent grey) and (c) TPB lines with GDC (transparent grey) (3).

The GDC particle sizes are close to that found in the Ni-YSZ cermet electrode (8), although the volume fraction is more than double. On the other hand, the Ni volume fraction and particle sizes are significantly smaller than those found in the conventional electrode. The smaller metal particle sizes are a result of the fact that the decomposition temperature for the nickel particles (500 °C) is significantly lower than the typical sintering temperature for the conventional electrodes (~1400 °C).

In general, smaller nickel particle sizes are preferable for larger TPB density. Single infiltration creates much smaller TPB segments than the conventional electrode fabrication methods. Note that a TPB segment is defined as the TPB length created by the perimeter of a single Ni particle at its interface with the scaffold in a porous electrode. Although infiltration repetitions inevitably increase the length of the TPB segments, they are still shorter than those found in conventional electrodes. The combination of multiple segments and smaller Ni particle sizes retained in infiltrated electrodes lead

to a large TPB length (and hence, high TPB density). From the quantitative analysis, the TPB densities in the 1xNi-GDC and 10xNi-GDC electrodes were found to be about 5 times and one-order of magnitude larger than those in the conventional electrode, respectively. But, however large the TPB length is, the analysis suggests that there is no percolating cluster observed in the tested region.

Table 4.1. Microstructural parameters from quantitative analysis (3).

| Microstructural parameters | | GDC scaffold | 1xNi-GDC | 10xNi-GDC | Conventional Ni-YSZ (8) |
|--|----------|--------------|----------|-----------|-------------------------|
| Sample size [μm] | X | 18 | 4.28 | 7.5 | 19.2 |
| | Y | 4.5 | 2 | 4.5 | 8.51 |
| | Z | 5.25 | 2.25 | 3 | 6.2 |
| Voxel size [nm] | X | 30 | 5 | 10 | 26.6 |
| | Y | 30 | 5 | 10 | 26.6 |
| | Z | 30 | 10 | 10 | 62 |
| Volume fraction [%] | Ni | 0.00 | 1.29 | 19.8 | 25.3 |
| | GDC/YSZ | 57.1 | 56.9 | 60.2 | 25.1 |
| | Pore | 42.9 | 41.8 | 20.0 | 49.6 |
| Particle/pore size [μm] | Ni | n/a | 0.102 | 0.354 | 1.38 |
| | GDC/YSZ | 0.844 | 0.748 | 0.706 | 0.73 |
| | Pore | 0.667 | 0.594 | 0.3 | 1.74 |
| Surface-to-volume ratio [$\mu\text{m}^2 \mu\text{m}^{-3}$] | Ni | n/a | 60 | 16.2 | 3.56 |
| | GDC/YSZ | 6.44 | 6.82 | 7.94 | 7.51 |
| | Pore | 8.58 | 10 | 21.1 | 4.12 |
| Specific surface [$\mu\text{m}^2 \mu\text{m}^{-3}$] | Ni | 0 | 0.77 | 3.21 | n/a |
| | GDC | 3.68 | 3.86 | 4.77 | n/a |
| | Pore | 3.68 | 4.16 | 4.22 | n/a |
| Contact area density [$\mu\text{m}^2 \mu\text{m}^{-3}$] | Ni-GDC | 0.00 | 0.24 | 1.88 | n/a |
| | Ni-Pore | 0.00 | 0.54 | 1.33 | n/a |
| | GDC-Pore | 3.68 | 3.63 | 2.89 | n/a |
| TPB density [$\mu\text{m} \mu\text{m}^{-3}$] | | n/a | 11 | 18.40 | 2.49 |

4.2.4 Estimation of the Ni phase content in infiltrated electrodes

The content of the Ni phase in the electrodes was estimated from the cell weight difference before Ni infiltration, and after infiltration procedure, heat treatment and reduction. The vol% and wt% Ni fraction increase in Ni-infiltrated GDC electrodes as a result of infiltration process repetitions are represented in Figure 4.7.

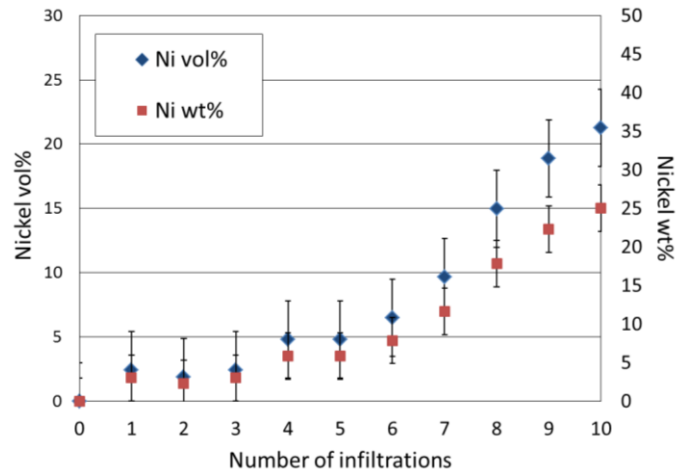


Figure 4.7. Mean vol% and wt% of Ni in Ni-infiltrated GDC electrodes as a function of number of infiltrations.

Following 10 infiltrations the wt% of Ni in the electrode was 25 ± 3 wt% (18.6-24 vol%). This value is in agreement with Ni content (19.8 vol%) estimated by the quantitative analysis of the 3-D image reconstruction.

4.2.3 Electronic conductivity measurements

The impact of the Ni loading on the performance of infiltrated electrodes is revealed in the electronic conductivity of the electrode and its catalytic activity – both characteristics are important for optimized high performance electrodes.

To study the impact of Ni content on electronic conductivity, the DC 4-probe conductivity of the reduced infiltrated electrodes was measured using the van der Pauw method as described in methodology (section 3.4.1). The van der Pauw measurements of electronic conductivity as a function of temperature for infiltrated electrodes with different Ni content as a consequence of infiltration repetitions are shown in Figure 4.8. For convenience, the electronic conductivity of pure Ni, and the mixed conductivity of GDC, are also presented. The thickness of the electrode, used for conductivity calculation, was estimated from SEM images of the corresponding electrodes. The contribution of the ionic conductivity of the YSZ electrolyte is negligible in comparison to the conductivity of Ni-CGO. According to Figure 2.5 the logarithm of conductivity, σ , of YSZ at 700 °C is $-2 \text{ S}\cdot\text{cm}^{-1}$ ($\sigma = 0.01 \text{ S}/\text{cm}$).

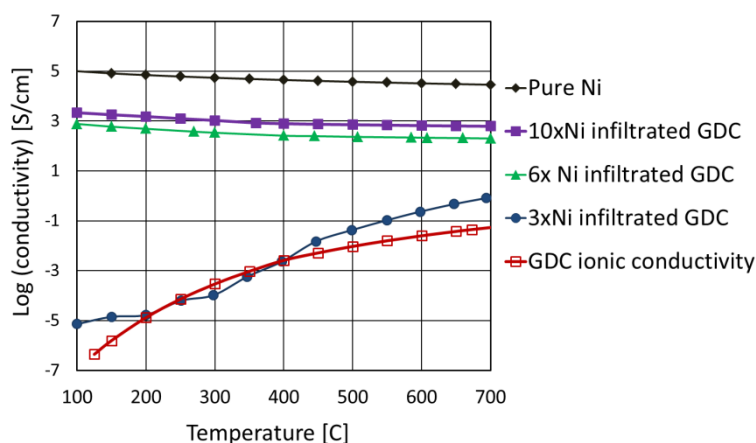


Figure 4.8. Temperature dependence of the DC electronic conductivity, measured by the Van der Pauw method, of infiltrated electrodes with different Ni loadings. Also shown are the electronic conductivity of nickel (9), the mixed conductivity of GDC (10) and cermet Ni-GDC electrode fabricated by screen printing.

Starting from 6 infiltration repetitions, a shift in conductivity was observed. The conductivity of the 6 and 10 times Ni-infiltrated electrode showed metallic behaviour, namely a decrease in conductivity with increasing temperature. At 700 °C the conductivity of the 10xNi-GDC (corresponding to 25 wt% of Ni content) electrode was as high as 620 S/cm. A similar conductivity was measured at 700°C for Ni-SDC electrodes prepared from NiO–SDC composite powders with significantly higher Ni content of 35 wt% (11). The shift towards metallic behaviour can be the result of a gradually growing Ni layer, formed inside and on top of the porous GDC scaffold. With additional Ni infiltrations the distance between neighbouring Ni nano-particles on the GDC surface inside the electrode become smaller. Because the GDC scaffold is electronically conductive in reducing atmospheres, it “assists” to overcome the distance between Ni particles during the measurement, as electrons can travel from one Ni particle to another through the GDC network.

In addition, with more infiltration repetitions, the excess Ni remains on top of the electrode, thereby creating Ni ‘islands’ (~1µm thick) as shown in Figure 4.9. Similar phenomenon of “island” grains of Ni with only restricted interconnectivity was observed in Ni infiltrated YSZ scaffold as reported by Busawon *et al.* (12). The excess of Ni is due to two reasons. First, drops of Ni(NO₃)₂ inevitably remain on top of the surface during the infiltration process when all the pores are already filled with the solution. And second, with more infiltrations the pores become smaller. This decreases the amount of solution that can be infiltrated, creating an additional solution excess on the electrode

surface. Although the excess solution has been gently removed after each infiltration, a small amount of it still remains. This phenomenon reflects the limitation of the infiltration technique.

Poor wettability between Ni and GDC and possible roughness of the electrode surface may prevent Ni ‘islands’ from being fully interconnected. However, Ni ‘islands’, formed on the electrode surface, can impact the interpretation of the electronic conductivity data significantly. In this case, it could be that some part of the conductivity measured in the experiment is associated with the Ni film on the surface and not with the bulk conductivity. This limitation should be taken into account when interpreting results of van der Pauw measurements of infiltrated electrodes. On the other hand, the combination of Ni layer on the electrode surface and silver paste together form an efficient current collector for the electrode, which is favourable for the electrode performance.

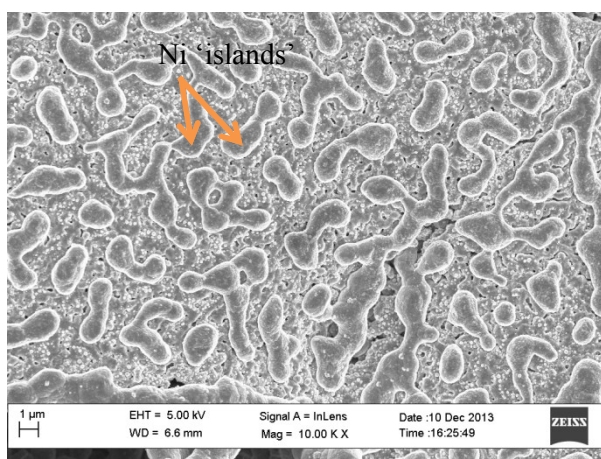


Figure 4.9. Ni film formed on top of the electrode following ten Ni infiltrations; The Ni ‘islands’ are $\sim 1 \mu\text{m}$ in thickness.

The results of the electronic conductivity measurements suggest that at least $11 \pm 3 \text{ vol}\%$ of Ni (6 infiltrations) is required for the shift to the metallic behaviour (Figure 4.8). This means that a continuous conductive path was achieved, either through the contribution of Ni on top of the electrode surface and / or Ni network in the bulk and / or GDC electronic contribution. The results of the 3-D image reconstruction quantitative analysis suggest that no continuous Ni phase was observed in the bulk (section 4.2.2). The fact that the measured electronic conductivity of the ten times infiltrated electrodes is about 2 orders of magnitude lower than the conductivity of pure Ni (Figure 4.8)

essentially indicates that it is combined conductivity (bulk and the Ni surface layer) measured and not only that of the Ni film on top of the electrode. However, the contribution of each is hard to estimate.

4.3 Results and discussion of the electrochemical performance of Ni-infiltrated GDC electrodes in fuel cell and electrolysis mode in humidified H₂-H₂O atmospheres

4.3.1 Validation of the 3-electrode setup measurements using symmetrical cells

The problems associated with thin electrolyte three-electrode measurements were discussed in section 3.4.4.

The validation criteria for the three-electrode measurements are the potential differences between the working and the reference electrode. If the electrodes are perfectly aligned this difference should be approximately half of the cell potential (13). This condition is achieved if the potential at the reference electrode corresponds to the potential of the middle plane in the electrolyte, i.e. half of the electrolyte contribution to impedance is measured in three-electrode setup (14). An effective way to verify this is to compare results of the three-electrode fuel cell impedance spectrum with the impedance spectrum from the corresponding symmetrical cell. Therefore, measurements between two electrodes of the symmetrical cell were conducted in a four-probe set-up for 10xNi infiltrated GDC electrodes at different temperatures in 50% H₂ – 50% N₂ (Figure 4.10).

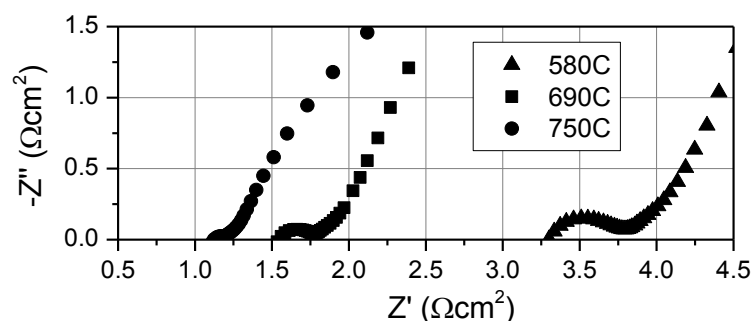


Figure 4.10. EIS spectra (100 mHz-100 kHz) measured in a symmetrical cell at different temperatures in 50% H₂ – 50% N₂, normalised for the individual electrode.

In a four electrode configuration the resistance of the leads is compensated as discussed in section 3.4.4. The thickness of the electrolyte was $\sim 200\ \mu\text{m}$. The values for the polarisation resistance in the symmetrical cell were multiplied by the geometric area of two electrodes. Therefore, the ASR of the symmetrical cell includes contribution from both electrodes.

The results shown in Figure 4.11 demonstrate that the electrolyte ASR in the symmetrical cell ($1.55\ \Omega\text{cm}^2$), measured from the high frequency intercept, is indeed approximately twice as large as that measured in the three-electrode setup for the fuel cell ($0.77\ \Omega\text{cm}^2$), as would be expected for a correctly aligned three-electrode geometry.

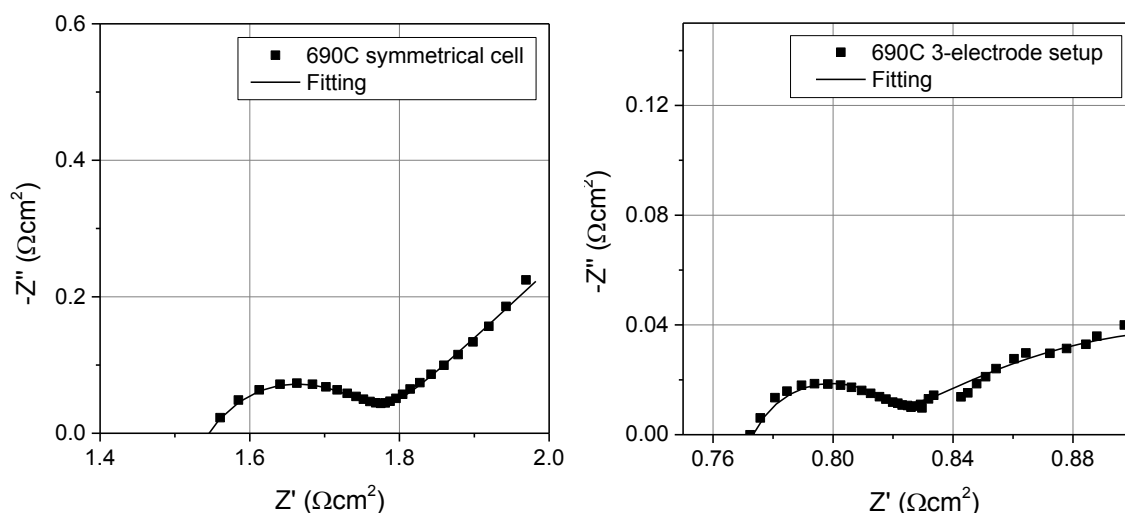


Figure 4.11. EIS spectra (100 mHz-100 kHz) measured at 690 °C in 50% H_2 – 50% N_2 in (a) symmetrical cell and (b) a fuel cell between reference and working electrodes. Note that the Ωcm^2 value refers to the total polarisation resistance contributed by both electrodes.

The diameter of the higher frequency arc is measured to be $0.1\ \Omega\text{cm}^2$ with the symmetrical cell, therefore the value for each individual electrode is half this, i.e. $0.05\ \Omega\text{cm}^2$. This value is very close to the value of $0.054\ \Omega\text{cm}^2$ measured in the three-electrode cell, showing good agreement between both methods. The activation energy of the high frequency process measured using both the two electrode and three-electrode cells is similar, as discussed later.

The shape of low frequency arcs measured with the symmetrical cell resembles a Warburg response, indicating a diffusion limiting process. This may be due to the different nature of the gas flow, as mentioned in 3.4.4. During symmetrical cell testing, gas flowed parallel to the electrodes,

while gas flow in the three-electrode fuel cell rig was perpendicular to the electrode, which would be expected to enhance mass transfer to the electrode. Therefore there might be a contribution of mass transfer outside the electrode to the low frequency response in symmetrical cell.

These results are representative for those observed with ink#2-based electrodes with 10 Ni infiltration repetitions. Therefore it was assumed that the results of 3-electrode measurements are valid for the specific cell configuration and cell dimensions used in the present study.

4.3.2 The effect of Ni loading

The effect of nickel concentration on the electrochemical performance of the cells was tested in electrolysis and fuel cell modes. Figure 4.12 demonstrates j - V curves measured in humidified 50% H₂ – 50% N₂ at 600 °C between working and reference electrodes for pure GDC scaffold (zero infiltrations), and 6 and 10 times infiltrated electrodes based on ink#2.

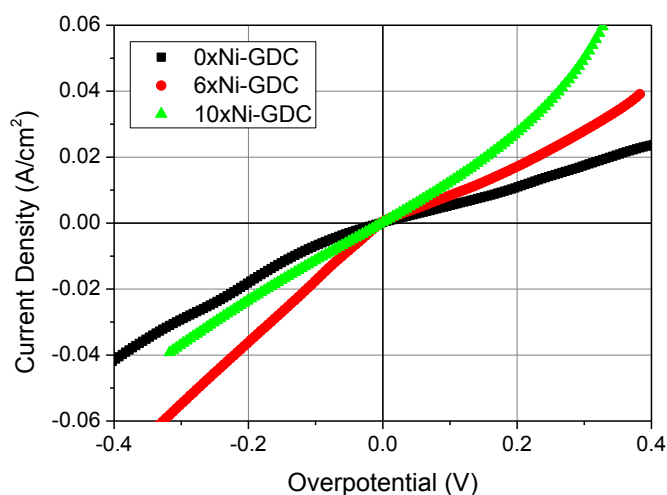


Figure 4.12. Current density vs overpotential of the cell with ink#2-based fuel electrodes infiltrated 0, 6 and 10 times, as measured between the reference and the working electrodes (the voltage drop includes the contributions from the infiltrated electrode and the uncompensated iR drop between the RE and WE). The cells were tested in humidified 50% H₂ – 50% N₂ at 600 °C.

Ten times infiltrated electrode showed the highest performance amongst other samples in fuel cell mode, whereas the performance of the 6 times infiltrated electrode was slightly higher in electrolysis mode. The pure GDC electrode displayed the lowest performance in both modes. In

general, the current density under the same overpotentials was higher in electrolysis mode for the electrodes with 0 and 6 infiltrations, while the current density of the electrode with the highest Ni content was higher in fuel cell mode. Similar non-symmetrical behaviour has been reported in the literature for composite Ni-GDC and Ni-YSZ electrodes at 800 °C in 70% H₂O – 30% N₂ (15). The reason for this non-symmetrical behaviour requires further study.

The AC measurements were performed between the reference and working electrodes, enabling the polarisation of the working electrode to be directly extracted by fitting the data to a corresponding equivalent electrical circuit. Figure 4.13a demonstrates the Nyquist plots of the fuel electrodes with 0, 6 and 10 times Ni infiltrated GDC scaffolds at 600 °C and humidified 50% H₂ – 50% N₂ under open circuit conditions. The value of the series resistance (R_{hfi}) was normalised to zero to compensate for the variable uncompensated iR drop between the RE and WE under different conditions (16) and to enable a clear comparison between the samples.

Corresponding equivalent circuits used for fitting are shown in Figure 4.13b-d, where L is an inductance, R_{hfi} is a high frequency intercept resistance, R_h is a high frequency resistance, R_m is a medium frequency resistance and R_l is a low frequency resistance, $CPE1$, $CPE2$ and $CPE3$ are constant phase elements. The fitting error was less than 15%.

Three processes in high, medium and low frequency ranges have been identified for pure GDC and 6 times infiltrated electrodes. Both electrical circuits represented in Figure 4.13b and Figure 4.13c fitted electrochemical impedance data of the 0 and 6 times infiltrated electrodes equally well.

The mid-frequency spectra of these electrodes resemble a depressed semi-circle with half tear-drop shape (45°) on the high frequency side implying it arises from the mixed conductive nature of the GDC scaffold (17, 18). If this is true the process can be fitted using Warburg element in the equivalent electrical circuit as shown in Figure 4.13c. To assess whether GDC behaves as a mixed conductor under the conditions to which the fuel electrode is exposed to in the experiment, thermodynamic analysis, as described below, was performed.

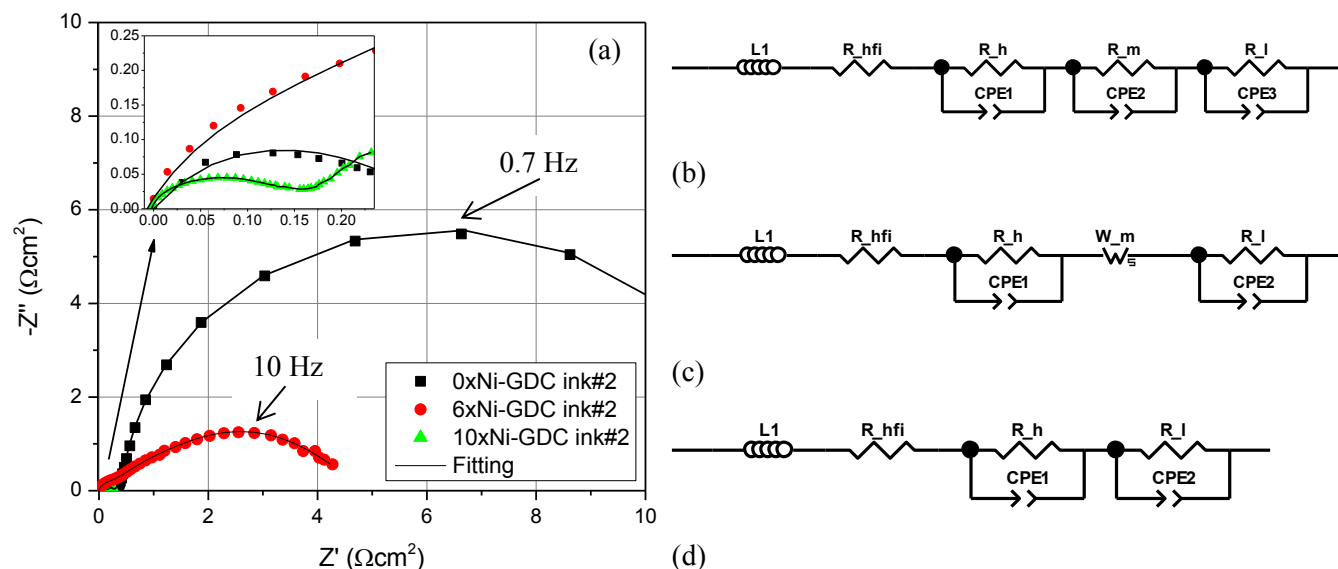


Figure 4.13. (a) Galvanostatic impedance spectra (100 mHz–100 kHz) of the ink#2-based fuel electrodes with 0, 6 and 10 Ni infiltration repetitions at open circuit and humidified 50% H₂ – 50% N₂ at 600 °C as measured between reference and working electrodes; (b) – corresponding equivalent circuit for 0 and 6 Ni infiltrations; (c) – alternative equivalent circuit for 0 and 6 Ni infiltrations and (d) – corresponding equivalent circuit for 10x Ni infiltrations of the ink#2-based GDC scaffold.

It is known that GDC becomes mixed-conducting in a reducing atmosphere at elevated temperatures. To estimate whether conditions would result in such mixed-conductive behaviour, oxygen partial pressures were calculated as a function of temperature as shown in Figure 4.14 and three different gas compositions. The fuel electrode was exposed to a gas composition of 3%H₂O – 48.5%H₂ – 48.5%N₂ in the case explained here. The partial pressure of oxygen was calculated from the partial pressure of hydrogen and steam. To determine the electronic conductivity of GDC at given gas conditions, the following thermodynamic data were used (10).

$$\log P_{\theta} = -3.697 \times 10^4 / T + 18 \quad 4.1$$

$$\sigma_e T = 3.456 \times 10^9 \exp(-2.475/kT) P_{O_2}^{-1/4} \quad 4.2$$

Here, P_{θ} represents the oxygen partial pressure at which ionic (σ_i) and electronic (σ_e) conductivities of GDC are equal ($\sigma_e = \sigma_i$).

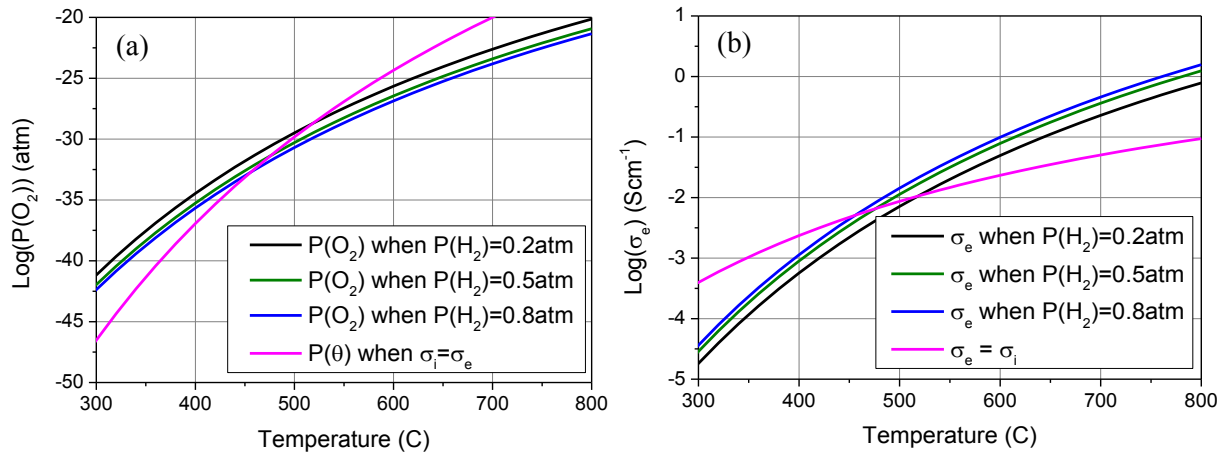


Figure 4.14. (a) Temperature dependence of the oxygen partial pressure according to different hydrogen partial pressures on the fuel electrode; (b) Temperature dependence of the GDC electronic conductivity according to different hydrogen partial pressures on the fuel electrode.

According to Figure 4.14a the partial pressure of oxygen on the fuel electrode, given the gas atmosphere ($P(\text{O}_2)$ when $P(\text{H}_2)=0.5\text{atm}$) in the legend), is lower than P_θ at temperatures above 470°C. This means that the electrode is subjected to a reducing atmosphere. In this case GDC becomes electronically conductive, due to the appearance of oxygen vacancies in the lattice, and the electronic conductivity in GDC prevails ionic ($\sigma_e > \sigma_i$). The values of electronic conductivity of the fuel electrode as a function of temperature are plotted in Figure 4.14b. The mixed-conductive nature of GDC at given gas compositions and temperatures explains why using a Warburg element in the equivalent electrical circuit (Figure 4.13c) resulted in a good fit.

The mixed-conductivity and catalytic properties of GDC imply that the electrochemical reaction can occur via the chemical diffusion of electrons and oxygen ions through the mixed conducting scaffold surface. In this case the reaction zone extends from the triple-phase boundary to the ceria-pore double-phase boundary (DPB) (18-20). The rate of the reaction will, therefore, depend on the mobility of electrons and ions in the mixed-conducting GDC scaffold. Both reaction paths, via TPBs and DPBs, are shown schematically in Figure 4.15. It is likely that the portion of each path (Figure 4.15), involved in electrochemical reaction, will be determined by the fraction of TPBs and DPBs occupying the electrode surface. To validate this statement, further experimental and modelling analyses are required.

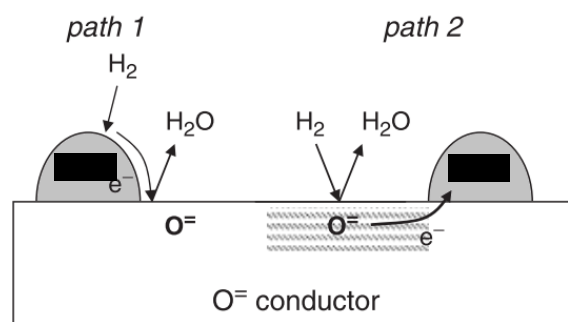


Figure 4.15. Schematic diagram showing the hydrogen electro-oxidation pathways (left) on Ni-YSZ-pore TPB and (right) on GDC-pore DPB. Adapted from (18).

Although the presence of DPBs implies that the electrochemical reaction can occur on the whole electrode area, the presence of the metal catalyst is still important. This is supported by the results shown in Figure 4.13 which suggest that the performance improves with increasing Ni loading.

The values of the electrode ASR associated with low, medium and high frequency ranges are summarised in Figure 4.16. The ASR was extracted from the fitted values of the equivalent circuit, and normalised to the geometric electrode area.

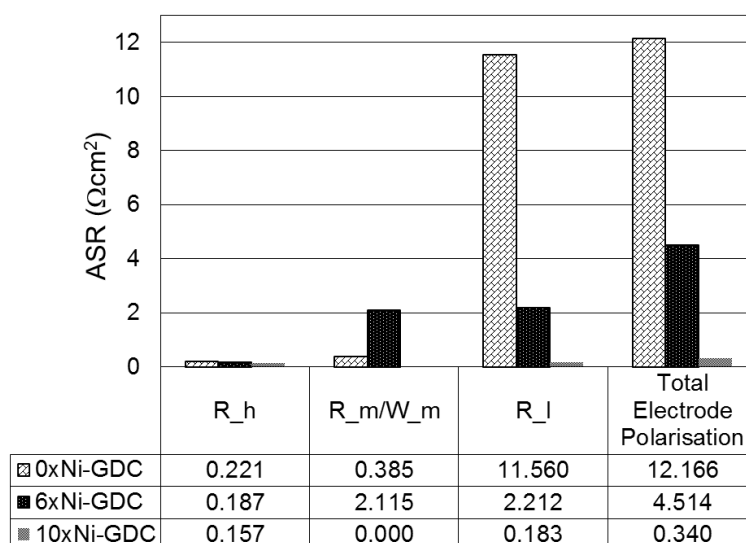


Figure 4.16. High, medium and low frequency resistances and total electrode polarisation at open circuit for ink#2-based fuel electrodes infiltrated 0, 6 and 10 times, as measured between the reference and the working electrodes at 600 °C in humidified 50% H₂ – 50% N₂. The values were taken from the best fit to the equivalent circuits shown in Figure 4.13b for 0 and 6 infiltrations, and Figure 4.13d for 10 infiltrations.

It follows from Figure 4.14b that at 600 °C both ionic and electronic conductivities of GDC are of the same order (~ 0.01 - 0.02 S·cm⁻¹). It has been reported in different studies that the grain

boundaries, because they are depleted of oxygen vacancies, serve as barriers to ion transport (17, 18, 21). Therefore, the impedance spectrum in the high-mid frequency ranges may include two contributors to resistance: one deriving from the ionic conductivity of GDC bulk and one from that of grain boundaries. Additional resistance accompanies the electronic conductivity of GDC (17, 18). The grain boundary effect becomes lower with temperature (17). The mid-frequency impedance can also be attributed to gas-solid interactions such as adsorption of reactant species, desorption of product species or surface migration of the adsorbed species (20, 22-25). The low-frequency range of the impedance spectra may be associated with gas diffusion and/or chemical capacitance (17, 18, 26, 27). Chemical capacitance originates from the variation in the oxygen stoichiometry of the mixed-conducting ceramic electrode. Electrochemical polarisation alters the oxygen content of the ceramic electrode. As a consequence, a chemical relaxation process, associated with the variation in the oxygen vacancy concentration, is observed as a large arc in the low-frequency range of AC impedance measurements (20, 21, 28). This may account for the relatively large low frequency ASR of the pure GDC electrode ($11.6 \Omega\text{cm}^2$).

In the case of 6xNi-GDC electrode, charge transfer can occur on both TPBs and DPBs. The high frequency arc may include charge transfer associated with the former while the latter may be shifted to a mid-frequency process. Based on the data presented here it is difficult to assign each process to the impedance arc quantitatively, and to do so further research is required.

Only two processes in high and low frequencies regions, commonly attributed to the charge transfer at the TPB region and gas diffusion, respectively, could be identified in the 10 times infiltrated GDC electrode (23). It is likely that with higher Ni concentration the resistance is mainly governed by charge transfer through TPBs and therefore the impedance spectrum is reduced to two processes. The charge transfer ASR decreased almost by 30% to $0.16 \Omega\text{cm}^2$ compared to the charge transfer ASR of non-infiltrated GDC. This suggests that the catalytic activity of the electrode increases with increase in Ni content and TPB length as found in the 3-D image reconstruction quantitative analysis. The chemical capacitance of 10xNi-GDC electrode may become lower due to a higher Ni content.

Interestingly, the area specific resistance of the electrode with the highest Ni content decreased dramatically from 12.2 to 0.3 Ωcm^2 mainly due to the drop in the low frequency resistance. The reason could be that higher Ni concentration homogeneously distributed throughout the electrode provides not only multiple TPBs and better electronic conductivity, but also leads to an enlarged effective active region (29). The active region in such circumstances is not limited to a few microns region from the electrolyte-electrode interface, and can include a larger volume of the electrode, thereby minimising mean diffusion path and easing mass diffusion from the areas close to the electrode surface.

To summarize, the significance of the Ni phase in infiltrated electrodes is threefold:

- a. It provides additional catalytic activity, revealed in a lower value of the high frequency resistance, associated with the charge transfer process, with Ni phase increase.
- b. It provides electronic conductivity and assists in uniform and effective current distribution inside the electrode. The electronic conductivity of GDC scaffold alone is about 4 orders of magnitude lower than that of the 10xNi-GDC electrode.
- c. It helps to enlarge the active region which in turn reduces average diffusion length and therefore reduces mass diffusion resistance.

4.3.3 The effect of scaffold porosity

The current density versus overpotential plot for the 10 times Ni infiltrated GDC ink#1 (micro-pores only) and ink#2 (micro- and macro-pores) fuel electrodes is shown in Figure 4.17.

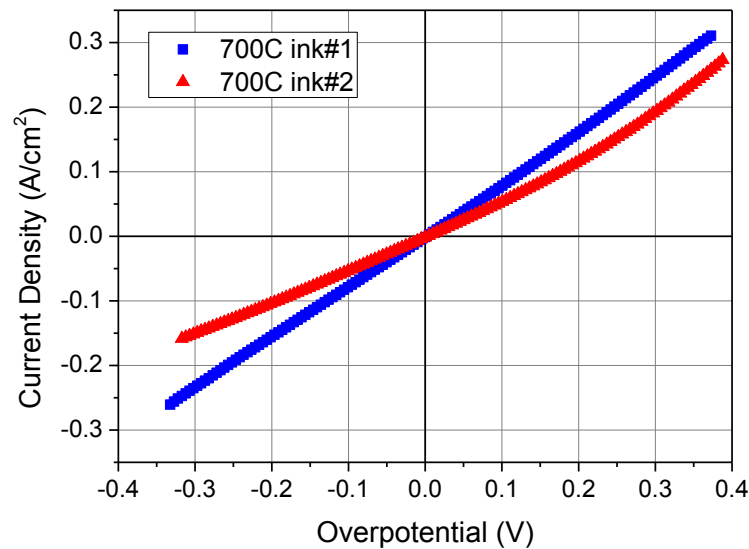


Figure 4.17. Current density vs overpotential of the cell with 10 times Ni infiltrated GDC fuel electrodes based on ink#1 and ink#2, as measured between the reference and the working electrodes (the voltage drop includes the contributions from the infiltrated electrode and the uncompensated iR drop between the RE and WE). The cells were tested in humidified 50% H_2 – 50% N_2 at 700 °C.

It seems that the performance of both electrodes is comparable, while a slightly higher current density was achieved with the ink#1 both in the fuel cell and the electrolysis modes. In addition, the electrode based on the ink#1 exhibits a nearly symmetrical behaviour in both modes.

The EIS response, as measured between the reference and the working electrodes, in humidified 50% H_2 – 50% N_2 at 700 °C for 10xNi-GDC ink#1 and ink#2 is shown in Figure 4.18. The total ASR of the ink#2-based electrode is approximately 1.8 times lower compared to ink#1-based electrode, as summarised in Figure 4.19.

This is due to the decrease in both high and low frequency processes assigned to charge transfer and mass transport polarisations, respectively. These results are surprising, as ink#1-based electrode is likely to contain more TPB than that based on the ink#2, hence the charge transfer polarisation was expected to be lower in the ink#1-based electrode. The high value of the low frequency arc in ink#1-based electrode implies high diffusion resistance, probably due to the extensive Ni coarsening that, in

consequence, may have led to some of the open porosity clogging. If true, this blockage may not only account for the increase in the low frequency arc, but also a reduction in available TPBs. In addition, Ni coarsening in general may lead to a decrease in TPB length as was verified by SEM analysis (Figure 4.4).

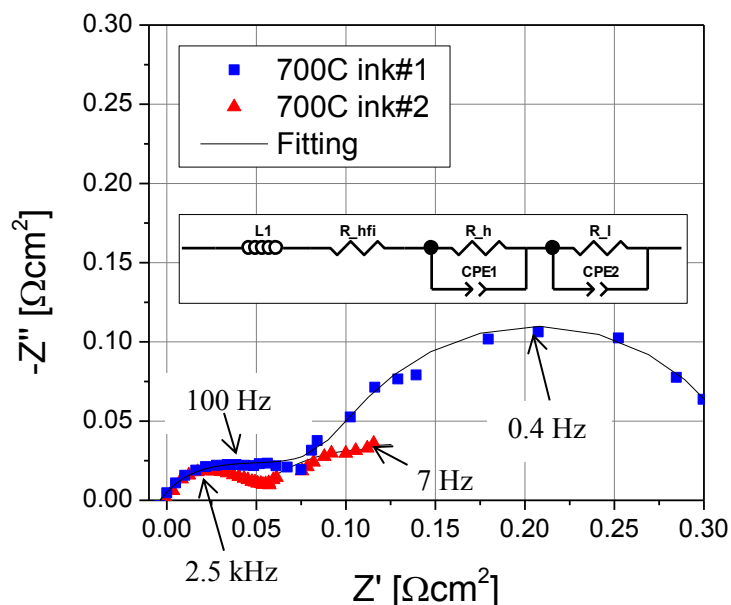


Figure 4.18. Galvanostatic impedance spectra (100 mHz-100 kHz) of the 10xNi infiltrated GDC ink#1 and ink#2-based fuel electrodes at 700 °C in humidified 50% H₂ – 50% N₂ under OCP, as measured between reference and working electrodes. The inset represents the corresponding equivalent electrical circuit.

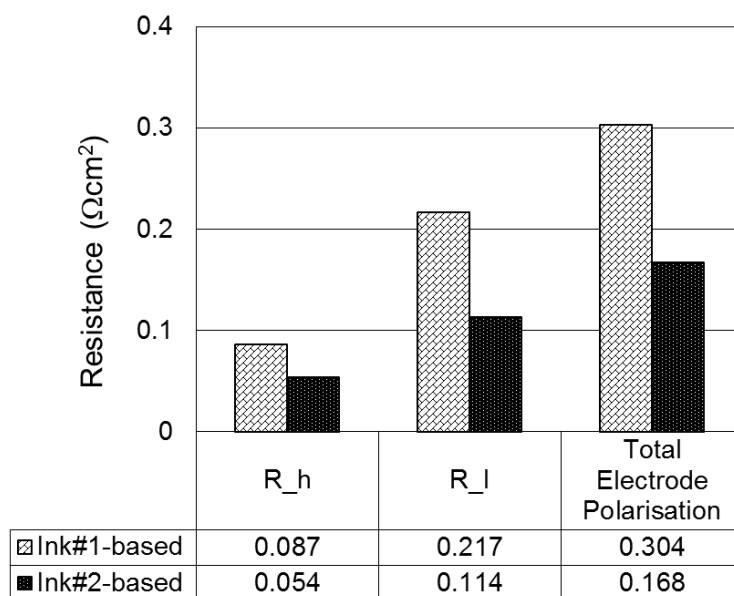


Figure 4.19. High and low frequency resistances and total electrode polarisation of 10xNi-GDC electrodes prepared from ink#1 and ink#2 tested at 700 °C in 50% H₂ – 50% N₂ under OCP, as measured between reference and working electrodes.

Moreover, the micro-pores of the ink#1 based electrode could be too small to maintain 10 Ni infiltrations in the first place, and/or the total porosity of the electrode was not sufficient. According to the 3-D image reconstruction, the open porosity of the 10xNi–GDC (ink#1) was only 20% (Table 4.1). The other reason for increased low frequency resistance in ink#1-based electrode could be a higher value of chemical capacitance due to a higher content of the GDC phase.

The j - V curves in Figure 4.17 and the impedance spectra in Figure 4.18 both give different results for the relative performance of ink 1 over ink 2. This apparent contradiction may be due to the uncertainty regarding the potential of the reference electrode in the three electrode measurements, although great care was taken to align the working and counter electrodes for the. It therefore appears that EIS gives more reliable information regarding the polarization resistance of the electrode. However, to assign a corresponding process associated with the EIS data can be difficult, especially when mixed-conducting materials are concerned.

Two important conclusions may be derived from these observations. Firstly, there is a certain amount of porosity and a pore size that should be maintained in infiltrated electrodes. And secondly, there is a certain amount of infiltration that may be tolerated by a scaffold with certain porosity to achieve an optimized performance. All these are due to the inevitable decrease in a pore size and porosity fraction with the increase in volume of the infiltrated phase. This implies that there is a local minimum in ASR plotted as a function of porosity / infiltrated material fraction ratio for each average pore size. It is likely that the ASR will start to increase after a certain threshold is reached as shown schematically on the sketch in Figure 4.20.

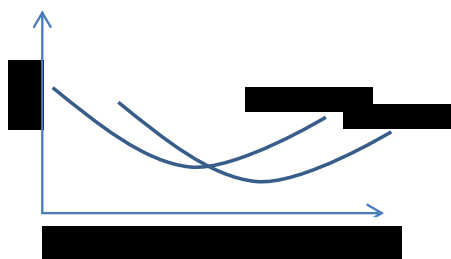


Figure 4.20. A schematic representation of the ASR as a function of porosity / infiltrated material fraction ratio for different average pore size.

The results of the present study provided experimental data for the initial one-dimensional numerical model of Ni-GDC infiltrated electrodes, which estimates the effect of the electrode microstructure on performance (6). Although the initial model did not take into account the infiltrated phase, it emphasizes the impact of the mean pore size of the mixed-conducting GDC scaffold on electrode performance. The ASR of the electrode with smaller mean pore size ($< 1 \mu\text{m}$) is associated with lower gas diffusivity especially at higher current densities, at which faster fuel diffusion through the porous electrode is required. The contribution of the nickel phase by enhancing the electrochemical activity around the TPB and electrical conductivity of the electrode will be taken into account to improve the accuracy of the model in the future work.

4.3.4 The effect of temperature

The current density vs overpotential plot of the cell with the 10 times infiltrated ink#2-based GDC electrode was measured at 5 temperatures, 550 °C to 750 °C with 50 °C increments, between the WE and CE in a four-electrode set-up, as shown in Figure 4.21. As expected the performance of the cell increased with temperature.

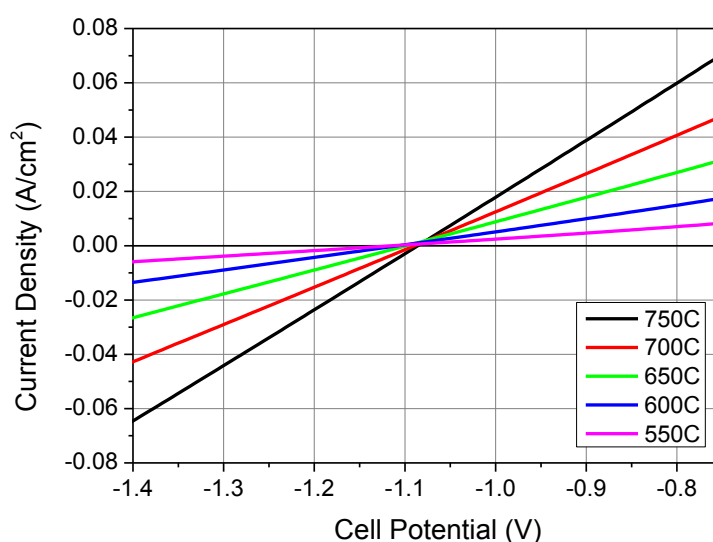


Figure 4.21. The j - V performance of the 10 times infiltrated ink#2-based GDC electrode in the range of 550-750 °C in a humidified 50% H_2 – 50% N_2 atmosphere in a two-electrode set-up.

The EIS spectra of this electrode at different temperatures are plotted in Figure 4.22. High frequency intercept in the Nyquist plot, which mainly accounts for the ohmic resistance of the electrolyte, varies from $\sim 3 \Omega\text{cm}^2$ at 750°C to $16 \Omega\text{cm}^2$ at 550°C .

According to Figure 2.5 the logarithm of conductivity, σ , of YSZ at 700°C is $-2 \text{ S}\cdot\text{cm}^{-1}$. Thus the ASR at 700°C can be calculated through conductivity and electrolyte thickness, L , for $300\mu\text{m}$ thick YSZ electrolyte as follows.

$$\text{ASR (YSZ @ } 700^\circ\text{C)} = R \cdot A = L \cdot \rho = \frac{L}{\sigma} = \frac{300 \cdot 10^{-4}}{0.01} = 3 [\Omega\text{cm}^2] \quad 4.3$$

The calculated value is close to that obtained in the experiment from the EIS spectrum ($\sim 3.9 \Omega\text{cm}^2$). Differences in the thickness of the YSZ electrolyte pellets ($\pm 50 \mu\text{m}$) can lead to variation in the values of high frequency intercept between different cells.

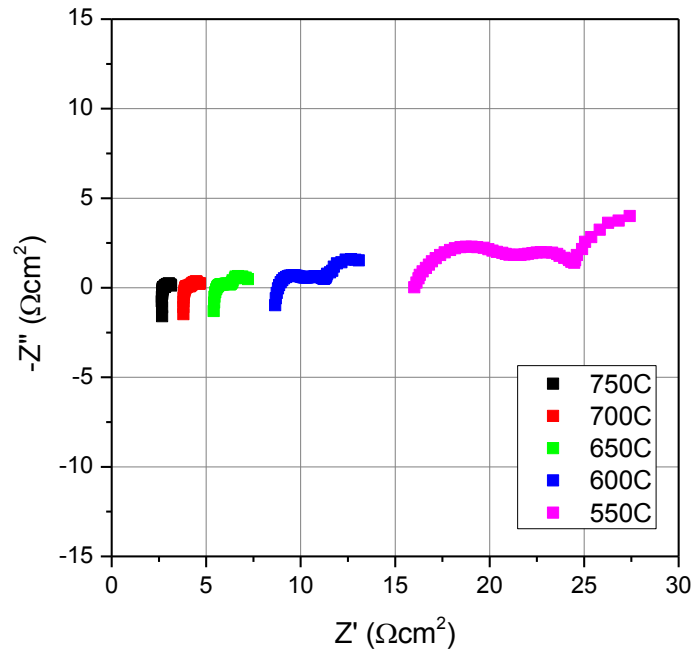


Figure 4.22. EIS measurements of the 10 times Ni infiltrated GDC electrode based on ink#2 at $550\text{--}750^\circ\text{C}$ in humidified $50\% \text{H}_2 - 50\% \text{N}_2$ under OCP in two electrode set-up, i.e. as measured between working and counter electrodes.

Figure 4.23 demonstrates the complex impedance response of the cell at open circuit and different temperatures for $50\% \text{H}_2 - 50\% \text{N}_2$ as measured in three-electrode configuration, i.e. between the working and reference electrodes (WE-RE).

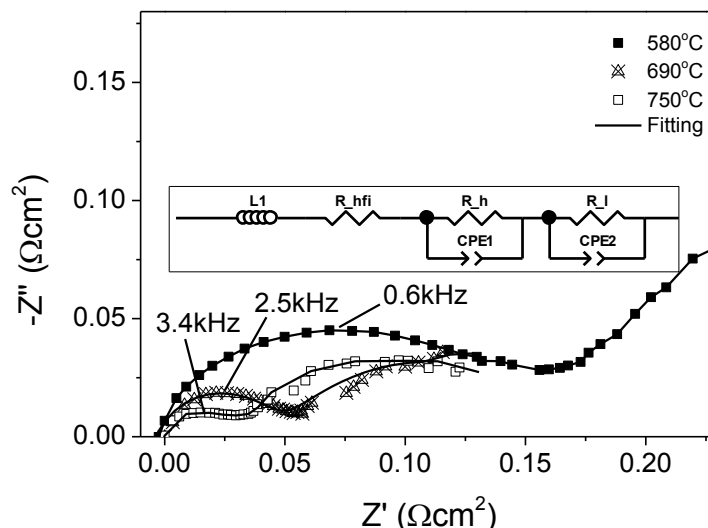


Figure 4.23. Galvanostatic impedance spectra (100 mHz-100 kHz) at open circuit and different temperatures for 50% H₂ – 50% N₂ as measured between reference and working electrodes. An inset demonstrates the corresponding equivalent circuit. The value of the series resistance (R_{hfi}) was set to zero for the data presented in this study to compensate for the variable uncompensated iR drop between the WE and RE under different conditions (16).

At least two processes, in the high and low frequency regions, commonly attributed to charge transfer at the TPB region and gas diffusion, respectively, could be identified (23).

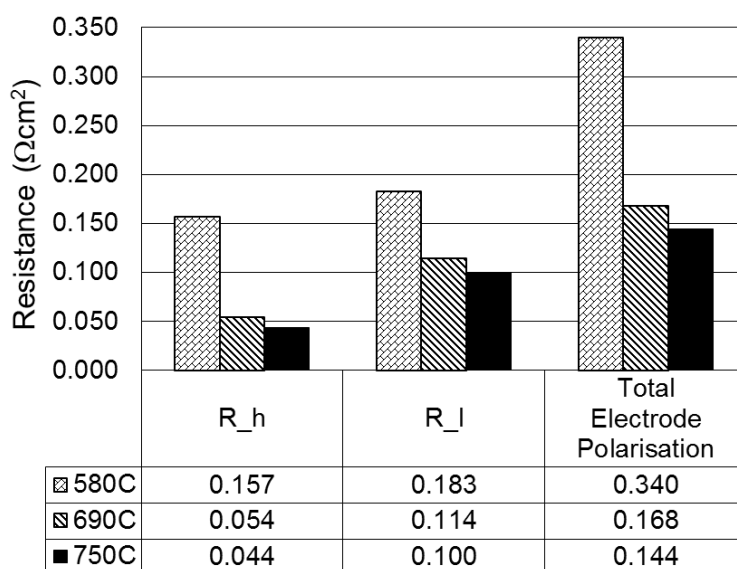


Figure 4.24. High and low frequency resistances and total electrode polarisation at different temperatures and open circuit for 50% H₂ – 50% N₂ as measured between reference and working electrodes.

The impedance spectra were fitted using the equivalent circuit shown in the inset of Figure 4.23. At OCP and 580 °C the polarisation of the working electrode was 0.340 Ωcm² and decreased further

to $0.144 \Omega\text{cm}^2$ as the temperature increased to $750 \text{ }^\circ\text{C}$. These values of resistances are within the ranges of those reported for conventional Ni-YSZ electrodes (30) and lower than $0.8 \Omega\text{cm}^2$ reported by Kim et al (20). Figure 4.24 displays the components of high and low frequencies polarisations of the electrode as well as its total ASR.

As expected, the total polarisation resistance of the electrode decreased with temperature. Temperature has a more pronounced effect on the high frequency resistance than on the low frequency resistance, though both show variation with temperature. The low frequency feature may contain a contribution from the chemical capacitance of the GDC scaffold (17, 20), which will be temperature and oxygen partial pressure dependant.

4.3.5 Effect of gas composition

To study the influence of H_2 partial pressure on the polarisation of the electrode, an experiment was carried out at fixed temperatures for three different $\text{H}_2\text{-N}_2$ concentrations. The total working electrode polarisation increased from $0.154 \Omega\text{cm}^2$ to $0.219 \Omega\text{cm}^2$ when the H_2 concentration was reduced to 20% (Figure 4.25).

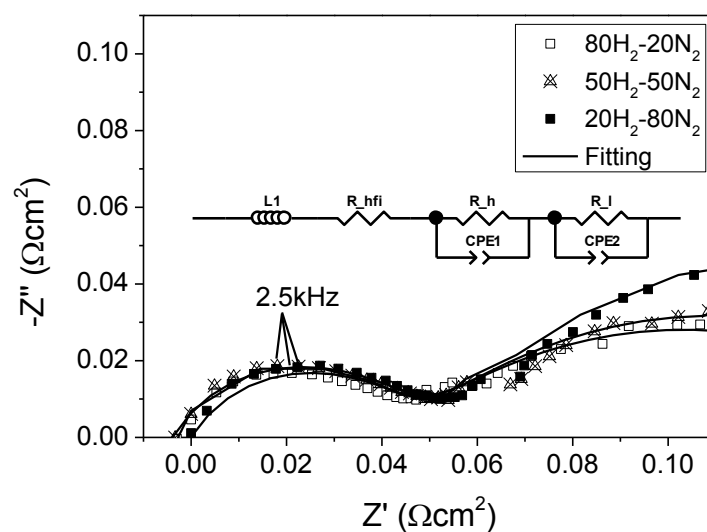


Figure 4.25. Galvanostatic impedance spectra (100 mHz-100 kHz) at open circuit for different $\text{H}_2\text{-N}_2$ concentrations at $690 \text{ }^\circ\text{C}$ as measured between the reference and working electrodes. The inset shows the corresponding equivalent electrical circuit.

The high frequency polarisation of the working electrode at all H₂ concentrations remained almost identical and equal to $\sim 0.05 \Omega\text{cm}^2$ (Figure 4.26).

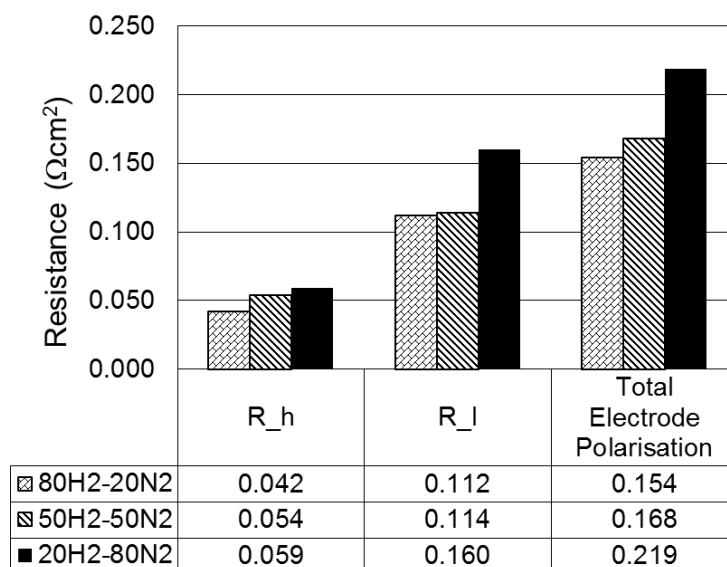


Figure 4.26. High and low frequency resistances and total electrode polarisation at open circuit for different H₂-N₂ concentrations at 690 °C as measured between the reference and working electrode.

However, the low frequency polarisation became more significant at lower H₂ concentrations. Assuming that gas diffusion is one of the rate-limiting processes at low frequencies, such an effect of hydrogen concentration on electrode resistance would be expected (31). Similar phenomena were revealed at 580 and 750 °C. Earlier reported findings suggest that gas diffusion significantly contributes to the polarisation in screen printed Ni/GDC electrodes, probably due to large gas stagnation zones inside the cell (31).

4.3.6 Activation energies calculation

Arrhenius plots of the electrode ASR over the entire test matrix measurements based on EIS data for high and low frequency polarisations are displayed in Figure 4.27 and Figure 4.28, respectively.

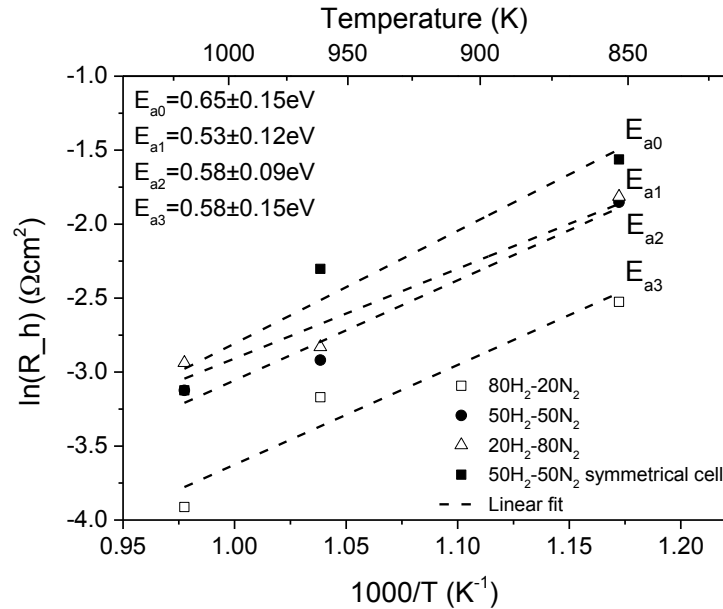


Figure 4.27. Arrhenius plot of the electrode ASR associated with higher frequency polarisation over the range of temperature and H₂/N₂ gas mixture ratios tested at ~OCP. Corresponding values for activation energies in both the symmetrical cell and the fuel cell are denoted.

The Arrhenius plots show good linearity over the wide range of temperatures for both high and low frequency polarisations. However the linear regression fits, giving the activation energies for each process, are different.

No significant variation in activation energy with different H₂/N₂ gas mixture ratio was observed for high frequency resistances. The activation energy associated with high frequency arc in a symmetrical cell was comparable with the values estimated for a fuel cell and lay within the standard error (0.65 ± 0.15 eV). The values (~ 0.53 - 0.58 eV) were in the range of charge transfer activation energies and close to 0.50 eV obtained in (32) for hydrogen oxidation on Ni-GDC anodes at temperatures from 550 to 650 °C. The activation energy for Ni-infiltrated electrodes in the present study was lower than that obtained by Jiang *et al.* (33) for Ni porous anodes infiltrated with GDC nano-particles (~ 0.75 eV) and significantly smaller than that of Ni/YSZ cermet anodes (~ 1.1 eV)

reported by Kromp *et al.* and Leonide *et al.* (34, 35). The relatively low values of charge transfer polarisation and activation energy suggests that Ni-infiltrated GDC electrodes can be considered for application in SOC devices. Improvement in the electrocatalytic oxidation of hydrogen on ceria-based electrodes has been shown in other studies (15, 36-38). The lower value of the charge transfer activation energy renders these electrodes appropriate for intermediate temperatures.

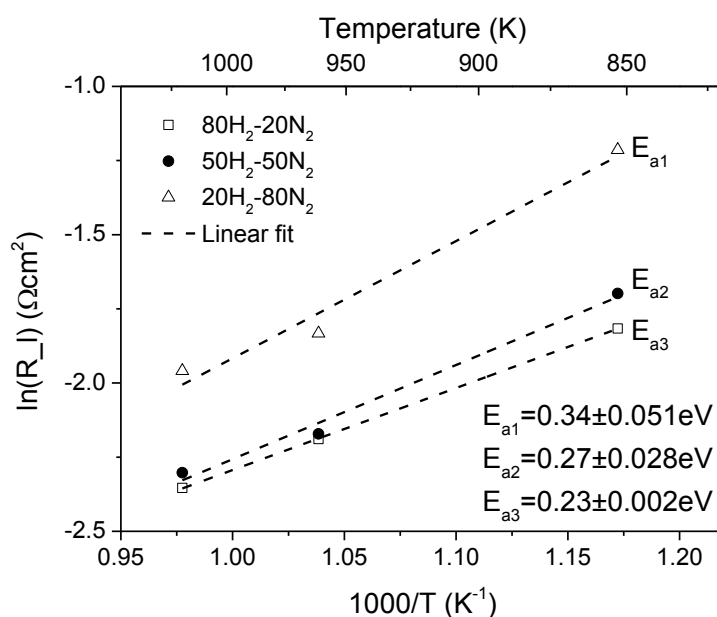


Figure 4.28. Arrhenius plot of the electrode ASR associated with low frequency polarisation over the range of temperature and H₂/N₂ gas mixture ratios tested at ~OCP.

The activation energies for the lower frequency polarisation were smaller than those for the high frequency and varied between 0.23 and 0.34 eV. They are also lower than the equivalent value of 0.45 eV reported by Lee *et al.* for Ni-GDC electrodes fabricated by tape casting (32). These variations are likely to be due to the differences in electrode microstructure and cell configuration, as well as the gas flow conditions. In addition the temperature dependence may account for the chemical capacitance, as was mentioned in 4.3.4. The fact that the activation energies of the low frequency process show a minor (but not a null) temperature dependence can imply that it is neither pure gas diffusion in the pores nor a simple chemical process, and that it is probably a combination of both processes. To validate this further investigation is required.

4.3.7 Short-term degradation study

Short-term degradation was studied in both GDC ink#1 and ink#2 based electrodes infiltrated 10 times each.

10xNi-GDC (ink#2-based)

In the course of 4 days (approx. 100 hrs) the cell was exposed to a range of temperatures between 580 and 750 °C. Several i - V curves and impedance spectra were recorded during the experiment, while most of the time the cell was held at OCP. Identical measurements were performed at the beginning and the end of the experiment to estimate the short term stability of the cell. The current density versus overpotential in three-electrode measurements is shown in Figure 4.29.

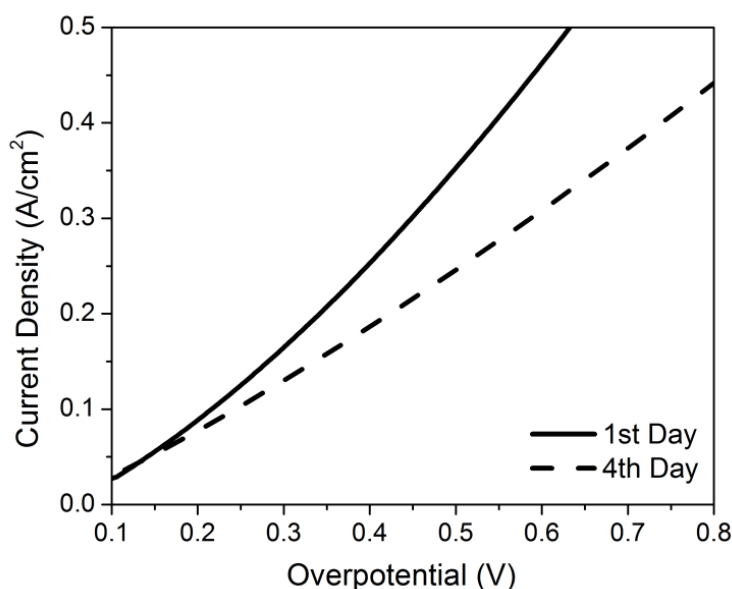


Figure 4.29. Current density vs overpotential on the first and fourth day of operation in 50% H₂ – 50% N₂ at 690°C as measured between the working and reference electrodes (the voltage drop includes the contributions from the infiltrated electrode and the uncompensated iR drop between the RE and WE).

Due to the three-electrode configuration the voltage drop includes the contributions from the infiltrated electrode and the uncompensated iR drop between the WE and RE (16). Some degradation of the cell was observed. The OCP at 690 °C in 50% H₂ – 50% N₂ atmosphere (as a reference condition) decreased from -1.106 V to -1.090 V. This may be attributed to sealing issues. The current density at an overpotential of 0.5 V decreased from 0.47 A/cm² to 0.3 A/cm².

Based on the EIS data (Figure 4.30) the main contribution to the increased ASR over time was ohmic losses as R_{hfi} increased from 0.774 to 1.306 Ωcm^2 (69%).

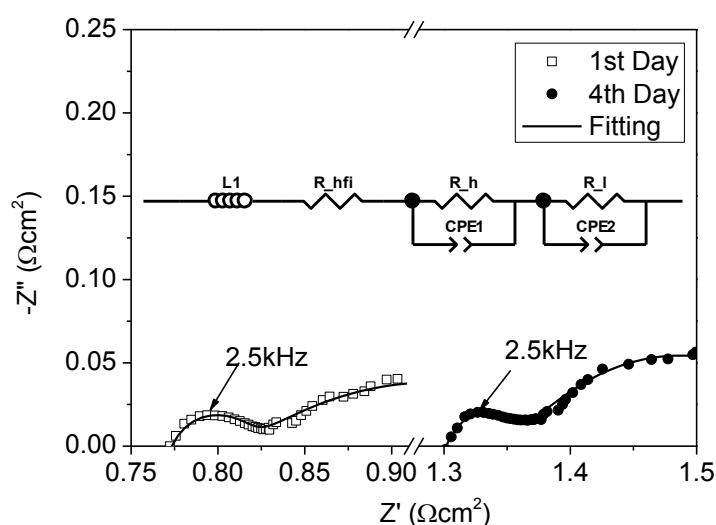


Figure 4.30. Galvanostatic impedance spectra (100 mHz-100 kHz) at OCP over time for 50% H_2 – 50% N_2 at 690 °C as measured between the reference and the working electrodes. The inset shows the corresponding equivalent circuit.

A relatively small change in the total electrode polarisation (the ASR) was observed (only 13%), as shown in Table 1.

Table 4.2. ASR values extracted from the equivalent circuit in the inset of Figure 4.30 for the cell operation over approximately 100 hrs at 690 °C under OCP and in 50% H_2 – 50% N_2 atmosphere.

| | $R_{hfi}, \Omega\text{cm}^2$ | $R_h, \Omega\text{cm}^2$ | $R_l, \Omega\text{cm}^2$ | Total electrode polarisation, Ωcm^2 |
|------------|------------------------------|--------------------------|--------------------------|---|
| 1st Day | 0.774 | 0.054 + | 0.114 = | 0.168 |
| 4th Day | 1.306 | 0.069 + | 0.121 = | 0.190 |
| Difference | 0.532 (+69%) | 0.015 + | 0.007 = | 0.022 (+13%) |

The microstructure of the electrode, inspected by SEM after the experiment is shown in Figure 4.4c-e. The formation of Ni agglomerates could be seen after cell exposure at 550-750 °C for 4 days. This modification of the microstructure can give rise to a local depletion of Ni on the GDC surface and, as a result, to a loss of TPB length and connectivity between Ni particles. Despite this, the total electrode polarisation increased only by 13% (Table 4.2), meaning that the electrochemical performance of the electrode was not affected appreciably during this period. This may be explained

by mixed conductivity and catalytic qualities of doped ceria towards H₂ electrochemical oxidation and is in agreement with recent findings (38, 39). Hence, the electrochemical performance may be insensitive to some disruption in Ni pathways, though clearly major loss of conductivity would be expected to impact electrochemical performance as well as ohmic losses. Microstructural changes in Ni-infiltrated GDC electrodes may originate from de-wetting between Ni and GDC phases and the high mobility of Ni nano-particles at elevated temperatures leading to particle coarsening (40). Therefore in order to take technological advantage of the enhanced properties of percolated Ni-infiltrated GDC electrodes this issue should be addressed. To overcome Ni agglomeration, and to ensure microstructural stability, it is possible to co-infiltrate the GDC scaffold with Ni in combination with low surface energy oxides (such as CeO₂, MgO, etc) which could play a role as anchoring sites between Ni and GDC, inhibiting metal diffusion. It has been shown that addition of MgO, TiO₂, Mn₃O₄, and Cr₂O₃ suppressed Ni agglomeration in Ni-YSZ anodes (40-42).

The increased ohmic losses may also originate from increased contact resistance to the electrode due to a possible volume expansion of GDC in reducing conditions, which may cause strain between YSZ and GDC and lead to degradation of the GDC-YSZ interface (43). Additionally, the solid state reaction between doped zirconia and ceria at high temperatures (1300-1500 °C), which may affect the conductivity, has been reported previously (44, 45). However, no structural changes in YSZ-GDC interface were observed in this study by SEM, and therefore at this stage the reason for the increased ohmic losses is not clear and requires further investigation. In addition, the loss of a percolating Ni network during the aging process may be another possible source of increasing R_{hfi}.

10xNi-GDC (ink#1-based)

The degradation of the GDC Ink#1-based electrode with 10 Ni infiltrations was estimated in fuel cell and electrolysis modes over a period of 40-60 hrs at 600 °C in a humidified 50% H₂ – 50% N₂ atmosphere under 10 mA and -10 mA current loadings as shown in Figure 4.31. In these data the fuel cell and electrolysis modes were run sequentially on the same cell. Similar features of the cell potential with time observed in this plot are due to the variations in the lab temperatures between day

and night time. During the night time, the air conditioning was switched off leading to temperature increase in the water bubbler (hence an increase in H_2O partial pressure) and decrease in a heat loss from the furnace in which the cell was held. These temperature instabilities in turn resulted in a decrease (in absolute values) of the cell potential during night time; during day time the cell potential returned to its original base line.

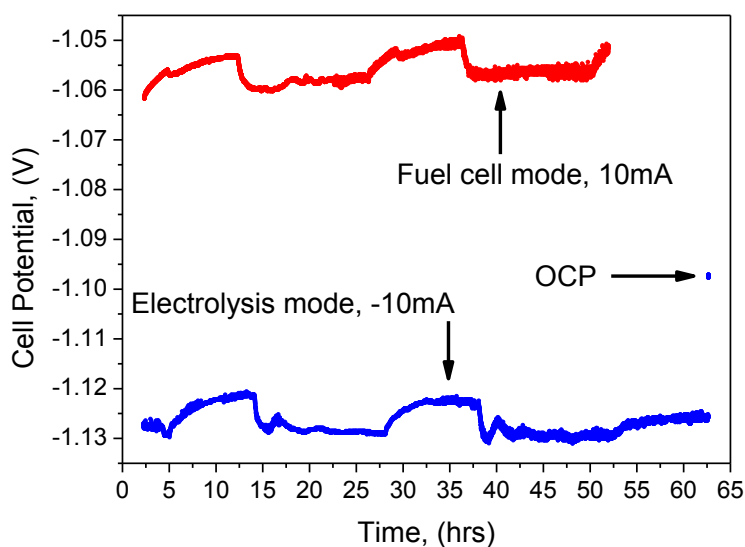


Figure 4.31. Potential variations with time of the cell with GDC Ink#1-based fuel electrode with 10 Ni infiltrations in fuel cell and electrolysis modes over a period of 40-60 hrs at 600 °C in a humidified 50% H_2 – 50% N_2 atmosphere under 10mA and -10mA current loadings, as measured between the working and the reference electrodes. The measurements were run sequentially on the same cell.

In general, the experiment lasted 13 days (~320 hrs in total), during this time several degradation measurements, as described above, as along with other measurements under OCP conditions were performed. The OCP value at the end of the experiment (-1.098 V) is close to the theoretical value at 600 °C (-1.116 V) indicating that appropriate sealing had been maintained during this period.

In the course of the degradation test the EIS spectra was measured every 5 hrs to track changes in the ASR. In Figure 4.32 and Figure 4.33 impedance spectra and j - V curves at 600 °C under OCP in a humidified 50% H_2 – 50% N_2 atmosphere on the 1st and 13th days of the experiment are represented, respectively.

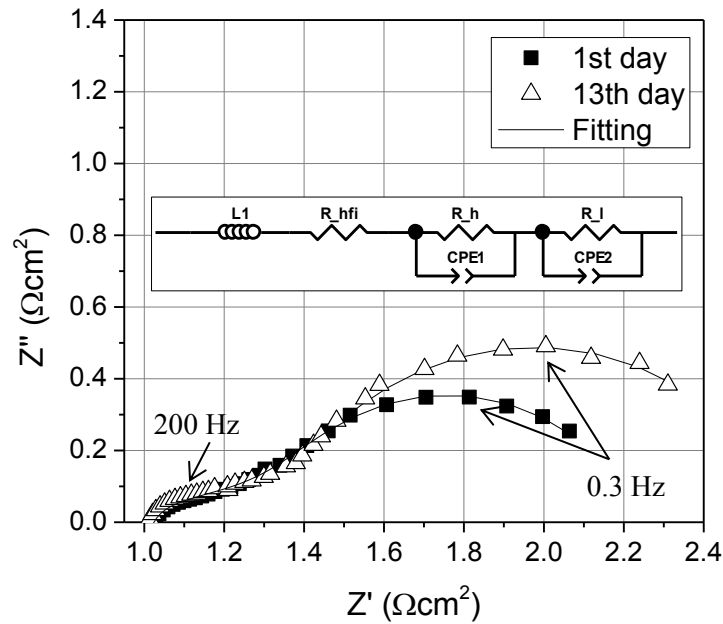


Figure 4.32. Galvanostatic impedance spectra (100 mHz-100 kHz) of the GDC Ink#1-based fuel electrode with 10 Ni infiltrations at 600 °C under OCP in a humidified 50% H₂ – 50% N₂ atmosphere as measured between the reference and the working electrodes on the 1st and 13th days of the experiment. The inset displays the corresponding equivalent circuit.

Virtually no differences in the current density and overpotential of 0.3 V in the fuel cell branch of the j - V curve were detected between the two measurements. The performance in electrolysis mode slightly decreased after 13 days of the experiment (Figure 4.33).

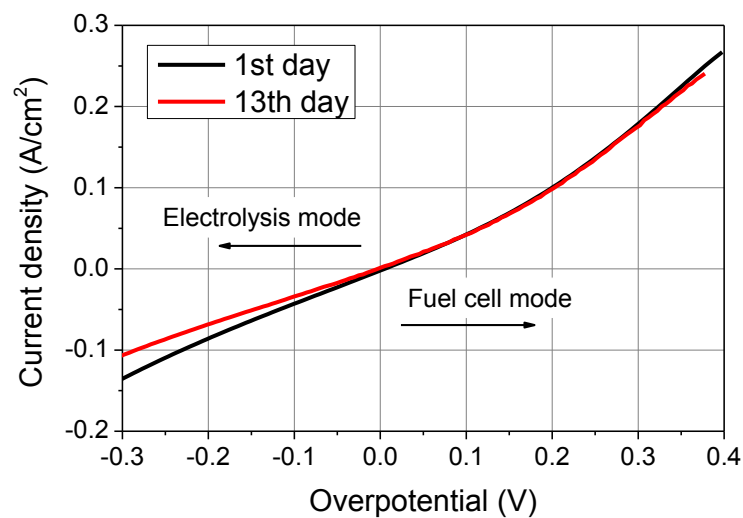


Figure 4.33. Current density vs overpotential of the GDC Ink#1-based fuel electrode with 10 Ni infiltrations at 600 °C under OCP in a humidified 50% H₂ – 50% N₂ atmosphere as measured between the working and reference electrodes on the 1st and 13th days of the experiment.

Table 4.3 summarizes the ASR of the electrodes on the 1st and the last day of the experiment. In contrary to the short-term degradation results for GDC ink#2 based electrode (Table 4.2), the ohmic resistance of the GDC ink#1 based electrode did not change even after longer experiment times (~320 hrs). It can be explained by the fact that the more homogeneous scaffold structure (ink#1-based) is more stable during prolonged exposure to high temperatures.

Table 4.3. ASR values extracted from the equivalent circuit in inset of Figure 4.32 for the cell operation over approximately 320 hrs at 600 °C in a humidified 50% H₂ – 50% N₂ atmosphere.

| | R_hfi, Ωcm ² | R_h, Ωcm ² | R_l, Ωcm ² | Total electrode polarisation, Ωcm ² |
|------------|-------------------------|-----------------------|-----------------------|--|
| 1st Day | 0.931 | 0.552 + | 0.885 = | 1.437 |
| 13th Day | 0.949 | 0.599 + | 1.110 = | 1.709 |
| Difference | 0.018 (+1.9%) | 0.047 (+8.5%) + | 0.225 (+25.4%) = | 0.272 (+18.9%) |

The total electrode polarisation on the 13th day of the experiment had risen by 18.9% from 1.4 to 1.7 Ωcm² (Table 4.3). This is mainly due to the increase in a low frequency arc resistance from 0.9 to 1.1 Ωcm² (25.4%) and to a minor extent due to the high frequency arc resistance increase from 0.5 to 0.6 Ωcm² (8.5%). SEM analysis of this sample (Figure 4.4f) indicates that Ni agglomeration and coarsening occurred, apparently to a higher extent than in a shorter ~100 hrs experiment. As discussed previously in section 4.3.3, Ni particle coarsening can give rise to pore blockage thereby obstructing the fuel species from reaching active reaction sites (thus increasing the diffusion polarisation) and leading to a loss of TPBs in general (leading to a charge transfer polarisation increase). The total electrode polarisation increase was found to be higher for longer experiment (18.9% (1.7 Ωcm²) for ~320 hrs versus 13% (0.12 Ωcm²) for ~100 hrs).

The loss of TPBs can be compensated by the mixed-conductive nature of the GDC scaffold. This phenomenon could clearly be seen in both degradation study cases as the charge transfer resistance was only slightly affected by Ni coarsening. This may account for the minor performance decrease found in the *j-V* curve. The reason for non-symmetrical behaviour between fuel cell and electrolysis modes performance is still unclear and requires further investigation.

From the comparison between short term degradation in electrodes based on ink#1 and ink#2, it can be concluded that the impact of Ni coarsening on the microstructure in the ink#1 based electrode will be more severe due to the blockage of fine pores. In contrast, Ni coarsening does not seem to affect gas diffusion appreciably in the ink#2-based electrode due to considerably bigger pores. However, the ink#1-based electrodes seem to be more robust and therefore mechanically stable for longer term operation. Further experiments are required to confirm this.

4.4 Conclusions for Chapter IV

The purpose of this chapter was to characterise microstructural development as well as electrochemical performance of Ni-infiltrated GDC electrodes across a wide range of temperatures and hydrogen concentrations. Two different GDC scaffolds were prepared forming only micro-porosity (ink#1) and combined macro- and micro-porosity (ink#2).

First, the qualitative and quantitative analysis of infiltrated electrodes microstructure, using 2-D and 3-D imaging methods, was presented. The conclusions from microstructure studies can be summarised as following.

- After ten infiltrations the full uniform coverage of almost equal size Ni nano-particles on a ceramic matrix was obtained in both ink#1-based and ink#2-based electrodes. In spite of the uniform coverage, the particles were individually dispersed. This may be as a result of poor wettability between the GDC scaffold and Ni.
- After experiments in humidified H_2-N_2 and at 550-750 °C, Ni particle coarsening can be identified, although to a different extent depending on experiment duration. The coarsening features relatively little Ni particle growth after a short-term experiment (~5 hrs), through snake-like coarsening after ~100 hrs, to coarse agglomerate formation after a longer-term experiment (~320 hrs).
- The 3-D image reconstruction quantitative analyses of the 1xNi-GDC and 10xNi-GDC samples suggest that the nickel particles are uniformly distributed inside the scaffold. This is in agreement with the SEM-EDX map of Ni distribution.

- The TPB densities in the 1xNi-GDC and 10xNi-GDC electrodes were found to be about 5 times and one-order of magnitude larger than those in the conventional electrode, respectively.
- Based on the 3-D image reconstruction quantitative analysis, the Ni volume fraction was found to be 19.8 vol%. This is in agreement with Ni concentration assessed by the weighing method.
- The 3-D image reconstruction quantitative analysis suggests that there is no percolating Ni clusters observed in the tested region. This is in agreement with 2-D imaging results but somewhat contradicts electronic conductivity measurements. Van der Pauw electronic conductivity method showed a shift to a metallic-like behaviour of the electrode after 6 Ni infiltrations. The excess of Ni on the electrode surface during infiltration creates a thin (~1 μm) Ni ‘islands’ with restricted connectivity that may cause the observed shift towards metallic behaviour. Therefore, the results of the van der Pauw technique probably represent both the bulk conductivity of the electrode and a contribution from surface Ni. The Ni ‘islands’ may have a positive effect on the electrode current collection and distribution.
- At 700 °C the conductivity of the 10xNi-GDC (25 wt%) electrode was as high as 620 S/cm. A similar conductivity was measured at 700 °C for Ni – SDC electrodes prepared from NiO – SDC composite powders with significantly higher Ni content of 35 wt%. This is probably due to a small initial Ni particle size and a more effective Ni particles distribution inside the infiltrated electrodes. The excess Ni on top of the electrode could also improve to the electrode conductivity; however its contribution is difficult to estimate.

The validity of using the three-electrode set-up, for the specific cell configuration and cell dimensions used in the present study, was confirmed by impedance measurements in a symmetrical cell. Symmetrical two-electrode and three-electrode fuel cell measurements show consistent results for the electrolyte resistance, and for the activation energy of the high frequency polarisation process.

Electrochemical performance in fuel cell mode was evaluated using three-electrode DC and AC measurements over a range of temperatures (550-750 °C) and hydrogen concentrations (20-80%). At 750 °C and 50% H₂ – 50% N₂ atmospheres the ASR of the anode was 0.14 Ωcm^2 , comparable or lower than state-of-the-art Ni-YSZ anodes. This was related to a large TPB length of infiltrated

electrodes (one-order of magnitude larger than those in the conventional electrode) as found using 3-D image reconstruction quantitative analysis.

The effect of Ni concentration in ink#2-based GDC scaffold on the electrode performance was studied with pure GDC, 6 and 10 Ni infiltrations. The main findings can be summarised as follows.

- Based on j - V curve results in fuel cell and electrolysis modes, the 10 times infiltrated electrode showed the highest performance amongst other samples in fuel cell mode, whereas the performance of the 6 times infiltrated electrode was slightly higher in electrolysis mode. The reason for non-symmetrical behaviour requires further clarification.
- It is likely that the electrochemical reaction in Ni infiltrated GDC electrodes take place on the double phase boundary due to the mix-conducting nature of ceria. Even though the results suggest that the performance improves with increase in Ni concentration.
- The impedance spectra of the electrodes with pure GDC or low (6 infiltration) Ni concentration can be fitted into three semi-circles implying the mixed conducting nature of GDC under fuel gas conditions. The possibility of mixed-conductivity under the measurement conditions was confirmed by thermodynamic calculations.
- The mixed-conductivity of GDC implies that the electrochemical reaction can occur via the chemical diffusion of electrons and oxygen ions through the mixed conducting scaffold surface. In this case the reaction site extends from the triple-phase boundary to the ceria-pore double-phase boundary.
- In general, based on the data presented here it is difficult to assign a process to the impedance arc quantitatively, and to do so further research is required.

The threefold significance of the Ni phase in infiltrated electrodes was identified:

- The Ni phase provides additional catalytic activity, which revealed in a lower value of the high frequency resistance, associated with charge transfer process, with Ni phase increase.

- The Ni phase provides electronic conductivity and assists in uniform and effective current distribution inside the electrode. The electronic conductivity of GDC scaffold alone is about 4 orders of magnitude lower than that of the 10xNi-GDC electrode.
- The Ni phase helps to enlarge the active region which in turn reduces average diffusion length and therefore reduces mass diffusion resistance.

The effect of scaffold porosity on the electrode electrochemical performance was studied using 10 times Ni infiltrated GDC electrodes fabricated from ink#1 and ink#2. The main conclusions are that due to the inevitable decrease in a pore size and porosity fraction with the increase in volume of the infiltrated phase:

- There is a certain amount of porosity and pore size that should be maintained in infiltrated electrodes, and
- There is a certain level of infiltration that may be tolerated by a scaffold with certain porosity to achieve an optimized performance.

The optimal ratio between the porosity fraction, pore size and the infiltrated phase fraction should be further modelled and verified experimentally.

It appears that EIS gives more reliable information regarding the polarization resistance of the electrode. However, to assign a corresponding process associated with the EIS data can be difficult, especially when mixed-conducting materials are concerned.

The effect of temperature and hydrogen concentration on the high and low frequency features of the electrode EIS response was studied. The activation energy of the higher frequency response was found to be in the range of ~0.53-0.58 eV and was attributed to charge transfer. These values are found to be lower than those typically reported for Ni-YSZ electrodes. Low values of charge transfer polarisation and activation energy may suggest reasonably high electrochemical performance of the Ni-infiltrated GDC electrodes and their possible use at intermediate temperatures SOCs. The activation energies of the lower frequency region were attributed to a combination of gas diffusion

and chemical capacitance associated with the GDC scaffold. Though, further research is required to confirm this.

The results of the short-term (~100 – 320 hrs) degradation performance of infiltrated electrodes can be summarised as follows.

- To some extent, the loss of TPBs, due to Ni agglomeration and coarsening, can be compensated by the mixed-conducting nature of the GDC scaffold. This phenomenon could clearly be seen in both degradation study cases as charge transfer resistance was only slightly affected by Ni coarsening. Despite this, Ni coarsening may become a rate limiting factor over the longer-term and therefore must be addressed in future work.
- Ni particles coarsening can give rise to pore blockage thereby obstructing the fuel species from reaching active reaction sites (thus increase in a diffusion polarisation in both experiments) and leading to a loss of TPBs in general (thus a slight increase in charge transfer polarisation in both experiments). The total electrode polarisation increase was found to be higher for longer experiment (18.9% for ~320 hrs vs 13% for ~100 hrs).
- The ohmic resistance of the GDC ink#1 based electrode did not change after longer experiment duration (~320 hrs) compared to the increase of 69% in the ohmic resistance of the GDC ink#2 based electrode after a shorter experiment (~100 hrs). This can be explained by the fact that more homogeneous scaffold structure (ink#1-based) is more stable during prolonged exposure to high temperatures.

The results indicate the potential capability of Ni-infiltrated GDC electrodes for future application in SOCs due to the relatively low values of charge transfer polarisation and activation energy. Despite the early stages of developing this class of electrodes, the results are encouraging. At the same time there is clearly potential for further optimisation of the microstructure.

References for Chapter IV

1. S. P. Jiang, S. Zhang, Y. D. Zhen and W. Wang, *Journal of the American Ceramic Society*, **88**, 1779 (2005).
2. P. Nikolopoulos and D. Sotiropoulou, *J Mater Sci Lett*, **6**, 1429 (1987).
3. M. Kishimoto, M. Lomberg, E. Ruiz-Trejo and N. P. Brandon, *Journal of Power Sources*, **266**, 291 (2014).
4. M. Kishimoto, M. Lomberg, E. Ruiz-Trejo and N. P. Brandon, Towards the Microstructural Optimisation of Solid Oxide Fuel Cell Electrodes, in *15th International Heat Transfer Conference*, Kyoto (2014).
5. M. Kishimoto, M. Lomberg, E. Ruiz-Trejo and N. P. Brandon, 3-D Imaging and Characterization of Infiltrated Ni-GDC Electrodes, in *11th European SOFC & SOE Forum*, Lucerne (2014).
6. M. Kishimoto, M. Lomberg, E. Ruiz-Trejo and N. P. Brandon, *Journal of Power Sources (under review)* (2014).
7. M. Kishimoto, M. Lomberg, E. Ruiz-Trejo and N. P. Brandon, *ECS Transactions* **64**, 93 (2014).
8. M. Kishimoto, H. Iwai, M. Saito and H. Yoshida, *Journal of Power Sources*, **196**, 4555 (2011).
9. Properties of Precious Metals, Properties and Selection: Nonferrous Alloys and Special-Purpose Materials, in *ASM Handbook*, p. 699, ASM International (1990).
10. B. C. H. Steele, *Solid State Ionics*, **129**, 95 (2000).
11. M. Chen, B. H. Kim, Q. Xu, O. J. Nam and J. H. Ko, *Journal of the European Ceramic Society*, **28**, 2947 (2008).
12. A. N. Busawon, D. Sarantaridis and A. Atkinson, *Electrochemical and Solid-State Letters*, **11**, B186 (2008).
13. S. B. Adler, B. T. Henderson, M. A. Wilson, D. M. Taylor and R. E. Richards, *Solid State Ionics*, **134**, 35 (2000).
14. S. McIntosh, J. M. Vohs and R. J. Gorte, *Journal of The Electrochemical Society*, **150**, A1305 (2003).
15. P. Kim-Lohsoontorn, Y.-M. Kim, N. Laosiripojana and J. Bae, *International Journal of Hydrogen Energy*, **36**, 9420 (2011).
16. G. J. Offer, P. Shearing, J. I. Golbert, D. J. L. Brett, A. Atkinson and N. P. Brandon, *Electrochimica Acta*, **53**, 7614 (2008).
17. A. Atkinson, S. A. Baron and N. P. Brandon, *Journal of The Electrochemical Society*, **151**, E186 (2004).
18. W. Lai and S. M. Haile, *Journal of the American Ceramic Society*, **88**, 2979 (2005).
19. T. Nakamura, K. Yashiro, A. Kaimai, T. Otake, K. Sato, T. Kawada and J. Mizusaki, *Journal of The Electrochemical Society*, **155**, B1244 (2008).

20. J. Kim, D. Shin, J.-W. Son, J.-H. Lee, B.-K. Kim, H.-J. Je, H.-W. Lee and K. J. Yoon, *Journal of Power Sources*, **241**, 440 (2013).
21. J. Jamnik and J. Maier, *Physical Chemistry Chemical Physics*, **3**, 1668 (2001).
22. S. Primdahl and M. Mogensen, *Journal of The Electrochemical Society*, **144**, 3409 (1997).
23. S. P. Jiang and S. P. S. Badwal, *Solid State Ionics*, **123**, 209 (1999).
24. M. Orazem and B. Tribollet, *Electrochemical Impedance Spectroscopy*, John Wiley & Sons, Inc (2008).
25. S. P. Jiang and S. P. S. Badwal, *Journal of The Electrochemical Society*, **144**, 3777 (1997).
26. J. Jamnik and J. Maier, *Journal of The Electrochemical Society*, **146**, 4183 (1999).
27. S. Primdahl and M. Mogensen, *Journal of The Electrochemical Society*, **146**, 2827 (1999).
28. T. Kawada, J. Suzuki, M. Sase, A. Kaimai, K. Yashiro, Y. Nigara, J. Mizusaki, K. Kawamura and H. Yugami, *Journal of The Electrochemical Society*, **149**, E252 (2002).
29. M. Kishimoto, K. Miyawaki, H. Iwai, M. Saito and H. Yoshida, *Fuel Cells*, **13**, 476 (2013).
30. A. Hauch, M. Mogensen and A. Hagen, *Solid State Ionics*, **192**, 547 (2011).
31. P. V. Aravind, J. P. Ouweltjes and J. Schoonman, *Journal of The Electrochemical Society*, **156**, B1417 (2009).
32. K. T. Lee, C. M. Gore and E. D. Wachsman, *Journal of Materials Chemistry*, **22**, 22405 (2012).
33. S. P. Jiang, S. Zhang, Y. D. Zhen and A. P. Koh *Electrochemical and Solid-State Letters*, **7**, A282 (2004).
34. A. Kromp, A. Leonide, A. Weber and E. Ivers-Tiffée, *Journal of The Electrochemical Society*, **158**, B980 (2011).
35. A. Leonide, Y. Apel and E. Ivers-Tiffée, *ECS Transactions*, **19**, 81 (2009).
36. O. A. Marina, C. Bagger, S. Primdahl and M. Mogensen, *Solid State Ionics*, **123**, 199 (1999).
37. S. P. Jiang, *J Mater Sci*, **39**, 4405 (2004).
38. W. C. Chueh, Y. Hao, W. Jung and S. M. Haile, *Nature Materials*, **11**, 155 (2012).
39. T. Nakamura, T. Kobayashi, K. Yashiro, A. Kaimai, T. Otake, K. Sato, J. Mizusaki and T. Kawada, *Journal of The Electrochemical Society*, **155**, B563 (2008).
40. W. Z. Zhu and S. C. Deevi, *Materials Science and Engineering: A*, **362**, 228 (2003).
41. T. Klemensø, K. Thydén, M. Chen and H.-J. Wang, *Journal of Power Sources*, **195**, 7295 (2010).
42. B. Hua, W. Zhang, M. Li, X. Wang, B. Chi, J. Pu and J. Li, *Journal of Power Sources*, **247**, 170 (2014).
43. S. Wang, M. Katsuki, T. Hashimoto and M. Dokiya, *Journal of The Electrochemical Society*, **150**, A952 (2003).
44. A. Tsoga, A. Gupta, A. Naoumidis and P. Nikolopoulos, *Acta Materialia*, **48**, 4709 (2000).
45. K. Eguchi, N. Akasaka, H. Mitsuyasu and Y. Nonaka, *Solid State Ionics*, **135**, 589 (2000).

CHAPTER V

LASER SINTERING FOR SOC ELECTRODE FABRICATION

5.1 Introduction

The microstructure of the electrodes in SOCs plays a crucial role in determining the electrochemical performance of the cell. With the goal of ‘electrodes by design’ in mind, in this section the feasibility of using a direct metal laser sintering (DMLS) technique for electrode fabrication is explored. Additive laser manufacturing is a completely novel approach to the field of solid oxide cell electrodes fabrication. The main advantage of this technique is that precise control and design of microstructural parameters are possible due to laser – materials interaction, as described in the literature review, section 2.9. In addition this method may potentially offer fast and reproducible electrode fabrication, parameters that are important for scalability. On the other hand, the scientific and technical aspects of the production route and the effects of manufacturing parameters on the microstructural evolution during the process have not been well explored. Moreover there are numerous combinations of different parameters that make this method very complex. As a consequence, this technique currently relies upon experimental data (1).

In this chapter the methodology and design of the experiments are firstly outlined. These are followed by the results of the microstructure characterisation and electrochemical performance of the full cell. The feasibility of laser sintering technique for fuel cell applications and the challenges are discussed.

5.2 Objectives

The main objectives of this study are:

- To examine the feasibility of using DMLS for fuel cell preparation in the Ni-YSZ (powder) / YSZ (substrate) system.
- To explore the relationship between process parameters, microstructure and electrochemical performance of the cell.
- To identify effective processing parameters for electrode fabrication using DMLS.

5.3 Methodology of electrode fabrication using direct laser metal sintering

5.3.1 Equipment and design of the experiment

This study has been conducted in collaboration with the 3-D Systems (formerly CRDM) company and the experimental work was carried out on the 3-D Systems site. The EOSINT M 270 facility with 200 W YAG pumped fibre pulse laser ($\lambda=1.06 \mu\text{m}$, laser frequency 8000 Hz) in a 98.5% $\text{N}_2 - 1.5\% \text{O}_2$ atmosphere was used for 3-D laser sintering.

Three sets of experiments have been accomplished in this study. In each set of experiments either a Ni-YSZ cermet or a Ni metal powder were laser sintered on the top of dense YSZ pellets of 250-300 μm thickness and 20mm diameter (obtained from fuelcellmaterials.com) used as a substrate for the laser sintered layer. The pellet holder was custom made from stainless steel to hold the YSZ substrates. During SLS experiments the holder was heated to 80 °C.

The rationale behind the experiments was to create an electrode on the YSZ electrolyte and compare it to those formed by screen printing. Because this sort of experiment has never been reported before, the following process was used to find an appropriate combination of laser parameters/materials:

- a) Arbitrary parameters (laser, materials) over a relatively broad range were chosen at the beginning and
- b) Then the parameter window was narrowed down based on results of the previous iteration.

To achieve the objectives the research was divided into three steps:

- Step I – initial investigation: broad spectrum of laser parameters used.
- Step II – further investigation: narrowing laser parameter window and materials used, increasing number of samples.
- Step III – full cell preparation and electrochemical testing, fabrication parameters are based on the results from previous steps.

The detailed design of experiments, materials selection and laser parameters for each step will be further discussed in the subsequent sections.

5.3.2 Materials selection

In the first step a cermet powder consisting of 50 wt% Ni – 50 wt% YSZ was chosen for the laser sintering process. The powder particle size was chosen deliberately such that the YSZ particles were an order of magnitude smaller than Ni particles to enhance contact between the substrate and the cermet powder, and to ensure better accessibility of the laser to the Ni particle surface.

Table 5.1 summarised details of cermet powder size and preparation parameters.

Table 5.1. List of cermet Ni-YSZ powders used in DMLS experiment

| Sample | wt% (Powder source) | Original powder particles size, μm (Specific surface area, m^2/g) | Pre-sintered conditions | Sintering conditions |
|--------|---|---|-------------------------------|---|
| N1 | 50 wt% Ni (sigmaaldrich.com) | 0.8 | 1hr ball milling + dispersant | 1 hr at 1000 °C (N ₂ , H ₂) |
| | 50 wt% YSZ (tosoh.com) | 0.06 (16) | | |
| N2 | 50 wt% Ni (sigmaaldrich.com) | 0.8 | 1hr ball milling + dispersant | 2 hrs at 1000 °C (N ₂ , H ₂) |
| | 50 wt% YSZ (tosoh.com) | 0.06 (16) | | |
| N3 | 50 wt% Ni (sigmaaldrich.com) | 0.8 | 1hr ball milling + dispersant | 3 hrs at 1000 °C (N ₂ , H ₂) |
| | 50 wt% YSZ (tosoh.com) | 0.06 (16) | | |
| N4 | 60 wt% NiO-40 wt% YSZ (fuelcellmaterials) | (1-4) | as received from supplier | 2 hrs at 1000 °C (N ₂ , H ₂) |

To avoid segregation due to different particle sizes, the powders were ball milled together with zirconia milling balls of 3 mm diameter. Then the powders were calcined together for different periods of time (1, 2 and 3 hrs) to enlarge densification between powder particles and to ensure better contact between Ni and YSZ particles. For reference, a 60 wt% NiO-40 wt% YSZ powder without calcination (as received from supplier, Table 5.1) was also tested. Then all 4 batches were sent to 3-D Systems for a spreading characteristic test (spreadability or flowability) conducted by the 3-D Systems engineers. Spreadability is an important requirement because it affects the quality of the powder coverage on the substrate and, in turn, the integrity of the 3-D part. Therefore, passing the spreadability test is a prerequisite for further processing. The test includes passing the powder through the roller blade of the machine over the substrate, onto which the layer is to be laser sintered. The powder must be spread to form a smooth, thin, repeatable and uniform layer of powder.

To simplify the analysis and characterisation, and to narrow the range of parameters, in the second and in the third steps only Ni powder (5-15 μm diameter spherical particles, 99.8% Ni, obtained from Alfa Aesar) was used to create patterned laser sintered structures. In addition, to increase bonding between the Ni powder and the YSZ substrate, the surfaces of few YSZ pellets were pre-metallised by applying a thin Ni layer of ~ 50 nm using sputtering. The electronic conductivity of the samples was estimated at room temperature using a potentiometer by pressing the contacts of the potentiometer 5mm from each other onto the electrode's surface. The test was done several times, each time placing the contact tips in different directions. The microstructure was examined using a Scanning Electron Microscope LEO Gemini 1525 FEG-SEM.

5.3.3 Flowability test of powders in Step I

It was found that the powder N3 (calcined for 3 hrs at 1000 °C in $\text{H}_2\text{-N}_2$, Table 5.1) exhibited the best spreading characteristics. This is likely due to the prolonged calcination conditions (3 hrs) in which the powders agglomerated into larger and homogeneous particles (in terms of redistribution of YSZ and Ni particles). This lowered the surface energy of each particle so that the cohesion between powder particles themselves decreased and attachment to the blade was minimised (2). As a result, a

uniform coverage of the powder on the YSZ substrate was achieved. At the same time, each individual particle kept its original dimensions, because the temperature was not high enough to maintain particle growth. The SEM image of powder N3 is shown in Figure 5.1a-b. The original Ni powder is shown in Figure 5.1c.

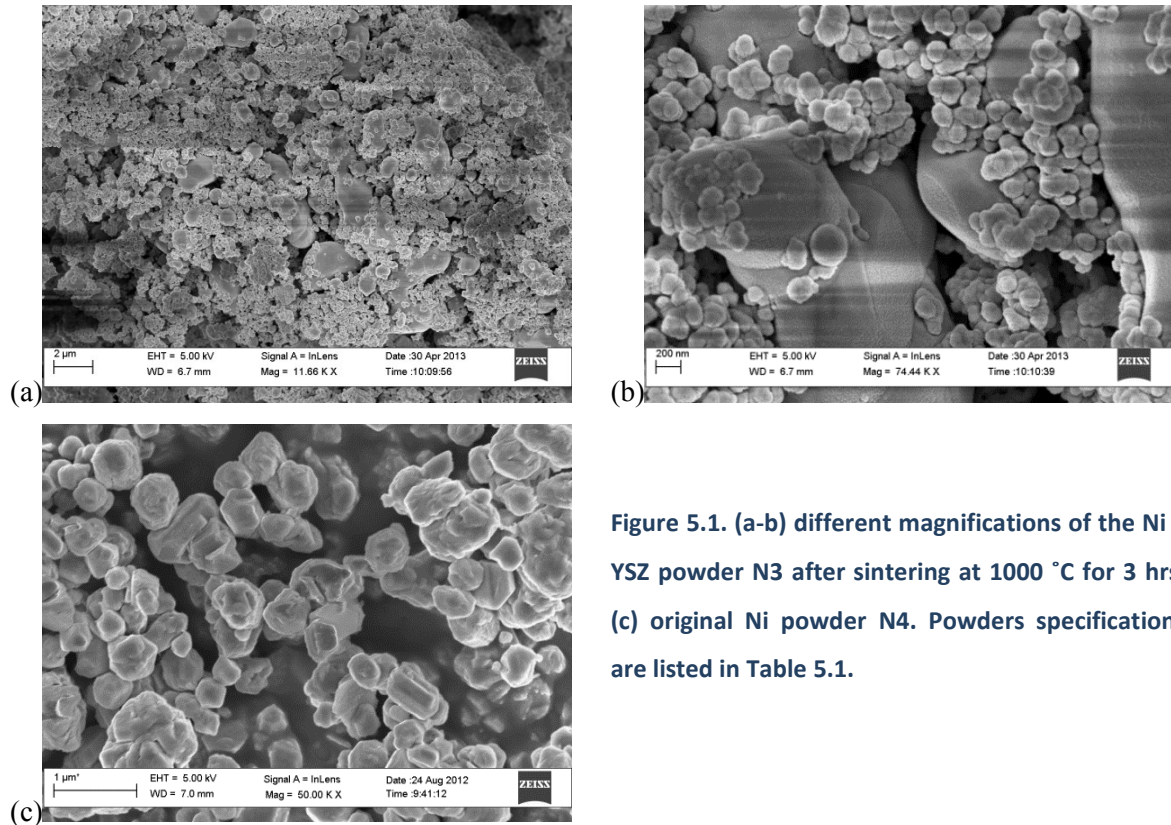


Figure 5.1. (a-b) different magnifications of the Ni – YSZ powder N3 after sintering at 1000 °C for 3 hrs; (c) original Ni powder N4. Powders specifications are listed in Table 5.1.

5.3.4 Estimation of the thermal shock resistance of the YSZ substrate

In the course of laser sintering the powder and the substrates are subject to high temperatures. To assess the resistance towards thermal shock, the thermal stress arising from the temperature gradient can be calculated as follows (3):

$$\sigma_{thermal} = \frac{\alpha \Delta T E}{(1 - \nu)} \quad 5.1$$

where $\sigma_{thermal}$ [Pa] is the fracture stress, α [1/K] is a thermal expansion coefficient, ΔT [K] is the temperature gradient, E [Pa] is the Young's modulus (or elastic modulus) and ν is the Poisson's ratio. By setting the peak tension equal to the fracture stress of YSZ, the temperature gradient, ΔT ,

that can be sustained by a material prior to a severe strength degradation, can be estimated (Equation 5.2). The properties of YSZ are provided in Table 5.2.

Table 5.2. Material properties of YSZ.

| Material | Thermal Expansion Coefficient, α (4, 5) | $\sigma_{fracture}$, MPa (6) | Poisson's ratio (7) | Young Modulus, GPa | K_{Ic} , MPam ^{1/2} (8) |
|----------|---|-------------------------------|----------------------|------------------------------|------------------------------------|
| 8mol%YSZ | 8·10 ⁻⁶ K ⁻¹ at 1000K 7·10 ⁻⁶ K ⁻¹ at 473K | 200 | 0.32 (for dense YSZ) | 155 at 900°C 190 at 200°C | 1.5 |

$$\Delta T = \frac{\sigma_{thermal}(1-\nu)}{E\alpha} \cong 110^{\circ}C \quad 5.2$$

Note that the equation 5.1 is independent of sample sizes only when samples are extremely large. Nevertheless, the equation may provide qualitative information. More accurate relationships for small objects (with dimensions less than 10⁻³ m) is a function of the Biot modulus, β , hence $\sigma_{thermal}$ is proportional to β . The Biot modulus is defined as $\beta = \frac{hL}{k}$ [no units] (9), where h is the heat transfer coefficient (for YSZ $h \sim 10^3$ Wm⁻²K⁻¹ (10)), L is the thickness (in our case the thickness of YSZ pellet $\sim 300 \cdot 10^{-6}$ m) and k is the thermal conductivity (for YSZ $k \sim 2$ Wm⁻¹K⁻¹ (11)). Thus, β lies around $\sim 1 \cdot 10^2$. ΔT is inversely proportional to β (and to the thickness), therefore ΔT is expected to be higher than the $\sim 110^{\circ}C$ value calculated above.

In ceramics the fracture toughness, K_{Ic} [MPa m^{1/2}], measures the resistance of a material to crack propagation according to eq. 5.3 (12):

$$K_{Ic} = Y\sigma_{fracture}\sqrt{\pi c} \quad 5.3$$

where Y is a geometric factor (~ 1) and c is a crack length.

Therefore from eq. 5.3 it is possible to estimate the minimum critical crack length above which the crack starts to propagate in the bulk and to cause fracture (eq. 5.4). Taking $K_{Ic} = 1.5$ MPam^{1/2} and $\sigma_{fracture} = 200$ MPa for YSZ (Table 5.2):

$$c = \frac{K_{Ic}^2}{\sigma_{fracture}^2 \pi} = 17.9 \times 10^{-5} m \approx 18 \mu m \quad 5.4$$

Hence the YSZ is expected to withstand cracks that are less than 18 μ m in length.

5.4 Results and discussion

5.4.1 General design of experiments

The laser variable parameters controlled in this study were laser speed (S) and laser power (P), whilst others, such as hatch spacing, laser diameter, were kept unchanged. The experiments were designed so that different settings of laser parameters could be tested with a limited number of samples. To allow that, 5 sub-samples of 4 mm in diameter were fabricated on each YSZ pellet as shown in Figure 5.2 (where the diameters of the fabricated electrodes are to scale relative to the YSZ substrate). Each pellet and sub-sample was labelled so that laser parameters could be correlated with the results of the sintering (Figure 5.2). Different combinations of laser power and laser speed were applied on each individual sub-sample. However, the energy density (defined as laser power divided by laser speed (Equation 2.13)) on each sub-sample within same pellet was kept unchanged on all samples except the first one. The energy density varied between pellets.

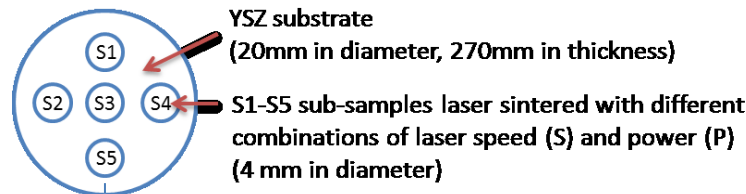


Figure 5.2. Diagram of the YSZ pellet (substrate) carrying 5 sub-samples (S1-S5) to be laser sintered.

Following is a description of each of the three steps of this study.

5.4.2 Step I – initial investigation

Design of experiments in Step I

In Step I four YSZ pellets with five sub-samples each (Figure 5.2) were fabricated by laser sintering, applying only a single layer of cermet powder. The parameters for each consecutive sample were set following visual inspection of the results from the previous sample. This reflected time and equipment availability constraints, as all samples in Step I had to be produced on the same day. Initially, wide spectra of laser speed (in the range of 200 – 4000 mm/sec) and laser power (in the

range of 20 – 190 W) were used to fabricate the samples. Depending on the results in subsequent trials the laser parameters were narrowed to meet the following success criteria:

- Absence of macro-cracks during fabrication (based on a visual inspection)
- Good adhesion of the powder to the substrate (based on a visual inspection)

Table 5.3 summarizes the details of the experiments in Step 1.

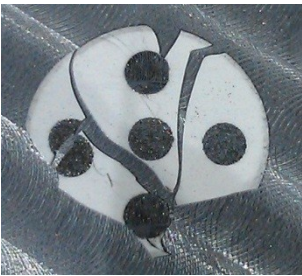
Table 5.3. Matrix of experiments in Step I.

| Sub - sample | Sample 1 | | | Sample 2 | | | Sample 3 | | | Sample 4 | | |
|--------------|---------------|----------|--------------|---------------|----------|--------------|---------------|----------|--------------|---------------|----------|--------------|
| | Speed, mm/sec | Power, W | Energy, J/mm | Speed, mm/sec | Power, W | Energy, J/mm | Speed, mm/sec | Power, W | Energy, J/mm | Speed, mm/sec | Power, W | Energy, J/mm |
| S1 | 160 | 40 | 0.25 | 800 | 40 | 0.05 | 800 | 40 | 0.05 | 667 | 20 | 0.03 |
| S2 | 400 | 40 | 0.1 | 800 | 40 | 0.05 | 2000 | 100 | 0.05 | 1333 | 40 | 0.03 |
| S3 | 560 | 40 | 0.07 | 800 | 40 | 0.05 | 2800 | 140 | 0.05 | 2000 | 60 | 0.03 |
| S4 | 800 | 40 | 0.05 | 800 | 40 | 0.05 | 3800 | 190 | 0.05 | 2667 | 80 | 0.03 |
| S5 | 160 | 40 | 0.25 | 800 | 40 | 0.05 | 400 | 20 | 0.05 | 3333 | 100 | 0.03 |

Results of laser sintering in Step I


In the first sample of Step I a relatively broad range of energy densities were used (0.05-0.25 J/mm) for sample fabrication, as evident from Table 5.4.

Table 5.4. Laser parameters used in Step I for sample 1 and the image of sample 1 after laser sintering.

| Sub - sample | Sample 1 | | | Sample after sintering |
|--------------|---------------|----------|--------------|--|
| | Speed, mm/sec | Power, W | Energy, J/mm | |
| S1 | 160 | 40 | 0.25 |  |
| S2 | 400 | 40 | 0.1 | |
| S3 | 560 | 40 | 0.07 | |
| S4 | 800 | 40 | 0.05 | |
| S5 | 160 | 40 | 0.25 | |

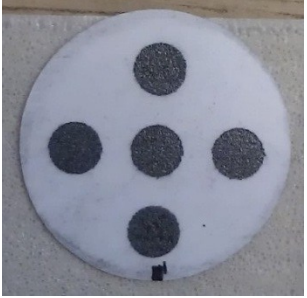
As can be seen from the image of the sample taken after the experiment, the only sub-substrate that did not crack was S4 subjected to the energy density of 0.05 J/mm (Table 5.4). This result was consistent with those obtained in sample 2 (Table 5.5), where all sub-samples were sintered under the same conditions of laser power and laser speed at the overall energy density of 0.05 J/mm (and similar conditions as those of S4 in Sample 1). Generally, no macro-cracks were observed in this sample except for one sub-sample that broke. The reason for this is not clear. As all the sub-samples were fabricated with similar conditions it is possible that the crack was caused by a local damage of the substrate.

Table 5.5. Laser parameters used in Step I for sample 2 and the image of sample 2 after laser sintering.

| Sub - sample | Sample 2 | | | Sample after sintering |
|--------------|---------------|----------|--------------|---|
| | Speed, mm/sec | Power, W | Energy, J/mm | |
| S1 | 800 | 40 | 0.05 |  |
| S2 | 800 | 40 | 0.05 | |
| S3 | 800 | 40 | 0.05 | |
| S4 | 800 | 40 | 0.05 | |
| S5 | 800 | 40 | 0.05 | |

In the next sample the energy density was kept as in the previous case (0.05 J/mm), but the laser power and the laser speed varied over the range of 20-190 W and 400-3800 mm/sec, respectively, to maintain 0.05 J/mm, as shown in Table 5.6.

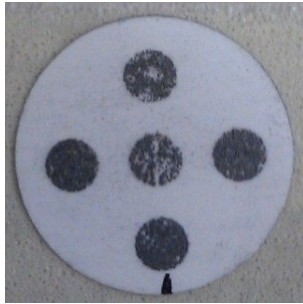
Table 5.6. Laser parameters used in Step I for sample 3 and the image of sample 3 after laser sintering.

| Sub - sample | Sample 3 | | | | Sample after sintering |
|--------------|---------------|----------|--------------|--|--|
| | Speed, mm/sec | Power, W | Energy, J/mm | Conductivity at T _{room} , Yes/No | |
| S1 | 800 | 40 | 0.05 | no |  |
| S2 | 2000 | 100 | 0.05 | no | |
| S3 | 2400 | 120 | 0.05 | yes | |
| S4 | 3800 | 190 | 0.05 | yes | |
| S5 | 400 | 20 | 0.05 | no | |

No macro-cracks were detected in sample 3. Additionally, electronic conductivity analysis revealed that sub-samples S3 and S4, sintered with the maximum laser power (120 and 190 W, respectively), were conductive at room temperature. In contrast, the sub-samples, sintered using lower laser power, were not conductive, although the energy input remained similar in both cases. These differences will be discussed further.

With the next sample the possibility of using even lower energy density was explored. Sample 4 was exposed to an energy density of 0.03 J/mm with varying parameters of laser speed and laser power, as shown in Table 5.7.

Table 5.7. Laser parameters used in Step I for sample 4 and the image of sample 4 after laser sintering.

| Sub - sample | Sample 4 | | | | Sample after sintering |
|--------------|---------------|----------|--------------|--|---|
| | Speed, mm/sec | Power, W | Energy, J/mm | Conductivity at T_{room} , Yes/No | |
| S1 | 667 | 20 | 0.03 | no |  |
| S2 | 1333 | 40 | 0.03 | no | |
| S3 | 2000 | 60 | 0.03 | no | |
| S4 | 2667 | 80 | 0.03 | no | |
| S5 | 3333 | 100 | 0.03 | no | |

The sample did not break, but the sub-samples S1 and S3 do not seem to be fully covered with a laser sintered layer. The non-uniform coverage of the sintered layer may be due to insufficient energy input or it may be caused by the non-uniformity in the powder layer applied before sintering. None of the samples were conductive.

Microstructure characterisation of laser sintered electrodes in Step I

The micrographs of laser sintered electrodes from Step I are shown in Figure 5.3a-c. The laser path can clearly be identified in the low magnification top view image (Figure 5.3a). On the same image micro-cracks perpendicular to the laser path can be seen.

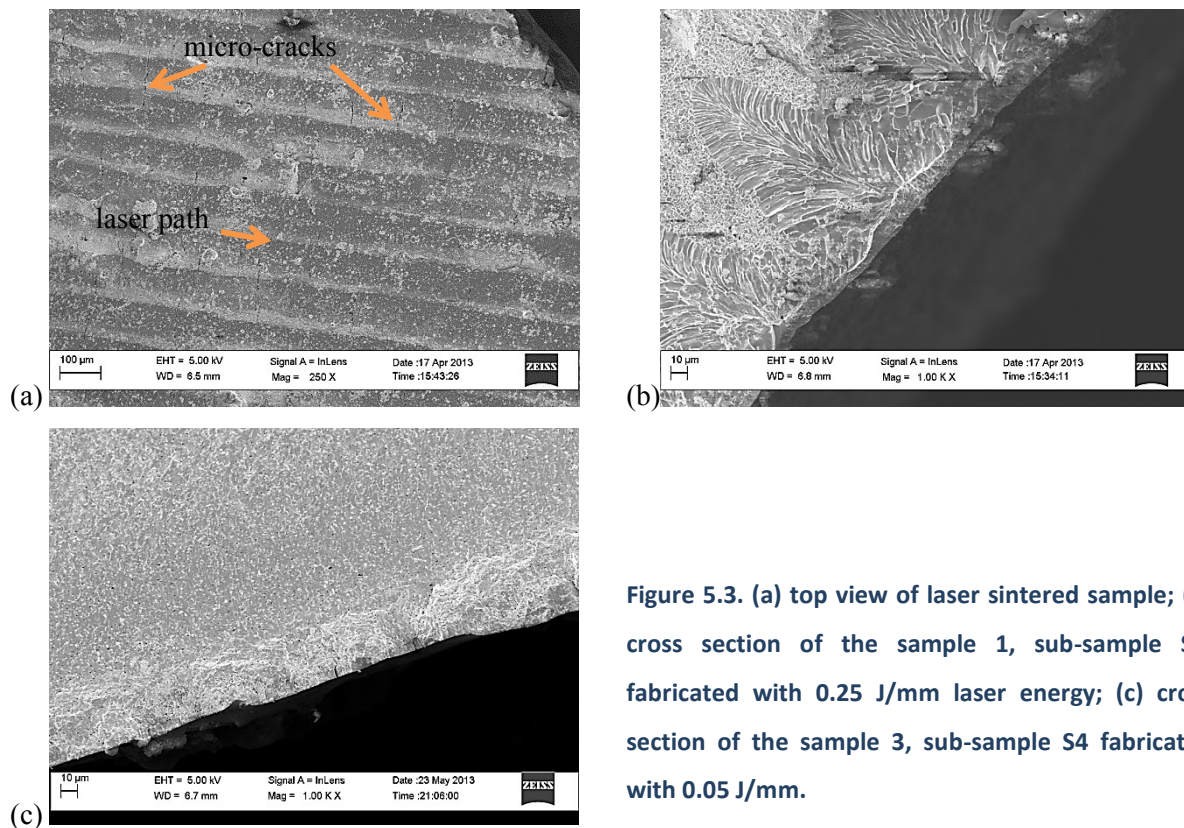


Figure 5.3. (a) top view of laser sintered sample; (b) cross section of the sample 1, sub-sample S5, fabricated with 0.25 J/mm laser energy; (c) cross section of the sample 3, sub-sample S4 fabricated with 0.05 J/mm.

The damage caused to the YSZ substrate is higher (120-150 μm depth) and more severe when higher laser energy is applied (0.25 J/mm in Figure 5.3b). This sample broke during the experiment. In contrast, the damaged region caused by the lower laser energy (0.05 J/mm in Figure 5.3c) is about 10-30 μm and contains fewer micro-cracks. Even though, this sample did not break during the experiment. This suggests that the micro-cracks were smaller than the minimum critical crack length calculated above (18 μm).

It is likely that the micro-cracks appeared due to two reasons:

- 1) Thermal shock caused by temperature gradients. In the near infrared range of wavelengths ($\lambda < 5 \mu\text{m}$) YSZ is almost transparent to radiation (13). However the absorbance of nickel in this range is higher (14) meaning that Ni powder interacts with the laser to absorb heat. When the laser couples with the powder, plasma above the powder is formed and it is the plasma that provides the heat to melt the powder. Due to the rapid heating of the powder by the plasma bed a steep temperature gradient develops.

This results in a temperature gradient in the YSZ and, since the thermal conductivity of YSZ is lower than that of Ni, thermal shock to the substrate is caused. Similar cracks due to thermal shock in alumina, formed during laser sintering, have been reported (15).

- 2) Stresses due to mismatch in thermal expansion coefficients between YSZ ($\alpha = 8 \cdot 10^{-6} \text{ K}^{-1}$ at 1000 K) and Ni ($\alpha = 13.3 \times 10^{-6} \text{ K}^{-1}$). Upon melting and cooling Ni expands and contracts as shown schematically in Figure 5.4 (16).

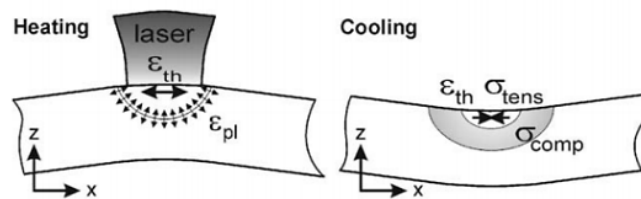


Figure 5.4. Tensile and compressive stresses caused to the substrate upon Ni powder melting and cooling during the laser sintering process (16).

The temperature gradient is higher when higher laser power is applied. This may account for the differences in microstructure in Figure 5.3b and Figure 5.3c.

Segregation of Ni and YSZ particles during the laser sintering process was observed. Following interaction with the laser, Ni particles tend to form lines, as shown in Figure 5.5a; YSZ particles formed agglomerated clusters (Figure 5.5b). This may be associated with low wettability between YSZ and Ni (17). This observation suggests that it may be preferable to laser sinter Ni and YSZ separately.

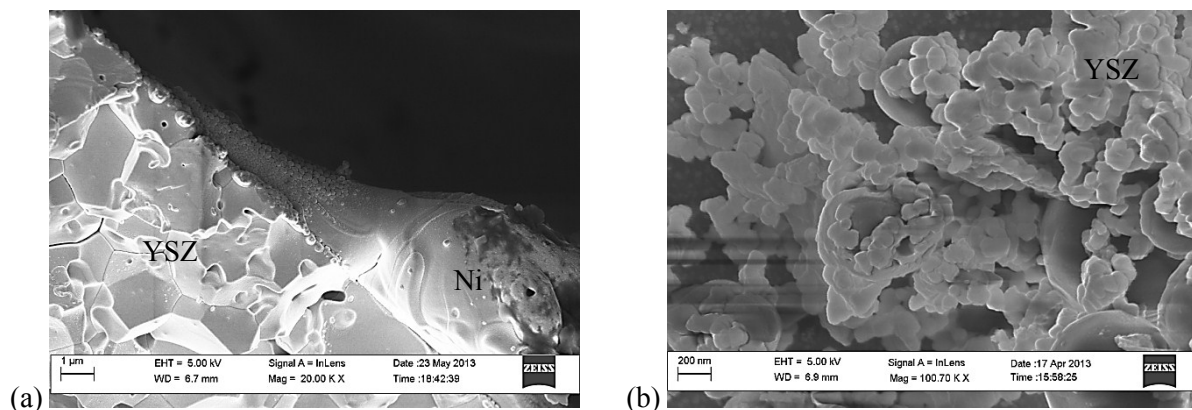


Figure 5.5. (a) Cross section showing laser sintered Ni stripe on the YSZ substrate and (b) top view of a feature sintered from YSZ powder of Sample 3 (S3).

The results from Sample 3 (Table 5.6) suggest that not only energy density is important for the quality of laser sintered parts, but also the combination of laser parameters (power and speed) used for fabrication. To understand the reason for differences in conductivity the microstructure of the pattern created on the substrate was closely inspected in SEM. Figure 5.6a and Figure 5.6b compare SEM images of sub-samples S2 and S4 from Sample 3, produced with 100 W and 190 W, respectively. To keep the same energy density of 0.05 J/mm the laser speed was adjusted to 2000 and 3800 J/mm for S2 and S4, respectively. The microstructure of the sub-samples is different. While the microstructure of the Ni path in S4 is flat and dense, the microstructure of Ni path in S2 is grainy and interrupted. This may possibly indicate the reason for conductivity of the electrode in S4.

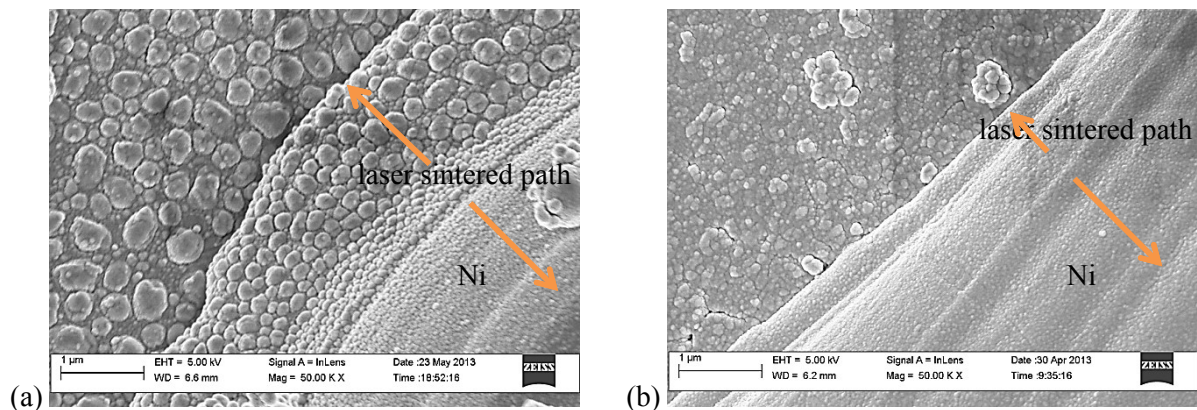


Figure 5.6. Sub-samples S2 and S4 (Sample 3) produced with 0.05 J/mm laser energy density using laser parameters of (a) 100 W and 2000 mm/s (b) 190 W and 3800 mm/s, respectively.

Although the laser beam rested for a shorter period of time on S4, the increased laser power was sufficient to generate enough heat and plasma for Ni particles to melt and to form a uniform continuous path. This suggests that a minimum laser power is required to cause powder melting. In addition, for the given energy density, using a higher laser speed allows less time for melted particles to grow. An instant melt/freeze would ensure insufficient time for coalescence and de-wetting from the substrate and to form individual disconnected metal ‘drops’.

Conclusions of Step I

The main conclusions that can be drawn from the results in Step I are as follows:

- The YSZ substrate could withstand a laser energy density of 0.05 J/mm or less without breaking.
- Micro-cracks were observed on all substrates; however the damage caused to the substrate decreased with decreasing energy density. YSZ is expected to withstand cracks less than 18 μm in length.
- It is likely that cracking in YSZ occurs due to a combination of thermal shock and the mismatch between the thermal expansion coefficients of YSZ and Ni.
- Although Ni and YSZ form unique structures during laser sintering, they were not mixed together to obtain a cermet network.
- Although the same energy density of 0.05 J/mm was applied, the samples were conductive only when the laser power was 120W or higher.
- Due to segregation between Ni and YSZ particles during the laser sintering process it was decided to continue experiments in Step II and III with Ni powder only.

5.4.3 Step II – further investigation

Design of experiments in Step II

In this stage the experiments were designed to achieve the following goals.

- a. Verification of the previous results,
- b. Further optimisation of laser parameters for electrode fabrication,
- c. Exploring the possibility to laser sinter a patterned Ni electrode with up to three layers of powder.
- d. Exploring the possibility to improve the adhesion between the Ni powder and the YSZ substrate by pre-metallisation of the YSZ.

The goals were achieved by varying and narrowing the laser parameters used for electrode fabrication and by enlarging the total number of substrates in one run. Each pellet and sub-sample was labelled so that laser parameters could be correlated with the results of the sintering. Table 5.8 outlines the matrix of samples. In Table 5.8 each row (R1-R4) indicates the number of layers fabricated and each column corresponds to the energy density applied on each pellet in that column (0.03-0.15 J/mm). The samples in the last row were pellets with a pre-metallised surface.

Table 5.8. Matrix of substrates (YSZ pellets) in Step II.

| Row number | Number of layers | (Lateral) Energy Density [Wsec/mm=J/mm] | | | | |
|------------|-------------------------|---|------|------|-----|------|
| | | 0.03 | 0.05 | 0.07 | 0.1 | 0.15 |
| R1 | L=1 | 1.1 | 1.2 | 1.3 | 1.4 | 1.5 |
| R2 | L=2 | 2.1 | 2.2 | 2.3 | 2.4 | 2.5 |
| R3 | L=3 | 3.1 | 3.2 | 3.3 | 3.4 | 3.5 |
| R4 | L=2; pre-metallised YSZ | 4.1 | 4.2 | 4.3 | 4.4 | 4.5 |

Table 5.9 summarizes the laser parameters applied for each individual sub-sample (S1-S5) within the samples (1.1-4.5) listed in Table 5.8. In total $5 \times 5 \times 4 = 100$ sub-samples were fabricated.

Table 5.9. Laser parameters used in Step II for each sub-sample.

| (Lateral) Energy Density [Wsec/mm=J/mm] | | | | | | | | |
|---|--------------|----------|--------------------|--------------|----------|---|--------------|----------|
| 0.03 | | | 0.05 | | | 0.07 | | |
| Samples 1.1-4.1 | LS mm/sec | LP, W | Samples 1.2-4.2 | LS mm/sec | LP, W | Samples 1.3-4.3 | LS mm/sec | LP, W |
| S1 | 1333 | 40 | S1 | 800 | 40 | S1 | 571 | 40 |
| S2 | 2000 | 60 | S2 | 1600 | 80 | S2 | 1143 | 80 |
| S3 | 2667 | 80 | S3 | 2000 | 100 | S3 | 1430 | 100 |
| S4 | 3333 | 100 | S4 | 2800 | 140 | S4 | 2000 | 140 |
| S5 | 4000 | 120 | S5 | 3800 | 190 | S5 | 2715 | 190 |
| (Lateral) Energy Density [Wsec/mm=J/mm] | | | | | | | | |
| 0.1 | | | 0.15 | | | Other details | | |
| Samples 1.4-4.4 | LS mm/sec | LP, W | Samples 1.5-4.5 | LS mm/sec | LP, W | Laser parameters for contour: 100W 3333mm/sec before and after scan (0.03 J/mm) Samples 4.1-4.5 - the surface of the substrate was pre-metallised | | |
| S1 | 200 | 20 | S1 | 133 | 20 | | | |
| S2 | 400 | 40 | S2 | 267 | 40 | | | |
| S3 | 800 | 80 | S3 | 533 | 80 | | | |
| S4 | 1400 | 140 | S4 | 933 | 140 | | | |
| S5 | 1900 | 190 | S5 | 1267 | 190 | | | |

Figure 5.7a presents the arrangement of the samples inside the chamber before the experiment. The Ni powder was spread on the YSZ substrate by a blade (Figure 5.7b) to achieve a uniform single

layer as shown in Figure 5.7c. The YSZ substrates with five laser sintered sub-samples each after the experiment are shown in Figure 5.7d.

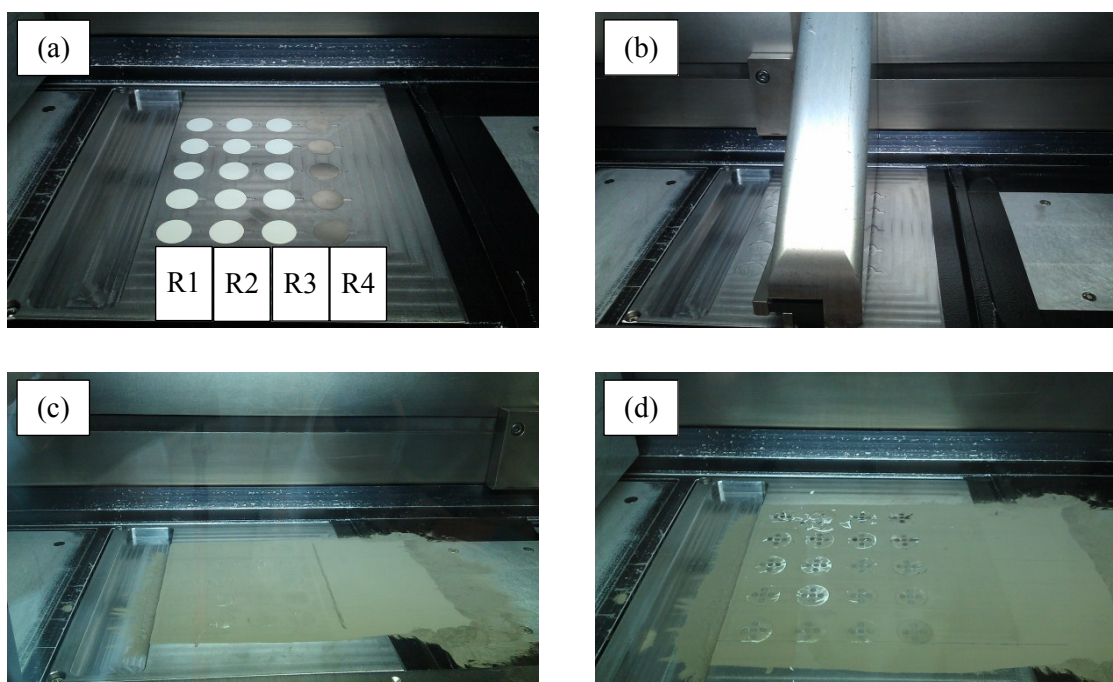


Figure 5.7. Laser sintering chamber during the experiment. (a) Four rows of five YSZ substrates (pellets) each used in Step II, in the last row (R4) of samples are Ni pre-metallised; (b) adjustment of a blade spreading the layers of powder (the image was taken before experiment); (c) YSZ substrates covered with Ni powder; (d) pellets with five laser sintered sub-samples each, after the experiment.

Results of laser sintering in Step II

All samples fabricated with energy density higher than 0.05 J/mm (Samples 1.3 – 4.5), independently of the combination of laser power and laser speed, broke after one layer was sintered. This is in agreement with results obtained in Step I.

Among samples prepared with the laser energy of 0.05 J/mm, only Sample 1.2 (one sintered layer) did not break and the others, with two or three layers, broke. In contrast, none of the samples fabricated with 0.03 J/mm (Samples 1.1-1.4) broke even after three laser sintered layers. Between the two consecutive layers there was a time gap of about one minute to allow spreading of the next powder layer. This is sufficient time for the substrate to cool down. Therefore, the cracking was not caused by the build-up of the temperature on the substrate. Two possible explanations can be put forward to explain why repetitive laser sintering caused the substrate break.

- According to the conclusions of Step I, the damage to the substrate is caused across the whole range of energy densities and is proportional to the energy density. The accumulation of the thermal stresses is therefore a function of the energy density. Hence, the results might suggest that in samples 2.2-4.2, fabricated with higher energy density (0.05 J/mm), the accumulation of thermal stresses after applying repetitive laser energy exceed the critical value for crack propagation and caused substrate failure.
- Alternatively (or rather complementary), a lower energy density may cause a smaller fraction of the powder to melt (providing the laser power component is enough to melt the powder, as follows from the results of Step I). This means that the absolute volume of melted Ni is bigger with higher laser energy density and it becomes even bigger with the application of additional layers. Therefore, upon melting and cooling bigger particles of Ni cause higher stresses on the YSZ substrate due to thermal expansion coefficient mismatch between Ni and YSZ (13.3×10^{-6} and $8 \cdot 10^{-6} \text{ K}^{-1}$, respectively). Higher stresses associated with differences in thermal expansion coefficients can result in micro-cracks, which eventually may exceed the critical length for crack propagation.

It thus becomes clear that there is a trade-off between sufficient laser power (that causes the powder to partially or fully melt), on one hand, and an energy density limit (above which there are significant thermal stresses affecting bulk integrity), on the other.

Microstructure characterisation of laser sintered electrodes in Step II

Figure 5.8a and Figure 5.8b show SEM micrographs of the Ni patterned electrode surface corresponding to samples 2.2 and 4.2, respectively. The samples were laser sintered in identical conditions (laser power 120 W and laser speed 4000 mm/sec); the difference between the two is that in sample 4.2 the substrate was pre-metallised with Ni by sputtering.

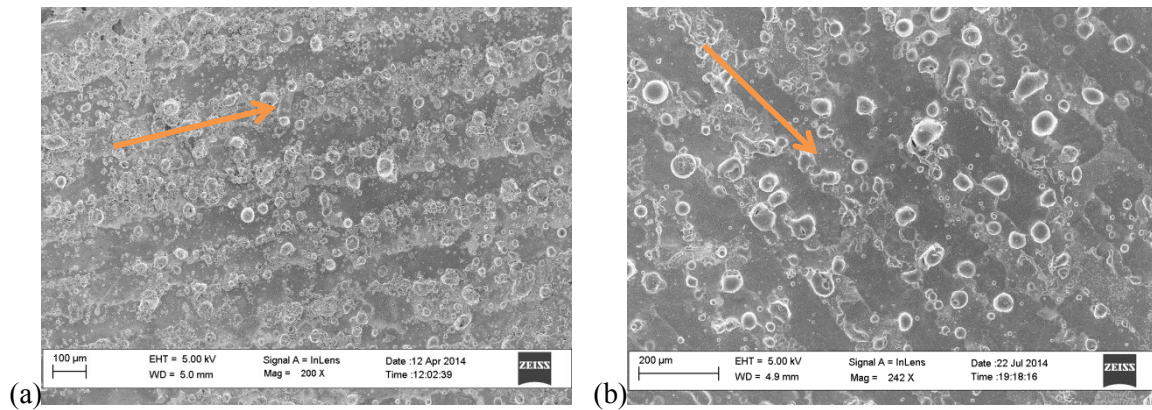


Figure 5.8. The surface of the laser sintered patterned fuel electrodes with (a) non-metallised YSZ surface (Sample 2.2) and (b) pre-metallised YSZ surface (Sample 4.2).

In both electrodes (Figure 5.8a-b) the pattern of about 100 µm wide sintered stripes can clearly be seen, however the edge of the stripes and their surface is not homogeneous. In addition, in both samples the pattern includes multiple separated Ni particles forming ‘balls’ of up to 50 µm in diameter. Balling is a well-known phenomenon associated with the DMLS process (2, 16, 18-20). Balling occurs when the molten material does not wet the underlying substrate. In the system where solid, liquid and gaseous phases come in contact, the equilibrium on the triple line will occur according to the Young equation (Figure 5.9a), where σ_{sv} , σ_{lv} and σ_{sl} are surface energies of solid, liquid and gas phase, respectively, and θ is a contact angle (21). When the total surface of the molten pool becomes larger than that of a sphere with the same volume, the balling effect takes place (Figure 5.9b). Thus, the laser parameters should be selected in such a way that the length to diameter ratio of the molten pool is as small as possible (16).

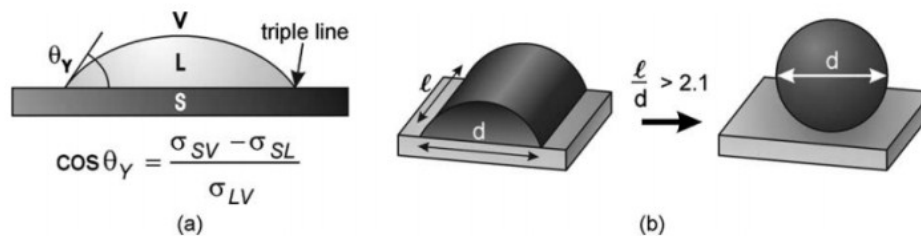


Figure 5.9. (a) Wetting of a liquid on a solid substrate and the Young equation with σ_{sv} , σ_{sl} and σ_{lv} the surface free energies of the solid-vapour, solid-liquid and liquid-vapour interfaces, respectively; (b) transition from half cylinder to sphere depending on the dimensions of the molten laser pool (16).

A process window for laser sintering iron-based powder was experimentally identified as shown in Figure 5.10 (16). It suggests that ‘balling’ phenomenon occurs at low laser speeds and high laser powers.

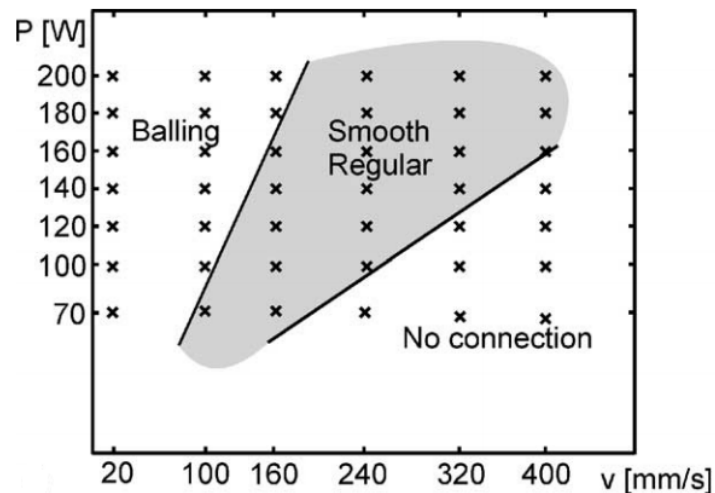


Figure 5.10. Process window for iron-based powder (16).

According to the SEM images it was hard to tell the differences between the single layer and the multilayer structures, mainly due to the ‘balling’ phenomenon.

The micro-cracks were detected in all samples, independently of laser parameters or pre-metallisation of YSZ surface. The possible reasons for micro-cracking have been discussed in the results of Step I. The effect of pre-metallisation of the YSZ surface is discussed in detail in the results of Step III.

Conclusions of Step II

The main conclusions of Step II can be summarised as follows:

- It was discovered that using 0.05 J/mm and higher laser energy densities caused the YSZ substrate to break, when attempting to laser sinter more than one layer. Two failure mechanisms were suggested. First, the intensity of thermal stresses accumulation in each run, which subsequently can lead to a critical crack length. Second, the increasing mismatch

between YSZ and Ni due to Ni particle growth with every additional sintered layer leading to cracking. These two mechanisms could both take place at the same time.

- A trade-off should be maintained between sufficient laser power (that causes the powder to partially or fully melt) and laser energy density limit (above which significant thermal stresses accumulation affects bulk integrity).
- The results suggest that the maximum laser energy of 0.03 J/mm, comprised of 120 W laser power and 4000 mm/sec laser speed, seem to be acceptable parameters for cell fabrication, at least as long as up to three laser sintered Ni layers are concerned.
- From microstructural examination it can be concluded that the patterned electrode is prone to a balling phenomenon. Poor wettability can account for the balling phenomenon in this particular system. In general the wettability can be improved by small additions of materials that reduce surface energy (such as phosphorous). In our case the selection of materials would be dictated by the application. Pre-metallisation of the YSZ surface with sputtered Ni was suggested to improve wettability and adhesion between Ni and YSZ. The results will be discussed further in Step III.
- Further optimisation of the process parameters is required to decrease the balling phenomenon. The optimisation of parameters would be limited by the trade-off between laser power and energy density, as discussed above.

5.4.4. Step III – full cell preparation and electrochemical testing

Design of experiments in Step III

In this stage a full fuel cell with patterned laser sintered anode was fabricated and tested to obtain initial electrochemical results. For this purpose the LSCF-GDC counter (11 mm in diameter) and reference (16 and 18 mm inner and outer diameters) electrodes were first screen printed on the YSZ electrolyte as described in section 3.2.2. Then the patterned electrode (11 mm in diameter) was laser sintered on the other side of the substrate, as illustrated in Figure 5.11.

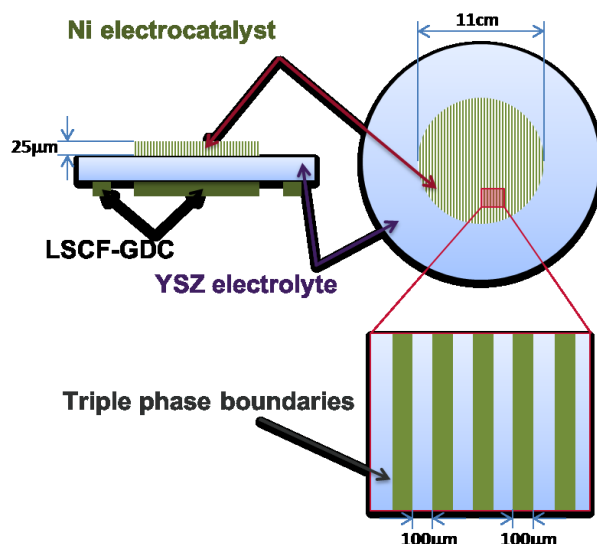


Figure 5.11. Diagram of the YSZ pellet with screen-printed LSCF-GDC air electrode on one side and patterned laser sintered Ni electrode on the other side; dimensions are included.

The arrangement and the labelling of samples in the chamber during laser sintering in detailed in Table 5.10.

Table 5.10. Matrix of samples and details of experiments in Step III (full cell preparation).

| Row number | Number of layers (L) | (Lateral) Energy Density [Wsec/mm=J/mm] | | | |
|------------|-------------------------------------|---|----------------------------------|----------------------------------|----------------------------------|
| | | 0.02 | 0.03 | 0.04 | 0.05 |
| R1 | L=1 | 1.1 S1=6000mm/sec P1=120W | 1.2 S2=4000mm/sec, P2=120W | 1.3 S3=3000mm/sec, P3=120W | 1.4 S4=2400mm/sec, P2=120W |
| R2 | L=2 | 2.1 | 2.2 (Tested) | 2.3 | 2.4 |
| R3 | L=3 | 3.1 | 3.2 | 3.3 | 3.4 |
| R4 | L=2; pre-metallised substrate | 4.1 | 4.2 (Tested) | 4.3 | 4.4 |

The laser sintering conditions in Table 5.10, i.e. number of layers and laser properties (laser speed ($S1-S4$) and laser power ($P1-P4$)), were chosen according to the results of the previous experiments. The judgment of the results was based upon visual inspection only according to criteria listed in Step I. This was due to time limitations and lack of equipment availability, so laser sintering in Step II and Step III needed to be carried out on the same day. There were some overlaps in laser parameters used in between the steps (Table 5.9 and Table 5.10) to explore repeatability. The laser properties listed in the first row of Table 5.10 (R1) were kept the same for the samples of the same

column. Additionally, the surface of the samples in R4 was sputtered with Ni to form a thin metal layer as described in Step II.

The electrochemical performance of laser sintered electrodes was tested in Samples 2.2 (R2) and 4.2 (R4) as marked in Table 5.10. The impedance spectra (100 mHz – 100 kHz) and i - V curves were measured in three electrode set-ups (as was explained in section 3.4.4) in a humidified 50% H₂ – 50% N₂ atmosphere at 600 – 700 °C. Current collection was provided through silver paste.

Since the full cells were prepared on the same day as sub-samples in Step II, the micro-cracks were detected *post factum*. As was discussed in the results of Step I, the damaged region of the sample fabricated with 0.05 J/mm was about 20 – 30 μm. It is therefore expected that the damaged region of the fuel cells fabricated with lower energy density (0.03 J/mm) will be even smaller. Despite the micro-cracks, it was decided to proceed with full cell electrochemical testing, as discussed in the following section.

Electrochemical performance of laser sintered patterned electrodes

The OCP was close to its theoretical value during the cell tests at the considered temperatures. This is a good indication that no macro-cracking of the electrolyte had occurred, which otherwise would have led to a decrease in OCP due to gas crossover. The i - V curve of the laser sintered patterned electrode (Sample 2.2 from Table 5.10), normalised to the unit length of the triple phase boundary, is shown in Figure 5.12.

The total length of triple phase boundaries of the patterned electrode was estimated assuming that the interface line between YSZ and Ni is perfectly straight and continuous. A schematic representation of the patterned electrode is shown in Figure 5.11. The width of each stripe is 100 μm and the distance between two neighbouring stripes (i.e. hatch spacing) is 100 μm, the diameter of the entire electrode is 11 cm. Based on these dimensions, the total length of the TPB was calculated to be 0.96 m and the TPB length per unit area is therefore 1.01×10^4 m/m². TPB density of the same order of magnitude was previously reported in patterned electrodes (8.7×10^4 m/m²) (22). However, the actual

TPB length in our electrodes is likely to be larger due to micro-scale roughness of the Ni/YSZ interface. Ni micro-particles that are not interconnected with the main pattern will further increase the total TPB length. However, it should be noted that these are likely not to be active, unless in direct contact with the current collector.

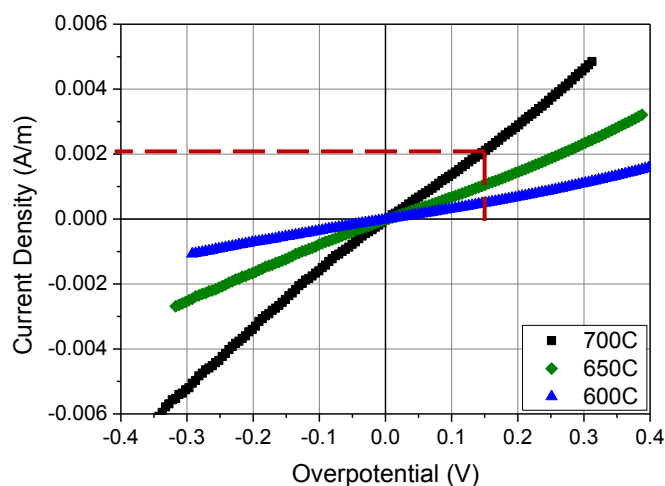


Figure 5.12. Current linear density (per unit length of TPB) vs overpotential of the cell with laser sintered patterned electrode (Sample 2.2), as measured between the reference and the working electrodes (the voltage drop includes the contributions from the infiltrated electrode and the uncompensated iR drop between the RE and WE). The cell was tested in humidified 50% H_2 – 50% N_2 under OCP in a 600-700 °C temperature range. Parameters for electrode fabrication are Energy Density = 0.03 J/mm (Laser Speed = 4000 mm/sec, Laser Power = 120 W).

In order to compare the performance of the patterned electrode and the conventional Ni/YSZ porous electrode, the area specific resistance (ASR) of the latter should be converted to a linear specific resistance (LSR), i.e. resistance per unit of TPB length. It is possible to estimate LSR [Ωm] using the TPB density (l_{TPB} [m/m^3]) and the thickness of the porous electrode (d [m]) according to 5.5:

$$LSR = ASR \cdot \frac{l_{TPB}V}{A} = ASR \cdot \frac{l_{TPB}Ad}{A} = ASR \cdot l_{TPB} \cdot d \quad 5.5$$

where A is the area of the electrode and V is the overpotential. Kishimoto *et al.* have calculated the overpotentials for Ni-YSZ porous electrodes in the range between 800 °C and 1000 °C (23). These results are shown in Figure 5.13 and are used to benchmark the polarisation of the patterned electrodes obtained in the present work. Values of l_{TPB} and d for Ni-YSZ porous electrode obtained by Kishimoto *et al.* are listed in Table 5.11. The ASR value is estimated from Figure 5.13 for the

electrode exposed to humidified H₂ at 800 °C while the cell was biased, so that the current density is 150 mA/cm².

Table 5.11. Parameters for Ni-YSZ cermet electrode taken for calculation of LSR (23).

| Parameter [units] | Value |
|--|----------------------|
| l_{TPB} [m/m ³] | $2.49 \cdot 10^{12}$ |
| d [m] | $5.0 \cdot 10^{-5}$ |
| ASR [Ωm^2] @ 800 °C $\Delta V=0.1$ V | $6.7 \cdot 10^{-5}$ |

In the present study, the patterned electrodes were tested at 700 °C and therefore the results cannot be directly compared to the results obtained for porous Ni/YSZ electrodes by Kishimoto *et al.* However, Suzue *et al.* have shown that there is almost linear dependence of the overpotentials of Ni/YSZ porous electrodes with working temperature at high current densities (24). The overpotential at 1 A/cm² was found to increase ca 1.5 times when the temperature was decreased from 800 °C to 700 °C (24).

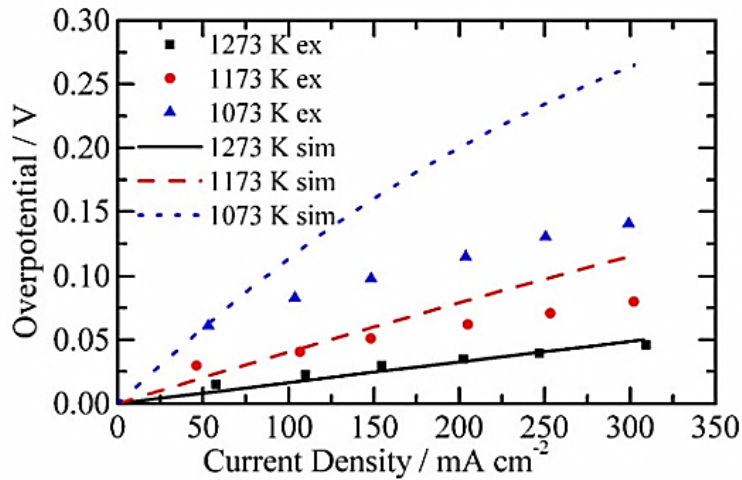


Figure 5.13. Ni-YSZ anode overpotentials in various temperatures at 3% humidified condition (23).

It is, therefore, reasonable to assume that the overpotentials obtained by Kishimoto *et al.* for porous electrodes at 800 °C would translate into ca 1.5 larger overpotentials at 700 °C, such that the overpotential at 150 mA/cm² would be ~0.15 V. Therefore the LSR of the Ni-YSZ porous electrode is:

$$LSR = ASR \cdot l_{TPB} \cdot d = \frac{0.15}{1500} \cdot 2.49 \cdot 10^{12} \cdot 5 \cdot 10^{-5} = 1.25 \times 10^4 \Omega\text{m} \quad 5.6$$

The current per unit of TPB length in the patterned electrode is 2×10^{-3} A/m when the overpotential is 0.15 V as shown in Figure 5.12. Therefore, the *LSR* for the patterned electrode is equal to 75 Ω m. The difference in the *LSR* between the cermet and the patterned Ni-YSZ electrodes is three orders of magnitude and that requires further analysis.

The discrepancy in the *LSR* values of the patterned and the porous electrodes is likely to be the result of several factors. First, the active volume of the porous electrodes is limited to few microns next to the electrolyte as discussed in literature review (section 2.7.1). In other words, even though a porous electrode may have much longer TPB lines due to its thickness, only a fraction of the TPB lines will participate in the electrochemical reaction. Assuming that only 20% of the electrode thickness is active, the *LSR* of the porous cermet electrode is further reduced to $1.25 \times 10^4 \times 0.2 = 25 \times 10^2$ Ω m. Second, part of the TPB lines in active region of the porous electrode may become inactive due to the restricted gas access and imperfect connectivity of the Ni network. Although Kishimoto *et al.* (23) found that the connectivity of the phases was relatively good in their electrode – the amount of the isolated (inactive) Ni phase was only ~8% – this value may vary in different electrodes. Therefore, the length of the active TPB in a real porous cermet electrode is lower than the total calculated TPB. This leads to a lower value of *LSR* per the unit of TBP length.

On the other hand, when the patterned electrode is considered, it should be taken into account that the interface between Ni and YSZ will not be perfectly linear in a real electrode. The interface roughness will result in a larger TPB length, as was previously mentioned. Consequently, the *LSR* of the patterned electrode is likely to be underestimated in the calculations above, and the *LSR* of the porous electrodes are likely to be overestimated, at least as far as the active TPB length is concerned. By addressing all these issues it may be possible to eliminate the discrepancy in *LSR* between the patterned and porous electrodes.

Figure 5.14 shows the impedance spectra of the patterned electrodes measured in three electrode configurations, i.e. between working (WE) and reference electrodes (RE). The results in Figure 5.14a correspond to the Ni electrode that was laser-sintered directly on YSZ surface. The spectra in Figure 5.14b are for the Ni patterned electrode that was sintered on a pre-metallised YSZ surface, i.e.

a thin Ni layer (ca 50 nm) was sputtered on the entire surface of the substrate before laser-sintering the electrode. In both cases the impedance spectra were normalised to the unit length of TPB as was discussed in the previous paragraphs. The value of the series resistance was normalised to zero to compensate for the variable uncompensated iR drop between the RE and WE under different conditions and to enable a clear comparison between the samples.

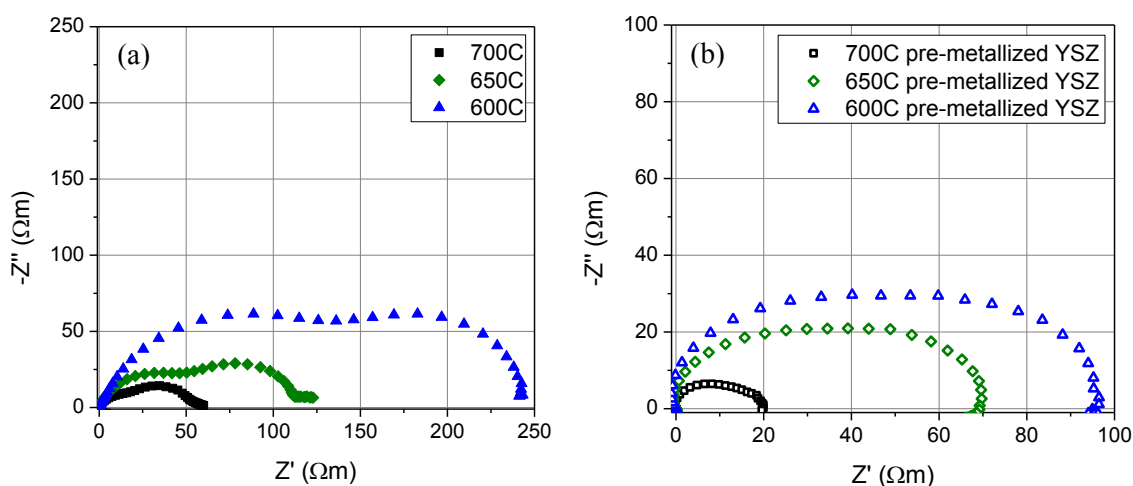


Figure 5.14. Galvanostatic impedance spectra (100 mHz-100 kHz) of the laser sintered patterned electrodes normalised for length of TPB on (a) YSZ substrate (Sample 2.2) and on (b) YSZ substrate pre-metallized with Ni (Sample 4.2), tested in humidified 50% H_2 – 50% N_2 under OCP over a 600-700 °C temperature range, as measured between reference and working electrodes. Conditions for both electrodes fabrication are Energy Density = 0.03 J/mm (Laser Speed = 4000 mm/sec, Laser Power = 120 W).

The electrodes which were used to obtain spectra in Figure 5.14 were laser-sintered using the following parameters: 4000 mm/sec laser speed and 120 W of laser power. At all temperatures, the polarisation of the electrode sintered on the pre-metallised YSZ surface was two times lower than the polarisation of the electrode sintered without pre-metallisation of the YSZ surface. Since both electrodes were prepared with the same laser parameters, the difference in the electrodes polarisation may originate from a different TPB length. SEM-EDX analysis have been performed in order to gain better understanding of the morphological differences between the electrodes sintered on the pre-metallised and bare YSZ surfaces. Figure 5.15 compares SEM micrographs and EDX maps of Ni distribution on the pre-metallised YSZ surface (Figure 5.15a-d) and the surface without pre-metallisation (Figure 5.15e-f).

Figure 5.15a-b shows that Ni (green) on the pre-metallised YSZ surface is well interconnected and forms a relatively well defined pattern. However, the interface between Ni and YSZ is very rough (Figure 5.15c-d), which confirms our previous hypothesis pertaining to the TPB length calculation.

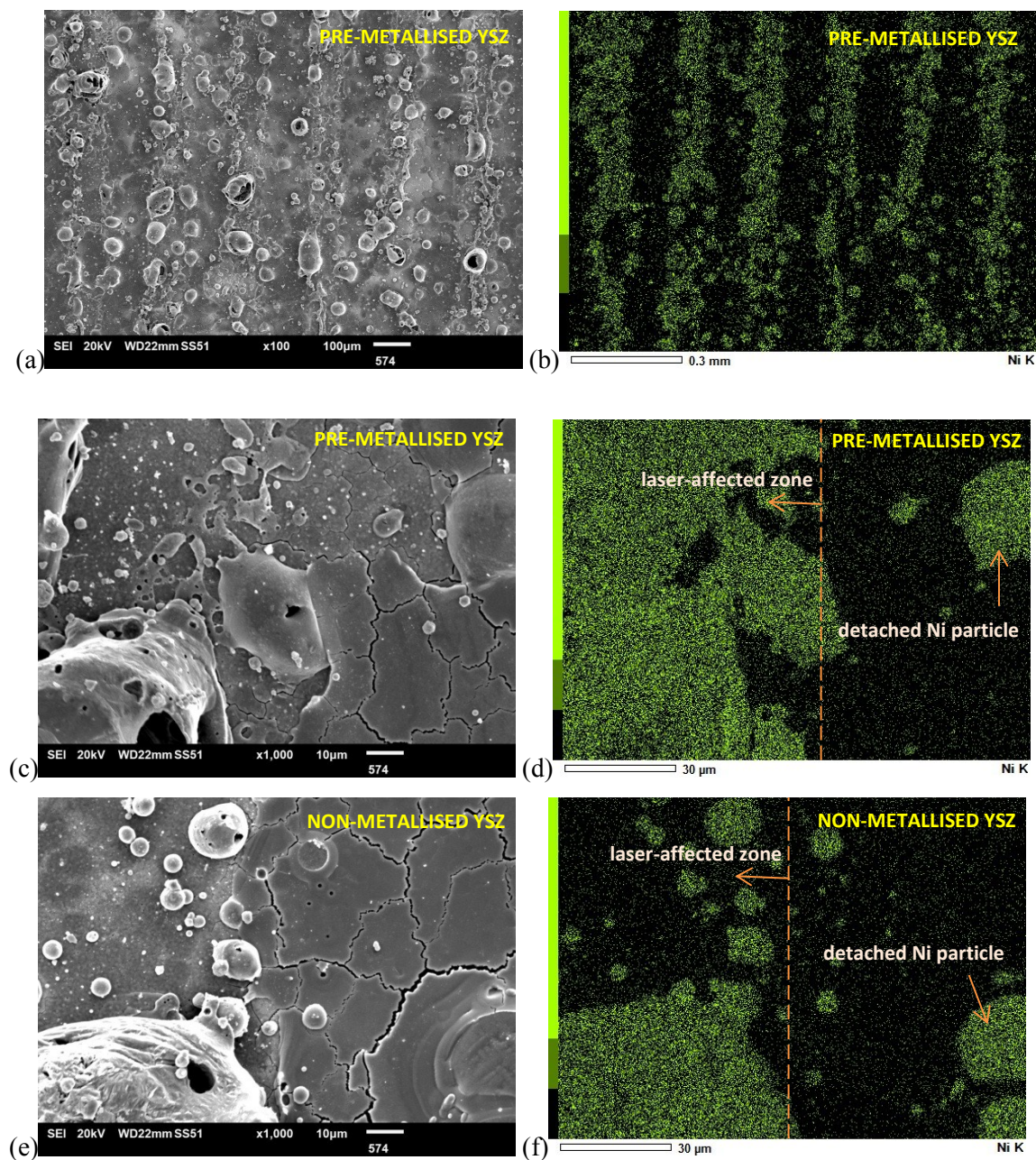


Figure 5.15. (a) – (d) Laser sintered Ni pattern on pre-metallised YSZ surface, (a) and (c) SEM image; (b) and (d) SEM-EDX map of Ni distribution (green); (e) – (f) Laser sintered Ni pattern on non-metallised YSZ surface, (e) SEM image, (f) SEM-EDX map of Ni distribution (green).

In contrast, the pattern created on the non-metallised YSZ surface is not well defined and the Ni is not interconnected, forming ‘islands’ on the YSZ surface, which are likely to be electrochemically

inactive (Figure 5.15e-f). Therefore, the active TPB length is likely to be shorter than that calculated, causing the difference in polarisation values (Figure 5.14).

The SEM-EDX analysis suggests that the Ni patterns sintered on the pre-metallised YSZ surface are better defined and more continuous than those laser sintered on the non-metallised YSZ. This may imply that the bonding between the sputtered Ni and the Ni particles within the powder used for laser sintering facilitates a better Ni adhesion to the substrate. To verify this further study is required. Still, the TPB lines in Figure 5.15b appear to have very irregular shape, compared to a shape of patterned Ni electrodes on YSZ obtained elsewhere (22, 25-27), so that it is difficult to assume them as lines. This further supports the assumption that *LSR* of the patterned electrode calculated above is likely to be underestimated.

Detached Ni particles were also found in the surface that was not affected by laser heat (Figure 5.15d,f). This can be as a result of vaporization (28). During laser sintering the temperature of the exposed powder particles exceeds the melting point (1453 °C for Ni) under high power densities. A further increase of the temperature can cause the material to evaporate. The rapidly moving evaporated powder particles expand and generate a recoil pressure on the molten pool. Under high pressures material expulsion occurs, which may lead to the anchoring of detached particles at some distance from the molten pool (16).

Conclusions of step III

The main conclusions from Step III can be summarised as follows.

- The full cells with patterned Ni fuel electrode (laser sintered with 120 W laser power and 4000 mm/sec laser speed), YSZ electrolyte and LSCF-GDC air electrode were successfully fabricated and tested in H₂-N₂ environment and 600-700 °C temperature range. The results of electrochemical performance and SEM-EDX mapping of Ni distribution of two cells, with pre-metallised and non-metallised YSZ surface, were compared.

- Discrepancies in the *LSR* values between patterned and porous electrodes can be related to the difficulty in estimating accurately an effective TPB length in a patterned electrode, as well as determining the amount of active TPBs in a porous electrode.
- SEM-EDX mapping results suggest that pre-metallisation of the YSZ substrate favours the formation of more defined and continuous Ni pattern and facilitates better adhesion. This can be attributed to the bonding between Ni layer sputtered on the YSZ and Ni within the powder layer during laser sintering. This requires further investigation.
- The fact that micro-cracks were introduced to the substrate surface during the laser sintering questions the cell suitability for a long-term use. This requires further research.

5.5 Overall conclusions

To link conclusions to the objectives, the study was summarised in Table 5.12.

Table 5.12. Conclusions from the study linked to the objectives.

| |
|---|
| <p>Objective N1: To examine the feasibility of using DMLS for fuel cell preparation in the Ni-YSZ (powder) / YSZ (substrate) system.</p> <ul style="list-style-type: none"> • Full cells with a patterned Ni fuel electrode (laser sintered with 120 W laser power and 4000 mm/sec laser speed), YSZ electrolyte and LSCF-GDC air electrode were successfully fabricated and tested in a H₂-N₂ environment and over a 600-700 °C temperature range. • The fact that micro-cracks were introduced to the substrate surface during the laser sintering questions the cell suitability for a long-term use. This requires further research. |
| <p>Objective N2: To explore the relationship between process parameters, microstructure and electrochemical performance of the cell.</p> <ul style="list-style-type: none"> • Although Ni and YSZ form unique structures during laser sintering, they were not mixed together to obtain a cermet network. This may be due to de-wetting and differences in optical properties influencing interaction with the laser beam. • Micro-cracks were observed on all substrates; however the damage caused to the substrate |

decreased with decreasing laser energy density. YSZ is expected to withstand cracks less than 18 μm in length.

- It is likely that cracking in YSZ occurs due to thermal shock and mismatch between thermal expansion coefficients of YSZ and Ni.
- The patterned electrode is prone to a balling phenomenon. Poor wettability may account for the balling phenomenon in this particular system. Pre-metallisation of the YSZ surface with sputtered Ni was suggested to improve wettability and adhesion between Ni and YSZ.
- SEM-EDX mapping suggests that pre-metallisation of the YSZ substrate favours the formation of more defined and continuous Ni pattern and facilitates better adhesion between Ni and YSZ. This can be attributed to the bonding between Ni layer sputtered on the YSZ and Ni within the powder layer during laser sintering. The mechanism requires further investigation.
- Discrepancies in the *LSR* values between patterned and porous electrodes can be related to the difficulty in estimating accurately an effective TPB length in patterned electrodes as well as the amount of active TPBs in porous electrodes.

Objective N3: To identify effective processing parameters for electrode fabrication using DMLS.

- The YSZ substrate could withstand a laser energy density of 0.05 J/mm or less. Under the same energy density, the samples were conductive only when the power was 120 W or higher. This is likely due to sufficient heat generated to (fully or partially) melt the powder to create a continuous metallic pattern.
- It was discovered that 0.05 J/mm laser energy density caused the YSZ substrate to break, when attempting to laser sinter more than one layer. Two mechanisms were suggested. First, the intensity of thermal stresses accumulating in each run can subsequently lead to a critical crack length. And second, the increasing mismatch between YSZ and Ni due to Ni particle growth with every additional sintered layer may lead to the formation of a critical crack length and its propagation through the substrate. Both mechanisms could occur.

- A careful balance should be maintained between sufficiently high laser power to melt Ni particles (i.e. > 120 W) and sufficiently low laser energy density to prevent the accumulation of thermal stresses in YSZ (i.e. < 0.05 J/mm). As a consequence of this trade-off, only a narrow laser parameter window was found to be effective for the studied system (Ni powder - YSZ substrate).
- The results suggest that the maximum laser energy of 0.03 J/mm, combined with 120 W laser power and 4000 mm/sec laser speed, seem to be acceptable parameters for full cell fabrication, at least as long as up to three laser sintered Ni layers are concerned.
- Further optimisation of the laser parameters window is required to decrease the balling and evaporation phenomena.

References for Chapter V

1. A. Simchi, *Materials Science and Engineering a-Structural Materials Properties Microstructure and Processing*, **428**, 148 (2006).
2. I. Gibson, D. Rosen and B. Stucker, *Additive Manufacturing Technologies. Rapid Prototyping to Direct Digital Manufacturing*, Springer US (2010).
3. K. T. Faber, M. D. Huang and A. G. Evans, *Journal of the American Ceramic Society*, **64**, 296 (1981).
4. H. Hayashi, T. Saitou, N. Maruyama, H. Inaba, K. Kawamura and M. Mori, *Solid State Ionics*, **176**, 613 (2005).
5. User's Manual Chapter 17 Material Expansion Coefficients, in, database Editor, The University of Chicago
6. J. Kondoh, H. Shiota, K. Kawachi and T. Nakatani, *Journal of Alloys and Compounds*, **365**, 253 (2004).
7. A. Selçuk and A. Atkinson, *Journal of the European Ceramic Society*, **17**, 1523 (1997).
8. A. J. A. Winnubst, K. Keizer and A. J. Burggraaf, *Journal of Materials Science*, **18**, 1958 (1983).
9. G. Fargas, D. Casellas, L. Llanes and M. Anglada, *Journal of the European Ceramic Society*, **23**, 107 (2003).
10. J. Manara, M. Arduini-Schuster, H. J. Rätzer-Scheibe and U. Schulz, *Surface and Coatings Technology*, **203**, 1059 (2009).

11. K. W. Schlichting, N. P. Padture and P. G. Klemens, *Journal of materials science*, **36**, 3003 (2001).
12. D. Jones and M. Ashby, *Engineering Materials Volume 2, An Introduction to Microstructures, Processing and Design*, Butterworth Heineman, Oxford (1998).
13. D. L. Wood and K. Nassau, *Appl. Opt.*, **21**, 2978 (1982).
14. A. D. Rakic, A. B. Djuricic, J. M. Elazar and M. L. Majewski, *Appl. Opt.*, **37**, 5271 (1998).
15. B. Qian, L. Taimisto, A. Lehti, H. Piili, O. Nyrhilä, A. Salminen and Z. Shen, *Journal of Asian Ceramic Societies*, **2**, 123 (2014).
16. J. P. Kruth, L. Froyen, J. Van Vaerenbergh, P. Mercelis, M. Rombouts and B. Lauwers, *Journal of Materials Processing Technology*, **149**, 616 (2004).
17. P. Nikolopoulos and D. Sotiropoulou, *J Mater Sci Lett*, **6**, 1429 (1987).
18. R. Li, J. Liu, Y. Shi, L. Wang and W. Jiang, *Int J Adv Manuf Technol*, **59**, 1025 (2012).
19. M. Islam, T. Purtonen, H. Piili, A. Salminen and O. Nyrhilä, *Physics Procedia*, **41**, 835 (2013).
20. H. J. Niu and I. T. H. Chang, *Scripta Materialia*, **41**, 1229 (1999).
21. N. Eustathopoulos, M. G. Nicholas and B. Drevet, *Wettability at High Temperatures*, Pergamon Press, Oxford (1999).
22. W. G. Bessler, M. Vogler, H. Stormer, D. Gerthsen, A. Utz, A. Weber and E. Ivers-Tiffée, *Phys Chem Chem Phys*, **12**, 13888 (2010).
23. M. Kishimoto, H. Iwai, M. Saito and H. Yoshida, *Journal of Power Sources*, **196**, 4555 (2011).
24. Y. Suzue, N. Shikazono and N. Kasagi, *Journal of Power Sources*, **184**, 52 (2008).
25. A. Utz, H. Störmer, A. Leonide, A. Weber and E. Ivers-Tiffée, *Journal of The Electrochemical Society*, **157**, B920 (2010).
26. R. Radhakrishnan, A. V. Virkar and S. C. Singhal, *Journal of The Electrochemical Society*, **152**, A210 (2005).
27. A. Bieberle, L. P. Meier and L. J. Gauckler *Journal of The Electrochemical Society*, **148**, A646 (2001).
28. M. V. Allmen, *Laser-beam Interactions with Materials*, Springer-Verlag, Berlin (1987).

GENERAL CONCLUSIONS AND OUTLOOK

6.1 General conclusions and significance of this study

In order to create high performance ‘electrodes by design’ the relationship between the fabrication routes and the performance of the electrode needs to be established. This research explored the novel fabrication techniques for Ni-based SOC electrodes. It was demonstrated that this approach provides greater control over the electrode performance through adjustment of the process parameters.

Infiltrated electrodes

Fuel electrodes were fabricated by infiltration of Ni nano-particles into GDC porous scaffolds in the first part of present study. It was experimentally demonstrated in this work that the pore size and the amount of catalytic/metal phase in infiltrated electrodes can be independently controlled. The direct consequence of this is greater control of the electrode design and therefore a potential for the performance optimisation. Previous studies of infiltrated electrodes only report the results for the systems with relatively small amounts of infiltrated material that is not percolated (1). Here, it is demonstrated that the infiltration of GDC scaffold with 25 wt% of Ni leads to electrical conductivity similar to conventional cermet electrodes with Ni content of 35 wt%. This study also provides insights into the effect of different microstructural factors (e.g. porosity, pore size, Ni content) and operation parameters (temperature, gas concentration, duration) on the performance of infiltrated electrodes, as discussed below.

The effect of porosity on the electrode performance has been demonstrated by infiltrating two GDC scaffolds – one with only micro-porosity and the other with combined macro- and micro-porosity – with Ni-nanoparticles. It was found that the sample with macro pores exhibited lower diffusion resistance. The study explores the microstructure development during multiple Ni infiltrations of GDC scaffolds using 2-D and 3-D imaging. The experimental results of this research provided data for 3-D image reconstruction quantitative analysis (2) and modelling of infiltration electrodes performance (3-6). For the first time the 3-D image reconstruction quantitative analysis was applied to characterise the microstructure of infiltrated electrodes. The 3D image reconstruction was carried out by Dr. Masashi Kishimoto. The effect of Ni content of the performance of the electrode was studied by testing several electrodes after different number of infiltrations. FIB-SEM analysis of these samples demonstrated that even a single infiltration results in a 5 times larger TPB density compared to the conventional electrodes.

The electrochemical performance of the infiltrated electrodes, as well as short-term degradation in different concentrations of H₂ was reported for the temperature range of 550-750 °C. At 750 °C under the flow of 50% H₂-50% N₂ the ASR of the infiltrated electrode was found to be 0.14 Ω·cm², which is comparable to state-of-the-art Ni-YSZ anodes. It should, however, be noted that careful optimisation of all parameters has the potential to significantly improve the performance of Ni infiltrated GDC electrodes. The results of short-term degradation studies suggest that the degradation in Ni infiltrated GDC electrodes is driven primarily by agglomeration of Ni particles and subsequent loss of TPBs. The loss of TPBs can be compensated by the mixed-conducting nature of the GDC scaffold to a certain extent. However, the Ni coarsening may become a significant contributor to the electrode degradation when a long-term performance is considered. It is emphasized in the study that the combination of Ni and GDC has synergetic effects, not only in terms of catalytic properties, but also in terms of the electrodes electronic conductivity.

Finally, infiltrated electrodes were shown to be suitable for the study of carbon deposition mechanisms by Raman spectroscopy. This research was performed by Vlad Duboviks and reported elsewhere (7). In brief, the electrodes were found resistant to carbon deposition under the mixture of

CO₂ and CO at OCP, however adding significant amount of CH₄ facilitated carbon deposition in the bulk of the electrode. Cu-infiltrated GDC electrodes were found resistant to carbon formation in both CO₂-CO and CO₂-CH₄ gas mixtures. While copper is known to be resistant towards carbon formation, its relatively low melting temperature inhibiting high temperature sintering was preventing its application in SOC electrodes. Since the metal infiltration technique avoids high sintering temperatures, Cu-GDC electrodes can potentially be used for upgrading biogas via CO₂ electrolysis without causing deleterious carbon deposits. The results of these studies are beyond the scope of this thesis, though mentioned here to emphasize the impact of the present study.

Laser-sintered electrodes

Results of the feasibility study of using a direct metal laser sintering (DMLS) technique for electrode fabrication were reported in Chapter V. The heat generated by plasma from laser-powder interactions was used to sinter Ni patterns on the YSZ substrate. The findings of the parametric study described in Chapter V helped to identify the window of parameters suitable for Ni patterned electrodes fabrication by establishing a relationship between laser parameters and the resulting electrode microstructure.

Patterned Ni fuel electrode was successfully laser sintered on YSZ electrolyte using 120 W laser power and 4000 mm/sec laser speed. LSCF-CGO air electrode was screen printed on the other side of the electrolyte to form the full cell. The cell was successfully tested in a H₂-N₂ environment over a 600-700 °C temperature range. However, the fact that micro-cracks were introduced into the substrate surface during the laser sintering questions the cell suitability for a long-term use. It was found that there is a poor adhesion between Ni particles and YSZ substrate, probably due to poor wettability between the materials. Pre-metallisation of the surface with sputtered Ni was suggested to improve the bonding.

It was shown that a careful balance should be maintained between sufficiently high laser power to melt Ni particles (i.e. > 120 W) and sufficiently low laser energy density to prevent the accumulation of thermal stresses in YSZ (i.e. < 0.05 J/mm). As a consequence of this trade-off, only a narrow laser parameter window was found to be effective for the studied system (Ni powder - YSZ

substrate). Further optimisation of the laser parameters window is required to decrease the Ni balling and evaporation phenomena. The main challenges associated with laser sintering in the Ni-YSZ system are a mismatch in thermal expansion coefficients between Ni and YSZ, poor wettability between them, as well as the build-up of thermal stresses in YSZ substrate. In a real fuel cell, this may lead to YSZ electrolyte fractures during operation and therefore the failure of the cell.

6.2 Outlook

While considerable progress has been achieved in this research, several challenges associated with ‘electrode by design’ approach and, specifically, with infiltrated or laser sintered electrodes still remain to be solved. Future research should be built upon the results obtained in the present study. The following key directions are identified for future investigation.

Infiltrated electrodes

1. Standardisation of experimental procedure. The infiltration method of electrode preparation includes many variables, including concentration of the solution, solvent, temperature and duration of the decomposition, amount of infiltrating solution used in one infiltration repetition, etc. Therefore, the resultant microstructure will be sensitive to these parameters. To avoid variations associated with fabrication method, and to enable comparison between different studies, it is desirable to devise a standard procedure to be used for the infiltration method.

2. Agglomeration of nickel nano-particles in infiltrated electrodes. One of the main concerns raised in the present study was Ni agglomeration and coarsening. These may lead to a loss of TPBs and open porosity blockage that in turn may result in decreased electronic conductivity of the electrode and increased mass diffusion polarisation. Therefore, a strategy to restrict Ni particle agglomeration is required. The research can be focused on co-infiltration of oxides particles that were proven to pin Ni particles and to restrain coarsening (8). In addition, it was discussed that the mobility of Ni particles may be a consequence of low wettability between the ceramic scaffold and the metallic phase. Hence, finding a way to improve wettability may decrease unwanted agglomeration.

3. Decreasing fabrication time. Infiltration is a time consuming process. Fabrication time becomes an important factor when scalability is concerned. It is desirable, therefore, to look for fabrication techniques that will be faster, and at the same time will enable the microstructural benefits to be attained. For instance, promising alternatives to infiltration are electroless/electrolytic deposition and microwave assisted infiltration for SOC electrode fabrication. These techniques are under extensive research in the Imperial College group.

4. Understanding processes affecting electrode performance. It is essential to enhance fundamental understanding of the processes that account for electrode resistance. Specifically, there is a difficulty to quantitatively assign impedance arcs seen with GDC scaffolds to specific process(es) with high certainty, especially in the low frequency range.

5. Developing a suitable porosity in the scaffold. As was discussed in Chapter IV the scaffold plays a crucial role in microstructure optimisation. Specifically, the finding suggests that (a) there is a certain amount of porosity and pore size that should be maintained in infiltrated electrodes, and (b) there is a certain level of infiltration that may be tolerated by a scaffold with certain porosity to achieve an optimum performance. Therefore, the optimal ratio between the porosity fraction, pore size and the infiltrated phase fraction can be further modelled and verified experimentally.

6. Testing infiltrated electrodes with other fuels. The presented study concentrated on the electrode performance in H₂ environments. However, it would be useful to study the performance of Ni infiltrated GDC electrodes with other fuels, for example hydrocarbons (natural gas, biofuels, etc).

7. Testing infiltrated electrodes in electrolysis mode. In the present study the cell was operated in electrolysis mode with 3% H₂O. It would be useful to study the performance of Ni infiltrated GDC electrodes for (co-)electrolysis of CO₂ and/or H₂O to form syngas (H₂ and CO) and/or H₂. It could be of particular interest to test infiltrated electrodes in electrolysis mode with CH₄ and CO₂ as a potential route for biogas upgrade (9).

8. Long term degradation study. In this study, short term degradation tests in H₂ environment were carried out. It would be valuable to assess the performance of infiltrated electrodes over the long-term.

Laser sintered electrodes

In general, the use of laser sintering technique seems to be challenging for direct laser sintering of Ni or Ni-YSZ powders on YSZ substrates. Based on the conclusions drawn from this study, the following routes / recommendation for future SOC electrode preparation by laser sintering can be identified.

- 1. Optimisation of parameters.** Further optimisation of laser parameters required for laser sintering process to fabricate Ni-YSZ electrodes is required. Other materials used for SOCs, such as mix-conducting ceramics, can be considered.
- 2. Materials selection.** It seems that the majority of problems were caused due to the incompatibility between YSZ and Ni in terms of wettability, thermal expansion coefficients and differences in the interaction with the laser. Therefore, to improve the process, Ni electrodes could be laser sintered independently with a desirable structure and then the electrolyte could be tape cast / screen printed onto the Ni.
- 3. Cermet materials.** The possibility of laser sintering porous cermet materials requires further investigation.
- 4. Creating an electrode with graded porosity.** Electrodes with hierarchical porous structure can be an attractive option for efficient cell performance. In graded electrodes the amount of active sites can be maximized by lowering the pore size in the vicinity of the electrolyte. On the other hand the mass diffusion polarization can be minimized by creating bigger pore size close to the electrode surface.

Finally, the two techniques, infiltration and laser sintering, can be combined together. Since the additive manufacturing is generally very promising to fabricate well-defined microstructures, it can be

used to prepare a porous scaffold. The metal phase can subsequently be introduced to the scaffold by infiltration, or any other alternative technique. The combination of the two techniques can potentially enable ‘electrodes by design’ in order to create high performance SOC electrodes.

6.3 Disseminations

Papers in peer-reviewed journals

- M. Lomberg, E. Ruiz-Trejo, G. Offer, N. P. Brandon, (2014). Characterization of Ni-Infiltrated GDC Electrodes for Solid Oxide Cell Applications. *Journal of the Electrochemical Society*, 161(9), F899–F905. doi:10.1149/2.0501409jes
- M. Kishimoto, M. Lomberg, E. Ruiz-Trejo, N. P. Brandon, (2014). Enhanced triple-phase boundary density in infiltrated electrodes for solid oxide fuel cells demonstrated by high-resolution tomography. *Journal of Power Sources*, 266, 291–295. doi:10.1016/j.jpowsour.2014.05.038
- M. Kishimoto, M. Lomberg, E. Ruiz-Trejo, N. P. Brandon, Numerical Modelling of Infiltrated Ni-GDC Electrode Reconstructed with Focused Ion Beam Tomography, *Journal of Power Sources*, (under review)
- V. Duboviks, M. Lomberg, R. C. Maher, L. F. Cohen, N. P. Brandon, G. J. Offer, Zero carbon deposition in metal-infiltrated CGO electrodes for biogas upgrading in Solid Oxide Electrolysis Cells, *Energy Environmental Science*, (under review)

Conference proceedings

- M. Lomberg, E. Ruiz-Trejo, G. Offer, J. Kilner and N. P. Brandon, Characterization of a Novel Ni-Impregnated GDC Electrode for Solid Oxide Fuel Cell and Electrolysis Cell Applications *ECS Trans.* 2013 57(1): 1349-1357; doi: 10.1149/05701.1349ecst (13th International Symposium on Solid Oxide Fuel Cells (SOFC-XIII) Okinawa, Japan.)
- M. Lomberg, G. Offer, J. Kilner, N. P. Brandon, Co-Electrolysis of Steam and Carbon Dioxide in Solid Oxide Electrolysis Cell with Ni-Based Cermet Electrode: Performance and Characterization, Imperial College London, London/UK (10th European SOFC Forum B04 (2012) 537-542, Lucerne, Switzerland.)

- M. Kishimoto, M. Lomberg, E. Ruiz-Trejo and N. P. Brandon, Towards the Microstructural Optimisation of SOFC Electrodes Using Nano Particle Infiltration, ECS Transactions 64, 93 (2014).

Oral presentations

- M. Lomberg, C. Bocking, G. Offer, N. P. Brandon, Additive Laser Manufacturing for Solid Oxide Cells Electrodes Fabrication, (Symposium M: Fuel Cells, Electrolyzers and Other Electrochemical Energy Systems, MRS 22-25 April 2014 San Francisco)
- M. Lomberg, M. Kishimoto, E. Ruiz-Trejo, G. Offer, N.P. Brandon, Characterization of Novel Ni-Impregnated GDC Electrode for Solid Oxide Cells Application, The Hydrogen & Fuel Cell Researcher Conference, December 2013, Department of Chemical Engineering University of Birmingham, UK.

Poster presentations

- M. Lomberg, E. Ruiz-Trejo, G. Offer, J. Kilner and N. P. Brandon, Characterization of a Novel Ni-Impregnated GDC Electrode for Solid Oxide Fuel Cell and Electrolysis Cell Applications ECS Trans. 2013 57(1): 1349-1357; doi: 10.1149/05701.1349ecst (13th International Symposium on Solid Oxide Fuel Cells (SOFC-XIII) Okinawa, Japan.)
- M. Lomberg, E. Ruiz-Trejo, G. Offer, J. Kilner, N. P. Brandon, Characterization of a novel Ni-impregnated GDC Electrode for Solid Oxide Electrolysis Cell application, Workshop on Electrolysis and CO₂-recycling (09-11 April 2013), Riso Laboratories, DTU, Denmark.
- M. Lomberg, G. Offer, J. Kilner, N. Brandon, Co-Electrolysis of Steam and Carbon Dioxide in Solid Oxide Electrolysis Cell with Ni-Based Cermet Electrode: Performance and Characterization Imperial College London, Energy Futures Lab; London/UK (10th European SOFC Forum B04 (2012) 537-542, Lucerne, Switzerland.)
- M. Lomberg, G. Offer, J. Kilner, N. Brandon, Co-electrolysis of steam and carbon dioxide in solid oxide Electrolysis cell with Ni-based cermet electrodes: Performance and characterization, Israel Materials Engineering Conference – IMEC-15, February 28-March 1, 2012, Dead Sea, Israel.

Other contributions

- M. Kishimoto, M. Lomberg, E. Ruiz-Trejo, N.P. Brandon, Towards the Microstructural Optimisation of SOFC Electrodes Using Nano Particle Infiltration, ECS and SMEQ Joint International Meeting October 5-10, 2014, Cancun, Mexico.

- M. Kishimoto, M. Lomberg, E. Ruiz-Trejo, N. Brandon, 3D Imaging and Characterisation of Infiltrated Ni-GDC Electrodes, 11th European SOFC and SOE Forum 2014, 1 – 4 July 2014, Lucerne, Switzerland.
- M. Kishimoto, M. Lomberg, E. Ruiz-Trejo and N. P. Brandon, Towards the Microstructural Optimisation of Solid Oxide Fuel Cell Electrodes, in 15th International Heat Transfer Conference, Kyoto, Japan (2014).

References for Chapter VI

1. B. Mirfakhraei, S. Paulson, V. Thangadurai and V. Birss, *Journal of Power Sources*, **243**, 95 (2013).
2. M. Kishimoto, M. Lomberg, E. Ruiz-Trejo and N. P. Brandon, *Journal of Power Sources*, **266**, 291 (2014).
3. M. Kishimoto, M. Lomberg, E. Ruiz-Trejo and N. P. Brandon, Towards the Microstructural Optimisation of Solid Oxide Fuel Cell Electrodes, in *15th International Heat Transfer Conference*, Kyoto (2014).
4. M. Kishimoto, M. Lomberg, E. Ruiz-Trejo and N. P. Brandon, 3D Imaging and Characterization of Infiltrated Ni-GDC Electrodes, in *11th European SOFC & SOE Forum*, Lucerne (2014).
5. M. Kishimoto, M. Lomberg, E. Ruiz-Trejo and N. P. Brandon, *Journal of Power Sources (under review)* (2014).
6. M. Kishimoto, M. Lomberg, E. Ruiz-Trejo and N. P. Brandon, *ECS Transactions* **64**, 93 (2014).
7. V. Duboviks, M. Lomberg, R. C. Maher, L. F. Cohen, N. P. Brandon and G. J. Offer, *Energy & Environmental Science (under review)* (2014).
8. T. Klemensø, K. Thydén, M. Chen and H.-J. Wang, *Journal of Power Sources*, **195**, 7295 (2010).
9. S. D. Ebbesen, J. B. Hansen and M. Mogensen, *ECS Transactions*, **57**, 3217 (2013).